

Entanglement-Enhanced Matter-Wave Interferometry

by

Graham P. Greve

B.A., University of Chicago, 2014

A thesis submitted to the
Faculty of the Graduate School of the
University of Colorado in partial fulfillment
of the requirements for the degree of

Doctor of Philosophy

Department of Physics

2021

Committee Members:

James K. Thompson, Chair

Dana Z. Anderson

Eric A. Cornell

Adam M. Kaufman

Kelvin H. Wagner

Greve, Graham P. (Ph.D., Physics)

Entanglement-Enhanced Matter-Wave Interferometry

Thesis directed by Prof. James K. Thompson

Using cavity quantum electrodynamics, I have explored interactions between light and matter. In one set of experiments, collective measurements of atomic ensembles of ^{87}Rb atoms are used to generate large amounts of spin-squeezing in a proof-of-principle quantum sensor. These correlations between atoms are a fundamental quantum resource, capable of improving sensor resolution beyond the limits set by individual particle wavefunction collapse. Strong atom-light coupling and quantum non-demolition measurements enable an unprecedented factor of 60 in directly observed phase enhancement beyond the standard quantum limit. These techniques are extended to generate deterministic squeezed states using real-time feedback and homogeneously entangled ensembles guided along the cavity.

In a second set of experiments, momentum-squeezed states are generated by the two most successful cavity-mediated approaches to entanglement: quantum non-demolition measurements and one-axis twisting. Said states are inserted into the first Mach-Zehnder light-pulse matter-wave interferometer with metrological enhancement due to entanglement. In this sensor, free-falling atoms simultaneously traverse two paths through space while also entangled with each other, exploiting the many-body nature of the system. Both Raman and Bragg transitions are used to coherently manipulate matter-waves along the cavity axis, providing sensitivity to gravity. These experiments set a path for a future generation of quantum-enhanced sensors engaging in applied and fundamental physics.

Along the way, we have developed new techniques with potential for broad impacts on physics. These include experiments demonstrating a novel laser cooling mechanism based on Raman adiabatic passage and an atom-loading protocol which maximizes coupling to an intracavity standing wave; methods for driving higher-order transverse cavity modes, generating axially-

smooth intracavity potentials, and narrowing laser linewidths with external optical feedback; and a proposal for continuous real-time tracking of a quantum phase – a fundamentally new capability for precision metrology.

Dedication

To those who face the inferno of the living with constant vigilance and apprehension.

Acknowledgements

First and foremost, James Thompson has been the best advisor one could ask for. His scientific curiosity, lucidity, and precision have served as a model throughout my time at JILA. His help with the experiment during these several years has been invaluable. My undergraduate advisor, Jon Simon, also deserves recognition for his passion and for forever imparting in me the vast opportunities in this rapidly-expanding field of physics.

I was fortunate to work at times with three excellent graduate students – Josh Weiner, Kevin Cox, and Athreya Shankar – all were exemplary scientists and, more importantly, compassionate people. Additional credit is due for the years of support provided by the staff in the electronic shop and machine shop. Fellow graduate students Chengyi Luo and Vanessa Koh have been diligent and quick to learn. I'm sure the experiment is well off in their steady hands.

Outside of lab, I have had a fantastic supporting cast formed mostly from fellow physics students. Albert, Geoffrey, Ignas, Karmela, Michael, and Steve at the University of Chicago; Adam, Andrea, Brant, Brendan, Cale, Charlie, Chris, Ian, James, Jeff, Jen, John, Katie, Lindsay, Ryan, Will, and Zach here in Boulder – I'm thankful I found each of you.

Finally, the numerous opportunities and advantages I have had in life originate with my family, and I will always cherish the formative years spent with my wonderful parents, brother and sister. Thank you for the freedom and trust, for the encouragement, and for the lessons you have taught me. To Rachel, as well, I owe many beautiful memories and an optimism for the future. I have been so lucky in all regards but most obviously for the unending love and support of others.

Contents

Chapter	
1	1
1.1	1
1.2	3
1.3	4
1.4	6
1.5	8
1.6	10
2	13
2.1	13
2.2	15
2.3	18
2.4	19
3	25
3.1	25
4	45
4.1	45
4.2	52

4.3	Narrowing laser linewidths with external optical feedback	54
4.4	Site-dependent loading	56
4.5	Axially-uniform potentials	59
4.6	LG ₀₁ blue dipole guide	60
5	Laser cooling	63
5.1	Measuring temperature	64
5.2	Doppler cooling	68
5.3	Polarization-gradient cooling into the red-detuned lattice	69
5.4	Gray molasses	70
5.5	Raman sideband cooling	71
5.6	SWAP cooling with Raman transitions	73
6	Spin-squeezing using cavity non-demolition measurements	84
6.1	Generating large amounts of useful entanglement	86
6.2	Deterministic spin-squeezing	100
6.3	Spatially homogeneous entanglement using time-averaged measurements	103
7	An entanglement-enhanced matter-wave interferometer	112
7.1	Setup and state preparation	113
7.2	Manipulating matter-waves in a high-finesse cavity	118
7.3	Squeezed momentum states	120
7.4	An entangled matter-wave interferometer	126
7.5	Supplementary details	130
8	Conclusion and outlook	138
8.1	Summary of accomplishments	138
8.2	Looking forward	139

Bibliography	142
---------------------	------------

Appendix

A Acronyms	155
B Raman SWAP cooling: models and simulations	157
C Statistics of inhomogeneous coupling	166

Tables

Table

3.1	System parameters and symbol glossary	26
3.2	Transfer cavity parameters	44
6.2	Parameters for the 18 dB squeezing experiment	97
6.3	Quantum efficiency summary table	98
7.1	Spectroscopic enhancement results for Ch. 7.	113
A.1	Frequently used acronyms	156
B.1	SWAP cooling adiabatic transfer trajectories	163

Figures

Figure

1.1	Rubidium-87 and Bloch sphere overview	5
1.2	Entanglement on the Bloch sphere	7
1.3	Optical and matter-wave interferometers	11
2.1	Introduction to inhomogeneous coupling	15
2.2	Conditional vs. deterministic squeezing	17
2.3	Introduction to one-axis twisting	19
2.4	Raman transitions for interferometry	20
2.5	Mach-Zehnder interferometer sensitivity transfer functions	24
3.1	Rubidium experiment timeline	25
3.2	Optical cavities and spacers overview	30
3.3	Cavity linewidths, transverse mode spacing, and superradiance	31
3.4	2D MOT setup	34
3.5	An interference filter extended cavity diode laser	38
3.6	Homodyne detector circuit diagram	40
3.7	Homodyne detection and path length stabilization	41
3.8	Agile microwave control	43
4.1	Frequency locking chains	46
4.2	Feedback fundamentals with the JILA loop filter	47

4.3	Modulation transfer spectroscopy	48
4.4	Beat note lock of atomic probe to cavity probe laser	50
4.5	Pound-Drever-Hall setup and error signal	52
4.6	Automated relocker	54
4.7	Narrowing lasers with external optical feedback	55
4.8	Site-dependent selection	58
4.9	Homogeneous lattice.	59
4.10	LG ₀₁ donut dipole guide.	62
5.1	Thermometry: ballistic expansion	66
5.2	Velocimetry and sideband spectroscopy	68
5.3	Physical setup of Raman sideband cooling	73
5.4	Landau-Zener transfers for single-photon and Raman transitions	75
5.5	Experimental setup for Raman SWAP cooling in ⁸⁷ Rb	76
5.6	Raman SWAP cooling results	79
5.7	Adiabatic transitions and momentum transfer	81
6.1	Continuous real-time tracking of a quantum phase	86
6.2	Conditional squeezing overview	88
6.3	Conditional spin squeezing results	90
6.4	Probe-induced axial oscillations and thermal radial motion	91
6.5	Atomic probe frequency stabilization scheme	92
6.6	Optical block diagram for conditional squeezing experiments	93
6.7	Electronic block diagram for conditional squeezing experiments	94
6.8	Anti-squeezing and quantum efficiency	99
6.9	Deterministic squeezing protocol	101
6.10	Deterministic squeezing sequence and results	102
6.11	Falling atoms in an optical dipole trap	105

6.12	Homogeneous squeezing sequence and results	107
6.13	Oscillations in probe coupling due to atomic motion	111
7.1	Cavity interferometer system overview.	114
7.2	Frequency hierarchy for the interferometer experiment	115
7.3	Energy diagrams for the interferometer experiment	117
7.4	Manipulating matter-waves in a high finesse cavity	119
7.5	Bragg-pulse superpositions and interferometry	121
7.6	QND momentum squeezing	124
7.7	Tomography of squeezed momentum states	127
7.8	Squeezed interferometer space-time diagram	128
7.9	Spectroscopic enhancement of a squeezed matter-wave interferometer	129
7.10	Interferometer fringes and phase enhancement vs. time	130
7.11	Matter-wave interferometry timing diagrams	132
7.12	Optics layout for the interferometer experiment	133
7.13	Unwanted Bragg transitions	136
7.14	Vibrometer data	137
B.1	Simulation of momentum states during adiabatic transfer	162
B.2	Optimizing momentum transfer in Raman SWAP cooling	165

Chapter 1

Introduction and background

1.1 The second quantum revolution¹

Beginning in large part with descriptions of wave-particle duality, a heuristic interpretation of quantum mechanics was developed in the early 20th century. Born, de Broglie, Schrödinger, Heisenberg, and others worked to formalize the robust mathematical description still used today, though Einstein remained famously skeptical about the role of entanglement. The Einstein-Podolsky-Rosen (EPR) question [1] – whether a pair of particles can be entangled without local hidden variables – disrupted the physics community until, particularly with the advent of Bell’s inequalities, the debate was affirmatively settled to the satisfaction of most physicists. In parallel, the field greatly advanced our understanding of the structure of matter, and it led to transformative inventions including the transistor, the laser, atomic clocks, integrated circuits, and more. But even where the rules of quantum mechanics are known, the implications are not always fully appreciated or accessible.

It took many decades to realize experiments with verifiable amounts of entanglement. As we shall see, such entanglement provides a resource with which to enhance precision measurement experiments. The bulk of this dissertation involves generating unprecedented amounts of entanglement in atomic ensembles with a technique called *spin-squeezing*. Our contributions include lessons in using cavity-assisted quantum non-demolition measurements, deterministically

¹This description is inspired by Alain Aspect’s talk at the 26th International Conference on Atomic Physics, held in Barcelona, Spain.

creating entangled states, producing homogeneously entangled states, and combining entanglement with delocalization in a matter-wave interferometer – all of which stand to benefit current quantum sensors. Such quantum sensors perform precision measurements that are at the forefront of exploration into new and fundamental physics [2–7], and quantum entanglement has already begun to enhance these pursuits [8, 9]. A quantum revolution, however, would not be possible without developing new techniques to control and isolate quantum objects. As a consequence, much attention has been given in this work to the setup, techniques, and measurements that were useful along our particular journey.

Nevertheless, the concept of entanglement remains deeply confounding when considered in a classical framework. A simplified analogy [10] has us consider a bakery that simultaneously produces entangled pairs of cakes, each in a separate oven. The baker finds that when both ovens are opened early, both cakes have risen 9% of the time. Let’s suppose that, as with a soufflé, opening the oven can ruin the cake to a point that it is not worth tasting for quality. Now, the baker also finds that every time the left oven is opened early, the right-side cake tastes good if baked to completion. Every time the right oven is opened early, the left-side cake tastes good. Perhaps the cakes come from the same batter and an early rising batter is the key to a tasty cake. Logically, we expect that if both cakes are fully cooked, then both cakes will taste good at least 9% of the time. The great surprise is that despite our expectation of congruent events, despite thousands of careful tests, *these two entangled cakes never taste good at the same time*².

Now we are in the midst of a second quantum revolution marked by rapid experimental progress. Feynman and others foresaw that entanglement was much more than an academic fact (or a baking curiosity). Entirely new fields have developed to exploit its unique capabilities: quantum information and cryptography, quantum computation and simulation, and quantum metrol-

²As explained carefully in [10], this experiment has been performed using entangled photons, where the initial quantum mechanical polarization state is written $|\psi\rangle = \frac{1}{2} |B_L\rangle |B_R\rangle - \sqrt{\frac{3}{8}} (|B_L\rangle |G_R\rangle + |G_L\rangle |B_R\rangle)$. The good- (G) and bad- (B) tasting eigenstates are related to the rising (R) and not-rising (N) eigenstates through $|B\rangle = \sqrt{\frac{2}{5}} |N\rangle + \sqrt{\frac{3}{5}} |R\rangle$ and $|G\rangle = \sqrt{\frac{2}{5}} |R\rangle - \sqrt{\frac{3}{5}} |N\rangle$.

ogy. The first revolution, built upon the concept of wave-particle duality, harnessed both conceptual and technological breakthroughs to change society. This second revolution utilizes the power of entanglement and individual quantum objects in much the same way.

1.2 Dissertation overview

- Chapter 1 provides an introductory description of cavity quantum electrodynamics as well as context for spin-squeezing, quantum sensors, and matter-wave interferometers.
- Chapter 2 expands upon these topics, providing a theoretical framework for the rest of the dissertation.
- Chapter 3 describes the physical setup of the experiments.
- Chapter 4 details various experimental techniques including frequency locking, a hollow dipole trap for guiding atoms, and a scheme for selectively loading atoms at sites of maximal probe coupling.
- Chapter 5 is a brief departure on various laser cooling methods. In particular, our development of Raman sawtooth wave adiabatic passage (SWAP) cooling is examined.
- Chapter 6 includes results of entanglement-generating experiments in the older apparatus. Using quantum non-demolition (QND) measurements, we observe a $60\times$ sensor improvement due to spin-squeezing, deterministically-squeezed states using feedback, and entanglement between free-falling atoms using spatially-averaged measurements.
- Chapter 7 demonstrates the generation of entangled momentum states through one-axis twisting and QND measurements. These states are then inserted into the first Mach-Zehnder light-pulse interferometer with phase resolution below the standard quantum limit.
- Chapter 8 summarizes results one last time with a view toward the future.
- Appendix A provides a glossary of acronyms.

1.3 Quantum sensors, the Bloch sphere, and the standard quantum limit

The utility of quantum sensors comes from the qubit as a quantum object. It is useful to describe a rubidium atom as a two-state (spin- $1/2$) system with energy eigenstates $|\uparrow\rangle$ and $|\downarrow\rangle$. An understated fact of quantum mechanics is that every 87 -rubidium atom is described by this same system, independent of when it was manufactured or where it exists. In rubidium, the labels $|\uparrow\rangle$ and $|\downarrow\rangle$ usually refer to the hyperfine ground state manifolds separated by $\omega_{\text{HF}} \approx 2\pi \times 6.835$ GHz. Magnetic sublevels and optically-accessible transitions represent experimental complications or conveniences (Fig. 1.1(a and b)). The quantum superposition principle explains that each atom i may be in a simultaneous combination $|\psi\rangle_i = \frac{1}{\sqrt{2}}(a|\uparrow\rangle_i + b|\downarrow\rangle_i)$ with weights a and b describing the probability for a measurement of spin to project the qubit into one eigenstate or the other.

The Bloch sphere is an incredibly powerful framework for visualizing this system. The north and south poles of this sphere correspond to $|\uparrow\rangle$ and $|\downarrow\rangle$ respectively. A superposition state is represented in longitude, and a and b are generally complex numbers so a phase is encoded in latitude. We describe a collection of N identical atoms by a collective Bloch vector $\vec{J} = \langle \hat{J}_x \hat{x} + \hat{J}_y \hat{y} + \hat{J}_z \hat{z} \rangle$ of length $|\vec{J}| \leq N/2$ in a fictitious coordinate space (Fig. 1.1(c)) [11]. Coherences between the states are encoded in \hat{J}_x and \hat{J}_y while the population difference is $\hat{J}_z = \frac{1}{2}(\hat{N}_\uparrow - \hat{N}_\downarrow)$ using collective projection operators $\hat{N}_\uparrow = \sum_i |\uparrow\rangle_i \langle \uparrow|$ and $\hat{N}_\downarrow = \sum_i |\downarrow\rangle_i \langle \downarrow|$ for sums running over all atoms. For brevity, we will frequently write $N_\uparrow \equiv \langle \hat{N}_\uparrow \rangle$ and $N_\downarrow \equiv \langle \hat{N}_\downarrow \rangle$.

The position and momentum of an atom can be manipulated in a variety of ways, some of which will be introduced later. The typical “rules of the game” for quantum sensors, however, involve a limited number of operations which are conveniently represented on the Bloch sphere. Coherent rotations about an axis are governed by the Rabi formula,

$$N_\uparrow(t) = \frac{\Omega^2}{\Omega^2 + \Delta^2} \sin\left(\frac{\sqrt{\Omega^2 + \Delta^2}}{2}t\right)^2 \quad (1.1)$$

for a state initialized in $|\downarrow\rangle$, Rabi frequency Ω , detuning from resonance Δ , and pulse duration

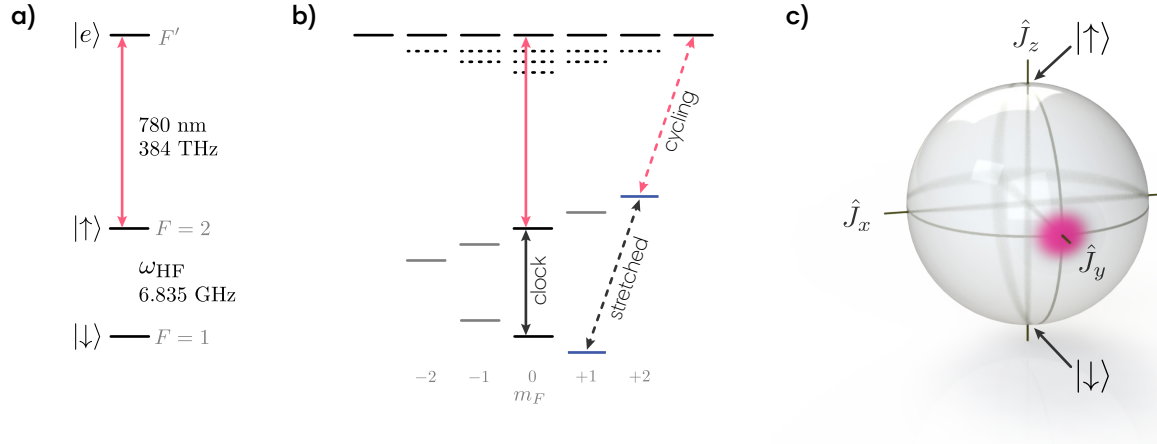


Figure 1.1: **(a)** Simplified Rubidium-87 D₂-line energy diagram showing the ground hyperfine states and one excited state $|e\rangle$. **(b)** Level structure demonstrating excited state structure, Zeeman sublevels (with ground states shifting $m_F \times 0.7$ MHz/G in a magnetic field), and the clock vs. stretched transition. **(c)** The Bloch sphere with basis states $|\uparrow\rangle$ and $|\downarrow\rangle$. The pink noise blob corresponds to a quasi-probability distribution of the orientation of the Bloch vector from trial to trial. A typical quantum sensor works by estimating an accrued azimuthal phase $\phi(t)$.

t .³ This coupling Ω may come in the form of microwaves, as in Ch. 6, or two-photon Raman transitions, as in Ch. 7. For example, a resonant π pulse with $t = \frac{\pi}{\Omega}$ rotates the state to its antipodal position on the Bloch sphere. A $\pi/2$ pulse with $t = \frac{\pi}{2\Omega}$ with phase chosen to define a rotation axis \hat{x} results in a rotation from the superposition to the equator – a superposition represented by the Bloch vector oriented along \hat{y} as in Fig. 1.1(c).

The most precise quantum sensors encode the sensed quantity (*e.g.* field, acceleration, time, *etc.*) in a phase ϕ that accrues in such superpositions. For an atomic clock, for example, the basis states are selected to be insensitive to environmental perturbations, and an evolving phase is read out through Ramsey interferometry and compared against a stable local oscillator (LO)⁴. In an atomic magnetometer, the Zeeman effect shifts the transition frequency between magnetically-sensitive states depending on magnetic field strength, resulting in a corresponding change to the

³Adiabatic passage (Sec. 5.6) is a special case where the Bloch vector precesses about an axis which is smoothly tuned from $\delta = -\infty \rightarrow +\infty$. The elegant result is a highly-efficient transfer of population from one state to the other.

⁴For now, the SI second is defined by 9,192,631,770 periods of the radiation corresponding to the unperturbed hyperfine frequency in cesium-133.

accumulated phase. An electric field detuned from the transition frequency provides an analogue effect through the AC Stark shift (also called the light shift or Stark effect). Here, red-detuned (below resonance) vs. blue-detuned (above resonance) light results in opposite azimuthal phase shifts on the Bloch sphere.

The accumulated sensor phase ϕ must be estimated from quantum measurements to extract the desired information, typically by a rotation about a fixed axis that converts the signal to a population measurement. But projection measurements of a superposition come with an important drawback. The number of atoms N_{\uparrow} can be precisely measured but the details surrounding the collapse of the quantum state can be considered probabilistic. Coin-flipping is a useful analogy. Testing the probability p_0 for heads vs. tails involves flipping the coin many times. Even if $p_0 = 0.5$, each coin flip is independent (uncorrelated) so we expect a Gaussian distribution of results: flipping $N = 1000$ coins results *on average* in 500 landing heads but with standard deviation \sqrt{N} in the number of heads minus the number of tails. Quantum sensors using uncorrelated qubits suffer from the same issue: the independent quantum collapse of each atom leads to an rms angular uncertainty called *the standard quantum limit (SQL)* [12, 13]:

$$\Delta\theta_{\text{SQL}} = 1/\sqrt{N} \text{ rad.} \quad (1.2)$$

1.4 Spin-squeezing

Quantum projection noise leads to the coherent spin-state (CSS) distribution shown on the Bloch sphere in Fig. 1.2(a). The only options for improving fractional precision are to use more atoms or to engineer correlations (entanglement) so that the measurement result of “coin #1” actually gives information about the state of other coins. Using N atoms in a quantum sensor is akin to running N experiments in parallel, but adding entanglement brings the sensor beyond the single-particle paradigm. In other words, quantum entanglement between atoms allows the atoms to conspire together to reduce their total quantum noise relative to their total signal for phase estimation [13, 14]. Maximally-entangled Greenberger-Horne-Zeilinger (GHZ or Schrödinger “cat”)

states (Fig. 1.2(b)) are useful for quantum information, but such states are notoriously prone to decoherence. Gaussian spin-squeezed states (Fig. 1.2(c, d)) have gained increasing popularity in recent years due to their accessibility and utility. As we will see, the spin-squeezing we create is a particularly elegant form of entanglement for metrology as quantum noise is redistributed out of the sensor's phase quadrature and into an orthogonal, unmeasured quadrature. In this dissertation, we realize deeply-entangled states with as much as a 60-fold improvement in phase resolution, but in principle, squeezed states can approach the fundamental quantum bound for metrology known as *the Heisenberg limit* [15],

$$\Delta\theta_{\text{HL}} = 1/N \text{ rad.} \quad (1.3)$$

The history of atomic spin-squeezing goes back many decades [13, 16]. It is closely related to and partly motivated by the copious work done with squeezed light. Significant sensitivity improvements were first seen in free space atomic systems by optically probing ensembles with high resonant optical depth [17–19]. After many years, quantum mechanics is now fulfilling its promise to enhance sensors in the search for new physics including gravitational waves [8] and dark matter [9].

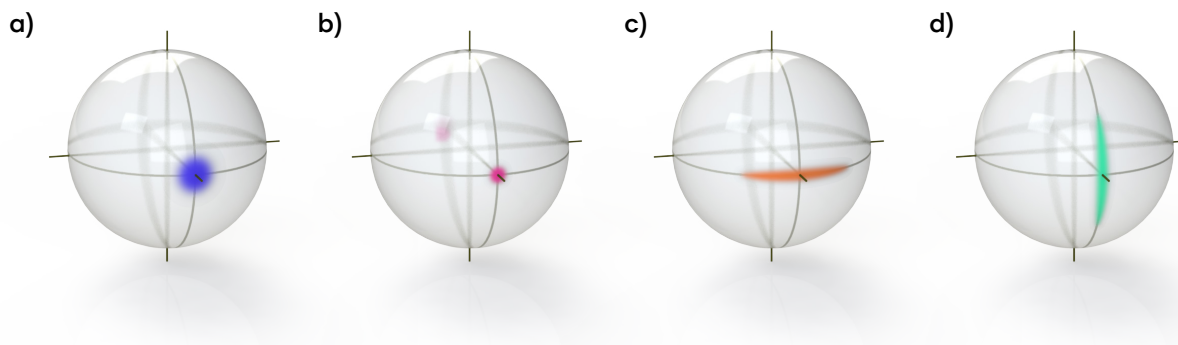


Figure 1.2: **(a)** A coherent spin state arising with each unentangled atom in an identical superposition. **(b)** A maximally-entangled GHZ state with all atoms in one of two possible eigenstates. **(c)** A population-squeezed state, as created by quantum non-demolition measurements. **(d)** A phase-squeezed state, useful for quantum phase sensing.

Quantum-enhanced atomic sensors are not far behind their optical counterparts. Collective cavity-QED systems have now succeeded in generating large amounts [20, 21] of directly observed

entanglement using laser-cooled atomic ensembles [20–25], and the proof-of-principle demonstration of an entanglement-enhanced matter-wave interferometer in Ch. 7 broadens the class of accessible applications. Introducing entanglement into state-of-the-art sensors is a lively area of research, and exploiting the many-body nature of the system will be key for the next generation of quantum devices.

1.5 Cavity quantum electrodynamics

The workhorse for creating squeezing in our experiments is the interaction between atoms and light. For atoms in cavities, the Jaynes-Cummings model of cavity quantum electrodynamics (QED) describes the interaction of a two-level atom with a single electromagnetic mode. The Tavis-Cummings model extrapolates to describe N atoms in a single-mode cavity:

$$\hat{\mathcal{H}} = \hbar\omega_c \hat{a}^\dagger \hat{a} + \sum_{i=1}^N \hbar\omega_a \frac{\hat{\sigma}_i^z}{2} + \hbar g_0 \left(\hat{a} \hat{\sigma}_i^+ + \hat{a}^\dagger \hat{\sigma}_i^- \right). \quad (1.4)$$

where \hbar is the reduced Planck constant; \hat{a} and \hat{a}^\dagger are creation and annihilation operators for a photon in the cavity mode with frequency ω_c ; the raising and lowering operators of each atom are $\hat{\sigma}_i^+ = |\uparrow\rangle_i \langle \downarrow|_i$ and $\hat{\sigma}_i^- = |\downarrow\rangle_i \langle \uparrow|_i$ with transition frequency ω_a ; and g_0 is assumed identical among atoms for now. In our case, we are chiefly interested in the $5^2P_{3/2}$ D₂ manifold which we represent as a single excited state $|e\rangle$ with transition wavelength $\lambda = \frac{2\pi c}{\omega_a} = 780$ nm. Besides the atom number N , three system parameters emerge with importance: the full-width at half maximum (FWHM) cavity linewidth or power decay rate κ , the excited state decay rate Γ , and the single-photon Rabi frequency (or vacuum Rabi frequency) $2g_0$.

The cavity linewidth is fundamental as information dissipates to the outside world via the decay of fields through, in our case, two cavity mirrors. The linewidth $\kappa = f_{\text{FSR}} (T_1 + T_2 + 2T_{\text{loss}})$ is set by mirror power transmission and loss coefficients and the cavity free spectral range, $f_{\text{FSR}} = \frac{c}{2L}$ for linear cavity length L and speed of light c . The free spectral range will also reappear with import as it is the inverse of the round trip time for light which sets the longitudinal cavity mode spacing.

The atomic linewidth Γ plays an analogous role, representing coupling to the free-space con-

tinuum through spontaneous emission. For the ^{87}Rb D₂ line, $\Gamma = 2\pi \times 6.065$ MHz will be referred to as the linewidth of the optically-excited state $|e\rangle$. The lifetime of the excited state is $\tau = 1/\Gamma = 26$ ns. This timescale is fast compared to most parameters in our system, and as a result, the fractional population in the excited state can be conveniently neglected during many calculations through adiabatic elimination of the excited state.

The single-photon Rabi frequency reflects the frequency at which a single excitation is exchanged between the atom and cavity field⁵. We consider a TEM₀₀ standing-wave mode at atomic transition frequency ω_a , $1/e^2$ waist w_0 , and mode volume $V = \frac{\pi w_0^2 L}{4}$. The vacuum energy in this mode is $\frac{1}{2}\hbar\omega_a = \epsilon_0 E_v^2 V$ for rms vacuum field E_v , and hence an atom's dipole coupling $g \equiv \mu E_v/\hbar$ (with interaction strength characterized by dipole matrix element μ) gives the vacuum Rabi frequency for our 780 nm rubidium transitions,

$$2g_0 = |\langle J = 1/2 || e\vec{r} || J' = 3/2 \rangle| \sqrt{\frac{1}{\hbar\epsilon_0} \frac{\omega_a}{V}}. \quad (1.5)$$

The parameters κ , Γ , and g_0 combine into the cooperativity (sometimes called the Purcell factor),

$$\mathcal{C} \equiv \frac{4g_0^2}{\kappa\Gamma}, \quad (1.6)$$

a dimensionless parameter that characterizes the atom-photon coupling regime for a system. Somewhat surprisingly, \mathcal{C} is a purely geometrical quantity (independent of atom or transition) that roughly reflects the probability for an excited atom to scatter a photon into the cavity rather than into free-space. Even more importantly, the collective cooperativity $N\mathcal{C}$ is fundamentally related to processes such as superradiance and spin-squeezing [28–31]. The quantity $N\mathcal{C}$ plays a role similar to the resonant optical depth in free space experiments, setting the rate at which information can be extracted from the system relative to the rate of single-particle decoherence. This collective enhancement with N is an important phenomenon in cavity QED, leading also to stronger atom-light coupling via the collective vacuum Rabi splitting $\Omega_\uparrow = 2g_0\sqrt{N_\uparrow}$ that enables resolving

⁵Conventions for electromagnetic modes and cavities can be found in Siegman's *Lasers* [26] and atomic conventions may be found in Steck's *Alkali D Line Data* [27].

projection noise. The framework for discussing cavity-mediated interactions and entanglement continues with Ch. 2.

1.6 Introduction to matter-wave interferometers

Interferometry makes use of the superposition principle to extract phase information from a system. Two or more parts of this superposition are sent along different conceptual paths, spatial or otherwise, which differ in terms of each trajectory's susceptibility to a sensed quantity. The ever-growing list of applications includes automotive, sea, air and space navigation; flow visualization; biological research; and detection of gravitational waves. Interferometers are particularly suited for inertial sensing, either as gyroscopes detecting rotations through the Sagnac effect⁶ or as accelerometers. Mechanical, resonating, and optical accelerometers and gyroscopes now comprise mature technologies with established markets.

Optical interferometers have been employed for well over a century. Just as optical interferometers can be improved using non-classical correlations, so too can their atomic counterparts. In this work, the term *atom interferometer* is used to include all atom-based interferometers including Ramsey interferometers such as atomic clocks. *Matter-wave interferometers* will refer to a subset of sensors characterized by the use of external momentum states to distinguish the interferometer trajectories. These sensors combine particle delocalization and interference to enable extraordinary measurement precision, accuracy, and bandwidth for a broad and ever-growing range of applications including: searches for dark matter [32, 33], dark energy [34], and gravitational waves [35, 36]; measurements of the fine structure constant [4, 5]; tests of fundamental physics [6, 7, 37, 38]; and inertial sensing [39–41]. Such devices come in many packages and topologies, employing a wealth of clever techniques for improving precision and avoiding external noise. The basis states, the Raman and Bragg transitions, and the effectively infinite-range interactions demonstrated in Ch. 7 are scalable and compatible with today's most precise experiments. With the direct observation of

⁶The Sagnac effect will not be discussed further, but a rotation at rate Ω can be detected by a matter-wave interferometer as $\Phi = 2m\Omega \cdot A/\hbar$, where m is the atomic mass and A is the physical area enclosed by the paths.

phase resolution below the standard quantum limit, we have entered an era of quantum control that aims to truly get the most out of our systems.

Light-pulse matter-wave interferometers operate in direct analogy to optical interferometers, except the role of light and matter are reversed. A Mach-Zehnder interferometer splits light with a beam splitter, redirects the beams, and interferes the waves at a final beam splitter (Fig. 1.3). This language is re-appropriated for the $(\pi/2 - \pi - \pi/2)$ operations of the matter-wave interferometer relevant for this dissertation [42]. For atomic basis states $|\uparrow\rangle = \begin{pmatrix} 1 \\ 0 \end{pmatrix}$ and $|\downarrow\rangle = \begin{pmatrix} 0 \\ 1 \end{pmatrix}$, the light-pulse beam splitters \hat{B} and mirror \hat{M} are modeled by unitary matrices

$$\hat{B} = \frac{1}{\sqrt{2}} \begin{pmatrix} 1 & i \\ i & 1 \end{pmatrix}; \quad \hat{M} = \begin{pmatrix} 1 & 0 \\ 0 & e^{i\Phi} \end{pmatrix}$$

where a relative phase Φ has been inserted by hand. The probability to measure each output mode is $P(\downarrow) = \left| \langle \downarrow | \hat{B} \hat{M} \hat{B} | \downarrow \rangle \right|^2 = \sin^2(\frac{\Phi}{2})$, $P(\uparrow) = \left| \langle \uparrow | \hat{B} \hat{M} \hat{B} | \downarrow \rangle \right|^2 = \cos^2(\frac{\Phi}{2})$. If that phase is smoothly varied through multiple radians, the result is a canonical sinusoidal interferometer fringe.

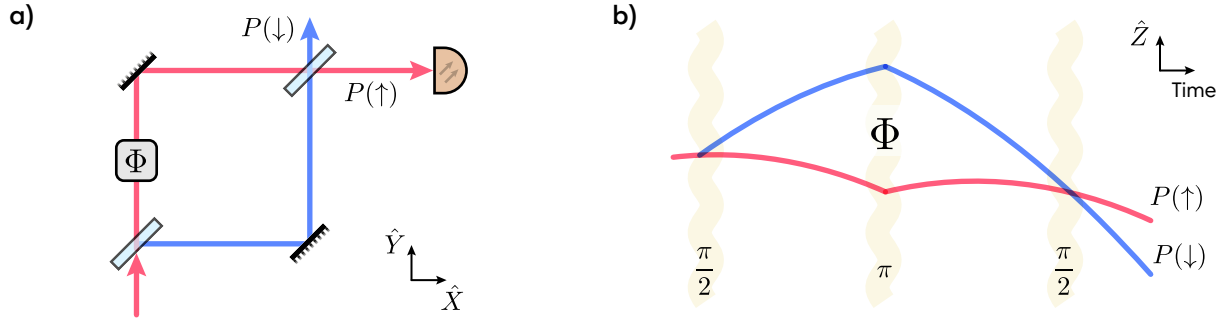


Figure 1.3: **(a)** A Mach-Zehnder optical interferometer. Light traverses both paths (red and blue) and interferes at the output beam splitter. **(b)** A Mach-Zehnder matter-wave interferometer. Atoms traverse both paths, accelerating under gravity and receiving momentum kicks from $\pi/2$ (beam splitter) and π (mirror) light pulses.

To first-order, the total interferometric phase scales with the space-time area enclosed by the matter-wave interferometer,

$$\Phi = a \cdot k_{\text{eff}} \cdot T_{\text{evol}}^2, \quad (1.7)$$

where $\hbar k_{\text{eff}}$ is the momentum imparted by the beam splitter pulses, a is a uniform acceleration to be measured, and the interrogation time T_{evol} is ideally half of the sequence duration. Considerable engineering has gone into magnetic shielding, vibration isolation, and designing miniature, low power, and portable instruments for use in noisy environments. The stability of matter-wave interferometers can ultimately be improved by increasing the momentum separation, increasing the evolution time, and maximizing the duty cycle for interrogation, but the emphasis of Ch. 7 is on decreasing the single shot noise below the standard quantum limit via entanglement. More framework for Mach-Zehnder matter-wave interferometry is found in Sec. 2.4.

Chapter 2

More detailed descriptions

2.1 Optical lattices and homogeneous coupling

Optical lattices are periodic potentials resulting from the interference of two or more beams. In this dissertation, they play a role in trapping, guiding, and cooling atoms and they determine the statistics of quantities such as spectroscopic enhancement. 3D and 2D lattices are excellent for organizing dense arrays of atoms [43], but for our purposes, we are concerned with the properties of a 1D lattice¹. The conservative interaction between the light field and the atom's induced dipole moment causes the AC Stark shift (also frustratingly called the light shift) of potential energy. For a field with detuning Δ from the $|\uparrow\rangle \rightarrow |e\rangle$ atomic transition frequency ω_a , the dipole approximation and rotating wave approximation give an interaction Hamiltonian [44]

$$\hat{\mathcal{H}}_I \approx \left(\frac{\hbar\Omega}{2} |e\rangle \langle \uparrow| \hat{a} e^{i\Delta t} + \frac{\hbar\Omega^*}{2} |\uparrow\rangle \langle e| \hat{a}^\dagger e^{-i\Delta t} \right). \quad (2.1)$$

If the detuning Δ is large compared to the Rabi frequency Ω , second order perturbation theory gives the shifts in energy

$$E_S = \pm \frac{\left| \langle \uparrow | \hat{\mathcal{H}}_I | \downarrow \rangle \right|^2}{\hbar\Delta} = \pm \hbar \frac{\Omega^2}{4\Delta} \quad (2.2)$$

where the positive and negative signs correspond to the AC Stark shift on $|\uparrow\rangle$ and the excited state $|g\rangle$ respectively. The sign of the energy shift therefore depends on the sign of the detuning. By

¹A 2D triangular lattice is used during Raman sideband cooling in Sec. 5.5. The presence of a 1D intracavity lattice technically constitutes the only 3D lattice used in this work.

convention, *blue detuning* refers to $\Delta > 0$ and *red detuning* refers to $\Delta < 0$. The conservative potential for a blue-detuned trap is repulsive and atoms seek intensity minima. A red-detuned trap is attractive and atoms seek intensity maxima.

Consider an electric field $E_1 = E_0 e^{i(\omega_0 t + k_L z)}$ with wavenumber $k_L = 2\pi/\lambda_L$ incident along a two-mirror cavity axis \hat{Z} . Within the cavity, the counter-propagating field interferes to form a standing wave intensity pattern, the axial potential $U(z) = \frac{\hbar\Omega_0^2}{4\Delta} \sin(k_L z)^2$. The peak intensity is thus four times larger than the intensity for a single beam running wave. The total AC Stark shift is proportional to intensity and determines the trap parameters, but often in rubidium we are also concerned with the *differential shift* between $|\uparrow\rangle$ and $|\downarrow\rangle$ as both states are perturbed by the same field. Clearly, the differential Stark shift becomes less relevant as the laser is further detuned.

One more helpful approximation is adopted throughout this dissertation. The bottom of this sinusoidal standing wave looks like a quadratic harmonic oscillator potential, $\sin(k_L z)^2 \approx k_L^2 z^2$ for small z . To good approximation, the axial trap frequency is $\omega_{\text{ax}} = k_L \sqrt{\frac{2U_0}{m_{\text{Rb}}}}$ for trap depth $U_0 = \frac{\Omega^2}{4\Delta}$ and rubidium mass m_{Rb} . For temperature units, we simply rescale the trap depth by \hbar/k_B for the Boltzmann constant k_B . Here we have been discussing the axial potential, but the Gaussian modes supported within the cavity also provide a radial trapping potential [26]. Fortunately, a Gaussian is also expanded as a quadratic, $e^{-\frac{2r^2}{w_0}} \approx 1 - \frac{2r^2}{w_0}$, so the above picture still applies. Little more will be said except that the timescale for radial trapping frequency differs by a few orders of magnitude in our experiment. Typical axial trap frequencies are of order $\omega_{\text{ax}} \sim 2\pi \times 100$ kHz and typical radial trap frequencies are of order $\omega_{\text{rad}} \sim 2\pi \times 1$ kHz.

Finally, trapping atoms at periodic “pancakes” along the cavity axis leads to a recurring topic within this dissertation: *inhomogeneous coupling* between the standing wave lattice and the standing wave probe modes. In general, atoms are spaced at $\lambda_L/2$ intervals and they couple to a probe with unrelated wavelength λ_p . Atoms at positions with no probe light do not contribute to a measurement. Because atoms are spread out over 10^3 lattice sites spread over 1 mm, the distribution of atom-probe couplings is essentially uniform. More will be said in Ch. 4, and there are a number of ways to avoid this including site-dependent loading (Sec. 4.4), spatially-averaging the position

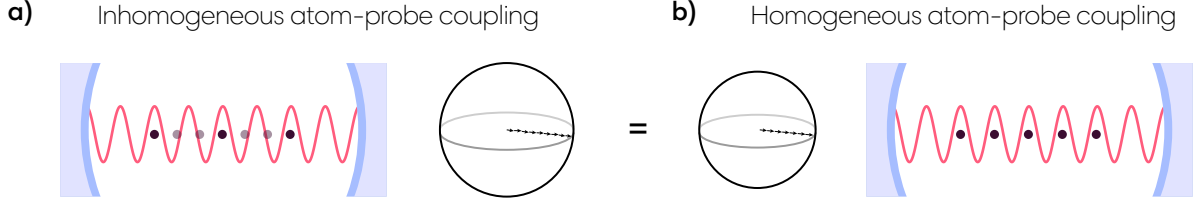


Figure 2.1: Equivalence between **(a)** an inhomogeneously-coupled ensemble of N_0 atoms and **(b)** slightly fewer N homogeneously-coupled atoms and a smaller Bloch sphere [45]. In this case, spatial inhomogeneity arises from a mismatch between probe and the periodic trapping of the 1D intracavity lattice (not shown).

of the atoms (Sec. 6.3), probing with a running wave in a ring cavity, or using a commensurate lattice [21]. For several of our experiments, atoms are trapped over many wavelengths of the probe standing wave such that the atom-probe couplings form a nearly uniform distribution. In this case, we simply define effective quantities $N = \frac{2}{3}N_0$, $g_{\text{eff}}^2 = \frac{3}{4}g_0^2$, and $\mathcal{C} = \frac{3}{4}\mathcal{C}_0$ [20, 45–47] relative to a system with completely homogeneous coupling. This ensures consistency between the measured projection noise and the size of the observed vacuum Rabi splitting discussed in the next section.

2.2 Cavity quantum non-demolition measurements

Quantum non-demolition measurements are used to gain information about atoms through their effect on a probing field. In the weak-excitation limit, where the number of cavity photons or atomic excitations is small compared to N , the atom-cavity Hamiltonian (Eq. 1.4) in the $|\uparrow\rangle \rightarrow |e\rangle$ rotating frame becomes [29]

$$\hat{\mathcal{H}}_{\text{QND}} = \hbar\delta_c\hat{a}^\dagger\hat{a} + \hbar\sqrt{N_\uparrow}g_0\left(\hat{j}\hat{a}^\dagger + \hat{j}^\dagger\hat{a}\right) \quad (2.3)$$

with cavity detuning $\delta_c = \omega_c - \omega_a$ and atomic raising and lowering operators $\hat{j}^\dagger \approx \hat{J}_+/\sqrt{N_\uparrow}$ and $\hat{j} \approx \hat{J}_-/\sqrt{N_\uparrow}$ modifying the collective raising and lowering operators $\hat{J}_\pm = \sum_i \hat{\sigma}_i^\pm$. The $\sqrt{N_\uparrow}$ collective enhancement factor that emerges is crucial for resolving projection noise.

Without atoms, the cavity has a single Lorentzian transmission profile associated with ω_c . Reference [29] uses input-output theory to derive the eigenfrequencies of the new normal modes

for the coupled atom-cavity system,

$$\omega_{\pm} = \frac{\delta_c \pm \sqrt{\delta_c^2 + \Omega_{\uparrow}^2}}{2}. \quad (2.4)$$

The coupling of light to atoms in $|\uparrow\rangle$ modifies the round-trip phase of light through repeated absorption and emission, giving rise to a separation of the normal modes by the collective vacuum Rabi frequency $\Omega_{\uparrow} = \sqrt{N_{\uparrow}}2g_0$ at $\delta_c = 0$. The transmission or reflection dip associated with bare cavity resonance shifts (and broadens) as a result of atoms in $|\uparrow\rangle$. Because the cavity does not reveal which atoms are in $|\uparrow\rangle$, scanning a probe laser across the dressed cavity resonance amounts to a collective population measurement, and the degree to which the measurement can be considered non-demolition is determined by the number of free-space scattered photons per atom required to resolve the frequency shift.

We now restrict ourselves to the problem of measuring an unentangled coherent superposition $|\psi\rangle = \prod_{i=1}^N \frac{1}{\sqrt{2}} (|\uparrow\rangle + |\downarrow\rangle)$ described by the Bloch vector $\vec{J} = J\hat{x}$. On average, $N_{\uparrow} = N_{\downarrow} = N/2$, but there are anti-correlated projection noise fluctuations in the populations, $\Delta N_{\uparrow} = \Delta N_{\downarrow} = \sqrt{N}/2$. In terms of the pseudospin projection operators ($\hat{J}_z = \frac{1}{2}(\hat{N}_{\uparrow} - \hat{N}_{\downarrow})$, etc.) the variances are $(\Delta J_z)^2 = (\Delta J_y)^2 = N/2$. The ratio of the rms spin projection noise amplitude to the length of the Bloch vector sets the standard quantum limit for angular resolution (Eq. 1.2), $\Delta\theta_{\text{SQL}} = \Delta J_z/|J| = 1/\sqrt{N}$ and $\Delta\phi_{\text{SQL}} = \Delta J_y/|J| = 1/\sqrt{N}$.

Using Eq. 2.4, the rms fluctuations of the mode frequency ω_+ due to ΔN_{\uparrow} give quantum projection noise in frequency units,

$$\Delta\omega_{\text{QPN}} = \left| \frac{d\omega_+}{dN_{\uparrow}} \right| \Delta N_{\uparrow} = \frac{g_0}{2\sqrt{2}} \frac{\Omega_{\uparrow}}{\sqrt{\Omega_{\uparrow}^2 + \delta_c^2}}. \quad (2.5)$$

The experiments of this dissertation are restricted to the far-detuned limit, $\delta_c \gg \Omega_{\uparrow}$, so we may further simplify $\omega_+ = \delta_c + \frac{g_0^2 N_{\uparrow}}{\delta_c}$ and $\Delta\omega_{\text{QPN}} = \sqrt{\frac{N_{\uparrow}}{2}} \frac{g_0^2}{\delta_c}$. More commonly, we write the cavity frequency shift $\omega'_c - \omega_c \approx \frac{g_0^2 N_{\uparrow}}{\delta_c}$. Experimentally, these quantities must be compared to fundamental and technical limitations on the detection system. The problem then reduces to measuring a cavity frequency shift with better than 10 – 100 kHz resolution without inducing too much single-particle

wavefunction collapse.

The non-demolition measurements described here localize a squeezed state with reduced fluctuations ΔJ_z , but the trial-to-trial J_z can be considered to be drawn from the original coherent state distribution. With *conditional squeezing*, the value of a pre-measurement J_{zp} is used to subtract quantum noise from a final measurement J_{zf} [16, 17]. Fluctuations in the quantity $(J_{zf} - J_{zp})$ are then compared to the standard quantum limit (Fig. 2.2(a)). It is crucial that the pre-measurement preserves the coherence or *contrast* of the quantum state. With high quantum efficiency and high collective cooperativity NC , cavity QND measurements have realized the largest amounts of spin squeezing to date [20, 21]. The pre-measurement can also be used to deterministically drive the state to a target J_z value such that J_{zf} alone demonstrates fluctuations below the standard quantum limit (Fig. 2.2(b)). The treatment of QND measurements here has glossed over details of spin-flips, excited state structure, atomic motion, inhomogeneous coupling, and other issues, but these details are discussed in the corresponding experiment chapters and in App. C.

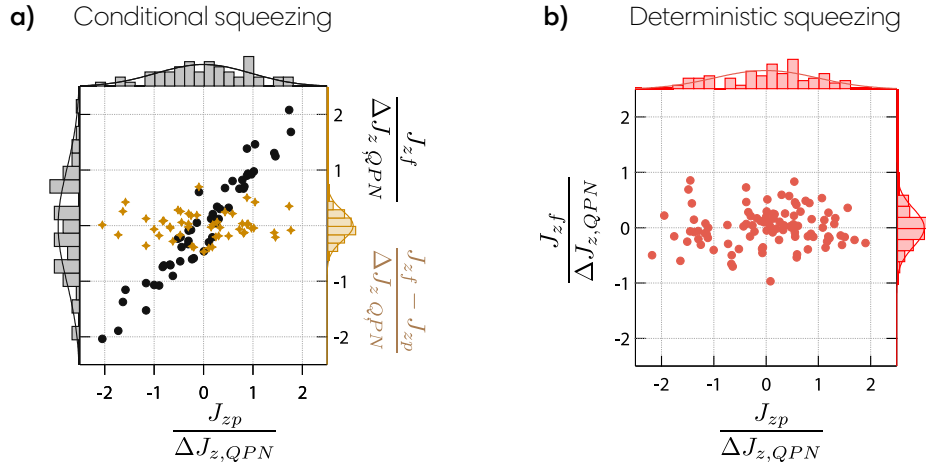


Figure 2.2: **(a)** In conditional squeezing, the pre- and final measurements are strongly correlated (black) but either measurement on its own has resolution worse than the standard quantum limit. Fluctuations of the difference $(J_{zf} - J_{zp})$ reveal sub-SQL statistics (gold). **(b)** With deterministically-squeezed states, the final measurement alone has sub-SQL resolution. Data is from the experiment in Sec. 6.2.

2.3 One-axis twisting via cavity squeezing

The linear Hamiltonian $\hat{\mathcal{H}} = \hbar\omega\hat{J}_z$ causes a precession on the Bloch sphere at a constant rate about \hat{z} . For example, the differential AC Stark shift between two states modifies the transition frequency to this effect. More interestingly, the nonlinear one-axis twisting Hamiltonian

$$\hat{\mathcal{H}}_{\text{OAT}} = \chi_{\text{OAT}}\hat{J}_z^2 \quad (2.6)$$

describes a precession at a rate proportional to J_z with resultant shearing of a coherent state into a metrologically useful spin-squeezed state [14]. Such states are also deterministically generated, independent of detector performance. This Hamiltonian has been realized with optical cavities and in other physical systems including collisional interactions [48–55]. Achieving these dynamics through cavity-mediated interactions has been described [30, 31] and demonstrated [25, 56] through an approach sometimes called *cavity feedback*. As with other squeezing mechanisms, there is a scaling of the observable squeezing $W \propto 1/\sqrt{N\bar{C}}$ set by dissipation. Much work has gone into characterizing the role played by curvature of the Bloch sphere, which sets a theoretical limit of $W \sim 1/N^{\frac{2}{3}}$ [31]. In contrast, interest in achieving the two-axis counter-twisting Hamiltonian $\hat{\mathcal{H}}_{\text{TAT}} = \chi \left(\hat{J}_z\hat{J}_y + \hat{J}_y\hat{J}_z \right)$ is driven by its Heisenberg-limited scaling, $W \sim 1/N$.

In the cavity-mediated one-axis twisting scheme, a fixed frequency drive tone is offset on the slope of a dressed cavity resonance by $\delta_p \gtrsim \kappa/2$ (Fig. 2.3(a)). The spin populations tune the cavity closer to or further from resonance with the drive tone such that the intracavity probe intensity is linearly dependent on J_z . This light creates an AC Stark shift on the states that therefore depends on the population of atoms in $|\uparrow\rangle$. In practice, the coherent state of an ordinary laser leads to phase fluctuations imparted by photon shot noise and a Hamiltonian $\hat{\mathcal{H}} \propto \hat{a}^\dagger \hat{a} \hat{J}_z$. Still, the unitary interactions drive shearing of the atomic quantum noise distribution with a resulting squeezed state minimum noise projection oriented at a small angle α_0 from \hat{z} (Fig. 2.3).

Experimentally, the protocol is simplified if one works symmetrically-detuned so as to be insensitive to atom number fluctuations, and with $\delta_p = \kappa/2$ to suppress free-space scattering. In our system, the cavity is near the $|\uparrow\rangle \rightarrow |e\rangle$ transition. Operating at larger detunings both enables

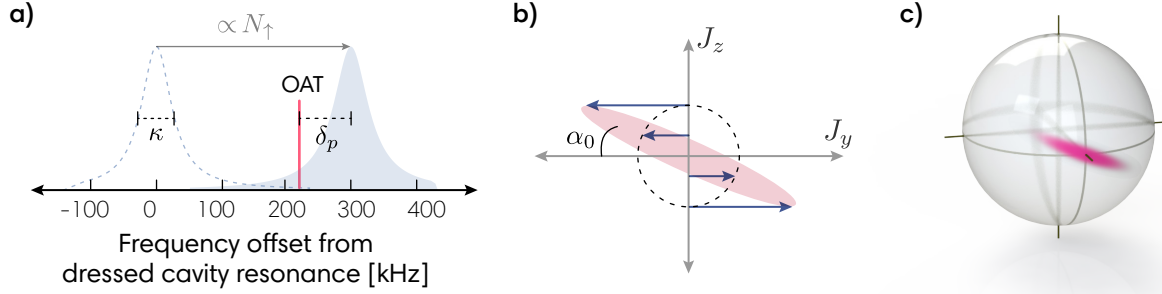


Figure 2.3: **(a)** For one-axis twisting, a tone is applied at a fixed frequency δ_p from the dressed cavity resonance. The amount of light entering the cavity interacts with the quantum state as a differential light shift, driving shearing of the quasi-probability distribution (pink) seen **(b)** in the J_y - J_z plane or **(c)** on the Bloch sphere.

linearized regime even in the presence of shot-to-shot total atom number fluctuations and reduces the QND interactions that can compete with the desired one-axis twisting interaction [57]. In general, as NC increases, one finds an optimal balance between scattering and QND broadening with δ_p further from cavity resonance. Finally, it is worth mentioning that one-axis twisting interactions are also amenable to extensions such as two-axis twisting for more squeezing [31] and signal amplification schemes [58–60].

2.4 Description of a Raman Mach-Zehnder interferometer

The toolkits of modern interferometers include various techniques: Bragg pulses (especially for large momentum transfer), Bloch oscillations, conjugate geometries, *etc.* In this dissertation, we opt to build a relatively simple light-pulse Mach-Zehnder interferometer using stimulated Raman transitions. This technique was first explored in Ref. [42] using moving beams of sodium atoms. This interferometer's sensitivity to gravity g originates from either Doppler shifts of the Raman tones or from laser phases imprinted at the position of a wavepacket. There are many excellent resources and reviews for matter-wave interferometry that explore the origins and equivalence of these ideas in further detail [61–64].

For our Raman transitions, there are two counter-propagating beams with wavevectors \vec{k}_1

and $\vec{k}_2 \approx -\vec{k}_1$ and optical frequencies ω_1 and ω_2 (Fig. 2.4). The beams have a difference frequency $\omega_L = \omega_2 - \omega_1$ near ω_{HF} , resonant with the ground states of a three-level atom. For simplicity, we write $k \equiv k_1 = -k_2$. The electric fields of the lasers are

$$E_1(z, t) = \hat{\epsilon}_1 E_{0,1} e^{i(\omega_1 t - k_1 z + \varphi_1^0(t))} + \text{c.c.} \quad (2.7)$$

$$E_2(z, t) = \hat{\epsilon}_2 E_{0,2} e^{i(\omega_2 t - k_2 z + \varphi_2^0(t))} + \text{c.c.} \quad (2.8)$$

with polarizations $\hat{\epsilon}_1, \hat{\epsilon}_2$, single-photon Rabi frequencies $\Omega_j = \frac{e}{\hbar} \langle \uparrow | \vec{r} \cdot \vec{E}_{0,j} | \downarrow \rangle e^{i\varphi_j^0}$ and initial phases φ_1^0, φ_2^0 . The phase difference between the two Raman lasers at the center of the wavepacket at a certain point in time will be denoted with ϕ . The intermediate state is adiabatically eliminated to reduce the problem to that of a two-level atom (see App. B or [61, 65]). The resulting dynamics are described by the Rabi formula using two-photon Rabi frequency $\Omega_{\downarrow\uparrow} = \frac{\Omega_1^* \Omega_2}{2\Delta}$ and the two-photon detuning δ of the lasers from the atomic transition frequency. When the lasers are not quite on resonance, the effective Rabi frequency is $\Omega_R = \sqrt{\Omega_{\downarrow\uparrow}^2 + \delta^2}$.

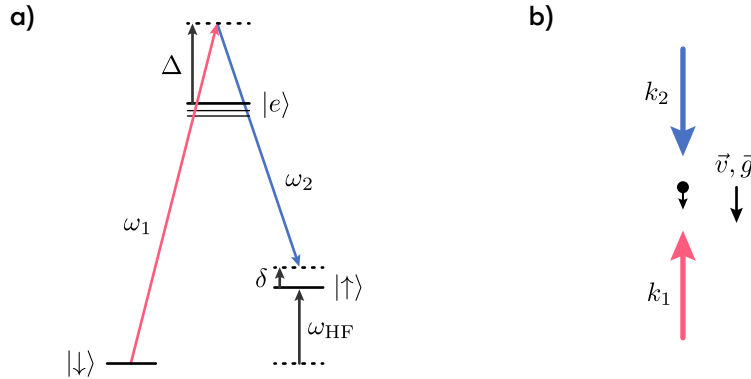


Figure 2.4: **(a)** Energy-level diagram for Raman transitions for interferometry. The excited state $|e\rangle$ has negligible population and will be adiabatically eliminated. **(b)** Beam configuration for velocity-sensitive Raman transitions.

In the presence of the lasers, the energies are $\hbar\omega_{\downarrow}$ and $\hbar\omega_{\uparrow}$ for the atomic states $|\downarrow\rangle$ and $|\uparrow\rangle$. Consider a cloud of ^{87}Rb atoms cooled, prepared in $|\downarrow\rangle$, and selected with the same momentum $p = mv_0$ along the cavity axis. Absorption from one beam and emission into the other necessitates $2\hbar k$ momentum kicks, and the internal spin state and the external momentum state of the atom

are correlated as a result. In particular, atoms in $|\downarrow, p\rangle$ are coupled to $|\uparrow, p + 2\hbar k\rangle$. Other states are neglected for this discussion as non-resonant, unpopulated, or adiabatically eliminated, and hence we will omit the momentum labels. Note that in an atom's frame of reference, the frequency of each Raman tone is Doppler shifted kv for an atom at velocity $v = gt$ after accelerating for time t , and hence the Raman resonance is shifted by $(k_1 - k_2)gt$. The total detuning from resonance δ is determined not only by the laser difference frequency ω_L but also by the atom's velocity, the recoil shift, AC Stark shifts, *etc.*,

$$\delta = \omega_L - \omega_{\text{HF}} - (k_1 - k_2)v - \hbar \frac{(k_1 - k_2)^2}{2m} \quad (2.9)$$

Mach-Zehnder interferometers are characterized by a $\frac{\pi}{2} - \pi - \frac{\pi}{2}$ pulse sequence separated by free evolution time T_{evol} as described in Sec. 1.6. The $\pi/2$ and π pulses have durations of τ and 2τ , respectively. The effects on the probability amplitudes C_\uparrow and C_\downarrow from each pulse and free evolution are given by

$$\begin{pmatrix} C_\downarrow(t) \\ C_\uparrow(t) \end{pmatrix} = M \begin{pmatrix} C_\downarrow(t_0) \\ C_\uparrow(t_0) \end{pmatrix} \quad (2.10)$$

with evolution transfer matrix [66, 67]

$$M(t_0, t, \Omega_R, \phi) = \begin{pmatrix} \cos\left(\frac{\Omega_R t'}{2}\right) e^{-i\omega_\downarrow t'} & -ie^{i(\omega_L t_0 + \phi)} \sin\left(\frac{\Omega_R t'}{2}\right) e^{-i\omega_\downarrow t'} \\ -ie^{-i(\omega_L t_0 + \phi)} \sin\left(\frac{\Omega_R t'}{2}\right) e^{-i\omega_\uparrow t'} & \cos\left(\frac{\Omega_R t'}{2}\right) e^{-i\omega_\uparrow t'} \end{pmatrix} \quad (2.11)$$

with $t' \equiv t - t_0$. The free evolution matrix simplifies with $\Omega_R = 0$ to

$$M(T_{\text{evol}}) = \begin{pmatrix} e^{-i\omega_\downarrow T_{\text{evol}}} & 0 \\ 0 & e^{-i\omega_\uparrow T_{\text{evol}}} \end{pmatrix}. \quad (2.12)$$

The full transfer matrix for the Mach-Zehnder interferometer is the product of five matrices,

$$M_{\text{MZ}} = M(2T + 3\tau, \phi_3, \Omega, \tau) M(T + 3\tau) M(T + \tau, \phi_2, \Omega, 2\tau) M(\tau) M(0, \phi_1, \Omega, \tau) \quad (2.13)$$

where the phases ϕ_1, ϕ_2, ϕ_3 are the Raman tone phase differences imprinted at the position of the center of the wavepacket during each of the Raman pulses. For population beginning in $|\downarrow\rangle$,

$C_{\downarrow}(0) = 1$, the probability of measuring an atom in $|\uparrow\rangle$ after the interferometer gives the interferometer fringe

$$P_{\uparrow}(2T + 3\tau) = \frac{1 - \cos(\phi_1 - 2\phi_2 + \phi_3)}{2} \quad (2.14)$$

and the interferometric phase $\Phi = \phi_1 - 2\phi_2 + \phi_3$ comes from the relative phase accumulated between the two arms of the interferometer as before. These phases can be evaluated with $\phi(t) = \int_{t_0}^t \delta(t') dt'$ at $\phi_j = \phi(t_j)$ where t_0 is the time of the first $\pi/2$ pulse.

As atoms accelerate due to gravity, the differential Doppler shift of the counter-propagating tones chirps linearly, and the difference frequency is ramped at $b = 2kg$ to remain on resonance. Evaluating Φ with $\omega_1 - \omega_2 - (k_1 - k_2) \cdot gt$ gives, to lowest order, the Mach-Zehnder interferometer phase shift:

$$\Phi = (2kg)T_{\text{evol}}^2. \quad (2.15)$$

Experimentally, the acceleration g is found by determining the value of b required to cancel the phase shift induced by gravity,

$$\delta\Phi = (2kg - b)T_{\text{evol}}^2, \quad (2.16)$$

In reality, the interferometer is also sensitive to phase noise from the Raman pulses, mirror vibrational noise, and to all mechanisms that modify the transition frequency during the sequence. Differentiating between a signal that arises from gravity versus some noise is a significant challenge, so to understand the sensitivity of this interferometer to gravity, laser phase noise, vibrations, and other effects, we consider $\delta\Phi$, the change in interferometric phase due to an infinitesimal phase jump $\delta\phi$ at time t :

$$g_s(t) = \lim_{\delta\phi \rightarrow 0} \frac{\delta\Phi(\delta\phi, t)}{\delta\phi}. \quad (2.17)$$

An interferometer is ordinarily operated on the side of fringe, $\Phi = \pi/2$, for maximum sensitivity. For infinitesimally short Raman pulses, the effect of a phase excursion during the evolution time yields $\delta P(|\uparrow\rangle) \approx \pm\delta\phi/2$ where the positive and negative responses differ for the first and second

windows. To model the effect of an excursion during a finite pulse, we break the transfer matrix into two composite pulses which occur with phases ϕ and $\phi + \delta\phi$. Following [66], we shift the time origin to be at the middle of the π pulse so that we can write the transfer function, odd and given only for $t > 0$ (Fig. 2.5(a)),

$$g_s(t) = \begin{cases} \sin(\Omega_R t) & 0 < t < \tau \\ 1 & \tau < t < T_{\text{evol}} + \tau \\ -\sin(\Omega_R(T_{\text{evol}} - t)) & T_{\text{evol}} + \tau < t < T_{\text{evol}} + 2\tau \end{cases} \quad (2.18)$$

The interferometric phase shift can then be calculated for an evolving differential phase between the Raman tones $\phi(t)$ as

$$\delta\Phi = \int_{-\infty}^{\infty} g_s(t) \frac{d\phi(t)}{dt} dt. \quad (2.19)$$

The frequency-dependent transfer function of the interferometer $H(\omega)$ comes from considering its response to a sinusoidal modulation $\phi(t) = A_0 \cos(\omega_0 t + \varphi)$. The rms response, averaged over a random distribution of φ , gives $\delta\Phi_{\text{rms}} = |A_0 \omega_0 G(\omega)|$ where $G(\omega) = \int_{-\infty}^{\infty} e^{-i\omega t} g_s(t) dt$ is the Fourier transform of the sensitivity function. The transfer function $H(\omega) = \omega G(\omega)$ yields the rms interferometric phase noise,

$$(\sigma_{\Phi, \text{rms}})^2 = \int_0^{\infty} |H(\omega)|^2 S_{\phi}(\omega) d\omega \quad (2.20)$$

for some power spectral density of Raman phase noise $S_{\phi}(\omega)$ (typically to be compared to the standard quantum limit in radians). Explicitly, the Mach-Zehnder transfer function is

$$H(\omega) = \omega \frac{4i\Omega_R}{\omega^2 - \Omega_R^2} \sin\left(\frac{\omega(T_{\text{evol}} + 2\tau)}{2}\right) \left[\cos\left(\frac{\omega(T_{\text{evol}} + 2\tau)}{2}\right) + \frac{\Omega_R}{\omega} \sin\left(\frac{\omega T_{\text{evol}}}{2}\right) \right] \quad (2.21)$$

which is plotted for our experiment in Fig. 2.5(b). The next steps in the procedure depend on the effect S_{ϕ} considered and are continued in [64, 66]. In our system, Raman laser frequency noise is suppressed by symmetrically detuning the tones from two cavity modes. Mirror vibrations alter the reference frame and appear as real inertial forces (Sec. 7.5.5) and start to become relevant close to the longest evolution times we use.

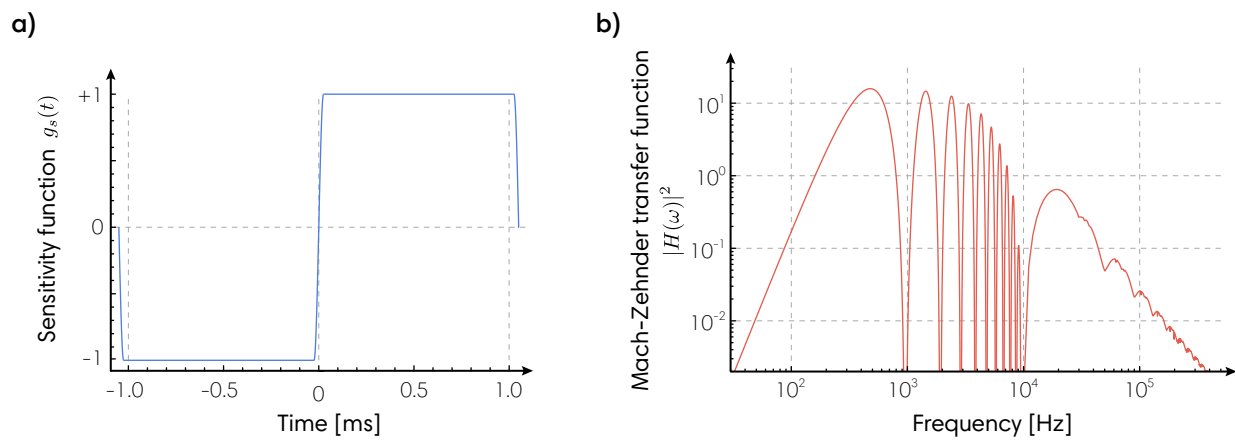


Figure 2.5: The Mach-Zehnder sensitivity transfer functions **(a)** $g_s(t)$ and **(b)** $|H(\omega)|^2$ plotted for our experimental parameters ($\Omega_R = 2\pi \times 10$ kHz, $T_{\text{evol}} = 1$ ms, $\tau = 25$ μ s). For the overall transfer function $|H(\omega)|^2$, oscillations are evident at $1/(T_{\text{evol}} + \tau)$ and the low-pass effect is set by $1/(\omega\Omega_R^2)$. Oscillations above 1×10^4 Hz are smoothed with rms values over a cycle.

Chapter 3

Experimental apparatus

3.1 Overview

The electronic structure and moderate mass of rubidium make it one of the simplest atoms to study, and the maturity of related technologies, *e.g.* optical coatings, laser diodes, commercial Bose-Einstein condensate sources, *etc.*, make it among the most practical. In atomic physics, the element remains among the most active scientific testbeds for exploring fundamental physics through quantum information and precision measurements. Since first light in 2007, the Thompson lab rubidium apparatus has intentionally facilitated flexible, principally proof-of-principle projects. Apart from a common preparation paradigm – collect atoms in a 3D magneto-optical trap (MOT), cool into a red-detuned intracavity lattice, optically-pump into an initial state – the projects have varied significantly.

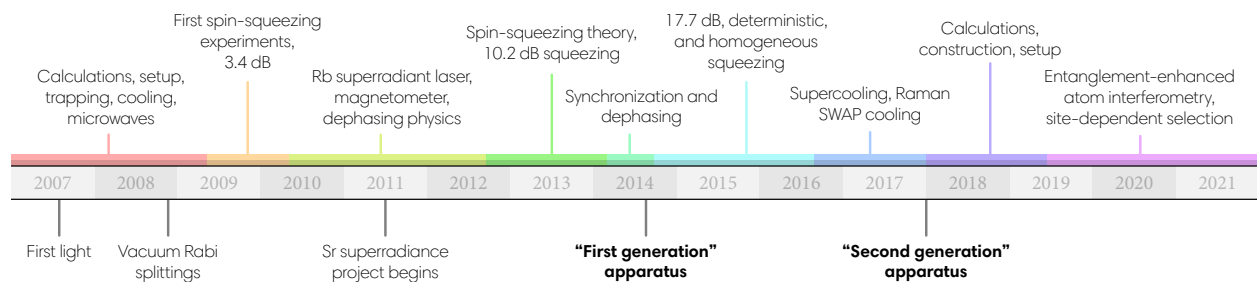


Figure 3.1: A timeline of Thompson lab rubidium experiment developments. The top labels attempt to delineate distinct experimental directions. The bottom labels mark a few important events and mark the first and second generation apparatus described in this work.

A timeline of the history of the apparatus is provided in Fig. 3.1. Two distinct systems were used during the work of this dissertation. The “first generation” apparatus detailed below was moved and improved during the summer of 2014. It was used beginning with various spin-squeezing experiments and retired at the end of the SWAP cooling experiment in 2017. For the “second generation” apparatus, the cavity was redesigned, a 2D MOT was added, and the vacuum system was rebuilt with future experiments in mind.

In this chapter, experiment subsystems are described with particular attention towards improvements unique to the second generation apparatus. A comparison of the typical experimental regimes is provided in Table 3.1. The rest of the chapter elaborates on the control system, vacuum chambers, glass cells, science cavities, atom sources and 2D MOT, magnetic coils, lasers, homodyne detector, microwaves, and transfer cavity.

Description	Symbol	First gen.	Second gen.
Typical atom number	N	5×10^5	1×10^3
Rb transition		Stretched/cycling	Clock
Cavity linewidth (FWHM)	$\kappa/2\pi$	3.15(10) MHz	56.2(2) kHz
Cavity finesse	\mathcal{F}	2532(80)	132000(1000)
Cavity length	L	1.85 cm	2.21 cm
Cavity free spectral range	$\text{FSR}/2\pi$	8.105 GHz	6.788 GHz
Mode waist	w_0	70(1) μm	72(1) μm
Cooperativity	\mathcal{C}	0.056(7)	2.76(5)

Table 3.1: System parameters for both cavity QED systems given for 780 nm light. Symbols are used throughout the dissertation. Cooperativities $\mathcal{C} = \frac{4g_0^2}{\kappa\Gamma}$ are given for the optical cycling transition assuming homogeneous atom-cavity coupling.

3.1.1 Control system and software

All of the experiments here are coordinated with software written in LabVIEW. The main program allows easy modification of control sequences, compiling spreadsheet-style input into instructions for several analog and digital input/output boards (PN: National Instruments PCIe

6259, PCI 6233, PCI 6733), direct digital synthesizers (DDSs, PN: Analog Devices AD9959), and CCD or CMOS cameras (PN: Basler scA640-70gm, scA750-60gm; FLIR Chameleon3 CM3-U3-1352M). The program also interfaces with several commercial instruments and provides a host of custom-tailored monitoring and data analysis tools. Sequences typically run with 1 Hz repetition rates synchronized with a 60 Hz line voltage trigger. Additional analysis is performed with Igor Pro, Mathematica, and Python.

3.1.2 Experiment chamber and vacuum system

The structural foundation of the apparatus is a spherical cube from Kimball Physics with 4.5" top/bottom, 2.75" side CF flanges. The top port supports the glass cell where the atoms are trapped and manipulated. The side and bottom ports are used for attaching electrical feedthroughs, vacuum pumps, and for the first generation, a rubidium source. One side port is reserved for an AR-coated window, and beams guided through this window bounce off a 45° mirror to couple into the cavity.

An ultra-high vacuum pressure is maintained within the experiment chamber as is necessary for long trap lifetimes. During the initial pump down with a dry scroll pump and turbo pump, it is imperative to wrap the apparatus with resistive heater tapes and "bake out" contaminants for many hours. After the initial pump down, low pressure is maintained within the science cell by an ion pump. For the first generation, a Varian VacIon Starcell (50 L/s, PN: 9191340) ion pump ran continuously to achieve typical pressures of 10^{-9} Torr. For generation two, it was replaced with a 75 L/s pump from Gamma Vacuum (PN: 75S-DI-2V-SC-N-N) that reaches pressures in the 10^{-8} Torr range, limited by the low-temperature bakeout necessitated by the construction of the science cell. Pressure P is read out by the pump controller's current and corroborated with the alkali-atom rule of thumb $P \leq 2 \times 10^{-8} \text{ Torr} \cdot \text{s}/\tau$ for MOT $1/e$ loading time τ [68]. A titanium sublimation pump is occasionally activated to little overall effect. Vacuum pressure inside the 2D MOT cuvette is maintained with a non-evaporable getter (NEG) for differential pumping as described in Sec. 3.1.5.

3.1.3 Glass science cell

Different glass cells are used to house the first and second generation cavities, providing ample optical access without the eddy currents associated with a metal chamber. Both cells are fused to a glass-to-metal transition and $4\frac{1}{2}$ " CF flange. The flange is attached to the top port of the spherical cube. The dimensions of the cells are approximately $2" \times 2" \times 5"$. These dimensions are kept tight to the cavity spacer for vacuum considerations and so that a microwave antenna can be placed fairly close to the atoms for fast hyperfine transitions.

The first generation apparatus uses a borosilicate glass (Borofloat) cell without anti-reflective (AR) coatings. As a result, each beam passing through the cell loses about 4% of power per surface, creating inconvenience when retroreflection is desired. Nonuniform wall thickness leads to "fringes" in the MOT beams that cause fluctuations in the MOT position. The design for the second generation cell has two significant changes. First, fused-silica ("quartz") is used for its smaller thermal expansion coefficient ($5 \times 10^{-7} \text{ K}^{-1}$) compared to Borofloat ($3 \times 10^{-6} \text{ K}^{-1}$). This left the possibility of heat fusing AR-coated plates without cracking the coating. Second, a 16 mm outer diameter quartz tube protrudes from one corner of the cell to attach a 2D MOT.

In the end, the JILA shop used a sodium-silicate bonding technique [69] to construct the second cell from $5" \times 2" \times 0.12"$ AR-coated plates from Specialty Glass Products. The AR coating is specified to have less than 0.2% (0.6%) reflectance at 0° (45°) angle of incidence at 780 nm. Additional right-triangular prisms from Esco Optics buttress the interior corners. Initial pump downs repeatedly revealed vacuum leaks along one edge that could not be filled by vacuum-compatible silicone sealer, so a TorrSeal-like epoxy was heavily applied in an act of desperation. Although the leaks stopped, the final pressure was limited by a bakeout that only reached 80°C .

3.1.4 Science cavity and spacer

An optical cavity is a resonator for light waves consisting of mirrors fixed to a spacer. Such cavities are vital to our experiments in a number of ways. The descriptions of a cavity field as a har-

monic oscillator and an atom as a two-level system form a versatile playground for modeling many other physical systems. The two mirrors set boundary conditions on optical fields that confine the geometry of the experiment. High finesse is akin to high optical depth, increasing the strength of infinite-range atom-light interactions. Collective effects arising from the indistinguishability of atoms in the cavity form the basis of our non-demolition measurements and sensor readout.

The squeezing experiments of Chapter 6 and the interferometry experiments of Chapter 7 rely on separate optical cavities. In both cases, two super-polished dielectric coated mirrors with 7.75 mm diameter, 4 mm thickness, and 5 cm radius of curvature are fixed to a rigid spacer to form a vertical, nearly confocal Fabry-Pérot resonator. Both mirrors are epoxied with TorrSeal to Piezomechanik HPCh 150/12-6/2 piezos for feedback up to kHz frequencies limited by the resonances of the loaded piezos. The transmission of the bottom (input) mirror is designed to be significantly higher than the top mirror, allowing $\sim 95\%$ of incident photons to return towards a homodyne detector. The dominant difference between the cavities is that the interferometry cavity had $50\times$ higher finesse. A summary of the other relevant experimental parameters is included in Table 3.1.

The first generation science cavity was used for spin-squeezing demonstrations between August 2014 and June 2016. The spacer was designed with optical access and rejection of acoustic noise in mind [70]. It was machined by hand out of a single block of Zerodur (Fig. 3.2(a)). A Macor jig was used for attaching the mirrors and piezos used in stabilizing the cavity length. Mirrors were supplied by Advanced Thin Films.

For the second generation cavity, a new spacer was needed that would not impede atoms coming from the 2D MOT. This spacer was machined out of Macor on a CNC machine (Fig. 3.2(b)). An “adjustable sled” design allows tuning the cavity length such that the free spectral range (FSR) is nearly equal to the rubidium hyperfine transition frequency, $\omega_{\text{HF}} \approx 6.835 \text{ GHz}$, $L \approx 2.19 \text{ cm}$. The piezos have a maximum throw of about 4 microns, and our target FSR is constrained to about $20 \mu\text{m}$ so that a reasonable amount of Raman light can enter the cavity non-resonantly. Although it would be possible to machine within this tolerance, accounting for the width of piezo, glass, epoxy,

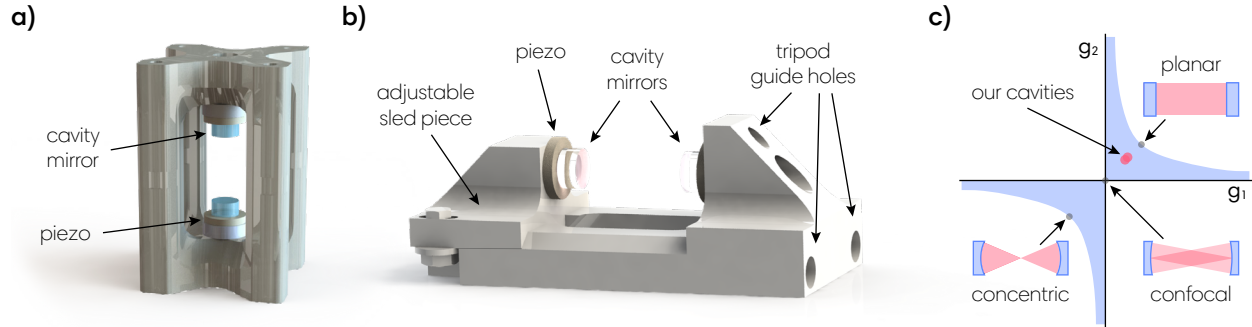


Figure 3.2: **Optical cavities and spacers.** (a) The first generation Zerodur spacer houses a moderate finesse cavity for generating large amounts of spin-squeezing. (b) The second generation Macor spacer supports a high finesse cavity. Ceramic screws are used to fine-tune the length for a free spectral range near ω_{HF} . Although the spacer is pictured horizontally here, it is mounted vertically on a tripod of Macor rods for free-fall interferometry. Both images were rendered in Solidworks. (c) A cavity-stability diagram shows both the first and second generation cavities are within the shaded island of stability: $0 \leq g_1 g_2 \leq 1$ where $g_i \equiv 1 - \frac{L}{R_i}$ for mirror radius of curvature R_i and cavity length L [26].

and mirror coatings seemed risky. The original cavity length set using calipers was off by roughly $700 \mu\text{m}$, but this was easily corrected and the ceramic screws and nuts were tightened to fix the free spectral range at $\omega_{\text{FSR}} = 6.788 \text{ GHz}$. Although the vibrational modes of an asymmetric spacer are concerning, finite element modeling in COMSOL predicts the lowest resonant eigenfrequencies to be around 5.2 kHz (bending) and 6.1 kHz (torsional), significantly above the lowest piezo resonance frequency. The cavity is mounted vertically on a tripod of Macor rods which are themselves fixed on a Macor base supported by four alumina posts. Small Viton balls dampen the vibrational couplings between parts. The rest of the complex vibration isolation system described for previous iterations of the experiment was abandoned when moving the first generation apparatus – the heavy hanging mass had a tendency to act as a pendulum.

The mirrors, which come from FiveNine Optics, are coated for high reflectivity between 780 nm and 795 nm for high finesse. The coating also has moderate transmissivity at the 760 nm and 820 nm lattice wavelengths for ease of use and to avoid parametric heating. The linewidth of the cavity is measured by the ring-down (exponential decay) of transmitted light after switching off

a resonant laser. In Fig. 3.3(a), a photodiode (PN: Hamamatsu S5971) with $10\text{ k}\Omega$ transimpedance resistor collects the decaying field from the sideband of the 780 nm Raman laser after the EOM modulation has been disabled with a fast switch (PN: Mini-Circuits ZASWA-2-50DR+). The exponential fit gives $\kappa = 1/\tau = 2\pi \times 56(2)\text{ kHz}$. This should be compared to the measurements two years prior ($2\pi \times 51.2(2)\text{ kHz}$) and to the design linewidth ($2\pi \times 50.5\text{ kHz}$, assuming 2 ppm loss per mirror). From the mirror specifications (Fig. 3.3(b)), the linewidths at $\{760\text{ nm}, 795\text{ nm}, 813\text{ nm}\}$ are approximately $2\pi \times \{160, 60, 170\}\text{ kHz}$.

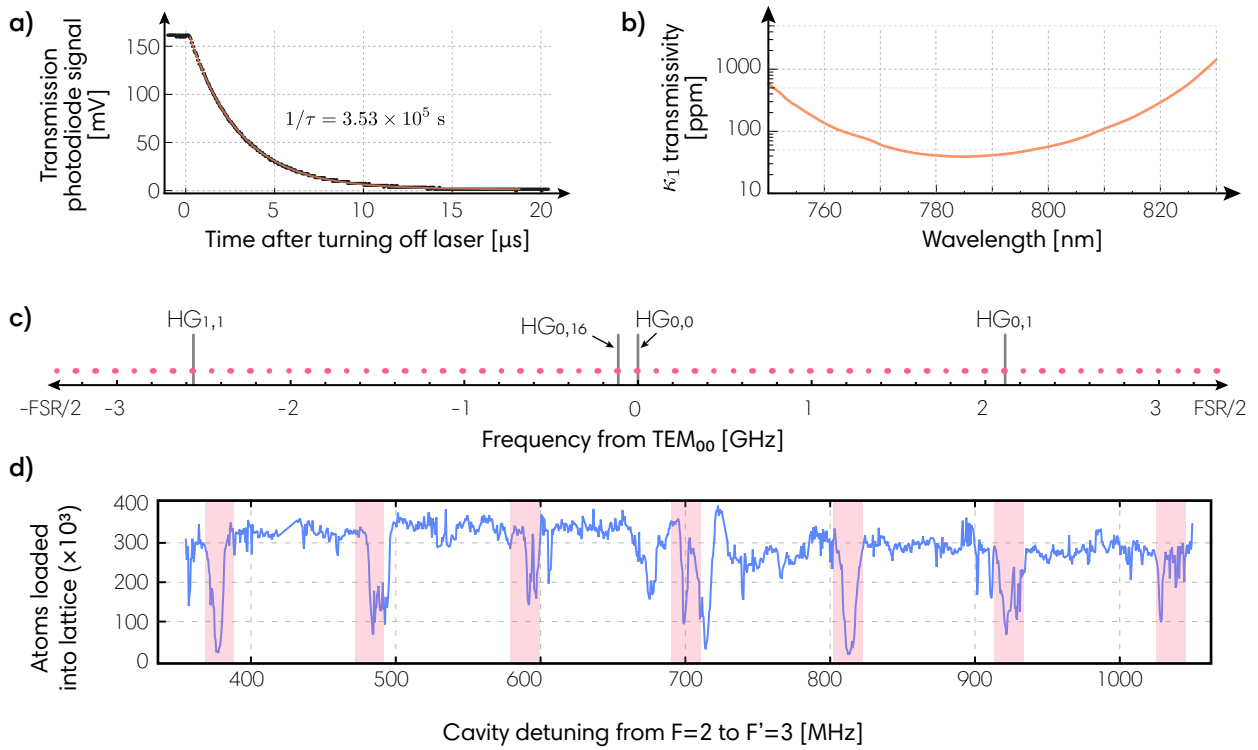


Figure 3.3: Second generation cavity linewidth, transmissivity, and atom loading fluctuations. (a) Cavity linewidth ring-down measurement for 780 nm light, after guiding rubidium ensembles into the bottom mirror for over 2 years. (b) Specified mirror transmissivity for the lossy mirror in parts per million (ppm). The transmission coefficient of the other mirror, and loss coefficients for both mirrors, are close to 2 ppm . (c) The predicted transverse mode frequencies of the 100 lowest-order $\text{HG}_{m,n}$ modes for our second generation cavity. For a given $\text{HG}_{0,0}$ mode, the frequency difference with the closest $\text{HG}_{m,n}$ mode is plotted. Modes are clustered with characteristic spacing near 110 MHz . (d) The number of atoms loaded into the lattice as a function of atomic detuning (*i.e.* cavity length). Pink rectangles are separated by about 110 MHz as the spacing of transverse modes coincides with inhibited loading.

With the high-finesse second generation cavity, we observe superradiance-inhibited atom loading at certain cavity lengths. For mirrors with $R_1 = R_2 = 5$ cm radius of curvature separated by $L = 2.2$ cm, the HG $_{m,n}$ mode frequencies are found by solving¹

$$\frac{\omega L}{c} - (n + m + 1) \arccos(\sqrt{g_1 g_2}) = q\pi \quad (3.1)$$

with longitudinal mode number q and $g_i = 1 - \frac{L}{R_i}$. Although an HG $_{0,0}$ mode and HG $_{0,1}$ mode are split by 2.1 GHz, the nearest HG $_{8,8}$ mode is only 110 MHz away from HG $_{0,0}$ (the longitudinal mode numbers differ by 5). It turns out that the transverse modes of this cavity are all clustered in groups with spacings of about 110 MHz (Fig. 3.3(a)). One consequence is that we must be wary of accidentally inserting tones on higher-order modes when using the cavity as a frequency filter.

The other practical impact of the higher-order transverse modes is that certain cavity detunings facilitate synchronization within the cavity that lead to superradiant emission. If a sufficient number of atoms overlap with the HG $_{m,n}$ cavity mode while loading a MOT such that the system enters the collective strong coupling regime, the dynamics of the collective excitation dominate over single-particle decoherence and the result is a pulse of light out of the cavity. These light pulses were seen on a CCD and correlated with reduced and fluctuating numbers of atoms trapped in the lattice for our experiments (Fig. 3.3(b)). Our solution was to operate the experiment in between the detunings that support this phenomenon.

3.1.5 Atom source and the 2D MOT

Prior to the interferometer experiment, the atom source was a rubidium ampoule located in a glass arm at the bottom of the vacuum chamber. Resistive bands warm the container to anywhere between 30°C - 100°C, creating enough background vapor pressure in the main chamber to load a MOT. One piece of lab lore holds that it is always difficult to see a MOT in the first 24 hours of breaking vacuum. Perhaps by the time rubidium has sufficiently coated the inside of a chamber, enough vapor pressure has accumulated to support a MOT.

¹By inverting these equations, the measured transverse mode splitting and L (from the free spectral range) provide a very accurate check on the radius of curvature, assuming the mirrors are symmetric.

It should also be mentioned that in one incident, we flooded the chamber with far too much rubidium vapor. Within an hour, the cavity finesse at 780 nm appeared about three times lower. A makeshift cryopump, formed by cooling the bottom of the chamber with dry ice, did not help restore the finesse, so we cleared the vapor with a turbo pump. However, the finesse of the cavity remained spoiled in a detuning-dependent way. As a last ditch effort, we ran current through a pair of heater coils wrapped around the mirrors. This worked for two weeks before the wires failed due to excessive current, after which the cavity finesse was reduced in a detuning-independent way. The 45° mirror was also coated with what was presumably rubidium.

The second generation system is designed specifically with a spin-squeezed interferometer in mind. To preserve the high-finesse mirrors, we opt to load from a 2D MOT rather than to fill the main chamber with a background vapor [71]. The 2D MOT setup is shown in Fig. 3.4. Atoms are collected inside a 1" × 1" × 2" rectangular Pyrex cuvette and pushed through a 1.5 mm aperture towards the main chamber. There are two Rb dispensers (PN: SAES RB/NF/3.4/12 FT10+10) and one neutral evaporative getter (NEG, PN: SAES St 171 LHI/4-7) to provide differential pumping within the cuvette. One Rb dispenser is typically run at 3.0 A during the day, the other kept ready in case of emergency, and the NEG runs continuously at 2.3 A after activation. The electrical leads are welded to stainless steel wires and isolated with a ceramic spacer disk and glass tubing. A polished (reflective) copper disk with 0.8 mm aperture is welded to a stainless steel tube to allow for differential pumping. The extensive experience of Hans Green and Dana Anderson's group were very helpful while designing this system.

The 2D MOT and repumper beams use roughly 50 mW and 2 mW, respectively. Cylindrical lenses create an elliptical beam profile that is sent to the long faces of the cuvette along two paths. The polarization is then circularized, and another quarter-wave plate in conjunction with a retroreflective mirror ensures that the counter-propagating beams also have the requisite polarization. A small amount of light from the MOT laser is split off to form a "push beam" incident along the 2D MOT axis, accelerating the atoms toward the main chamber by radiation pressure force. Light reflecting off the copper disk also provides some transverse cooling to the atoms which is

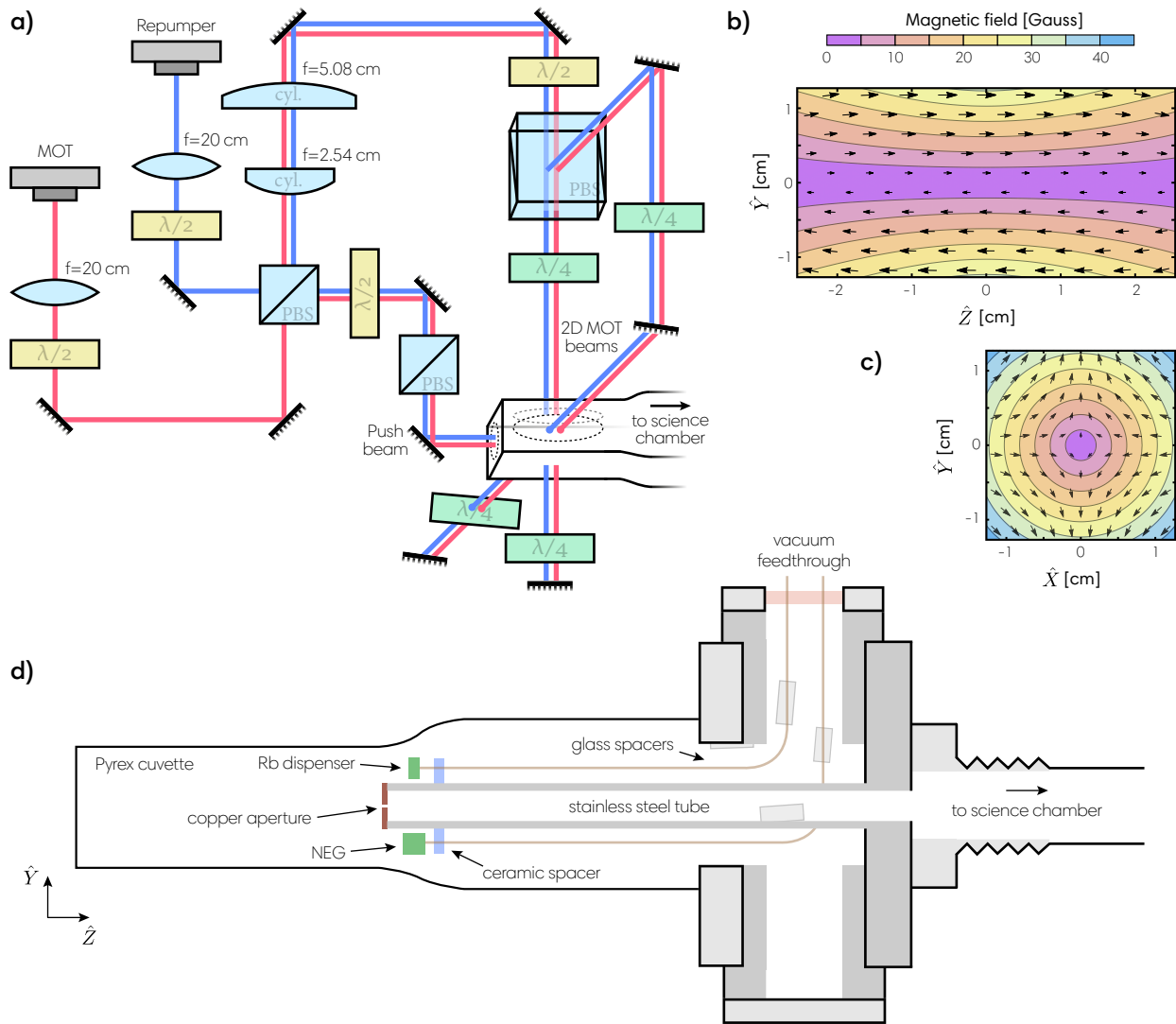


Figure 3.4: **The 2D MOT setup.** (a) Beams from the MOT and Repumper DBR lasers are overlapped to form the “2D MOT beams” and the “push beam”. Most of the power is sent to the 2D MOT beams transverse to the rectangular Pyrex cuvette. These beams are shaped by cylindrical lenses into ellipses with approximate $1/e^2$ waists $2\text{ cm} \times 0.75\text{ cm}$. Some of the available power is also sent to a push beam through the end of the cuvette, “pushing” atoms along \hat{z} towards the science chamber through a small aperture in a copper disk. Light from the push beam and its retroreflection on the copper disk also provide necessary cooling. (b) As described in Sec. 3.1.6, the 2D MOT coils surrounding the cuvette form a quadrupole field with a 24 G/cm gradient at the center. The magnetic vector field and magnitude, assuming 1.5 A current, are modeled along the cuvette and (c) looking down the cuvette towards the chamber. (d) A scaled cross-section of the 2D MOT setup shows the main chamber vacuum is separated from the cuvette by a copper aperture at the end of a stainless steel tube. Inside of the cuvette region are two rubidium dispensers and one NEG. Carefully placed spacers keep the getter leads electrically isolated.

instrumental in observing the 2D MOT.

3.1.6 MOT and bias coils

Magnetic fields are established by running current through magnet coils according to Ampere's law and the Biot-Savart law. The resulting fields are superposed, of course, with static magnetic fields from nearby optical isolators, the ion pump, and the Earth's interior. All coils described in this section are outside vacuum, wound with 20 AWG polyester-insulated copper wire (PN: Belden 8076), and stabilized with Araldite 2011 or 2012 epoxy.

A pair of elongated MOT coils provides the quadrupole field for the 3D MOT. Up to 3 A of current is run through 128 turns of anti-Helmholtz coils placed in electrical series. Both coils are 10 cm \times 4 cm and mounted 5 cm from the center of the cavity. The field gradient produced at the center of the cavity is about 34 G/cm, conventional for cold atom experiments.

Three pairs of Helmholtz bias coils are used for positioning the MOT at the center of the cavity, zeroing the magnetic field during polarization gradient cooling, and setting the Zeeman splitting and quantization axis during various other tasks. To facilitate adding the 2D MOT to the new science cell, it was necessary to wind new bias coils with more optical access. We chose to 3D print a lightweight set of six square bias coil frames, each approximately 26 cm \times 26 cm, fixed together into a cube by nylon screws. Acrylonitrile butadiene styrene (ABS) plastic is reliable up to 80°C but the coils do not heat significantly. Each coil uses 75 turns of wire. The maximum 1.5 A current provides a nearly uniform 3 G field. For rubidium, this corresponds to a 2.1 MHz Zeeman splitting between adjacent magnetic sublevels.

The 2D MOT coils are 3D printed and wound in a similar way. These coils are powered with up to 1.5 A in a "racetrack configuration" to produce an elongated quadrupole field [71]. The frames are roughly 2.5 cm \times 6.7 cm to fit tightly around the cuvette, and the 2D MOT retroreflection optics are directly attached to the frame. Each coil is 120 turns, allowing a magnetic field gradient up to 24 G/cm at the center of the cuvette.

3.1.7 Lasers

Nearly all aspects of an atomic physics experiment revolve around the description of a laser as a coherent frequency source. Lasers prepare ensembles in low-entropy states, carrying away momentum after addressing atomic transitions. The fields produce potentials to trap, guide, manipulate, and mediate interactions between atoms. The ability to adjust laser frequencies, phases, and amplitudes offers enormous flexibility. Nevertheless, practical details such as a laser’s spectral properties, stability against environmental perturbations, and output power also play a role in the functioning of an experiment.

Here we distinguish three separate laser architectures: distributed Bragg reflectors (DBRs), extended cavity diode lasers (ECDLs) with diffraction gratings, and “caterpillar” interference filter lasers (a class of ECDLs). The last two technologies have seen significant design and assembly within our lab. All of the lasers output 60 – 120 mW of near-infrared light. They are driven by low-noise laser current and temperature controllers built by the JILA electronics shop. Section 4.1 includes an overview of frequency stabilization techniques.

Distributed Bragg reflector lasers generate our MOT, repumper, and optical pumping light. Commercial DBR architectures are extremely robust against acoustic noise, and the ~ 500 kHz free-running linewidths do not inhibit trapping or certain laser-cooling schemes. With the external feedback scheme described in Sec. 4.3, we use DBRs with linewidths narrowed to about 1 kHz for probing the atoms, mediating atom-cavity interactions, and driving transitions for interferometry. All of our DBR diodes are nominally centered near 780 nm (PN: Photodigm PH780DBR080T8 and PH780DBR120TS).

Extended cavity diode lasers (ECDLs) provide the light for stabilizing the cavity, forming the far-detuned optical lattices, manipulating the atoms, probing their state, and observing SWAP cooling. These ECDLs use the Littrow design detailed in Justin Bohnet’s dissertation [70]. A diffraction grating provides optical feedback to the diode. Wideband wavelength selection is made by adjusting a fine-threaded screw to pivot the flexure-mounted grating. A piezo also adjusts the grating

angle of incidence with feedforward from the laser current to increase the mode-hop free tuning range into the multiple-GHz range. The diodes were nominally centered at 780 nm (PN: DL-7140-201S) or 795 nm (PN: Eagleyard EYP-RWE-0840-06010-1500-SOT02). The free-running ECDLs have FWHM Lorentzian linewidths around 200 kHz but the relative noise between the probe laser and a cavity mode was reduced to the equivalence of a laser with 5 kHz linewidth (or lower) using an intermediary locking chain [72]. To make such measurements, the measured phase noise of the locked probe laser is approximated as a flat power spectral density of instantaneous frequency noise $S_\nu(f) \approx \tilde{S}_\nu$ which is itself related to the Lorentzian FWHM $\Delta\nu$ through $\Delta\nu = \pi \times \tilde{S}_\nu$ [72].

An interference filter laser concept has gained recent popularity, promising improved stability against acoustic noise at similarly narrow linewidths [73, 74]. We designed and built a version used for the 760 nm blue-detuned lattice laser, and strontium-project labmates have built additional variations. Our implementation, shown in Fig. 3.5, forms a linear cavity between the rear reflecting surface of a diode centered at $\lambda_0 = 760$ nm (PN: Eagleyard EYP-RWE-0760-02010-1500-SOT12) and a 10% reflective output coupler placed at the focus of a pair of lenses. This “cateye” configuration of lenses results in reduced sensitivity to processes that would cause misalignment. A Fabry-Pérot etalon (0.3 nm FWHM interference filter centered at $\lambda_0 = 767.9$ nm, PN: Iridian GX000004) was held in a micrometer-adjustable rotation mount. The angle of incidence θ between the optical path and the beam selects a single external cavity mode according to $\lambda' = \lambda_0 \sqrt{1 - (\sin(\theta)/n_{\text{eff}})^2}$ for index of refraction $n_{\text{eff}} \approx 2$. The temperature is stabilized with two thermoelectric coolers (TECs, PN: LairdTech UT8-12-25-F2) placed in series between the aluminum base and heat sink block, but a commercial diode holder with integrated TEC may be a better option for the future. When designing for maximal stability against perturbations, care should be taken to avoid springs, especially in mounting the output coupler and diode.

The lasing mode is the result of a competition between several gain factors: the semiconductor gain profile, the interference filter’s transmission window, the diode cavity from rear to front facet ($L = 1.5$ mm), and the external cavities from each diode facet to output coupler ($L = 65$ mm) [75]. Each cavity has an associated finesse $\mathcal{F} = 4\sqrt{r_1 r_2}/(1 - \sqrt{r_1 r_2})^2$ for amplitude reflection coef-

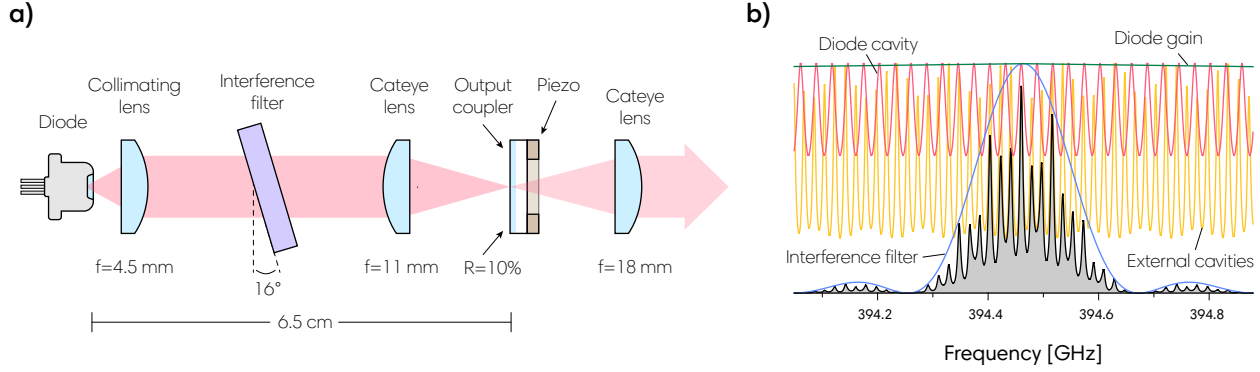


Figure 3.5: **Interference filter lasers.** (a) Schematic for the 760 nm interference filter extended cavity diode laser. (b) An example interference laser mode spectrum (black) is the product of the diode gain (green, assumed to be a relatively broad Gaussian), diode cavity (red, $L = 1.5$ mm, anti-reflective coated facet $r_2 = 0.017$ specified, $r_1 = 0.92$ estimated), external cavities (gold, $L = 65$ mm and 66.5 mm, $r_1 = 0.017$ and 0.92 , $r_2 = \sqrt{0.1}$), and interference filter (blue, 0.3 nm FWHM). The highest peak determines the laser oscillation frequency. Adapted from [75].

ficients r_1, r_2 , giving rise to an Airy function mode structure,

$$T(\omega) = \frac{1}{1 + \mathcal{F} \sin^2(2n\omega L/c)}, \quad (3.2)$$

with length L and index of refraction n . The laser oscillates at the frequency for which the product of these contributions, which may be unstable in time or temperature, is largest. As seen in Fig. 3.5(b), the long external cavity gave narrow resonances with depth determined by the amount of feedback, but a change in the external cavity length is liable to pull the frequency or mode-hop the laser. The output coupler is therefore mounted on a ring-actuator piezo (PN: Piezomechanik HPCh 150/12-6/2) to stabilize the cavity length and to feedforward on current, extending the mode hop-free tuning range to over 10 GHz. The linewidth is measured to be near 40 kHz using the power spectral density of transmitted light when locked on side of fringe to a broad cavity. This linewidth is also corroborated by measuring the transmission lineshape as the laser is swept through a narrow cavity resonance. Tests on the strontium-project interference filter lasers have shown longer external cavities are correlated with lower linewidths, as is to be expected.

Tapered amplifiers (TAs) (Eagleyard gain chips PN: EYP-TPA-0780-00500-3006-CMT03-0000 and EYP-TPA-0780-01000) are required to reach the optical powers needed for a MOT and for

Raman sideband cooling. The lifetime of lasers and TAs can be extended considerably by limiting the operating current and powering off overnight. Our older TA has operated at 1500 mA out of 3000 mA for over 10 years, which seems to exceed other reported lifetimes.

3.1.8 Homodyne detector

We use balanced homodyne detection [76] to obtain information about the atom-cavity system. In homodyne detection, a strong local oscillator (LO) field is overlapped with the signal field at a non-polarizing beam splitter cube and sent into two photodiodes. The difference of photocurrents is a direct DC measurement record of one quadrature of the signal field. By definition, the LO and signal are at the same frequency, and the measured quadrature is selected by adjusting the phase of the LO. Measuring the I quadrature gives information about the signal field's amplitude, but the Q quadrature contains all of the field's information when the probe is on cavity resonance. Compared to heterodyne detection, which can generally measure the useful quadrature only 50% of the time, homodyne detection has no fundamental reduction in quantum efficiency. In addition, noise that is common-mode to both photodiodes cancels out. The main drawback for the technique is its sensitivity to relative path length fluctuations between the LO path and the signal path, so the relative phase between these two fields must be stabilized.

We use the circuit in Fig. 3.6 to measure the response of the probing field's Q quadrature to the presence of atoms in a cavity. This detector was designed, built, and tested by Elissa Picozzi, Kevin Cox, and James Thompson. The photocurrents of two photodiodes (PN: Hamamatsu S5972) are combined to form an AC output, a DC DIFF output, and a DC SUM output. To stabilize the relative phase against path length fluctuations, light near the Rb D₂-line is split into a probing path and an LO path. The probing path is incident on the cavity and includes both a carrier *path length stabilization* tone (rejected at the cavity) and small $f_s = 81.1$ MHz EOM sidebands, the lower of which is the *atomic probe sideband* tone near cavity resonance. The LO path is shifted to be near the atomic probe tone's frequency with an 81.1 MHz AOM before being sent to the detector. Using the 81.1 MHz beat note from the detector's AC output, the relative phase is stabilized using a phase-

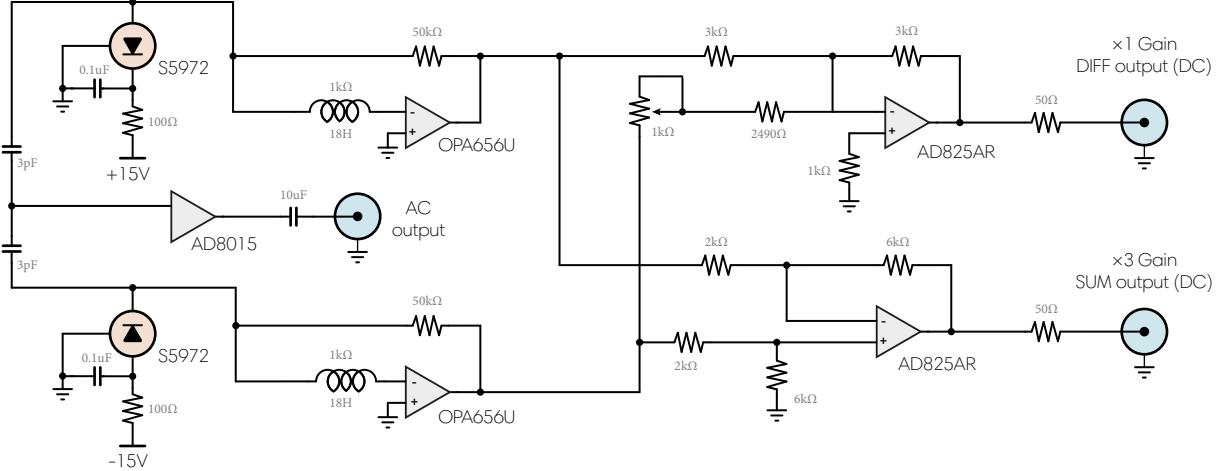


Figure 3.6: **Homodyne detector circuit diagram**, omitting power supplies and bypass capacitors. The AC output uses a high frequency transimpedance amplifier (PN: AD8015) for the 80 MHz path length reference tone. The DIFF path is used for probing the number of Rb atoms in $|F = 2\rangle$ with a bandwidth from DC to 1.5 MHz. The SUM path is used in calibrating probe power. A potentiometer on the DIFF stage allows cancellation of intensity noise on the homodyne reference tone to better than 3×10^{-4} .

frequency detector that feeds back on the VCO that drives the LO path AOM. This setup is shown in Fig. 3.7(a). The bandwidth of the path length phase lock is about 50 kHz.

The phase ϕ_s of the path length stabilization reference frequency selects the detected quadrature. Reference [29] introduces an invaluable model for the full complex field response normalized to the incident field when probing the atom-cavity system. A useful result is the bare cavity reflected field response for linewidth κ and loss rate from the transmissive mirror κ_1 , written as a function of the detuning from resonance δ_p :

$$F(\delta_p) \equiv I_r + iQ_r \xrightarrow{0 \text{ atoms}} F(\delta_p) \approx 1 - \frac{\kappa_1}{i\delta_p + \kappa/2}. \quad (3.3)$$

We detect the reflected field of an asymmetric (mostly-reflective) cavity, so the phase quadrature Q_r appears as a dispersive lineshape when sweeping through resonance. As described in Sec. 1.5, the presence of atoms in $|\uparrow\rangle$ shifts the dressed cavity frequency, and the challenge is to estimate this frequency shift to infer the atom number (Fig. 3.7(b)). The phase quadrature thus gives maximal sensitivity for resolving small frequency shifts, and hence atom number, when parked on

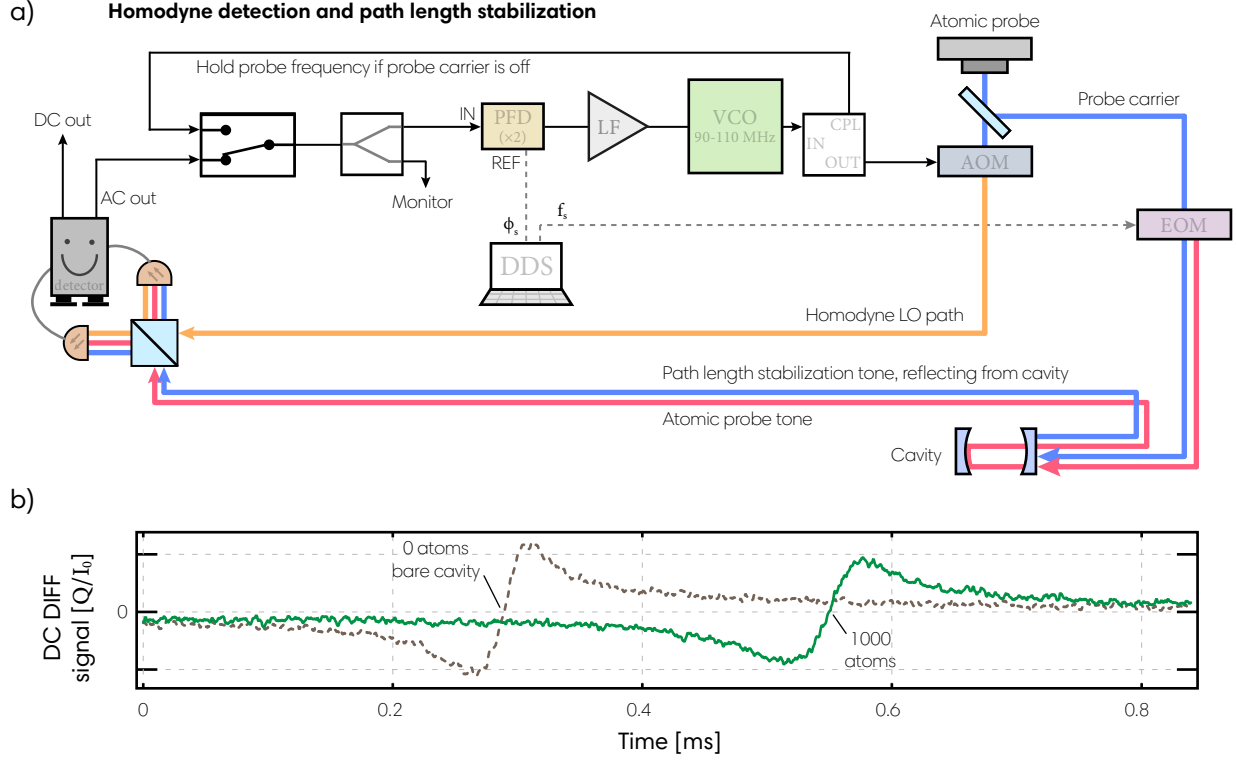


Figure 3.7: **Homodyne detection.** (a) Setup for probing and path length stabilization. The atomic probe sideband tone (red) carries atom-cavity information at the homodyne LO tone frequency (orange). The path length stabilization tone (blue) encodes information about relative path length fluctuations which is fed back to the LO frequency using a phase-frequency detector (PN: Analog Devices HMC440), an AOM, and a DDS reference that is phase coherent with the sideband frequency. (b) Typical DC DIFF measurement of the reflected Q quadrature. A dispersive signal measures the bare cavity resonance frequency (dashed brown) or the shift from $N_f = 10^3$ atoms (green). Here the atomic probe is swept linearly from a known frequency at 1.5 MHz ms^{-1} . The reduction of amplitude and linewidth broadening are explained in [29].

resonance as in Chapter 6.

This detector was designed for $50 \mu\text{W}$ of LO power incident on each port. The path length stabilization tone is only 50 nW and the signal fields are better described in terms of detected photons per probing window (from 5×10^1 to 5×10^4 photons per $100 \mu\text{s}$). We estimate the intensity mode-overlap between the cavity TEM_{00} and the LO beam is about 95(3)%. The technical noise from the detector (the portion of the noise not attributable to photon shot noise of the LO) sets another quantum efficiency of $Q_{\text{elec}} = 86(2)$. The photodiode sensitivity of 0.54 A/W reflects the probability to

turn a photon into photocurrent and corresponds to a quantum efficiency of $Q_{\text{PD}} = 0.86$.

3.1.9 6.8 GHz microwaves

A stub-tuned dipole antenna is used to drive microwave transitions between ^{87}Rb hyperfine ground states near $\omega_{\text{HF}} = 2\pi \times 6.835$ GHz. Frequency and phase noise must be extremely well controlled to perform rotations below the $\theta_{\text{SQL}} = 1/\sqrt{N}$ radian standard quantum limit for N atoms. As described in [77] and [78], a low-noise 100 MHz crystal oscillator (PN: Wenzel Sprinter 501-04517D or ULN 501-16843) is phase-locked to a 10 MHz signal (PN: SRS FS725 or a JILA-shared Cs reference clock). This oscillator drives a nonlinear transmission line from which all tones but the 68th harmonic are filtered out by copper pipe-cap filters. The 6.8 GHz signal is mixed at a single-sideband mixer with a tunable DDS signal near 35 MHz, allowing for control of microwave phase, frequency, and amplitude. A high-power amplifier (PN: Mercury Systems L0607-42) delivers up to 16 W of microwaves to drive hyperfine transitions with up to $\Omega = 2\pi \times 50$ kHz Rabi frequency. A similar microwave frequency chain is described in Ref. [79], though this report misstates the phase noise in our system.

After modulation, single sideband phase noise is -130 dBc/Hz at the relevant spectral components (10 kHz to 1 MHz offset from the 6.835 GHz carrier). Clock-transition spectroscopy line-shapes were broadened as little as 100 Hz at full width half maximum (FWHM) for atoms in a shallow potential. We estimate that this frequency source would limit the resolution of a basic Mach-Zehnder interferometer with $T_{\text{evol}} = 0.3$ ms to the standard quantum limit for 2.5×10^6 atoms [80].

Agile frequency control for the interferometer experiment Additional frequency control is required for the interferometer experiment. As the atoms accelerate due to gravity g , the relative Doppler shift for light propagating upwards versus downwards chirps linearly in time. The frequency difference between the Raman tones must therefore be swept at $b(t) = 2gk = 2\pi \times 25.11$ kHz to keep a transition on resonance. In addition, we need amplitude control to set the Rabi frequency during velocity selection and beam splitter operations, and phase control to set the ap-

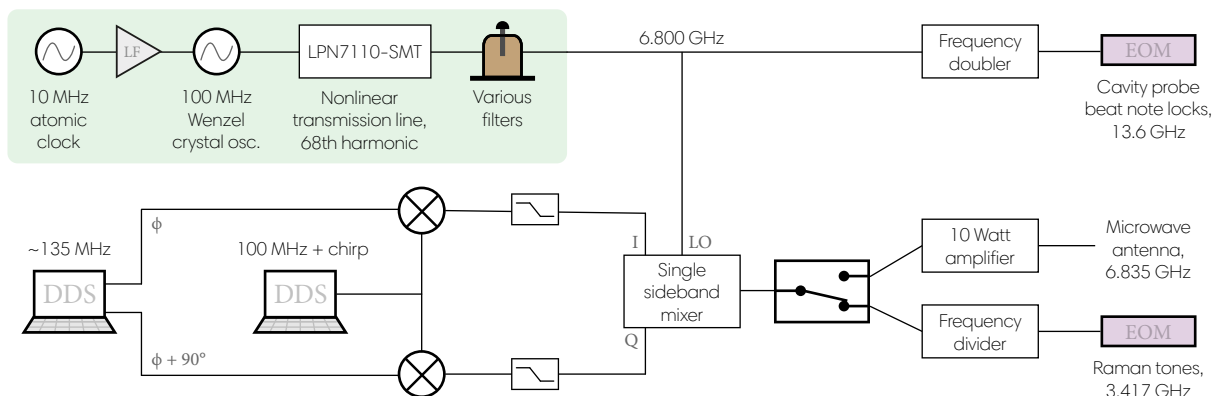


Figure 3.8: Agile frequency control. The 6.8 GHz low phase-noise microwave source (green box) remains virtually unchanged from [78]. The output is sent to a single sideband mixer (PN: HMC496LP3); the I and Q ports of this device must be 90° out of phase, but a DDS (PN: AD9959) controls the overall phase and amplitude. A second DDS near 100 MHz adds a common-mode 25 kHz/ms chirp associated with gravitational acceleration. The frequency divider was used so that first-order EOM tones would be separated by the hyperfine transition frequency. The doubler was used to create high-order EOM tones for bridging considerable frequency gaps between lasers.

appropriate rotation axes during the sequence. This is accomplished with the setup in Fig. 3.8, where two phase-coherent DDS channels near 135 MHz manage the phase, amplitude, and frequency changes. These channels are mixed down with a single channel at $100 \text{ MHz} + b(t)/2\pi$ and up-converted at the 6.800 GHz single sideband mixer mentioned earlier. Because the Raman tones are generated as first-order sidebands on an EOM, we use a low noise frequency divider (PN: Analog Devices HMC862A) to modulate the EOM near 3.417 GHz.

3.1.10 Transfer cavity

The transfer cavity spacer was built from Zerodur in 2008, resting in a metal canister with glass windows. A number of incidents reduced the finesse below the design specifications. One piezo wire shorted in 2011, but the remaining piezo allowed feedback for stabilizing the cavity length, *e.g.* to a spectroscopy setup. The original plan was to pump out the canister for additional thermal stability, but the middling vacuum pressures were ideal for creating a plasma when high voltages were applied to the piezo. As a result, the pressure is kept at atmosphere and the canister

provides some temperature stability and protection against air currents. The second piezo shorted before the atom interferometer experiment, and thus the length of the cavity could no longer be tuned reliably. Nevertheless, the transfer cavity is still useful as a passive frequency reference. Parameters for the cavity at the end of its lifetime are found in Table 3.2. A new ultra-low expansion (ULE) glass reference cavity was commissioned from Stable Lasers in 2021. The 10 cm ULE cavity has finesse $\mathcal{F} = 1.8 \times 10^5$ and linewidth near $\kappa = 2\pi \times 10$ kHz over the 760 – 830 nm range of wavelengths.

Transfer Cavity Parameter	Value
Cavity length	3 cm
Free spectral range	5 GHz
Linewidth at 795 nm	840 kHz
Finesse	6000
Mirror radius of curvature	5 cm
Mirror transmission	117 ppm
Round-trip loss (measured)	850 ppm
Maximum input power	100 mW

Table 3.2: Cavity parameters for the long-used, home-built transfer cavity.

Chapter 4

Methods

This chapter aims to clarify a few disjoint experimental methods. Section 4.1 reviews useful frequency stabilization techniques. Section 4.2 describes an electronic solution for automatically relocking servos. Section 4.3 outlines a scheme to narrow laser linewidths using feedback from external cavities. Section 4.4 presents a site-dependent atom selection approach to the inhomogeneous coupling problem. Section 4.5 covers the creation of axially-uniform “optical dipole traps”, and Sec. 4.6 introduces the blue-detuned “donut” dipole guide used for interferometry.

4.1 Frequency locking

Low-noise lasers and cavity frequency stabilization are crucial for cold-atom experiments. Maintaining phase coherence [81] is vital for processes including laser cooling techniques and homodyne detection. Despite our significant laser linewidths, we are able to manipulate and resolve the state of atoms by ensuring that noise on the cavity was common-mode with noise on the probing laser [72]. A variety of feedback techniques are used for setting and maintaining laser frequencies and cavity lengths. The aim of this section is to provide an overview of technologies that were useful for us and references for further exploration. A summary of the locking chains used for the work in this dissertation is provided in Fig. 4.1.

Feedback as a formal concept is covered in many helpful references including *Feedback for physicists: a tutorial essay on control* [82] and *Feedback Systems* (particularly the chapter on PID Control) [83]. Some of these ideas are used in virtually every lab but language can differ considerably.

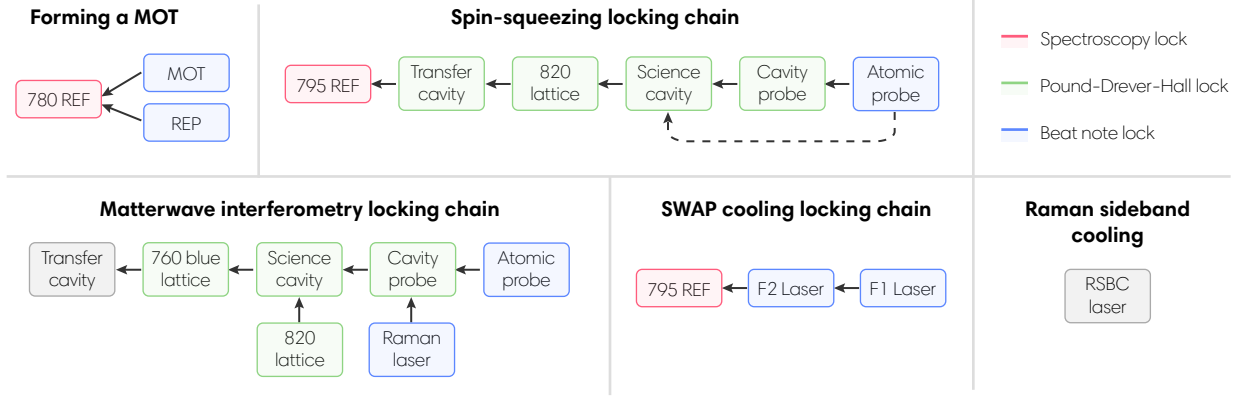


Figure 4.1: The locking chains used in the experiments of this dissertation. The dashed arrow in the spin-squeezing chain represents the atomic probe’s “active lock” to the dressed cavity resonance while it is also phase-locked to the cavity probe (Ch. 6).

Conceptually, the challenge is to design a system that creates an error signal voltage e indicating the deviation from a setpoint s ; the controller’s output voltage u must act on some physical object to guide the error signal back to the setpoint. With proportional-integral-derivative control, the output voltage is a sum of a term directly proportional to e , an integral term which accumulates past errors, and a derivative term which anticipates future errors:

$$u = k_p e + k_i \int_0^t e(\tau) d\tau + k_d \frac{de}{dt}. \quad (4.1)$$

JILA high-speed loop filters (LFs) allow fast PID control onto laser currents, VCO frequencies, variable attenuation, EOM modulation, piezo voltages, and more. The differential error signal inputs on these devices are labeled A and -B. This design uses two integrators and a few gain and span settings to tailor the complex, frequency-dependent loop gain $\mathcal{L}(f)$ detailed in Fig. 4.2(b). Importantly, real systems such as lasers, cavities, and electronic devices have gains and poles that must also be included in the full loop transfer function. Besides the output port, there is an optional PZT OUT with an additional bandwidth limit for driving piezos. Similar products are now available commercially.

Let us consider the model in Fig. 4.2(a). A noisy input voltage $V_{in}(t)$ is summed with the loop filter output which feeds back on $V_{set} - V_{out}(t)$. Creating a stable feedback loop amounts to

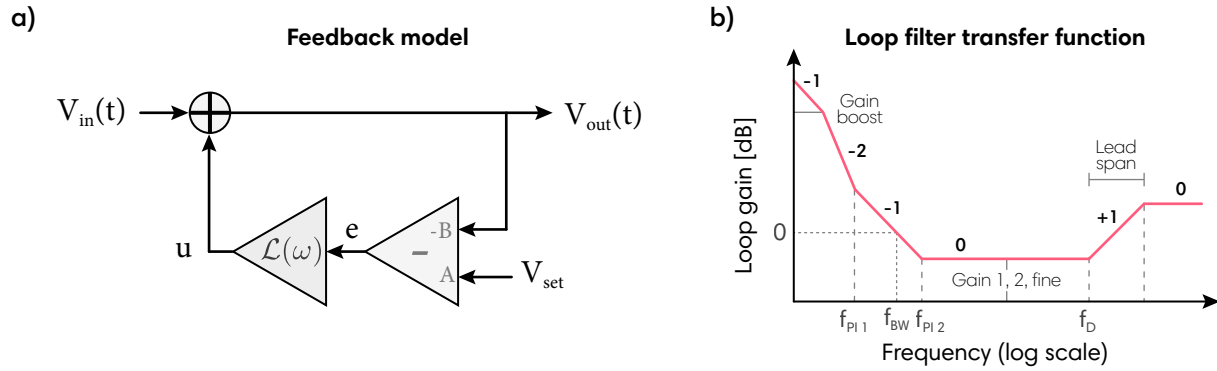


Figure 4.2: **Feedback and loop filters.** (a) Toy model for stabilizing a generic voltage. (b) JILA double-integrator loop filter transfer function. In the frequency domain, each integrator gives a slope of $1/f$, giving large gain at low frequency but causing a 90° phase lag. Each differentiator adds a slope of f , and the 90° phase advance can correct for some loss of phase margin at high frequency. Slopes of $1/f$ and $1/f^2$ are colloquially referred to as -1 , -2 , and so on.

designing a transfer function such that the output voltage approaches the setpoint in the recursive relationship

$$V_{\text{out}} = V_{\text{in}} + (V_{\text{out}} - V_{\text{set}}) \times \mathcal{L}(f) \quad (4.2)$$

i.e. $\mathcal{L}(f)$ should be made large for all frequencies in

$$V_{\text{out}} = \frac{V_{\text{in}} - V_{\text{set}} \mathcal{L}(f)}{1 - \mathcal{L}(f)}. \quad (4.3)$$

For large \mathcal{L} , the output voltage can approach the setpoint and noise can be properly suppressed at the frequency f . Problems occur near the unity gain frequency f_{BW} defined by $|\mathcal{L}(f_{BW})| = 1$, where noise will be amplified unless $\text{Re}[\mathcal{L}(f_{BW})] < 0$. The challenge then is typically to maximize the gain and unity gain bandwidth while ensuring that the system remains stable. In particular, adding each integrator results in greater gain under an additional $1/f$ slope but incurs a 90° phase lag. To ensure closed-loop stability, the phase margin, defined as the difference between the open loop phase lag vs. -180° , must remain positive. If the transfer function crosses the unity gain frequency f_{BW} with a slope of $1/f^2$, the double-integrator phase lag leads to positive feedback and uncontrolled oscillations. However, small amounts of excess phase margin loss may be tolerated

– the resulting unity gain noise bumps visible at f_{BW} are even helpful for characterizing the servo bandwidth.

4.1.1 Spectroscopy locks

Two separate spectroscopy setups were used during experiments involving the cavity. Both systems involved a room temperature rubidium vapor cell containing both ^{85}Rb (72.2% natural abundance, stable) and ^{87}Rb (27.8%, half-life 5×10^{10} years). The rough idea behind this technique comes from scanning a laser frequency across a particular resonance of some atomic species; a photodiode detects decreased transmission due to absorption in the cell and feedback can in principle stabilize the laser frequency to this wavelength. Because modulation spectroscopy is robust against temperature changes and laser amplitude or polarization drifts, and because the transition frequency is set by nature, the technique is useful as an “absolute” frequency reference at the start of a locking chain. Frequency precision is limited, however, by a broad excited state linewidth Γ .

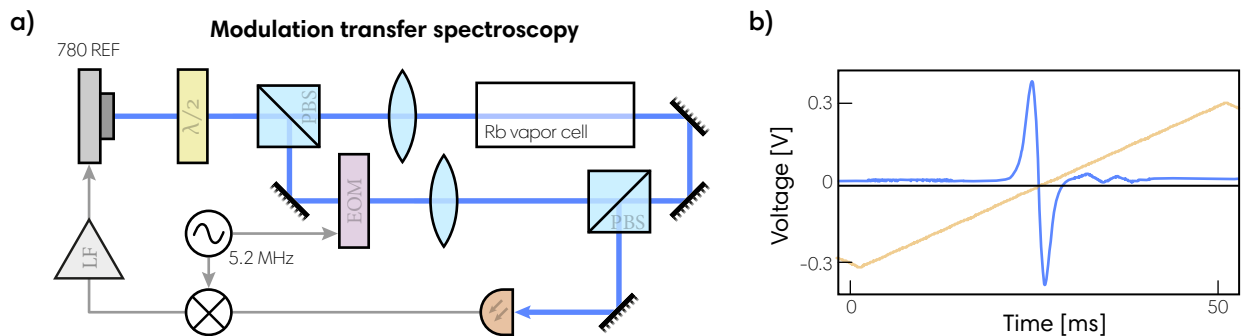


Figure 4.3: **Modulation transfer spectroscopy** [84]. **(a)** Setup for locking the 780 REF laser to the D_2 -line $|F = 3\rangle \leftrightarrow |F' = 4\rangle$ transition in ^{85}Rb . Laser light (blue) is detected by a photodiode (brown) to generate a photocurrent. The loop filter feeds back to the grating piezo voltage and the laser diode current. **(b)** A representative spectroscopy error signal for the 780 REF laser, saved on an oscilloscope. As the loop filter output voltage (yellow) is swept, the laser frequency crosses through the $|F = 3\rangle \leftrightarrow |F' = 4\rangle$ transition resonance.

In practice, our spectroscopy locks are built around phase-modulating a laser, and it is help-

ful to expand the electric field E_i in terms of Bessel functions $J_n(\beta)$ for modulation index β :

$$E_i = E_0 \sin(\omega_0 t + \beta \sin(\omega_m t)) \quad (4.4)$$

$$= E_0 \sum_{n=-\infty}^{\infty} (-1)^n J_n(\beta) \sin(\omega_0 t - n\omega_m t). \quad (4.5)$$

When detected on a high-speed photodiode, rf currents nominally cancel due to the opposite signs of the sidebands in Eq. 4.5. In the presence of a medium like atomic vapor, however, absorption and dispersion modify the response to each sideband separately, resulting in a dispersive-like error signal (Fig. 4.3(b)). In addition, a ~ 1 mW counter-propagating saturation beam is used to pump the atoms for Doppler-free spectroscopy. The backbone of our frequency chain is a 780 nm modulation transfer spectroscopy system [84] which locked the 780 REF laser frequency to the D_2 -line $|F = 3\rangle \leftrightarrow |F' = 4\rangle$ transition in ^{85}Rb . A 795 nm FM saturation spectroscopy lock [85] also sets the 795 REF laser frequency to the “crossover” feature halfway between the D_1 -line $|F = 3\rangle \leftrightarrow |F' = 2\rangle$ and $|F = 3\rangle \leftrightarrow |F' = 3\rangle$ transitions in ^{85}Rb .

4.1.2 Beat note locks

A beat note here refers to a heterodyne beating of laser tones at two frequencies ω_1 and ω_2 and electric field amplitudes E_1 and E_2 . The polarization, divergence, and spatial alignment of two beams are tuned to maximize the mode overlap at a high-speed photodiode (typically PN: Hamamatsu GaAs 4176-03). Eliminating components at frequencies outside of the photodiode bandwidth reveals a signal at the difference frequency,

$$I \propto |E_1 \cos(\omega_1 t) + E_2 \cos(\omega_2 t)|^2 \quad \rightarrow \quad I_{\text{BN}} \approx E_1 E_2 \cos[(\omega_1 - \omega_2) t]. \quad (4.6)$$

Our beat note locks are implemented with the help of a phase-frequency detector (PFD, PN: Analog Devices HMC440) which is chosen for its low phase noise floor and convenient frequency range. The PFD takes a reference input 20 – 1000 MHz and a VCO input $20 \text{ MHz} < \omega_1 - \omega_2 < 2 \text{ GHz}$ which is divided internally by a fixed integer frequency division ratio. This device acts as a sort of comparator with charge pumps outputting an error signal voltage that indicates which signal

is crossing zero first (phase) or more often (frequency). Negative feedback is used to drive the error signal to zero, at which point the signals are equal in phase and frequency. Feeding back on one laser to stabilize a beat note to a reference frequency ensures the lasers are phase locked and coherent.

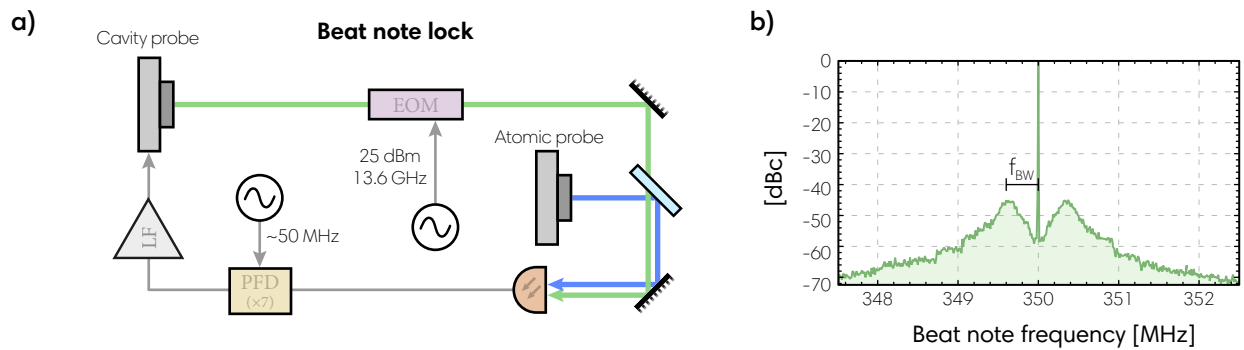


Figure 4.4: **Offset beat note locking.** (a) Phase lock between the atomic probe and cavity probe lasers. A fiber-coupled EOM modulated at 13.6 GHz adds 9th order sidebands to the cavity probe. The 50 MHz reference frequency and $\times 7$ PFD division ratio ensure the lasers are locked $122.4 \text{ GHz} + 350 \text{ MHz}$ apart. (b) The beat note between the atomic probe carrier locked to a cavity probe sideband, as measured by a spectrum analyzer. Unity gain bumps are seen at $f_{BW} \approx 400 \text{ kHz}$ but the vast majority of the power is concentrated in the carrier.

This type of lock is tremendously useful for setting a frequency difference between lasers (as with the 1.3 GHz offset between MOT and REF lasers) and for controlling changes in homodyne phase due to path length fluctuations (see Sec. 3.1.8). For bridging large frequency gaps between lasers, multiple techniques are used. As long as the beat note is within the bandwidth of a GaAs photodiode, it can be mixed down, as with the 6 GHz REP to REF beat note. If the frequency gap is larger, a fiber EOM on one laser path is modulated, and we stabilize a beat note created between a high-order sideband and the laser to be locked (as with the 12th-order 13.6 GHz cavity probe sideband used in locking the atomic probe). Finally, although feeding back on the VCO input on the PFD is more common, it is also possible to feed back on the reference port, as with the “active lock” used to keep the probe on cavity resonance in Sec. 6.

The linewidth of a beat note on a spectrum analyzer is related to the laser linewidth but with some important caveats. First, it is a relative measurement, so the feedback gain should be

decreased as much as possible in order to make accurate statements about free-running (intrinsic) linewidths. Second, the beat note is a convolution of both lasers so a narrow reference laser (or some simplifying assumption) is needed to resolve the linewidth of the laser under test. Finally, the Lorentzian linewidth of a laser may be obscured by the Gaussian-shaped noise near the carrier, so it can be more useful to fit a Lorentzian to only the wings of the lineshape. Fortunately, there are more robust ways to measure laser linewidths such as self-heterodyne techniques or measurements of instantaneous frequency fluctuations.

4.1.3 Pound-Drever-Hall locks

Locking a laser frequency relative to a cavity resonance is one of the most important experimental techniques available to us. Pound-Drever-Hall (PDH) locking adapts a technique for stabilizing microwave resonators [86] to the optical domain [87, 88]. Importantly, the technique decouples laser frequency noise from intensity noise. As seen in Fig. 4.5, a laser is phase-modulated by an EOM, $E_i = E_0 \sin(\omega_0 t + \beta \sin(\omega_m t))$, and detected in reflection on a high-speed photodiode. For a purely phase-modulated beam, there would be an exact cancellation of rf currents due to the sign reversal of the equal-intensity sidebands, but the reflected electric field incorporates the detuning-dependent cavity response. In a typical application, sidebands at ω_m thus act as phase references in stabilizing the frequency of the carrier. Mixing the photodetector signal with an LO at ω_m gives access to the familiar dc error signal lineshape as a function of the detuning from cavity resonance δ_p ,¹

$$e(\delta_p) = -2 |E_0|^2 J_0(\beta) J_1(\beta) \text{Im} [F(\delta_p) F^*(\delta_p + \omega_m) - F(\delta_p) F^*(\delta_p - \omega_m)], \quad (4.7)$$

using the cavity response function $F(\delta_p)$ from Eq. 3.3.

PDH locking in this form is used for stabilizing the red and blue lattice lasers to the transfer cavity. It is used for locking the cavity probe with 50 nW detected by avalanche photodiode (APD,

¹Assuming small modulation index $\beta < 1$ so the Bessel expansion is valid and modulation frequency $\omega_m \gg \kappa$ so the sidebands are completely rejected by the cavity.

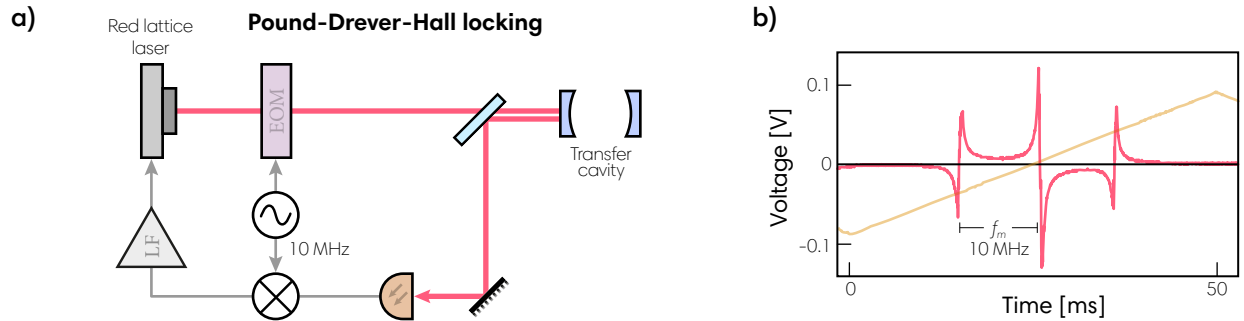


Figure 4.5: **Pound-Drever-Hall locking.** (a) A typical PDH setup for locking an optical frequency to a cavity resonance, including modulation of an EOM and demodulation at a mixer. (b) A PDH error signal for locking the red lattice to the science cavity. As the loop filter output voltage (yellow) is swept, the sidebands and carrier cross through the cavity resonance [87]. In this case, $f_m = 10$ MHz sidebands are added by modulating the laser current rather than phase modulation through an EOM, but the end result is the same.

gain ≈ 150) during the squeezing experiments. Feeding back on cavity piezos also allows for locking the science and transfer cavities to PDH error signals, although the bandwidth is limited to a few kHz by the loaded piezo resonances. Finally, we began locking to a weak sideband feature of the cavity probe during the interferometer experiment because little intracavity power could be tolerated. This technique allowed using about 50 pW in the resonant sideband with only 50 pW of the 3 μ W carrier tone leaking into the cavity non-resonantly.

4.2 Automated relocker

The standard JILA loop filter design includes a relay for switching between engaging a lock and repeatedly ramping the output voltage. When a lock drops, the output voltage typically rails, and in most setups the relay needs to be manually re-engaged. Dropped locks may be incidental, arising from acoustic perturbations, interrupted signals, or drifting parameters; but they may also be intentional. During the interferometer experiment, for example, we adiabatically release the atoms from a red-detuned lattice stabilized to the cavity resonance. Because the lattice light is temporarily turned off, there is no error signal to maintain the lock, and each run of the experiment necessitates relocking the lattice laser frequency upon completion. The “relocker” described here

is our solution.

The relocker can be considered a machine with three states: calibrating, listening, and relocking (Fig. 4.6(a)). It takes as input the unmodified error signal and the output of a loop filter (Fig. 4.6(b)). During the calibration process, average V_{ES} and peak-to-peak error signal ΔV_{ES} voltages are sampled and stored. The unmodified error signal is sent to the loop filter and lock is engaged; the in-lock output voltage V_{OUT} is stored, and the device begins listening for a drop event. If the output voltage deviates from V_{OUT} beyond a hard-coded threshold, the device enters the relocking subroutine: the error signal is replaced by a linear voltage ramp which causes the output voltage to sweep as well. Meanwhile, the error signal voltage is monitored. Once the error signal voltage crosses above and then back below a programmable threshold related to V_{ES}^2 , control is returned to the loop filter (Fig. 4.6(c)). If the output voltage indicates a successful relock, the device begins listening again, but if the relock attempt has failed, the relocking procedure quickly repeats.

The relocker is built around a PSoC5LP programmable microcontroller on a FreeSoC2 development board. The CPU interfaces with a printed circuit board that houses a few op-amps for voltage conversion and the digital switches for enacting state logic. The same functionality could be achieved with an Arduino, albeit with relaxed technical specifications. Relocking speed was not a primary concern, but after fine-tuning, the device achieved 100% relock rate with typical relock times of 10 ms.

Interfacing with a serial port is useful in reporting calibration settings and passing time traces to a monitoring program written in Python. A TTL is used to temporarily block relocking attempts in cases where the error signal is intentionally disrupted. There are numerous opportunities to further improve upon the design. Calibration settings could be stored in persistent memory or sent serially. The range of output voltage sweeps could be adaptive. Instead of setting the threshold and sign of the error signal programatically, these could also be adjusted through a user interface.

²For locking to a PDH signal, we monitor for a voltage below $V_{ES} - 0.4 \times \Delta V_{ES}$ and then a voltage above the same threshold, which is sufficient for ensuring the loop filter attempted to relock near the central slope even with the presence of noise.

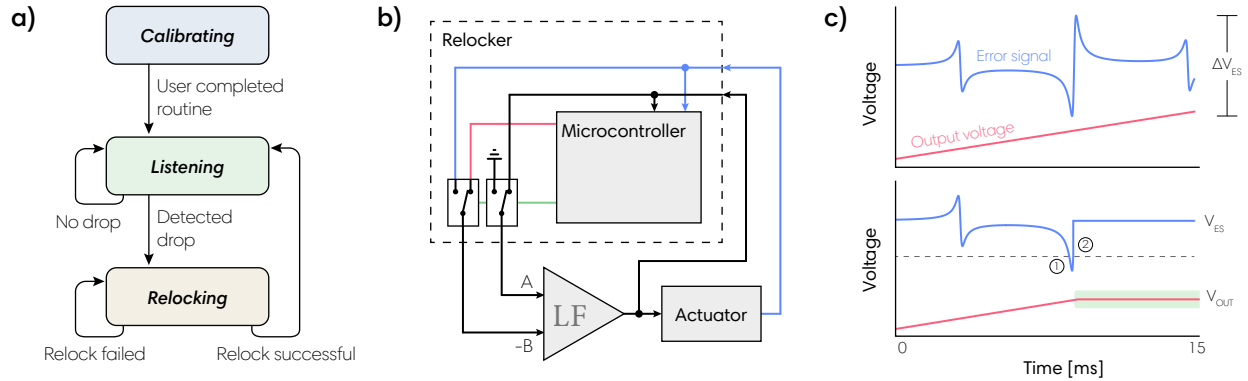


Figure 4.6: **Automated relocker.** (a) State diagram. (b) Connection diagram. The microcontroller switches loop filter inputs (green) and outputs a frequency ramp (red) according to its state. The actuator converts the loop filter output voltage to an error signal. (c) Theory of operation using a PDH error signal. A full sweep of the output voltage produces the entire lineshape (top), but if the relocker measures an error signal voltage below ① then above ②, control is passed back to the loop filter, re-engaging the lock (bottom). After re-engaging lock, the output voltage must settle within the tolerated region (green), *i.e.* must not rail, to be considered “successful”.

4.3 Narrowing laser linewidths with external optical feedback

Stabilizing a laser to a cavity is invaluable for removing low-frequency noise due to thermal or mechanical fluctuations, but in some situations, a laser with intrinsically narrow linewidth is desired instead. The history of narrowing diode lasers with optical feedback from an *external cavity* (as opposed to the diode’s internal cavity) goes back several decades [89]. Optical feedback from an electric field returning to a diode familiarly leads to instability which is typically circumvented with optical isolators. The same effect can also be harnessed to narrow the power spectrum by several orders of magnitude. Experimentally, the effect of the feedback depends on the strength and on the phase of the reflected field relative to the lasing field. An analytic expression for the linewidth has multiple solutions for most feedback strengths, leading to complex spectral properties [89], but for a narrow range of feedback strength, the linewidth is narrowed or broadened depending on the round-trip phase of the light.

We use optical feedback on our DBR lasers to reduce the ~ 500 kHz intrinsic Lorentzian linewidths to around 1 kHz. The temperature and vibration stability of a DBR makes it an attractive

candidate for the technique. The approach is similar to previous schemes involving electronic feedback onto a piezo [90] and onto an EOM [91] to control the round-trip external cavity phase shift.

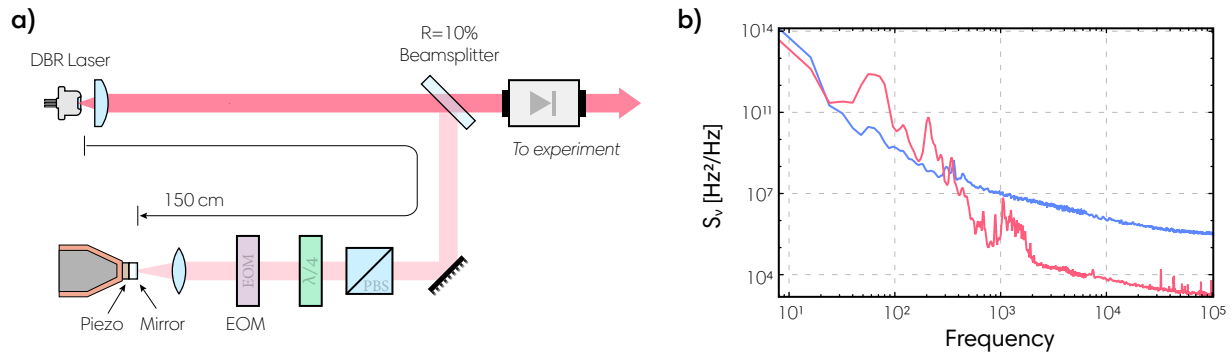


Figure 4.7: **Narrowing a laser with external optical feedback.** (a) About 10% of the DBR output power is picked off and sent to a 3 m long (round-trip) external cavity formed by a piezo-mounted mirror. Additional optics reduce the fraction of light returning to the laser to 10^{-3} to 10^{-4} relative to the output power. The lasing frequency is controlled by the piezo, and mode stability requires feeding back on the piezo and EOM. (b) $S_\nu(f)$ measured for a free-running DBR before (blue) and after (red) narrowing. Because the lasers are unlocked, there is a lot of low-frequency (Gaussian) noise, but the Lorentzian noise at high frequency is reduced several orders of magnitude for the narrowed laser.

In our setups, the current and temperature of the DBRs is left free-running. The lasing frequency is then pulled by a combination of the length of the external cavity as set by a piezo-mounted mirror and by the phase modulation of a free-space lithium niobate EOM. The feedback ratio for each path is set near 10^{-3} to 10^{-4} by a 10% pick-off plate, an ND filter, and a polarizing beam splitter cube which rejected a fraction of power set by a $\lambda/4$ -wave plate. Rather than measuring the feedback ratio accurately, we adjust the ratio to narrow the width of a laser beat note. The external cavity round-trip lengths are about 3 m in free space, and longer cavities are correlated with narrower achievable linewidths. The description of laser mode competition in Sec. 3.1.7 may also be helpful for intuition.

These narrowed lasers are locked, as usual, to beat notes or PDH error signals. The transfer function of the loop filter stabilizing the frequency of each laser is carefully designed to maintain

stability in the presence of resonances and filter poles. Electronic feedback is provided by two separate paths: slow feedback drives the piezo to change the length of the external cavity, primarily setting the laser frequency and providing dynamic range. The resonances of the piezo mounts are pushed above 40 kHz with guidance from Ref. [92]: a $2\text{ mm} \times 2\text{ mm}$ piezo is epoxied between a comparably-sized thin mirror and the tip of a lead-filled copper cone. The piezo path contains additional low-pass filtering. Fast feedback is handled by the EOM, but the crystal has a sharp resonance at 900 kHz set by its geometry. The unity gain bandwidths are limited near 500 kHz as a result.

We measure $S_\nu(f)$, the power spectrum of the relative frequency between two narrowed lasers, by beating the lasers against each other at a high-speed photodiode. The photodiode signal is sent through a frequency-to-voltage converter (two coaxial cables and a mixer which form an interferometer) and into a network analyzer. The frequency of the lasers is biased to the side of the interferometer fringe and the interferometer slope is used to convert a voltage noise spectrum to frequency units. In Fig. 4.7(b), the high-frequency (Lorentzian) components of the spectrum are reduced by three orders of magnitude, to less than 1 kHz after occasional tune-ups. A truly Lorentzian laser of FWHM $\Delta\nu$ has corresponding instantaneous frequency noise $S_\nu = \Delta\nu/\pi$. The observed low-frequency noise in Fig. 4.7 can be attributed to Gaussian processes including thermal and mechanical fluctuations which are ideally negligible *e.g.* after locking to a cavity.

4.4 Site-dependent loading

As we saw in Sec. 2.1, the standing wave modes of a two-mirror cavity lead to inhomogeneity in the coupling of individual atoms to intracavity light. Atoms are localized to lattice sites but the local probe intensity at each site may differ considerably. As a result, trapping atoms in a lattice that is incommensurate with the probe standing wave can lead to reduced effective atom number, degraded coherence, optomechanical oscillations, and complicated analysis, all of which obscure underlying physics.

One solution is to use a commensurate trapping wavelength λ_L that is a multiple of the prob-

ing wavelength λ_p [93]. However, the trapping wavelength may be desired as a system parameter, for example with state dependent or magic wavelength traps. Available mirror coatings may also inhibit this option. Another possibility in certain experiments is to use the running wave modes of a ring cavity. In Sec. 4.5, we describe a dipole trap configuration based on interference of cavity modes, maintaining radial confinement while allowing atoms to move and time-average away probe inhomogeneity [94].

Here we demonstrate one more technique for homogenizing the coupling between lattice and probing lasers. Atoms are held in an incommensurate 813 nm standing wave lattice and pumped into $|\uparrow\rangle \equiv |F = 2, m_F = 0\rangle$. A *Stark shift beam* blue-detuned one free spectral range from the atomic probe beam is incident on the cavity, providing a spatially-dependent frequency shift to the atoms (Fig. 4.8). Due to the opposite parity of adjacent longitudinal modes near the center of the cavity, atoms with high coupling to the atomic probe have no coupling to the Stark beam. A microwave π -pulse transfers the atomic probe-coupled atoms to $|\downarrow\rangle \equiv |F = 1, m_F = 0\rangle$ and a blow-away beam transverse to the cavity removes the remaining atoms with radiation pressure force. Atoms can be optically-pumped back to $|\uparrow\rangle$ and the process repeated for improved selectivity.

Nearly all of the physics here is captured by the Rabi formula, as the probability for each atom to undergo a transition depends on g_i , the position-dependent coupling of the i^{th} atom to the probe, through

$$P(g_i) = \frac{\Omega^2}{\Omega^2 + \Delta^2} \sin^2 \left(\frac{\pi \sqrt{\Omega^2 + \Delta^2}}{2\Omega} \right), \quad (4.8)$$

for $\Delta \equiv \delta_m - (g_i/g_0)^2 \delta_s$, where Ω is the microwave Rabi frequency detuned δ_m from resonance and δ_s is the peak AC Stark shift. A significant detuning due to the AC Stark shift beam makes a transition very improbable for any atoms not at antinodes, and only atoms that undergo a transition will survive.

Although the site-dependent selection approach involves discarding many atoms, this may not inhibit certain experiments, and the degree of homogeneity scales favorably with the number of retained atoms. With a completely incommensurate lattice, the ensemble-averaged coupling nor-

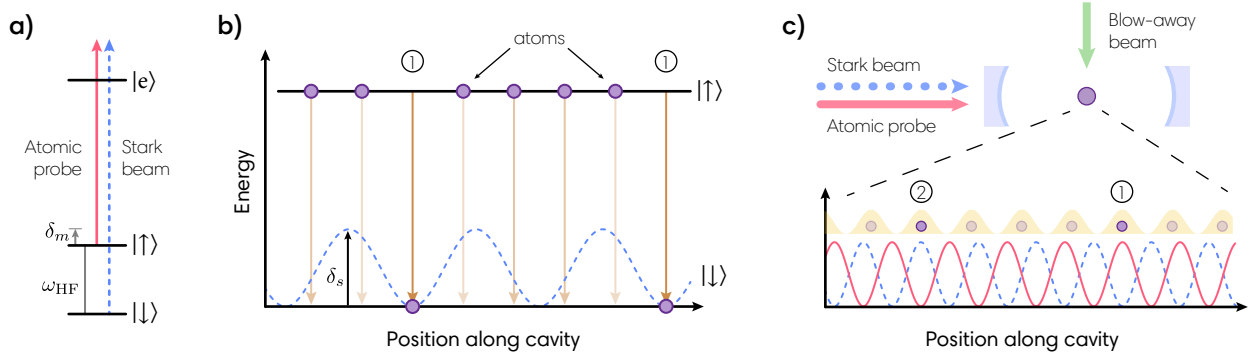


Figure 4.8: Site-dependent selection for homogeneous atom-cavity coupling. (a) Level diagram. The atomic probe and Stark beam are split by one free spectral range so that their standing waves are out of phase near the center of the cavity. (b) The Stark beam can be thought of as dressing the energy levels of $|\downarrow\rangle$ in a position-dependent way. Atoms at the maxima of the atomic probe remain resonant and still undergo microwave transitions, but the rest will be blown away. (c) Experimental setup and microscopic view showing the phase mismatch of the atomic probe (red), Stark beam (blue dashed), and lattice (yellow). Atoms are initially localized to the lattice sites but only survive if they are uncoupled to the Stark beam as at ①.

normalized to the maximal coupling is $\langle (g_i/g_0)^2 \rangle = 0.5$. Using the site-dependent selection scheme, we observe an increase in the normalized coupling to $\langle (g_i/g_0)^2 \rangle = 0.88(1)$ after one site-selective cycle [95]. At this point, 11% of atoms remain compared to 18% from a theoretical model. For this demonstration, $\delta_s = 2\pi \times 32.7 \text{ kHz}$, $\Omega = 2\pi \times 0.17 \text{ kHz}$, and $\delta_m = -2\pi \times 2.7 \text{ kHz}$. Because the remaining atoms are localized to the quadratic part of the probing potential, they are less susceptible to optomechanical oscillations associated with the force induced by the gradient of the probe standing wave. After two site-selective cycles, fractional amplitude of probe-induced oscillations are reduced to 32% of the oscillations measured without site-dependent selection [95].

This scheme allows atoms to remain tightly trapped (*i.e.* in the Lamb-Dicke regime) and leaves the lattice wavelength as a degree of freedom. Shaping the microwave pulses might improve performance in the future. While we do not rely on the scheme for the upcoming squeezing or interferometry experiments, it remains a broadly-useful tool for physics based around atom-cavity interactions.

4.5 Axially-uniform potentials

Another approach to the inhomogeneous coupling problem involves transforming a standing wave lattice into an axially-smooth potential by interfering multiple modes within the cavity. This technique is useful in creating homogeneous coupling for spin-squeezing [94] and interferometry, but the same idea was explored much earlier in Ref. [96]. For creating this axially-uniform lattice, multiple TEM_{00} longitudinal modes of a cavity are driven by a laser modulated at the free spectral range ω_{FSR} . The opposite parity of fields injected on adjacent modes ensures that near the center of the cavity, the combined axial potential is approximately uniform, $U(z) \sim \sin(k_0 z)^2 + \cos(k_0 z)^2 = 1$, but radial confinement remains strong (Fig. 4.9). A typical optical dipole trap (*i.e.* optical tweezers) relies on the field gradient at the tightly-focused waist of a running wave beam. The same optical dipole force is at play in our standing-wave configuration, hence our occasional description for this technique as a “dipole trap”.

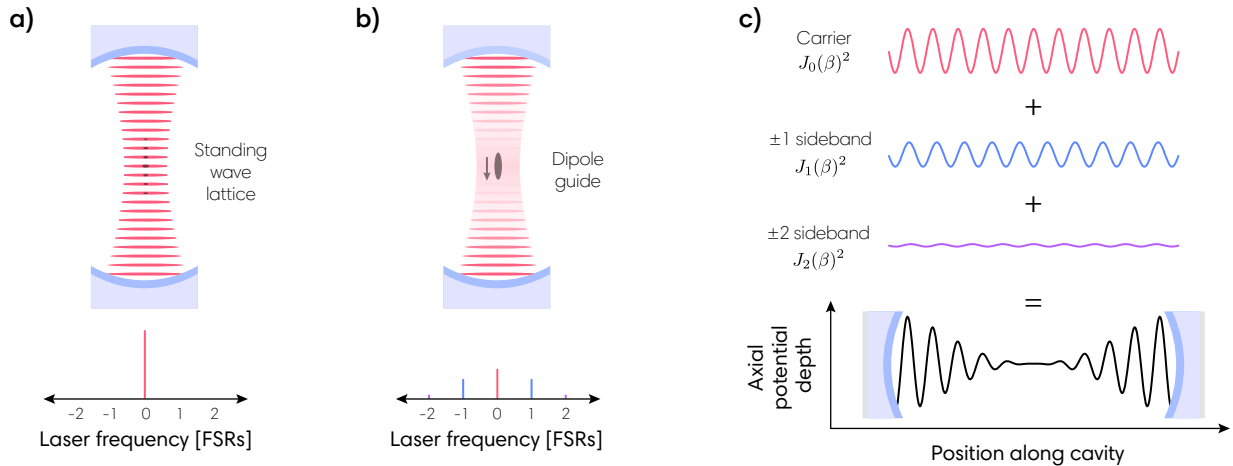


Figure 4.9: **Creating axially-uniform intracavity potentials.** (a) Ordinary standing wave lattice, with axial fringes shown as red disks. The number of “pancakes” and spacing are not to scale. (b) Adding sidebands at multiples of the cavity free spectral range creates a dipole trap with uniform axial potential at the center of the cavity. (c) The superposition of longitudinal modes leads to destructive interference at the cavity center and constructive interference at the cavity mirrors. The axial potential depths shown here have exaggerated wavelengths but correspond to axial trap depths calculated for $\beta = 1.21$.

More carefully, the axial component of the potential at a distance z from the cavity center can

be written

$$U(z) = U_0 \left[\sum_{n \text{ odd}} J_n^2(\beta) \cos^2((k_0 + \delta k_n)z) + \sum_{m \text{ even}} J_m^2(\beta) \sin^2((k_0 + \delta k_m)z) \right], \quad (4.9)$$

where $J_n(\beta)$ is the n^{th} Bessel function for modulation index β , $\delta k_n = n\omega_{\text{FSR}}/c$ is the change in wavevector for sidebands offset by n cavity free spectral ranges. Interference terms between the sidebands oscillate at ω_{FSR} and can safely be ignored. A trade-off in modulation index is made between minimizing the potential at $z = 0$ vs. extending the region with potential below a minimum threshold. In Ref. [94], the atomic ensemble can be a few mm long, so we opt for a modulation index that roughly maximizes the region where $|U| < 0.1U_0$. Tuning the modulation frequency away from the free spectral range or changing the modulation depth with time could offer additional degrees of freedom. In Fig. 4.9(c), the first few sidebands are plotted with exaggerated wavelength for $\beta = 1.21$.

4.6 LG₀₁ blue dipole guide

Atoms in the interferometer experiment undergo free-fall along the cavity axis but require radial confinement. The dipole trap configuration of the previous section comes close to achieving this, but atoms are susceptible to Bragg scattering from the residual axial potential. The axially-uniform lattice technique is combined with a 760 nm blue-detuned Laguerre-Gaussian LG₀₁-like “donut” mode to create the *blue dipole guide*. The LG₀₁ field is truly zero on-axis, allowing atoms to accelerate freely under gravity, but the rms radial position due to finite temperature still necessitates using modulation at ω_{FSR} to reduce axial potentials. The repulsive blue-detuning ensures that atoms are confined to the cavity mode ($r_{\text{rms}} \ll w_0$) for the entirety of the interferometer sequence.

The donut-mode LG₀₁ profile is constructed from the ± 1 st diffraction orders of a binary-mask fork-pattern hologram plate [97]. Mechanical stress-induced birefringence on the cavity mirrors breaks cylindrical symmetry, splitting the Hermite-Gaussian modes in the decomposition $\text{LG}_{01} = \text{HG}_{01} + e^{i\frac{\pi}{2}} \text{HG}_{10}$ by an amount $\delta_{\text{HG}} = 100 - 500$ kHz depending on the cavity piezo voltage [98]. Prior to entering the cavity, the ± 1 -order diffraction patterns from the forked phase plate

are sent along two separate paths. A δ_{HG} offset is added using two AOMs on one path (typically $\delta_{\text{HG}} = 350$ kHz for work presented). An EOM on the other path provides sidebands for locking the cavity to this laser via Pound-Drever-Hall. The two paths are overlapped at a polarizing beam splitter and sent into the cavity (Fig. 4.10(c)). Because δ_{HG} is much greater than the radial trap frequency, the atoms experience the time-averaged radial trapping potential of an LG_{01} mode.

The diffraction plate was created following Ref. [97], via chromium deposition of 133 lines/mm on an AR-coated 1" wedged blank. Other techniques including spatial light modulators are available. The pattern for these LG_{0l} plates can be written

$$P_{0l}(x, y) = \frac{1}{2} \sum_{n=-\infty}^{\infty} \text{sinc}\left(\frac{n\pi}{2}\right) \cos\left[n\left(k_x x - l \arctan\left(\frac{y}{x}\right)\right)\right], \quad (4.10)$$

where k_x is the frequency of lines far from the dislocations at the center of the plate (Fig. 4.10(a)). The same phase pattern is produced by interfering a TEM_{00} mode with the desired LG mode. Optimal performance requires careful placement of the plate at a beam waist and carefully centering the beam on the fork pattern. The total measured transmission efficiency is about 46%, with 24% of the transmitted power going into each of the ± 1 -order modes and 44% remaining in the 0th-order mode.

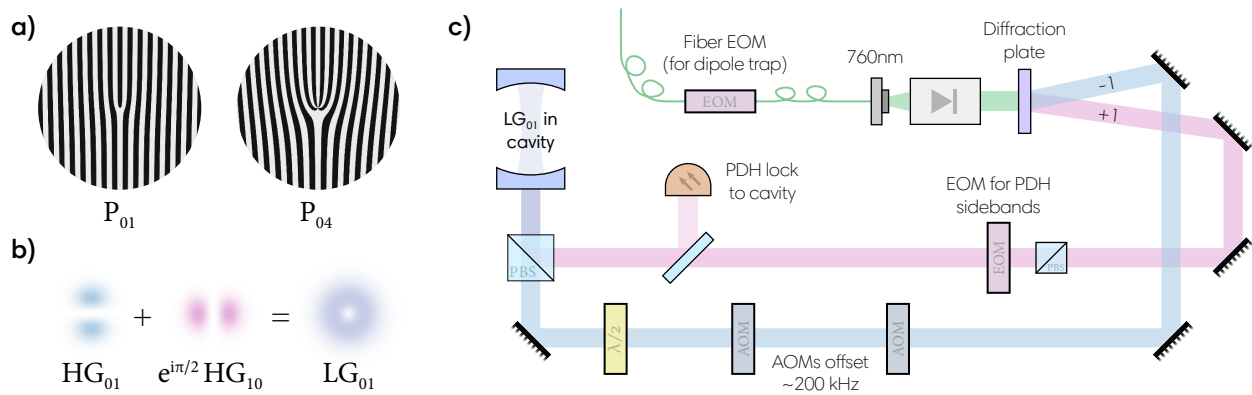


Figure 4.10: **Creating an intracavity LG_{01} donut dipole guide.** (a) Close up ($\times 200$) of the diffraction plate fork patterns used for creating the LG_{01} blue-detuned dipole guide and LG_{04} modes for testing. (b) First-order HG modes are combined into an LG_{01} -like mode within the cavity. (c) Relative tilt and stress on the cavity mirrors breaks cylindrical symmetry, so we use a diffraction plate to create two LG_{01} modes and offset their frequency by δ_{HG} . The modes are recombined to form a donut-like mode within the cavity which is verified by a CCD measuring in transmission. The total power is controlled by an AOM placed prior to the fiber EOM (not shown).

Chapter 5

Laser cooling

Advances in AMO physics are predicated on the ability to cool and control particles. Laser cooling techniques have revealed new frontiers for neutral atoms, ions, and mechanical resonators [99–101]. Although the “final book” on the subject has not been written, our lab frequently finds use for Metcalf and van der Straten’s *Laser cooling and trapping* [102]. Understanding methods and limitations for removing entropy from a system is a fundamental goal of AMO and continues to be widely explored [101, 103–108].

Some notable cooling mechanisms have been explored but never used in our system, including velocity-selective coherent population transfer (VSCPT) [109], cavity cooling [104], delta-kick cooling [110], and electromagnetically-induced transparency (EIT) cooling [111]. Other methods such as interferometric cooling [108] and microwave projection cooling [112, 113] are also valuable for the inspiration and insight they provide. In 2016, we briefly investigated the prospects for a collective cavity-mediated cooling mechanism called supercooling [114]. The scheme involved engineering superradiance using a Raman transition within the cavity QED weak-coupling regime. We were able to observe superradiance with a single-photon counting module (PN: Excelitas AQRH-10-FC) and extend it for a few milliseconds with repumping, but ultimately, we became concerned that heating due to repumping photon recoils would exceed cooling in our implementation.

The rest of this chapter summarizes the laser cooling and thermometry techniques that were implemented at various points in our experiment. Basic descriptions and parameters are provided for Doppler cooling, polarization-gradient cooling (PGC), and lambda-enhanced gray mo-

lasses. Particular attention is given to Raman sideband cooling (RSBC, Sec. 5.5), which required subtle changes from typical setups, and Raman sawtooth-wave adiabatic passage (SWAP) cooling (Sec. 5.6), which was a new technique developed within our lab. With SWAP cooling, we achieve a 1D equilibrium temperature of $5.9(3) \mu\text{K}$ – far below the Doppler cooling limit. The prospects for using SWAP cooling to avoid spontaneous emission while laser cooling new atomic or molecular species remains very exciting.

5.1 Measuring temperature

Temperature is an important diagnostic for our system, uniquely helpful for understanding the potentials and pulses experienced by the atoms. Typically, we are concerned with relative improvements rather than absolute measurements, though during the SWAP cooling experiment, lowering the temperature was the explicit goal. Here we will explore four distinct techniques for measuring temperature: fluorescence time-of-flight, dispersive cavity measurements of radial expansion, Raman velocimetry, and lattice sideband spectroscopy. More sophisticated temperature measurements are available, for example through obtaining the Doppler width from $g^{(2)}$ correlations or through heterodyne measurements to extract the spectrum of emitted light [104].

Fluorescence measurements. With fluorescence imaging, an atom absorbs a resonant photon and re-emits it for collection on a detector. Because the universe can in principle detect which atom emitted the photon, this is a destructive measurement that leads to quantum collapse. In practice, we snap off the confining lattice at $t = 0$, allow the cloud some dark time to expand from its initial rms width σ_i , and then turn on the MOT beams for fluorescence during a typical $100 \mu\text{s}$ exposure (Fig. 5.1(a)). It's possible to measure only atoms in $|\uparrow\rangle$, but adding a repumper for $|\downarrow\rangle$ atoms improves the signal-to-noise significantly. By integrating over the vertical distribution of atoms trapped in a lattice, we have sufficient signal-to-noise to measure radial temperature, but axial temperatures can be difficult (unless we simply assume that the atoms have equilibrated to

equal axial and radial temperatures). We rely on a simple Gaussian ballistic expansion fit model,

$$\sigma(t) = \sqrt{\sigma_i^2 + \frac{k_B T_{\text{rad}}}{m_{\text{Rb}}} t^2} \quad (5.1)$$

for Boltzmann constant $k_B = 1.38 \times 10^{-23} \text{ J K}^{-1}$ and rubidium mass $m_{\text{Rb}} = 1.443 \times 10^{-25} \text{ kg}$. Our rudimentary imaging systems are based around inexpensive CCD cameras (PN: FLIR CM3-U3-13S2M-CS) and 2" optics placed anywhere from 3" to 18" from the atoms. Technical noise limits the precision of the close-in camera to 80 atoms/shot, and we see signal-to-noise limited temperature fits after about 10 ms of ballistic expansion. Other complications such as the presence of background atoms and finite exposure times make fluorescence a very approximate technique for us.

Radial ballistic expansion. We can instead leverage our cavity dispersive measurements to monitor the average coupling of the atomic cloud as it expands out of the cavity mode (Fig. 5.1(b)). Here, atoms are held in a lattice with radial trap frequency ω_{rad} until the lattice is turned off, allowing atoms to disperse on a timescale fast compared to their falling. The probability to find an atom at position x and y after time t is

$$P(x, y, t) = \int_{-\infty}^{\infty} P_x \left(x - \frac{p_x t}{m} \right) P_x \left(y - \frac{p_y t}{m} \right) P_p(p_x) P_p(p_y) dp_x dp_y$$

with 1D position and momentum distributions (normalized with \mathcal{A}_x and \mathcal{A}_p)

$$P_x(x) \equiv \mathcal{A}_x \exp \left(-\frac{m\omega_{\text{rad}}^2 x^2}{2k_B T} \right); \quad P_p(p) \equiv \mathcal{A}_p \exp \left(\frac{-p^2/2m}{k_B T} \right).$$

Each atom in $|\uparrow\rangle$ contributes to the shift from atoms in N_{\uparrow} with a weighting that accounts for its radially-dependent cavity coupling. With atomic probe beam waist $w_0 = 70 \mu\text{m}$, the number of atoms in the cavity in N_{\uparrow} inferred from the cavity shift is modeled as

$$N_{\uparrow}(t) \propto \int_0^{\infty} \exp \left(\frac{-2r^2}{w_0^2} \right) P(x, y, t) 2\pi r dr = \frac{m_{\text{Rb}} w_0^2 \omega_{\text{rad}}^2}{m_{\text{Rb}} w_0^2 \omega_{\text{rad}}^2 + 4k_B T (1 + \omega_{\text{rad}}^2 t^2)}. \quad (5.2)$$

In Fig. 5.1(b), the radial expansion timescales are compared for a PGC-cooled ensemble at $5 \mu\text{K}$ and a Raman-sideband cooled ensemble around $0.5 \mu\text{K}$. Even after several milliseconds, a large

fraction of the ensemble is within the cavity mode. For this data, the red lattice and blue-detuned dipole guide must be temporarily disabled during expansion. An automated relocker is used on the lattice, and for durations less than 10 ms, the cavity PDH lock could re-engage automatically.

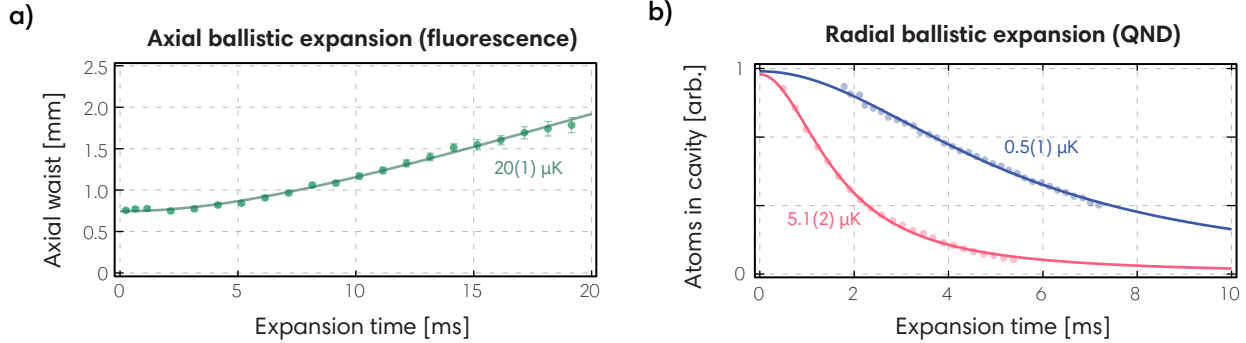


Figure 5.1: **(a)** Ballistic expansion of the axial distribution after polarization gradient cooling (PGC), measured with fluorescence on a CCD. **(b)** Radial temperature measurements of atoms after gray-molasses (red) and Raman sideband cooling (RSBC), using dispersive measurements of the atomic coupling to the cavity mode.

Raman velocimetry. Two-photon (Raman) velocimetry is a useful thermometry technique when the axis of interest is colinear with a set of Raman beams ω_1 and ω_2 (Fig. 5.2(a)). This was the preferred technique for our one-dimensional SWAP cooling and for measuring the axial temperature during the interferometry experiment. The idea is to spectroscopically excite a portion of atoms using the counter-propagating (velocity-selective) pair of Raman tones, transferring only a narrow velocity class from $|\downarrow\rangle$ to $|\uparrow\rangle$ where the relative population is subsequently measured with fluorescence or dispersive population measurements sensitive to the number of atoms in $|\uparrow\rangle$ [115]. A full velocimetry scan requires many trials, scanning the two-photon detuning between the Raman tones to fully cover the Doppler width of the ensemble. Power-broadened or Fourier-broadened distributions must be avoided at low temperatures by using a sufficiently low-power, long-duration excitation pulse.

Sideband spectroscopy. A final temperature diagnostic, sideband spectroscopy, measures

excitations of axial lattice modes (Fig. 5.2(b)). Sideband spectroscopy assumes atoms are in a harmonic potential with quantized motional states n described by a thermal Maxwell-Boltzmann distribution

$$P_n = \frac{\bar{n}^n}{(\bar{n} + 1)^{n+1}} \quad (5.3)$$

for the average number of motional excitations \bar{n} . The red and blue sideband transitions remove and add one motional quanta, respectively. Because $|n = 0\rangle$ has no lower energy state to transition to, an atom in the motional ground state is unaffected by the red sideband. Consider an atom in an electronic ground state but motional superposition, $|\psi\rangle = \sum_{n=0}^{\infty} c_n |n\rangle |\downarrow\rangle$. The probability to excite the atom with the red or blue sideband using a resonant pulse of duration t is

$$P_{\text{red}} = \sum_{n=1}^{\infty} \frac{\bar{n}^n}{(\bar{n} + 1)^{n+1}} \sin^2\left(\frac{\Omega_{n;n-1}t}{2}\right); \quad P_{\text{blue}} = \sum_{n=0}^{\infty} \frac{\bar{n}^n}{(\bar{n} + 1)^{n+1}} \sin^2\left(\frac{\Omega_{n;n+1}t}{2}\right) \quad (5.4)$$

with motional state-changing modified Rabi frequency $\Omega_{n,n+1} \equiv \Omega_{n+1,n}$ as in Ref. [116]. The takeaway (explored in Ref. [116] and elsewhere) is that the ratio of the probabilities $R = P_{\text{red}}/P_{\text{blue}} = \bar{n}/(\bar{n} + 1)$ is quickly learned from comparing the red and blue sideband peak heights after a spectroscopic scan. This ratio is independent of experimental parameters like drive time and Rabi frequency. Inverting the relationship yields the mean occupation of the motional state,

$$\bar{n} = \frac{R}{1 - R}. \quad (5.5)$$

As an example, we measured $\bar{n} = 0.7$ after cooling atoms in a lattice with PGC and a short stage of lambda-enhanced gray molasses. We were also able to verify the adiabaticity of lowering the lattice from $20E_{\text{rec}}$ to $3E_{\text{rec}}$ by then raising it back up and measuring the same \hat{n} and atom number. In a deeper trap, we measured $\bar{n} = 0.4$ after Raman sideband cooling. Sideband spectroscopy has the added bonus of re-affirming the axial trap frequency, and the asymmetric lineshape reflects the radial distribution as atoms off-axis experience shallower trapping frequencies.

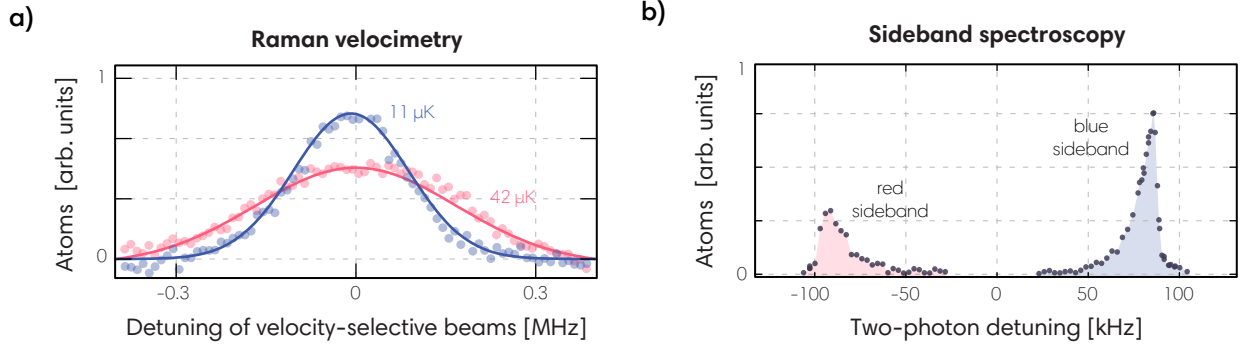


Figure 5.2: **(a)** Velocimetry results from the SWAP cooling experiment. The red data corresponds to the 42 μK initial distribution, cooled with PGC. The blue distribution corresponds to 11 μK after four cycles of SWAP cooling. **(b)** Sideband spectroscopy with $\bar{n} = 0.8$ in a red-detuned lattice with peak $\omega_{\text{ax}} = 2\pi \times 88$ kHz. The radial distribution of atoms leads to inhomogeneous trap frequencies.

5.2 Doppler cooling

Doppler cooling is the workhorse in most AMO systems, and it forms the basis of the magneto-optical trap (MOT) that begins all experiments in this dissertation. For a laser with wavelength λ red-detuned slightly below an atomic transition frequency, the Doppler shift of an atom moving towards the source increases the probability to absorb a photon compared to that of an atom moving away. Each photon absorption induces an $\hbar k \equiv \hbar \frac{2\pi}{\lambda}$ momentum change. Heating from the spontaneous emission of the excited state sets the Doppler cooling limit $T_{\text{D}} = \frac{\hbar\Gamma}{2k_{\text{B}}} = 146 \mu\text{K}$ in ^{87}Rb , where $\Gamma = 2\pi \times 6.066$ MHz is the decay rate of the optically-excited $5^2P_{3/2}$ state.

Doppler cooling techniques have been widely applied to produce atoms and molecules at mK to sub- μK temperatures and high phase-space density [117–123]. However, standard Doppler cooling is limited in both final temperature and maximum force by the linewidth and wavelength of the available optical transitions – properties that are provided by nature and not under control of the experimentalist. Extending Doppler cooling to molecules is also notoriously difficult. After each photon absorption event, a molecule needs to return to the initial state via spontaneous emission for Doppler cooling to proceed, but it may decay instead into the abundance of accessible vibrational and rotational degrees of freedom [124, 125]. This challenge has motivated the devel-

opment of alternative techniques that rely on reducing the role of spontaneous emission relative to Doppler cooling.

To form a MOT, a spherical quadrupole magnetic field is generated by running current through anti-Helmholtz MOT coils. The atomic energy levels of atoms far from the trap center are shifted closer to resonance [102, 126]. Light red-detuned from the cycling transition ($|F = 2\rangle \rightarrow |F' = 3\rangle$) leads to repeated photon absorption and emission. The two ingredients together entail a spatially- and velocity-dependent damping force that typically traps an ensemble of $\sim 10^8$ atoms with a density of $1 \times 10^{10} \text{ cm}^{-3}$ at a temperature near T_D .

In our system, six beam launchers send 1 cm diameter beams towards the center of the cavity, each containing 6.5 to 10 mW of MOT power and $100 \mu\text{W}$ of repumper power. In early setups, we used polarization optics to divide the beams along six separate pathways. After the squeezing experiments, we instead overlapped the MOT and repumper into an OZ Optics six-way fiber splitter, reducing the complexity of the optics table and the tendency for accidental misalignment. While accumulating atoms, the MOT laser is about 1.5Γ red-detuned from $F = 2 \rightarrow F' = 3$ and a repumper laser (REP) at the $F = 1 \rightarrow 2'$ transition restores atoms that scatter into $|F = 1\rangle$. The quadrupole field of a MOT enhances trapping via the spatially-dependent Zeeman shift which, together with photon polarizations, ensures outward-moving atoms are kicked in towards the center of the trap.

5.3 Polarization-gradient cooling into the red-detuned lattice

Additional atomic structure beyond hyperfine levels allows for a range of sub-Doppler cooling techniques [27, 102]. Such methods are needed to load our red-detuned lattice with significant atomic density. We create a sort of optical molasses via polarization-gradient cooling (PGC) that requires no additional lasers or polarization optics beyond those used for the MOT [127]. We simply disable the quadrupole field, set our bias coils to zero the magnetic field, tune our MOT laser frequency to be 7Γ blue-detuned from $F = 2 \rightarrow 2'$, and adjust intensities. The six beam launchers typically send about 6.5 mW of MOT power and $5 \mu\text{W}$ of repumper power for PGC.

The σ^+ and σ^- polarizations of the six beams form a polarization gradient and hence a spatially-varying AC Stark shift to each atom's ground state energy levels. When an atom travels to the maximum of the potential "hill", it has higher probability to scatter, optically-pumping into a state with a potential minimum. With careful tuning, we see this form of "Sisyphus cooling" achieve ensemble temperatures of 10 μK to 20 μK , but in principle, the limit is the photon recoil limit, $T_r = \frac{\hbar^2 k^2}{m_{\text{Rb}} k_B} \approx 360 \text{ nK}$ for rubidium mass m_{Rb} and $k/2\pi = 780 \text{ nm}$.

The red-detuned lattice is present during this process as an intracavity standing wave with "far-detuned" wavelength $\lambda_L = 813 - 823 \text{ nm}$. During the 5 - 20 ms loading period, a few hundred atoms are loaded into each of ~ 2500 lattice sites spread over 1 mm. Empirically, we see that the temperature after PGC is limited to about 10% of the red lattice trap depth. The ratio of temperature to trap depth sets the rms radial position of the atoms, so additional cooling is needed to improve the radial homogeneity of the atoms.

5.4 Gray molasses

Atoms are further cooled by a short stage of lambda-enhanced gray-molasses cooling. Similar to PGC, gray molasses relies on two-photon Raman transitions and a potential energy landscape created by counter-propagating σ^+ and σ^- beams [128]. The local polarization forms a "dark" linear superposition of $|F = 2, m_F\rangle$ states which decouples from the electric fields. Slow moving atoms remain in a dark state adiabatically, but faster moving atoms undergo diabatic transitions into "bright" states which are decelerated by light blue-detuned from the $|F = 2\rangle \rightarrow |F' = 2\rangle$ transition. The Λ -enhancement refers to the presence of an additional repumper tone which forms a Λ system as $|F = 1\rangle \leftrightarrow |F' = 2\rangle \leftrightarrow |F = 2\rangle$, turning the dark state into a superposition involving $F = 1$ states with decreased scattering rate.

We use a fiber-coupled EOM to add phase-coherent $\omega_{\text{HF}} = 2\pi \times 6.835 \text{ GHz}$ sidebands to the D₂-line MOT laser. While the atoms were held in a moderately-deep $\lambda_L = 813 \text{ nm}$ lattice (80 μK or 250 E_{rec} where $E_{\text{rec}} = \frac{\hbar^2}{2m} \frac{4\pi^2}{\lambda_L^2}$), the incoherent repumper laser is turned off. The MOT laser remains 7T blue-detuned of $F = 2 \rightarrow 2'$ with 2.5 mW per beam and 100 μW in a sideband near

$F = 1 \rightarrow 2'$. After applying lambda-enhanced gray-molasses cooling for 5 ms, we measure radial and axial temperatures as low as 5 μK .

5.5 Raman sideband cooling

In Raman cooling, a series of velocity-selective Raman pulses between ground-state hyperfine levels remove momenta [129, 130]. In one dimension, counter-propagating beams with frequencies ω_1 and ω_2 nearly complete the $|a\rangle$ to $|b\rangle$ Raman transition. When these frequencies are sufficiently detuned from $|i\rangle$, the excited state may be eliminated and the system is well-described as a two-level system. A detuned Raman pulse excites the atom from $|a\rangle$ to $|b\rangle$, while an optical pumping pulse tuned to $|b\rangle \leftrightarrow |i\rangle$ allows decay back into $|a\rangle$ (with momentum change spanning $\pm\hbar k$). By tuning a pulse using $\omega_1 - \omega_2 \equiv \Delta \neq 0$, some velocity class becomes resonant due to the Doppler shift and receives a $2\hbar k$ kick towards $v = 0$. The two photon resonance condition is $\delta = \omega_1 - \omega_2 - \omega_{\text{HF}} = 2k(v + v_{\text{rec}})$ with $k = \omega_1/c \approx \omega_2/c$. The chosen pulse states and detuning prevent atoms with $v \approx 0$ from being excited. A zero magnetic field is desired so that shifted magnetic sublevels do not broaden the Raman resonance. Extending the technique to additional dimensions works similarly.

Degenerate Raman sideband cooling (RSBC) is a clever extension that can achieve subrecoil temperatures [131, 132]. RSBC here works by creating a degeneracy between optical lattice vibrational modes and Zeeman sublevels. The technique is robust against experimental parameters and can even cool directly to degeneracy given enough laser power [133]. We began using RSBC during the interferometer experiment because small radial temperatures allowed more velocity selected atoms (*i.e.* a higher phase-space density) and higher pulse fidelity. We reached radial temperatures of 0.7(3) μK . Expanding RSBC to the axial dimension using the intracavity lattice may be a straightforward improvement for the future.

In our setup (Fig. 5.3), Helmholtz bias coils set a 0.11 G magnetic field along the cavity axis \hat{Z} so that the Zeeman splitting between adjacent states within a hyperfine manifold is nominally $2\pi \times 75$ kHz. Three RSBC beams form a triangular lattice in a plane perpendicular to \hat{Z} with axial

trap frequency $\omega_{\text{ax}} = 2\pi \times 75$ kHz. The polarizations of the three beams are twisted 10° from vertical to create the Raman coupling for driving the vibrational mode transition $|F = 1, m_F, n_{\text{tri}}\rangle \rightarrow |F = 1, m_F - 1, n_{\text{tri}} - 1\rangle$. It was vital to clean up the polarization at the input and output of the fibers using polarizing beam splitter cubes. A combination of σ^+ and π optical pumping light initializes atoms in $|F = 1, m_F = 1\rangle$ and this optical pumping light is kept on at a low intensity for continuous cooling. During the cooling, background radial confinement is still provided by the blue dipole trap and atoms are supported against gravity by the red intracavity lattice with trap depth of $\sim 250E_{\text{rec}}$

We are interested in the 2D potential for three co-planar vertically-polarized beams k_1, k_2, k_3 with amplitudes E_1, E_2, E_3 and frequency ω ,

$$U(r) = \left| E_1 e^{i(\vec{k}_1 \vec{r} + \omega t)} + E_2 e^{i(\vec{k}_2 \vec{r} + \omega t)} + E_3 e^{i(\vec{k}_3 \vec{r} + \omega t)} \right|^2. \quad (5.6)$$

A series expansion near the bottom of the potential reveals quadratic traps with approximately degenerate frequencies for $E_1 = \sqrt{2}E_2 = \sqrt{2}E_3$ and beams separated by $\theta_{12} = \theta_{13} = 113^\circ$. The introduction of a horizontal polarization component breaks the orthogonality for driving vibrational transitions between $|n\rangle \rightarrow |n - 1\rangle$. Without this component, the matrix element for the Raman coupling would be very close to zero [132].

The RSBC laser is an ECDL blue-detuned $2\pi \times 50$ GHz to the blue of the $|F = 1\rangle \leftrightarrow |F' = 2\rangle$ D_2 transition so that atoms are trapped at the nulls of the lattice, suppressing scattering off the cooling beams. The laser frequency does not need to be stabilized because the cooling method can tolerate many GHz of drift. About 10 mW is sent into a tapered amp (gain chip: Eagleyard EYP-TPA-0780-01000) built expressly for this setup, and the output power is divided into a 100 mW fiber launcher and two 50 mW launchers. All three launchers focus to beam waists of approximately $4 \text{ mm} \times 0.1 \text{ mm}$ extended elliptically along the cavity mode. The launchers are about 45 cm from the atoms.

The RSBC potential is ramped up exponentially over 0.4 ms, cooling happens for 1.2 ms, and the potential is ramped down over 0.3 ms. Smoothly transitioning the trap depth was crucial for

observing cooling (including using a 13 kHz low pass filter to smooth the VGA controlling AOM limiting the RSBC power). We then wait a quarter of the radial trap period from the combined red and blue lattices, 0.225 ms, for atoms to oscillate back to the center of the cavity, converting potential energy back to kinetic energy, at which point we repeat the entire cycle. The cycle is also repeated a third time, except after the cooling window, the red lattice is smoothly lowered from $80\ \mu\text{K}$ to $3\ \mu\text{K}$ over 3 ms. The RSBC potential is gradually lowered for the last time, and the red lattice is turned off entirely to allow the atoms to fall under gravity.

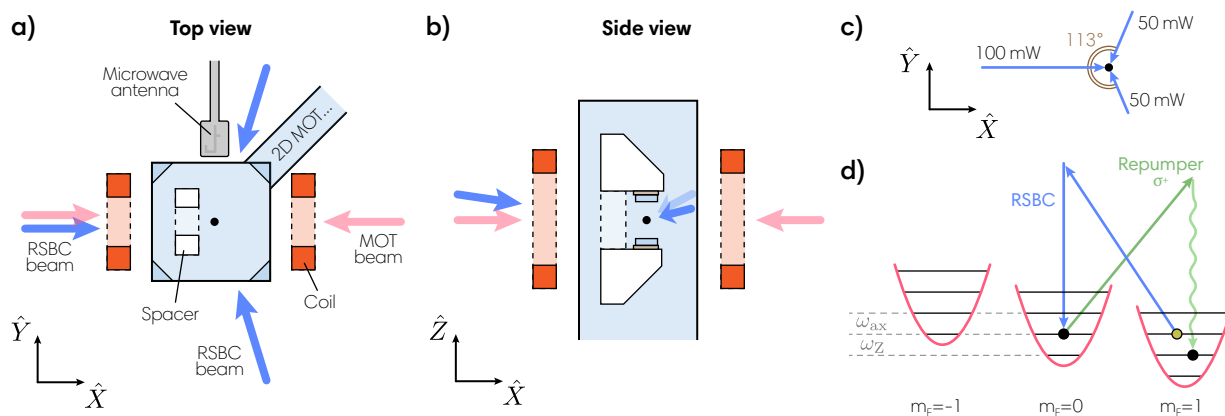


Figure 5.3: **Raman sideband cooling.** Physical setup with RSBC beams (blue): **(a)** top view and **(b)** side view, showing the cavity spacer (white), the MOT coils (orange) and the necessity for non-planar and nonequilateral beam geometry when launching into the glass cell. **(c)** The pyramidal lattice was calculated for a 2:1:1 power ratio and 113° between the strong beam and each weak beam. **(d)** A single Raman sideband cooling cycle. Atoms are held in an RSBC lattice with axial trap frequency equal to the Zeeman splitting, $\omega_{ax} = \omega_Z$. An atom in $|m_F = 1, n = 2\rangle$ (yellow) undergoes a two-photon Raman transition to $|m_F = 0, n = 1\rangle$, and repumping brings it back to $|m_F = 1, n = 1\rangle$ with the net result of reducing the motional excitation n by one quanta.

5.6 SWAP cooling with Raman transitions

A new laser-cooling mechanism called Sawtooth Wave Adiabatic Passage (SWAP) cooling was demonstrated by the strontium side of the Thompson lab using a narrow-linewidth transition in ^{88}Sr [134]. SWAP cooling uses counter-propagating lasers that are slowly swept in frequency

through an atomic resonance to facilitate Landau-Zener adiabatic transfers [135, 136]¹. Repeated transfers enable the removal of many photon-recoils of momentum from atoms or molecules before spontaneous emission occurs. This technique is robust against laser frequency noise and small changes in atomic transition frequency. SWAP cooling has now been used for slowing dysprosium [137] and for rapidly forming denser Sr MOTs [138], and further exploration continues in various groups [139–142].

The proof-of-principle experiments described in the remainder of this chapter use ⁸⁷Rb to demonstrate that the SWAP cooling mechanism does not require a closed, single-photon transition [143]. Instead, it is amenable to atoms and molecules with at least two long-lived ground states bridged by a two-photon transition. Cooling molecules remains a significant challenge, and without dwelling on the dissimilarities between molecules and atoms, any cooling scheme that suppresses the probability to scatter into undesired states is potentially of interest for the field. In Sec. 5.6.2, some arguments are provided for the merits of SWAP cooling in a regime where little to no free-space scattering is permitted.

For SWAP cooling with a single-photon transition, counter-propagating lasers address the atoms just as in standard Doppler cooling. The frequency is ramped in a sawtooth pattern through the transition frequency ω_a that separates a ground state $|a\rangle$ and a long-lived optically excited state $|b\rangle$ with lifetime $\tau = 1/\Gamma$ (Fig. 5.4). For an atom in motion, the relative Doppler shift of the two laser beams sets an important time ordering: the beam counter-propagating to the atom's motion first passes through resonance, driving an adiabatic transition from $|a\rangle$ to $|b\rangle$ along with a momentum kick associated with photon absorption that opposes the atomic motion. The co-propagating beam next drives a transition back from $|b\rangle$ to $|a\rangle$ via stimulated emission that, again, slows the atom. In net, each sweep ideally removes $2\hbar k$ of momentum regardless of the direction the atom is moving.

In our demonstration of SWAP cooling using two-photon transitions, there are two metastable ground states, $|a\rangle$ and $|b\rangle$ (Fig. 5.4(b)). Two lasers tuned off-resonance from an intermediate optically-

¹From numerous discussions, it may be helpful to explicitly state that the Landau-Zener adiabatic process differs from stimulated Raman adiabatic passage (STIRAP), although the techniques are intimately related.

excited state $|i\rangle$ engineer an *effective* optically-excited state with tunable lifetime (or, equivalently, linewidth) instead of relying on the properties of the original optical transitions. The laser dressing $|a\rangle$ is swept with an asymmetric sawtooth waveform through the two-photon resonance, driving adiabatic Raman transitions between $|a\rangle$ and $|b\rangle$. At the end of a cycle, some atoms may erroneously remain in $|b\rangle$, so optical pumping is briefly applied to return them to $|a\rangle$. In this manner, the limitations set by spontaneous emission can be bypassed: the Doppler temperature associated with the intermediate state no longer applies, and population loss to undesired states is avoided. After about 10 ms, we achieve a 1D equilibrium temperature 25 times lower than the usual $T_D = 146 \mu\text{K}$ cooling limit for standard Doppler cooling in ^{87}Rb .

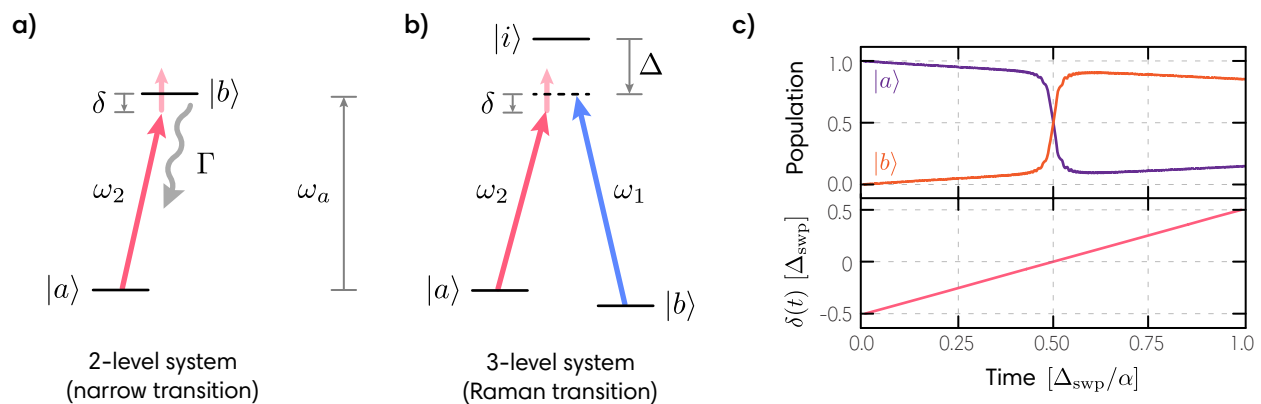


Figure 5.4: **Landau-Zener transfers for single-photon and Raman transitions.** SWAP cooling level diagrams for (a) a single-photon transition and (b) a two-photon Raman transition. In the Raman configuration, a large detuning Δ from the intermediate state ensures the lifetime of the excited state $|i\rangle$ is effectively infinite except when it is used in returning atoms to $|a\rangle$ following each sweep. (c) Landau-Zener adiabatic transfers are simulated in the presence of scattering. As ω_2 is swept through resonance (bottom, $\delta(t) = 0$), population is swapped between the atomic states (top). In units of the scattering rate, the sweep range is $\Delta_{\text{swp}} = \Gamma/3$, $\Delta = 300\Gamma$, $\Omega_{ab} = \Gamma/150$. The scattering rate Γ causes the decay of coherence.

5.6.1 Laser cooling rubidium with adiabatic transfers

Figure 5.5 shows our setup for demonstrating Raman SWAP cooling in ^{87}Rb . The two ground states are the hyperfine “clock” states: $|a\rangle \equiv |F = 2, m_F = 0\rangle$ and $|b\rangle \equiv |F = 1, m_F = 0\rangle$. These states are coupled by lasers at frequencies ω_1 and ω_2 , both far-detuned from the intermediate state

$|i\rangle$ by $\Delta \approx 2\pi \times 2$ GHz. The east/west bias coils establish a uniform magnetic field to set the quantization axis along \hat{X} , the propagation axis of the cooling beams. The cooling beams incident from $+\hat{X}$ are vertically polarized and the beams incident from the $-\hat{X}$ are horizontally polarized. Dipole selection rules disallow two-photon transitions with pairs of photons of the same linear polarization, *i.e.* the absorption and stimulated emission of pairs of orthogonal linearly polarized photons. As a result, only counter-propagating photons with difference frequency of $\omega_{\text{HF}} = 2\pi \times 6.835$ GHz drive the transitions, and internal state changes are always accompanied by a net photon recoil momentum of $2\hbar k$ where $ck \approx \omega_1 \approx \omega_2$.

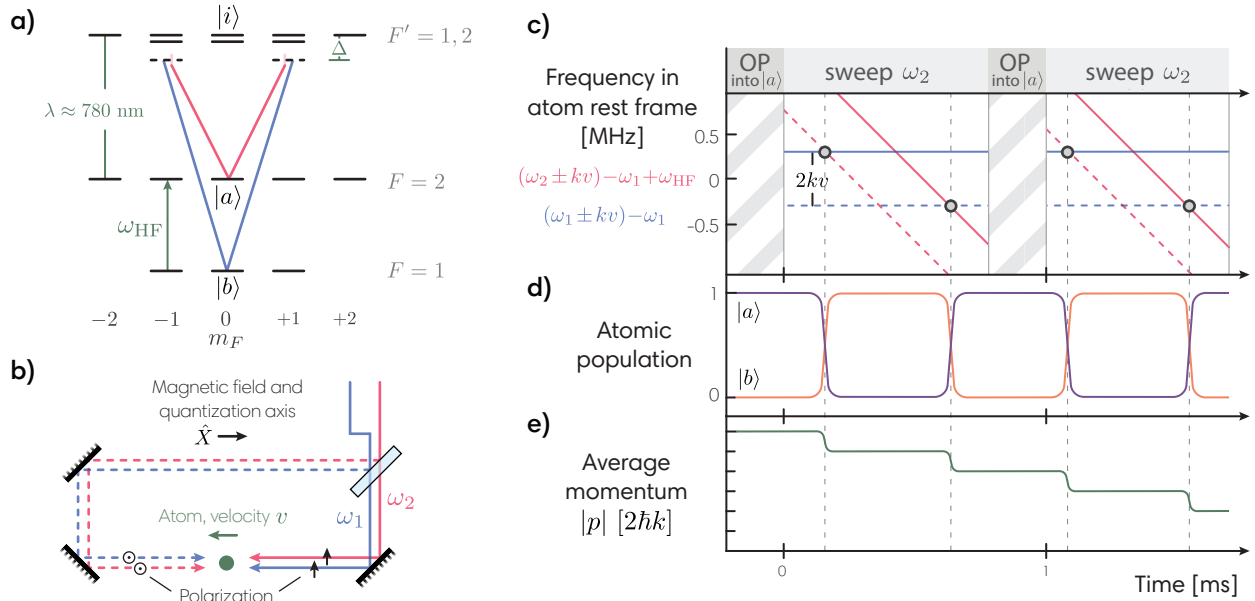


Figure 5.5: **Raman SWAP cooling scheme.** (a) ^{87}Rb level diagram. Two-photon transitions between $|a\rangle$ and $|b\rangle$ are induced by ω_1 (blue) and ω_2 (red). (b) Experimental layout. A moving atom (green) interacts with two pairs of counter-propagating laser beams (blue, red) with ω_2 swept in a sawtooth manner. (c) The four unique laser frequencies observed in the rest frame of the atom after considering the Doppler shifts that separate counter-propagating lasers in frequency by $2kv$. Offsets have been subtracted so that points marked with circles correspond to allowed two-photon resonances which involve pairs of orthogonally-polarized, counter-propagating laser beams. (d) Two-photon Landau-Zener transitions transfer an atom from $|a\rangle$ to $|b\rangle$ and back to $|a\rangle$ during each sweep. (e) The counter-propagating lasers ideally remove $4\hbar k$ momentum per cooling sweep.

The two independent lasers at ω_1 and ω_2 are phase-locked and their outputs are split into the $\pm\hat{X}$ (Fig. 5.5(b)). We arbitrarily choose to hold the frequency ω_1 fixed while the frequency

ω_2 is swept linearly in time, downward in frequency through the two-photon atomic resonance at $\omega_1 - \omega_2 \approx \omega_{\text{HF}}$. The Landau-Zener formula describes the probability to undergo a diabatic transition between two energy levels during the sweep [135, 136],

$$P_d = e^{-\xi} \quad \text{where} \quad \xi = \frac{\pi}{2} \Omega_{\text{ab}}^2 / \alpha, \quad (5.7)$$

with sweep rate $\alpha \equiv d\omega_2/dt$. Here, the two-photon Rabi frequency is $\Omega_{\text{ab}} \approx \frac{\Omega_1 \Omega_2}{2\Delta}$, and $\Omega_1 \approx \Omega_2$ are the single photon Rabi frequencies of the respective frequency components ω_1 and ω_2 .

If the sweep rate is kept low, the system undergoes an avoided crossing and adiabatically evolves into the opposite atomic state. The two-photon resonance condition $\delta(t) \equiv \omega_1 - \omega_2 - \omega_{\text{HF}} = \pm 2kv$ is met twice due to the Doppler shifts of the laser frequencies as seen by an atom moving at velocity v (Fig. 5.5(c)). Each adiabatic passage through imparts a net momentum change of $2\hbar k$ per transition, *i.e.* $4\hbar k$ per ideal sweep. The direction of the frequency sweep determines whether momentum is added or subtracted.

The Doppler shift becomes of order Ω_{ab} as the speed of an atom approaches zero. At this point, the time-ordering breaks down for the adiabatic transfers detailed previously and the slowing mechanism begins to fail [134]. The eventual failure of a transfer, either due to broken time-ordering, scattering, or imperfect adiabatic transfer efficiency, means there could be considerable probability to find atoms in $|b\rangle$ at the end of a sweep, and the next cycle would result in heating. We therefore apply π -polarized optical pumping light transverse to the cooling beams to return any misplaced atoms to $|a\rangle$ before each frequency sweep. Optical pumping in this scheme plays a role analogous to spontaneous emission in Ref. [134] for reducing entropy, breaking time reversibility and allowing for the compression of phase space. The optical pumping was applied for $100 \mu\text{s}$, though this is much longer than necessary given the fast decay rate for the excited state.

In our SWAP cooling experiment, the ω_1 laser is locked to a spectroscopy setup, and ω_2 is locked to the first-order sideband of a fiber EOM modulated by an rf signal generator (PN: SRS SG384) at the 6.8 GHz offset frequency plus a triggered sawtooth frequency ramp. Around 10^7 atoms are loaded into a 3D MOT and cooled to $42 \mu\text{K}$ with polarization gradient cooling to nar-

row the initial velocity distribution, reducing the required frequency sweep range. The atoms are initially pumped into $|a\rangle$ with π -polarized light applied by the transverse optical pumping beams. The cooling lasers are turned on with AOMs and ω_2 is swept for of order 1 ms and over 1 MHz (to cover the Doppler width of the distribution) as shown in Fig. 5.5(c) with the intended atomic state populations and momentum changes shown in Fig. 5.5(d and e). The SWAP sequence of optical pumping and sweeping is repeated several times, until a significant fraction of atoms are physically displaced from the cooling/velocimetry beams due to an imbalance in repumping beam power.

The final 1D temperature of the atoms is measured by velocimetry as described in Sec. 5.1. Atoms are returned to $|a\rangle$ as part of the final SWAP cycle and then transferred to $|b\rangle$ with a microwave π -pulse so that a small background of atoms in $|a\rangle$ can be blown away. Velocity-selective Raman transitions are applied with the cooling beams for 90 μs to drive atoms within a small velocity range back to $|a\rangle$ [115]. The population in $|a\rangle$ is finally determined using fluorescence and the resulting Voigt profiles² are fit to extract the temperature (Fig. 5.6(a)). Velocimetry allows better precision than time-of-flight measurements of the cloud's ballistic expansion in this setup, but the two methods returned consistent results.

From an initial temperature of 42(3) μK , atoms are cooled in 1 dimension to 10 μK after the application of 9 sweeps with fixed two-photon Rabi frequency $\Omega_{ab} = 2\pi \times 22 \text{ kHz}$ and sweep range of $\Delta_{\text{swp}} \equiv 2\pi \times 0.8 \text{ MHz}$ (purple points in Fig. 5.6(b)). The sweep range Δ_{swp} is chosen to include 95% of the atoms when accounting for the Doppler shifts of the initial velocity distribution. Because the initial sweeps narrow the velocity distribution, the cooling rate and final temperature can be optimized by progressively decreasing the two-photon Rabi frequency and sweep range. For the green points in Fig. 5.6(b), after three sweeps, the Rabi frequency is reduced to $\sqrt{0.5} \times \Omega_{ab}$ and the sweep range is reduced to $0.5 \times \Delta_{\text{swp}}$ such that the Landau-Zener adiabaticity parameter ξ (Eq. 5.7) remains unchanged. After two additional cycles, sweeps are performed with two-photon

²The Maxwell-Boltzmann temperature distribution $G(v, T) = \sqrt{\frac{m}{2\pi k_B T}} e^{-\frac{mv^2}{2k_B T}}$ convolves with the excitation pulse Lorentzian $L(v) = \frac{\Omega_{ab}/2k}{v^2 + \Omega_{ab}^2/4k^2}$, resulting in a Voigt profile $V(v, T) = \int_{-\infty}^{\infty} G(v', T)L(v - v') dv'$. In our parameter regime, the resulting lineshape has only minor deviation from a Gaussian, but we easily correct for this effect.

Rabi frequency $\sqrt{0.4} \times \Omega_{ab}$ and sweep range $0.4 \times \Delta_{swp}$. In this manner, the measured temperature reached $5.9(3) \mu\text{K}$ after 9 total sweeps.

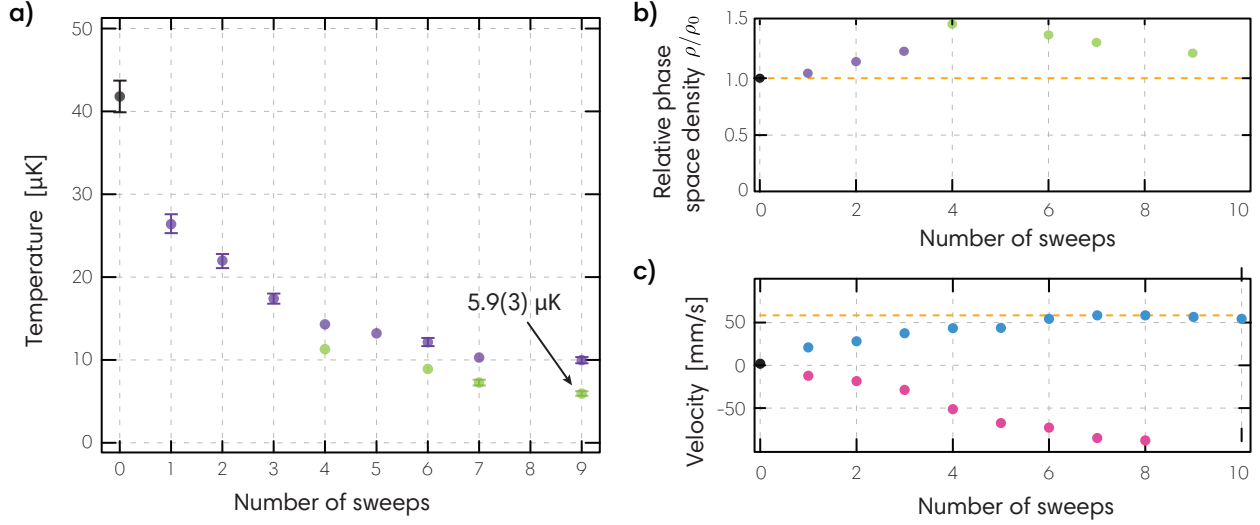


Figure 5.6: Raman SWAP cooling results. (a) Reduction in temperature, determined by velocimetry. The atomic ensemble is cooled as low as $5.9 \mu\text{K}$ in one dimension over the course of several sweeps. For the purple points, all sweeps used a two-photon Rabi frequency $\Omega_{ab} \approx 2\pi \times 22 \text{ kHz}$ and sweep range $\Delta_{swp} = 2\pi \times 0.8 \text{ MHz}$. For the green points, Ω_{ab} and Δ_{swp} were successively reduced between sweeps as described in the text. (b) The relative one-dimensional phase-space density for the corresponding purple or green points in (a). The phase-space density begins to decrease after four sweeps despite the decreasing temperature because atoms begin to leave the velocimetry beams. (c) To cool into a moving reference frame (blue points), we apply a frequency offset $\delta_{AOM} = 2\pi \times 150 \text{ kHz}$ in the lab reference frame between the beams from opposite directions. By sweeping ω_2 downwards, the atoms cool and equilibrate into a moving reference frame which has a velocity $v_F \equiv \delta_{AOM}/2k$ (dashed orange line). Reversing the sweep direction (pink points) caused the atoms accelerate in the opposite direction without bound.

As atoms are cooled, the entropy is reduced and the relative 1D phase space density $\rho/\rho_0 = \Delta x_0 \Delta v_0 / (\Delta x \Delta v)$ in Fig. 5.6(c) is increased modestly. Here Δx_0 and Δv_0 (Δx and Δv) are the measured cloud size and velocity spread before (after) cooling. Given that phase space compression cannot occur without dissipation, the lack of spontaneous emission in an ideal sweep is initially alarming. But one can achieve phase space compression without actually scattering a photon – it is sufficient that the atom *could have* scattered a photon were it within a particular region of phase space. When an atom's Doppler shift satisfies $kv \lesssim \Omega_{ab}$, there is significant probability of fin-

ishing a sweep in the wrong internal state so a scattered optical pumping photon signals that an atom has a small velocity. In the early cooling stages, when $kv \gg \Omega_{\text{ab}}$, the atom is always moved towards lower velocity without scattering a photon, so even *not scattering* a photon acts as information to the environment that reduces the probability that the atom is in the portion of phase space with $kv < \Omega_{\text{ab}}$. The loss of atoms from the effective cooling/imaging region limited the observed phase-space density after a few sweeps. Larger beam diameters or better balanced optical pumping beams would mitigate this issue.

To emphasize the critical role of the frequency sweep direction, a fixed relative offset frequency $\delta_{\text{AOM}} = 2\pi \times 150 \text{ kHz}$ is applied between the counter-propagating beams such that atoms are cooled into a moving reference frame with velocity $v_F = \delta_{\text{AOM}}/2k$. When the laser frequency is swept downward as before, the atoms are accelerated into and then equilibrate into the moving frame (blue points in Fig. 5.6(c) saturating at the predicted velocity, orange dashed line). In contrast, reversing the frequency sweep direction without changing δ_{AOM} accelerates the atoms in the opposite direction (pink points) even though the direction of the moving reference frame remains unchanged. As expected, the atoms are accelerated to speeds larger than $|v_F|$.

5.6.2 A model for Raman SWAP cooling with scattering

The choice of sweep rate α is optimized by considering two effects. First, adiabatic transfer can be extremely efficient, but the laser frequency must be swept slowly such that the Landau-Zener diabatic transition probability (Eq. 5.7) is small. Second, spontaneous emission from the excited states results in heating. To avoid scattering from the applied cooling beams, the probability to have not scattered a photon during the total sweep time should be close to unity, $\bar{P}_{\text{sc}} = e^{-R_{\text{sc}}\Delta_{\text{swp}}/\alpha} \approx 1$, and hence the sweep cannot be excessively slow. R_{sc} is the total spontaneous scattering rate from the far-detuned intermediate state(s). For a single laser and excited state, we have [27]

$$R_{\text{sc}} = \left(\frac{\Gamma}{2}\right) \frac{2(\Omega/\Gamma)^2}{1 + 4(\Delta/\Gamma)^2 + 2(\Omega/\Gamma)^2} \approx \frac{\Gamma}{2} \frac{\Omega^2}{2\Delta^2}. \quad (5.8)$$

In Fig. 5.7(a, circles), we explore the probability for successful adiabatic transfer from $|a\rangle$ to $|b\rangle$ using σ^+ -polarized beams from a single direction. The two-photon Rabi frequency is kept the same as above. This configuration allows Doppler-free, dipole-allowed transitions. The optimum sweep rate α near 1 MHz/ms maximizes the transfer efficiency as desired for efficient cooling. The measurements closely follow a prediction from numerically integrating optical-Bloch equations including scattering rates and measured Rabi frequencies (orange). For comparison, the red dashed line is the Landau-Zener $1 - P_d$ theoretical transfer efficiency which ignores free space scattering. A simple probability-based model of a full cooling sweep, assuming 79% chance to transfer each way while allowing for the possibility of a state change by free-space scattering, then predicts a $2.2\hbar k$ expected momentum reduction, the same as was measured for the first sweep of Fig. 5.6(b). Later sweeps are less efficient.

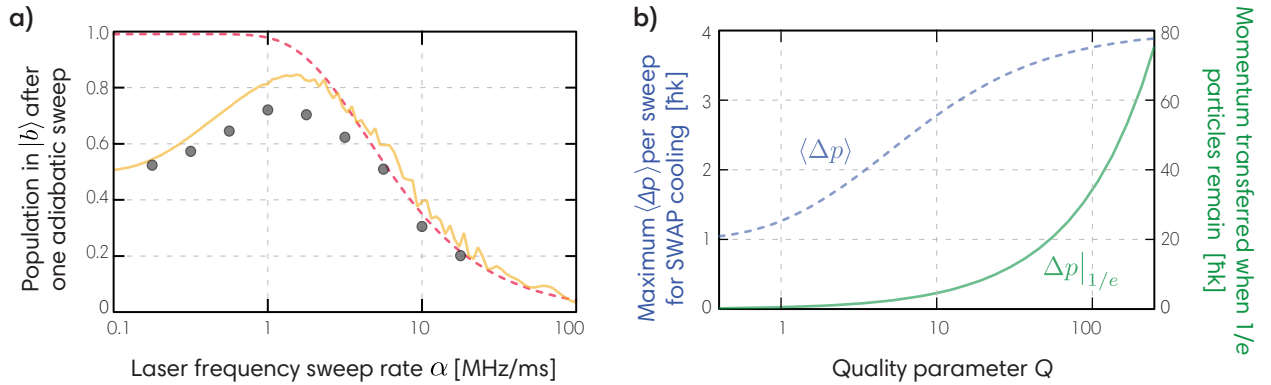


Figure 5.7: **Adiabatic transitions and momentum transfer.** (a) Population in $|b\rangle$ after one adiabatic transfer attempt (black points), measured using fluorescence detection. To drive a single transfer, we use co-propagating σ^+ -polarized light with fixed ω_1 and ω_2 swept through resonance at rate $\alpha = d\omega_2/dt$. Adiabatic transfers are performed with $(\Omega_{ab}, \Gamma, \Delta, \Delta_{\text{swp}}) = 2\pi \times (20 \text{ kHz}, 6 \text{ MHz}, 2 \text{ GHz}, 0.8 \text{ MHz})$. The familiar Landau-Zener prediction (red dashed) fails at low sweep rate due to off-resonant scattering from the intermediate state $|i\rangle$. A numerical simulation including off-resonant scattering and the experimental parameters (orange) shows better agreement with the data but some room for better modeling. (b, left) The achievable momentum transfer per SWAP cooling sweep (blue dashed) approaches the ideal $4\hbar k$ at large quality parameter $Q \equiv \frac{\pi}{2} \frac{\Omega^2}{\Gamma \Delta_{\text{swp}}}$. (b, right) With the worst-case scenario in mind where a particle is lost if it undergoes a single spontaneous emission event, we plot the predicted achievable momentum transfer when $1/e$ particles remain versus the quality parameter Q (green).

To further generalize predictions for how scattering will limit SWAP cooling, consider the $|a\rangle \leftrightarrow |i\rangle \leftrightarrow |b\rangle$ Λ -system shown in Fig. 5.4(b). For simplicity, we will assume that the intermediate state $|i\rangle$ decays with equal rates of $\Gamma/2$ into both $|a\rangle$ and $|b\rangle$ and that the large detuning limit $\Delta \gg \Gamma, \Omega$ is satisfied. For convenience, we also assume equal single-photon Rabi frequencies $\Omega_1 = \Omega_2 = \Omega$. The two photon Rabi frequency is then $\Omega_{ab} = \frac{\Omega^2}{2\Delta}$, and the total scattering rate is $R_{sc} = \frac{\Gamma\Omega^2}{4\Delta^2}$. Details supporting the following summary of results are provided in Appendix B.0.3.

For this toy model, we first find the optimum momentum transferred Δp during a cooling sweep after optimizing for sweep rate α . In Fig. 5.7(b, blue), Δp is plotted against a dimensionless quality parameter,

$$Q \equiv \frac{\ln(P_d)}{\ln(\bar{P}_{sc})} \approx \frac{\pi}{2} \frac{\Omega^2}{\Gamma \Delta_{swp}}. \quad (5.9)$$

The sweep range Δ_{swp} is not entirely free to change as it must sufficiently cover the Doppler width of the velocity distribution. For $Q \gg 1$ then, the momentum transfer per sweep saturates to the ideal value $4\hbar k$, and the effective force is $4\hbar k/t_{swp}$, where the time to complete each sweep is t_{swp} . At the optimized sweep rate, $t_{swp} = \frac{8 \ln(2Q)}{\pi} \frac{\Delta^2}{\Omega^4} \Delta_{swp}$. The quality parameter Q scales with laser intensity I and wavelength as $Q \propto I\lambda^3$, but interestingly, it does not depend on the dipole matrix element M between the states $|a\rangle, |b\rangle$ and the intermediate state $|i\rangle$. With these parameters, the sweep time scales as roughly $t_{swp} \propto \frac{\Delta^2}{M^4 I^2} \Delta_{swp}$.

Avoiding spontaneous emission is of primary importance for cooling molecules. In the worst-case scenario, every molecule that spontaneously emits a photon is completely lost into unaddressed “dark states”. In Fig. 5.7(b, green), we evaluate $\Delta p|_{1/e}$, the average momentum removed when $1/e$ molecules remain, by numerically optimizing the sweep rate. For $Q \gg 1$, the numerical result is well approximated by $\Delta p|_{1/e} \approx \frac{2.1Q}{\ln(4(Q+14))} \hbar k$ and one can remove many photon recoils of momentum from a molecule before it is likely to be lost. The optimized sweep time is well approximated by $t_{swp} \approx \frac{\ln(4(14+Q))}{3.2} \frac{\Delta^2}{\Omega^4} \Delta_{swp}$.

In principle, 3D cooling should be possible using additional pairs of cooling beams along \hat{Y} or \hat{Z} (where the 1D cooling above has been along \hat{X}). Experimentally, it may be difficult to quickly

change the direction of the magnetic field \vec{B} for cooling one dimension at a time, so the available laser polarizations become a subtle obstacle. One possibility is to set the magnetic field axis along $\hat{X} + \hat{Y} + \hat{Z}$ such that some polarization projection always facilitates two-photon transitions – but the light projected into π -polarization does not contribute to cooling and instead results in additional free-space scattering. In a second scheme, ω_1 and \vec{B} may be kept along \hat{X} while ω_2 is sent along each direction to be cooled. In this case, sweeps along \hat{Y} and \hat{Z} maximally reduce $2\hbar k$ (rather than $4\hbar k$) momentum per sweep, thus leading to a reduced cooling rate.

In the future, it may also be interesting to explore the manipulation of ensembles via accelerations and decelerations. The initial temperature, which constrains the required sweep range Δ_{swp} , was tens of μK in this experiment but it could potentially be orders of magnitude higher if the available laser power permits large Q . More complex waveforms for the laser intensity and detuning might also improve the cooling rate by decreasing the required sweep range [144].

Chapter 6

Spin-squeezing using cavity non-demolition measurements

Entanglement is a fundamental quantum resource, capable of improving precision measurements and required for all quantum information science. Advances in the creation, manipulation, and characterization of entanglement will be required to develop practical quantum computers, quantum simulators, and enhanced quantum sensors. Spin-squeezed states could be used to improve a variety of quantum sensors, with today's best atomic clocks [43, 145–147] being particularly promising candidates. In this chapter, we demonstrate creating large amounts of entanglement on *internal* degrees of freedom, the basis states of such sensors.

Collective (“joint”) measurements with atom-cavity systems have been the most effective means for generating highly-entangled squeezed states to date. With the first-generation apparatus described in Chapter 3, we directly observed up to $W^{-1} = 59(8)$ times (17.7(6) dB) reduction in quantum phase variance relative to the standard quantum limit [20]. The methodologies and experimental details that led to this result are present in Sec. 6.1. A separate atom-cavity system achieved up to 18.5 dB of spin squeezing using a similar non-demolition measurement scheme [21]. These are the largest reports of metrological enhancement in any system to date. In Sec. 6.2, a microcontroller is introduced to our system for generating deterministically squeezed states at particular J_z values. In Sec. 6.3, the standing wave lattice is transformed into an axially-smooth dipole trap so that atoms are free to fall. Using the atom's time-averaged coupling to the atomic probe to maintain squeezing was a large step towards cavity-based, spin-squeezed matter-wave interferometry. Many details of this chapter overlap with Kevin Cox's dissertation [148].

6.0.1 Real-time tracking of a quantum phase

As a detour to these topics, we had the pleasure to work with theorists Murray Holland and Athreya Shankar on a proposal for continuous real-time tracking of a quantum phase below the standard quantum limit [149]. Nearly all quantum sensors operate with the Ramsey sequence paradigm, estimating a quantum phase $\phi(t)$ between states of a superposition that evolves during an interrogation time. Unfortunately, the destructive readout of a Ramsey sequence requires resets and repeated trials to infer the phase from population measurements. In the scheme of Ref. [149], a single run gives continuous information about a time-varying signal. As an added bonus, phase-squeezed states develop as a natural result of the quantum non-demolition probing scheme. A sensor such as this is in some sense the holy grail of precision metrology, achieving sub-SQL resolution and dramatically improving bandwidth by avoiding state resets, not to mention the lack of noise from avoiding rotations and the unambiguity when accumulating multiple radians of phase.

In this proposal, nearly-balanced cavity-assisted Raman transitions interfere to create atom-cavity interactions that reveal the collective state of the atoms through a leaking cavity field $I(t)$. Homodyne detection of that field yields information about the environment of the sensor, and in principle allows for tracking a signal over time. Two lasers ω_1 and ω_2 are symmetrically-detuned ω_0 from the cavity mode and the cavity frequency completes both Raman transitions. By controlling the laser phases, balancing the Rabi frequencies $\Omega_1 = \Omega_2 \equiv \Omega_0$, and operating far-detuned from the atomic transition, the atom-cavity Hamiltonian is the sum of a Jaynes-Cummings and anti-Jaynes-Cummings interaction,

$$\hat{\mathcal{H}}_{\text{T}} = \frac{\hbar\Omega_{\text{T}}}{2}\hat{x}\hat{J}_x. \quad (6.1)$$

Here $\hat{x} = (\hat{a} + \hat{a}^\dagger)/\sqrt{2}$ is the amplitude quadrature, $\hat{y} = (\hat{a} - \hat{a}^\dagger)/\sqrt{2}i$ is the phase quadrature, $[\hat{x}, \hat{y}] = i$, and \hat{a}, \hat{a}^\dagger are cavity annihilation and creation operators. The interaction strength is $\Omega_{\text{T}} = \sqrt{2}\Omega_0 g_0/\Delta$.

The two drives can be considered to initialize counter-acting superradiant pathways that exactly cancel when $J_x = 0$ ($\phi(t) = 0$). For a small deviation in ϕ , however, the pathways add

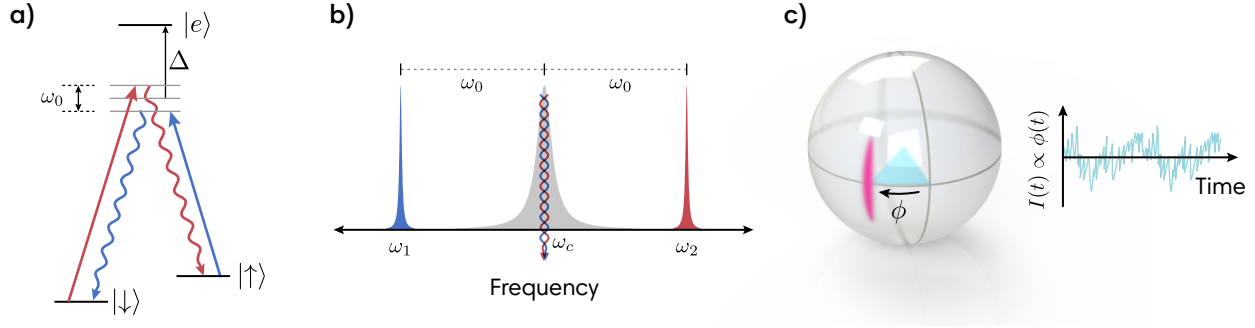


Figure 6.1: **Continuous real-time tracking of a quantum phase.** (a) Energy-level diagram and (b) frequency diagram for the quantum phase-tracking proposal. Cavity-assisted Raman transitions balance and interfere to drive a QND interaction. (c) Spin-squeezed states form naturally in the phase quadrature. The emitted cavity field $I(t) \propto \phi(t)$ is detected in homodyne.

constructively, giving rise to an output field. Even with $\langle \hat{J}_x \rangle = 0$, $\langle \hat{J}_x^2 \rangle \neq 0$ and quantum fluctuations source the Y quadrature of the cavity field. Measurement back-action in J_z arises due to the indistinguishability of these processes, as is required for a spin-squeezed state.

This scheme has not been realized thus far, and using rubidium poses some practical difficulties. One possibility is to use the $F = 1$ manifold and map the spin- $1/2$ system described in [149] onto a spin-1 system. Even so, one must worry about compensating the quadratic Zeeman shift while still lifting the degeneracy of the m_F levels. The scheme also has stringent requirements on phase noise and the driving laser linewidth but a proof-of-principle demonstration could be within grasp in current systems.

6.1 Generating large amounts of useful entanglement

In our spin-squeezing experiments [20], collective measurements of the atomic population are used to project an ensemble of rubidium atoms into an entangled state and verify this entanglement. Quantum noise of a *pre-measurement* cancels noise in the *final* measurement in this technique called conditional squeezing [16–19, 46, 47, 150–152]. It is worth saying explicitly that conditional squeezing refers to the use of a pre-measurement, not a post-selection of data or some other dubious data analysis technique.

The initial demonstrations of squeezing via cavity-based quantum non-demolition measurements [46, 47] have been followed by rapid gains in achievable metrological enhancements. High-finesse cavities set new records in the amount of useful entanglement by exploiting the $W \propto 1/\sqrt{NC}$ fundamental scaling with cooperativity \mathcal{C} in QND schemes [20, 21, 29]. Using an optically-cycling transition, the fundamental scaling improves further, to $W \propto 1/NC$ [20, 151]. The basis states of this chapter follow this insight. Although the magnetic sensitivity of the $|\uparrow\rangle \equiv |5^2S_{1/2}, F=2, M_F=2\rangle$ and $|\downarrow\rangle \equiv |5^2S_{1/2}, F=1, M_F=1\rangle$ states makes them unsuitable in a clock, they are good magnetometers and are useful for exploring the limits of our understanding. In truth, suitability for quantum sensing can be a subtle question to answer. For example, all of the population-squeezed states described here require additional operations for insertion in an atomic clock. After accounting for the impact of non-unitary state evolution on the performance of an atomic clock, our states still compare quite favorably to others [153]

In this section, probe light is sent into the cavity detuned $\delta_c = 2\pi \times 400$ MHz to the blue of the $|\uparrow\rangle$ to $|e\rangle \equiv |5^2P_{3/2}, F=3, M_F=3\rangle$ optical atomic transition as shown in Fig. 6.2(a). Atoms in $|\uparrow\rangle$ behave like small pieces of glass, imparting a phase shift to the reflected probe light which is seen as a shift from the empty cavity resonance frequency ω_c to ω'_c . The collective population N_\uparrow is inferred from this frequency shift. Because the $|\downarrow\rangle \leftrightarrow |e\rangle$ transition is so far from laser resonance, atoms in $|\downarrow\rangle$ hardly interact with the intracavity light. It is crucial that the collective, dispersive measurement of N_\uparrow does not collapse individual atom wavefunctions.

At the start of every experimental trial, a 3D MOT is formed from the background rubidium vapor pressure and cooled to about 10 μ K with polarization-gradient cooling (PGC). A far-detuned 823 nm intracavity lattice then traps $N = 4 \times 10^5$ atoms tightly on axis over a 1 mm extent. This allows for considerable overlap with the probe TEM₀₀ mode and it prevents atoms from moving significantly during the sequence. The cavity finesse is $\mathcal{F} = 2532(80)$ and the linewidth is $\kappa = 2\pi \times 3.15(10)$ MHz. A 1.1 Gauss bias magnetic field along the cavity axis sets the quantization axis. The spatially inhomogeneous coupling of atoms to the cavity mode is handled by considering an effective coupling and effective atom number, as in [29, 45, 47, 151]. Neglecting small correc-

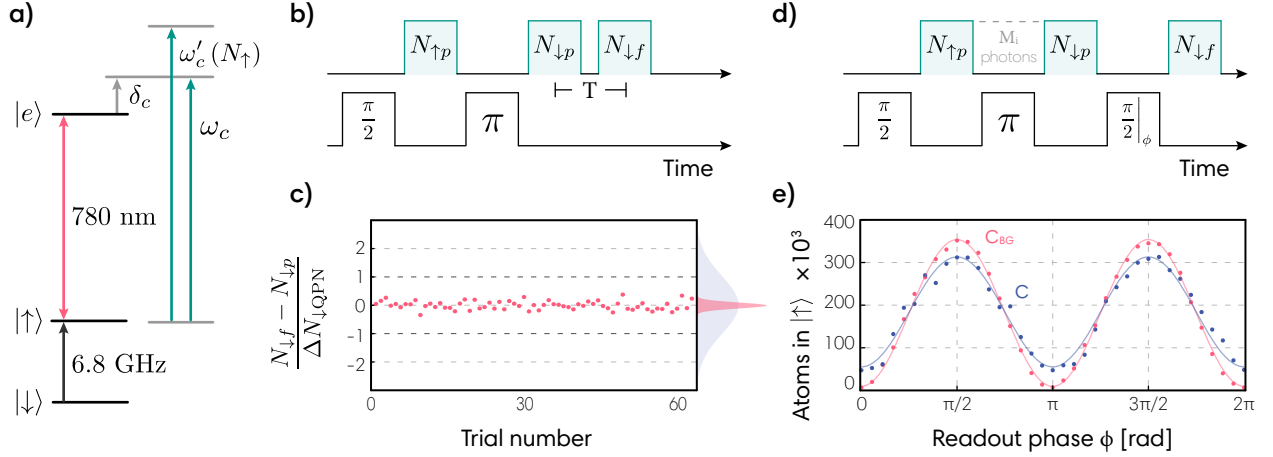


Figure 6.2: **Conditional squeezing overview.** (a) The relevant ^{87}Rb energy levels, bare cavity resonance frequency ω_c , and dressed cavity resonance frequency $\omega'_c(N_\uparrow)$. (b) Conditional squeezing sequence. Probe windows (teal) measure the population in N_\uparrow or N_\downarrow as labelled. Microwave pulses (black) prepare the initial superposition and enable a spin-echo protocol. (c) Spin noise reduction R at $M_i = 30 \times 10^3$ photons. The corresponding noise distribution (red) is drawn next to the initial coherent state distribution (gray). (d) Contrast measurement sequence. The phase ϕ is scanned to measure the fractional length of the Bloch vector after the pre-measurement. (e) Contrast data with $C_{BG} = 0.98$ (red, measured with $M_i = 0$ photons during the pre-measurement) and $C = 0.75$ (blue, for $M_i = 30 \times 10^3$ photons).

tions for radial inhomogeneity, the number of atoms N_0 , the single-atom Rabi frequency $2g_0$ at an antinode of the probe mode, and the cooperativity parameter C_0 at an antinode of the probe mode are related to the effective quantities by $N \approx \frac{2}{3}N_0$, $g_{\text{eff}}^2 \approx \frac{3}{4}g_0^2$, and $C \approx \frac{3}{4}C_0$ respectively.

The conditional squeezing sequence is shown in Fig. 6.2(b). At the beginning of each trial, atoms are optically pumped into $|\downarrow\rangle$ with over 90% purity, and the remaining atoms in $F = 2$ are blown away with a beam transverse to the cavity. A microwave $\pi/2$ -pulse places each atom into an equal superposition of spin states, preparing the collective Bloch vector along \hat{y} . At this point, a measurement of the spin projection J_z is made¹, followed by a spin-echo π -pulse, and then a pre-measurement with outcome labeled $J_{zp} = N_{\downarrow p}/2$. The final measurement $J_{zf} = N_{\downarrow f}/2$ immediately follows. Although a measurement of N_\uparrow at this point allows additional cancellation

¹The results of this measurement are not used in constructing a noise estimator here. Rather, the first measurement probe photons only serve to spin-echo probe-induced inhomogeneous light shifts. The window is labelled $N_{\uparrow p}$ in diagrams.

of quantum noise in principle, it was advantageous to avoid added noise from state rotations instead. The variance of the difference of the two population measurements normalized to quantum projection noise (QPN) is the spin noise reduction,

$$R \equiv \left(\frac{\Delta J_z}{\Delta J_{z,\text{QPN}}} \right)^2 = \left(\frac{\Delta(N_{\downarrow f} - N_{\downarrow p})}{\sqrt{N}/2} \right)^2. \quad (6.2)$$

Each population measurement outcome is obtained by measuring the Q quadrature of the reflected atomic probe field in homodyne and averaging the signal over a 40 μs window.

The Wineland parameter for enhancement of phase resolution is [13]

$$W = \left(\frac{\Delta\theta}{\Delta\theta_{\text{SQL}}} \right)^2 = \frac{R}{C^2} C_{\text{BG}} \quad (6.3)$$

i.e. to observe an enhancement in phase resolution, one must also evaluate the fractional atomic coherence or “contrast” that remains after pre-measurement, $C \equiv 2 \langle |\hat{J}| \rangle / N$. The coherence is determined in a separate set of experiments by using microwave rotations after the pre-measurement to rotate the Bloch vector such that its total length can be determined. $C_{\text{BG}} = 0.96$ is the background contrast as determined from measurements of the contrast at $M_i = 0$ probe photons. This small correction represents normalizing W with respect to the length of the Bloch vector in the absence of pre-measurement, giving a 0.2 dB improvement in the reported squeezing compared to what would be calculated with $W = R/C^2$.

In Fig. 6.3(a), the directly-observed noise reduction R is plotted against the average number of photons M_i incident upon the cavity during a single measurement window. Photon shot noise scaling is seen at low photon numbers, but at high photon numbers, other noise sources begin to contribute including scattering and optomechanically-induced decorrelations. Also apparent in Fig. 6.3(a), the contrast remaining after the pre-measurement decreases with increasing M_i , primarily due to undesired free space scattering causing collapse of individual atomic wavefunctions into $|\uparrow\rangle$. The directly-observed squeezing is optimized at $W = 17.7(6)$ dB near $M_i = 3.8 \times 10^4$.

The maximum quantum noise reduction $R^{-1} = 92(9)$ or 19.6(4) dB below QPN is limited partly by the technical noise between the probe laser and the cavity which set a floor about 25 dB

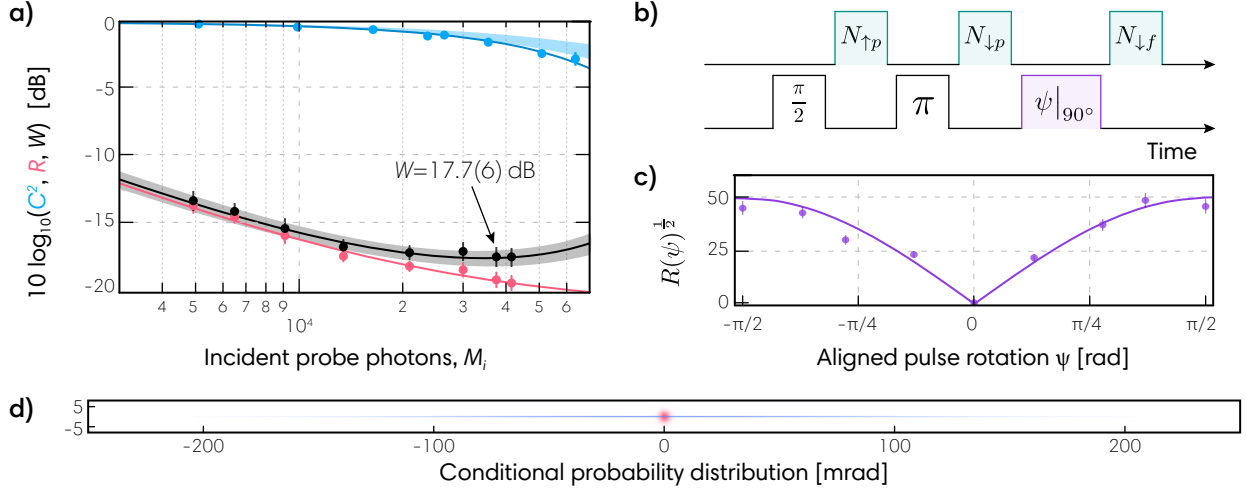


Figure 6.3: **Conditional spin squeezing results.** (a) Squared contrast C^2 (blue), spin noise R (red), and spin squeezing W (black) are plotted versus the average number of incident photons M_i in a single measurement window. The solid lines are fits to the data, the blue band is the predicted loss of contrast from free-space scattering, and the gray band indicates the total error bar for spin squeezing W . (b) A sequence with an additional microwave pulse aligned with the Bloch vector rotates the state through ψ to map out the conditional probability distribution. (c) The spin-projection R is plotted versus ψ and fit to an ellipse. (d) The reconstructed conditional probability distribution of the quantum state (blue) and the corresponding coherent spin state distribution (red) drawn with 1:1 aspect ratio.

below QPN (see Ref. [72] which used a precursory heterodyne detection system). Spin noise reduction was also limited significantly by optomechanics induced by toggling the probe light. Due to the incommensurate probing and trapping potentials, some atoms are located on the slope of the probe standing wave and thus experience a force that drives axial oscillations in the trap. In addition, the minima of the trapping potentials are spatially offset by the presence of the probe field. The ensemble average of each atom's time-dependent coupling to the probe mode results in the ringing shown in Fig. 6.4(a) (red) over a $40 \mu\text{s}$ probing period.

To partially cancel the optomechanical ringing, we employ a short, impulsive turn-on sequence. A $2.5 \mu\text{s}$ half power pulse induces ringing, and a full strength pulse applied one quarter of an axial oscillation period later coherently zeroes the initial axial ringing such that the atoms come to rest at the new trap minimum. As shown in Fig. 6.4(a), this technique significantly reduces the amount of ringing, but it only improved the optimal squeezing in Fig. 6.3 by an estimated 0.6 dB.

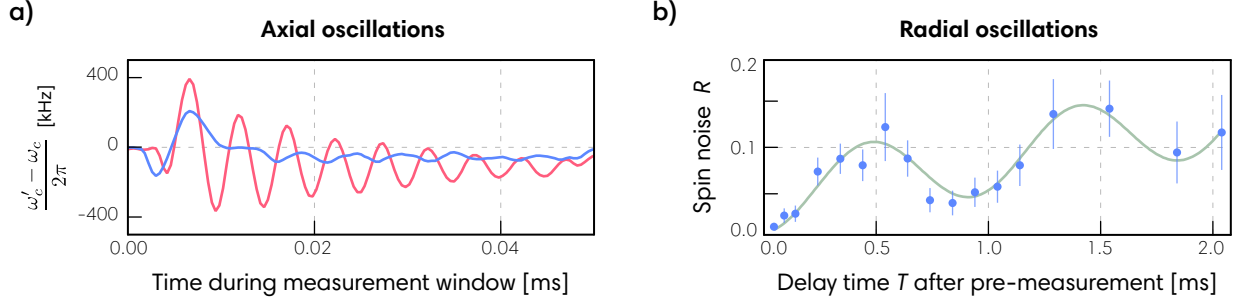


Figure 6.4: **Optomechanics.** (a) Probe-induced axial oscillations are apparent from turning on the probe for $40\ \mu\text{s}$ (red, 43 traces averaged) but can be greatly reduced with a half-power $2.5\ \mu\text{s}$ kick followed by a $2.5\ \mu\text{s}$ delay (blue, 30 traces averaged). The $2.5\ \mu\text{s}$ kick duration corresponds to a quarter of the axial trap oscillation period. An 80 MHz offset has been subtracted from the vertical axis. (b) Thermal radial motion reduces correlations during a time T between pre- and final measurements. Oscillations correspond to twice the radial trap frequency.

Tighter trapping or homogeneous coupling of atoms to the atomic probe (Sec. 6.3) are possible avenues toward reducing optomechanical effects.

Oscillations from radial motion are also important when considering quantum sensors, especially those operating with longer timescales. In Fig. 6.4(b), spin noise reduction R is evaluated versus delay time T between measurements using the sequence of Fig. 6.3(a). The results without atoms were subtracted to remove contributions from technical noise sources. The spin noise R oscillates at twice the radial frequency of the trapping potential ($\omega_{\text{rad}} \approx 2\pi \times 900\ \text{Hz}$) due to thermal motion. The monotonic increase in R was not explored further, but a 3D optical lattice or a smaller ratio of atomic temperature to lattice depth could help reduce oscillations in the noise due to radial motion.

6.1.1 Experimental details

Figure 6.5 explains the frequency locking chain and the use of multiple longitudinal cavity modes for this work. The UHV cavity is stabilized to the red lattice laser with 1.5 kHz servo bandwidth. A fiber EOM sideband of the lattice laser was stabilized to an independent transfer cavity with 1 MHz servo bandwidth, allowing 5 to 9 GHz of continuous tuning relative to the transfer

cavity. The transfer cavity is locked with 1.5 kHz PDH servo bandwidth to a 795 nm reference spectroscopy system to prevent long-term drift. All state rotations in this experiment were performed with microwaves broadcast by a stub-tuned dipole antenna placed just outside of the glass cell. Close to 2 W of microwaves near ω_{HF} produced a Rabi frequency of $2\pi \times 50$ kHz. Microwaves are gated by square-wave pulses of a fast TTL switch (PN: Mini-Circuits ZASWA-2-50DR+).

The atomic probe is used to determine the population in N_{\uparrow} through the shifted cavity mode frequency $\omega'_c - \omega_c$. Relative frequency noise between the atomic probe laser and the empty cavity is mitigated by stabilizing the atomic probe to a cavity probe 122.4 GHz away. The atomic probe is σ^+ polarized to take full advantage of the cycling transition for strong light-atom coupling as well as to avoid spontaneous Raman transitions to other ground states caused by spontaneous emission [29].

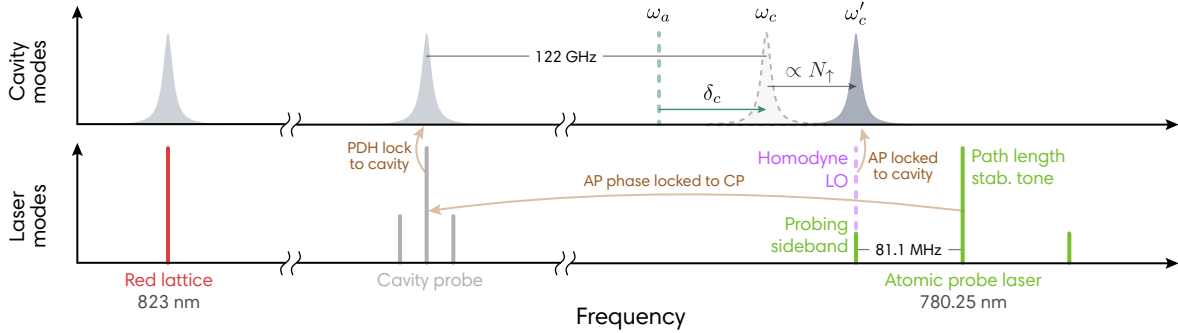


Figure 6.5: Experimental frequency diagram including the locking scheme of the atomic probe (green) and cavity probe (gray) lasers. The two longitudinal resonances of the cavity that these two lasers probe were separated by 122.4 GHz. The unshifted cavity mode at ω_c is detuned δ_c blue from the atomic resonance ω_a . The presence of atoms in $|\uparrow\rangle$ shifts this cavity mode to ω'_c . Frequency stabilization techniques and the homodyne local oscillator beam (purple dashed) are also shown.

The light reflected by the cavity is detected in homodyne to determine the detuning of the atomic probe from ω'_c , as described in Sec. 3.1.8. Near resonance, the reflected Q_r quadrature response of the field is related to the incident field $I_i \propto \sqrt{M_i}$ and the detuning δ_p between the probe light and the cavity resonance by [29]:

$$\frac{Q_r}{I_i} = \frac{4\delta_p}{\kappa} \left(\frac{\kappa_1}{\kappa} \right) \frac{(\kappa/\kappa')^2}{1 + \left(\frac{\sqrt{N_{\uparrow}} 2g}{2\delta'_c} \right)^2} \quad (6.4)$$

where $\delta'_c = \omega'_c - \omega_a$; ω_a is the optical atomic transition frequency, and the dressed cavity linewidth is $\kappa' = (\kappa + \Gamma (\sqrt{N_{\uparrow}}g/\delta'_c)^2)/(1 + (\sqrt{N_{\uparrow}}g/\delta'_c)^2)$. Experimental diagrams of the optics and electronics are shown in Fig. 6.6 and Fig. 6.7. Cavity and trap parameters are given in Table 6.2

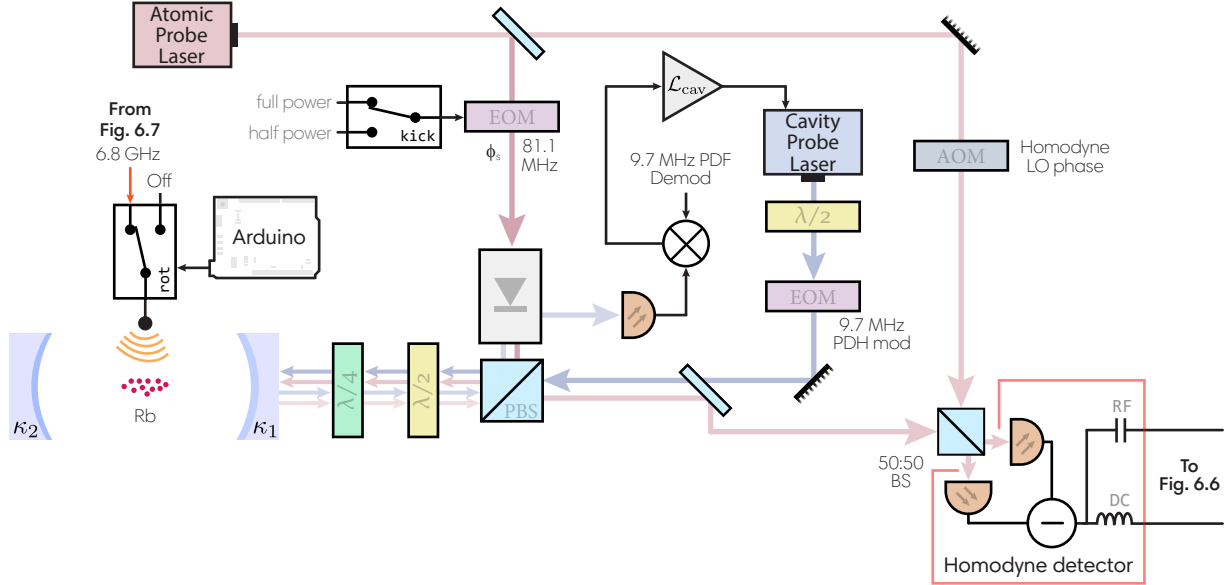


Figure 6.6: **Optical block diagram.** The resonance frequency of the optical cavity ω'_c is detected using homodyne detection of the atomic probe laser (red). Homodyne detection is performed on an $f_s = 81.1$ MHz sideband on the atomic probe laser. This sideband can be applied at half power by the kick switch to provide an extra impulsive kick to the atoms in order to cancel optomechanical ringing. The carrier of the atomic probe laser is detected in heterodyne (RF port) to provide a path length reference (see Fig. 6.7) for stabilizing the homodyne detection phase. The cavity probe laser (blue) is P.D.H. locked, via the \mathcal{L}_{cav} loop filter, to another longitudinal mode of the optical cavity, unshifted by atoms, and provides stabilization of the atomic probe laser's frequency to the cavity frequency. The atomic probe and cavity probe are separated optically via polarization. Real-time feedback is applied using an Arduino microcontroller that controls the sign and duration of 6.8 GHz μ -wave pulses. More details are given in Fig. 6.7.

The atomic probe's red sideband is turned on for approximately 40 μ s for each measurement, and the DC homodyne signal is used to actively lock the sideband's frequency to ω'_c . This "active lock" is achieved by feedback to the 90 MHz VCO that provides the frequency reference f_{ca} to which the cavity/atomic probe beat note is phase-locked. The frequency of the atomic probe and all derived tones are phase-locked via the loop filter \mathcal{L}_{SHA} . The characteristic settling time of the servo is 1 μ s for a unity gain frequency of 160 kHz. The first few μ s of each measurement are

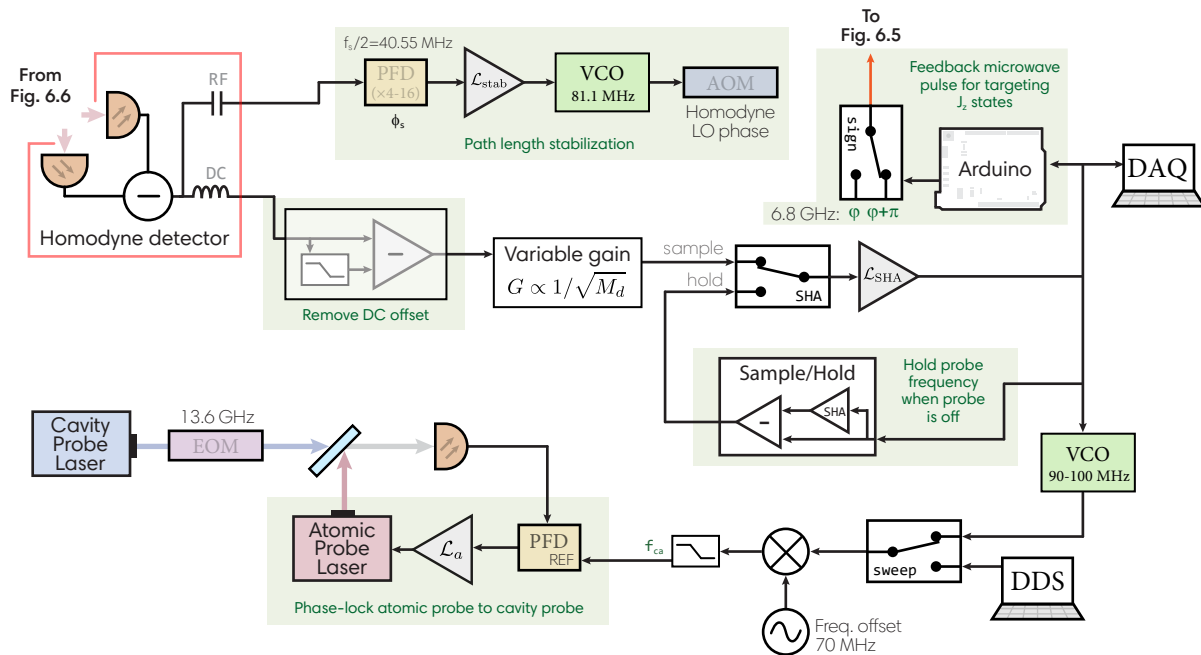


Figure 6.7: **Electronic block diagram.** The homodyne detection phase is stabilized by detecting the carrier of the atomic probe beam with the signal appearing at 81.1 MHz at the RF port. The phase of this signal is locked to a DDS frequency reference by applying feedback through the \mathcal{L}_{stab} loop filter to a VCO controlling the homodyne AOM. The homodyne difference signal (DIFF) is used to stabilize the atomic probe laser to the atom-shifted cavity mode at ω'_c . The signal is high-pass filtered at 1 Hz to remove slowly drifting DC offsets and then passed through a variable gain amplifier (used to maintain constant loop gain as M_i is varied) before entering the loop filter \mathcal{L}_{SHA} . The output of \mathcal{L}_{SHA} is used to control a VCO which provides a phase reference to a phase lock between the atomic probe laser and the cavity probe laser using loop filter \mathcal{L}_a . The cavity frequency ω'_c is detected by sampling the output of \mathcal{L}_{SHA} . When the atomic probe is off, a sample and hold circuit is used to hold the output of the loop filter. A separate synthesizer (DDS) can be used to perform sweeps of the atomic probe. Real-time feedback is applied by the Arduino based on the sampled output of \mathcal{L}_{SHA} . The Arduino can control the sign of the feedback by switching (sign) between two 6.8 GHz sources that are 180° out of phase.

discarded for this reason. To convert ω'_c to a voltage, we record the output of the \mathcal{L}_{SHA} loop filter, directly sampling at 2.5 MHz with the data acquisition computer (DAQ). This active lock improves the dynamic range of the detection system, removes sensitivity to scale-factor noise, creates more consistent optomechanical effects, and removes nonlinearities associated with the dispersive error signal. For diagnostics, it was occasionally useful to eschew the active lock and instead sweep the lower sideband frequency across the cavity resonance. To accomplish this, the atomic probe laser's

beat note with the cavity probe laser was phase-locked to a direct digital synthesizer (DDS) that provides a programmable reference frequency f_{ca} in place of the usual VCO.

Because the atomic probe lower sideband is turned off between measurements, its frequency must be held fixed using the sample-and-hold circuit shown in Fig. 6.7. Not only does this prevent riling but it's also necessary to avoid slewing. The circuit samples the loop filter voltage provided to the VCO that generates f_{ca} whenever the sideband is on. When the sideband is turned off, the circuit holds the output voltage of the loop filter so that f_{ca} remains at its previous value.

Trial-to-trial fluctuations in total atom number are significantly larger than fluctuations due to projection noise. To reduce the range over which the probe laser has to slew during the first $N_{\uparrow p}$ measurement, a “pre-centering” measurement is performed 1.5 ms before each experimental squeezing trial: a $\pi/2$ microwave pulse rotates atoms to a superposition of $|\uparrow\rangle$ and $|\downarrow\rangle$ and the probing sideband is centered by the feedback loop at ω'_c . The atomic probe frequency is then held while the probe light is switched off. The atoms are then optically pumped back to $|\downarrow\rangle$ for the actual spin squeezing measurements described earlier.

To vary the power in the probing sideband (as quantified by the number of incident probe photons in a single measurement window M_i), we adjust the phase modulation index for the EOM at f_s . For reference, a typical sideband/carrier power ratio for $M_i = 36500$ incident photons was 0.004. The power in the path length stabilization tone, and hence the open loop gain of the path length phase stabilization for homodyne detection, were relatively unaffected as M_i changed. By contrast, a variable gain amplifier (VGA; Analog Devices AD8337) had to be inserted after the homodyne detector to compensate for the open loop amplitude gain of the active lock which scales with $\sqrt{M_i}$. When the data acquisition computer changes the rf power that set M_i , it also simultaneously scales the VGA gain to keep the net loop gain fixed. DC offsets on the homodyne difference port are removed using a differential amplifier to subtract a low pass filtered trace ($\tau = 1$ s) from the fast $40 \mu\text{s}$ measurement windows.

With this approach, the atomic probe sideband could be locked to the dressed cavity resonance with a large dynamic range, from $M_i = 150$ to $M_i = 3 \times 10^5$. When $M_i \lesssim 100$ in a $40 \mu\text{s}$

window, the average number of detected photons within the servo's time scale of $1 \mu\text{s}$ approaches unity. Photon shot-noise would then impose rms fluctuations on the atomic probe's frequency that are comparable to the cavity half-linewidth, fundamentally reducing the signal to noise for estimating ω'_c .

M_i can be understood as an estimate of the average number of photons in the atomic probe lower sideband crossing a plane directly in front of the cavity input mirror during a $40 \mu\text{s}$ window, counting only those that are spatially mode matched to the cavity mode. Although there is up to 25% uncertainty in this calibration owing to the uncertainty in spatial mode-matching of the atomic probe mode and the homodyne reference beam, the only effect is on the prediction of contrast lost in Fig. 6.3 – it does not lead to any uncertainty in the amount of squeezing.

6.1.2 Quantum efficiency and the anti-squeezed quadrature

Compared to earlier work [47, 151], the quantum efficiency of the system is improved by nearly an order of magnitude. The cavity finesse is increased by a factor of 3.5, so the linewidth κ is smaller by the same factor. This cavity is primarily transmissive at a single end, *i.e.* the input mirror transmission coupling rate κ_1 is much greater than the output mirror's transmission coupling rate κ_2 . As a result, measurement of the probe light in reflection accounts for a quantum efficiency $Q_{\text{cav}} = \kappa_1/\kappa = 0.83(3)$. This eliminated the need for detecting transmitted cavity light.

To determine the probe detuning δ_p , we estimate the ratio Q_r/I_i from the detected fields Q_d/I_d . Vacuum or photon shot noise that appears in the detection of the Q_d quadrature limits the resolution on our ability to determine ω'_c . We express the noise in the ratio as

$$\frac{(\Delta Q_d)^2}{I_d^2} = \frac{1}{4M_i Q_1^{(0)}} + (\Delta f_l)^2 + r M_i^n, \quad (6.5)$$

where the one-window quantum efficiency $Q_1^{(0)}$ includes fundamental losses of signal to noise resulting from both photon losses and technical noise floors shown in Table 6.3. The additional terms represent noise contributions from the technical noise floor $(\Delta f_l)^2$ associated with residual frequency noise on the atomic probe laser relative to the cavity mode frequency, and noise from

Cavity & probing parameters (probe $\lambda = 780$ nm)	
Single-atom cooperativity $\mathcal{C} = \frac{4g_{\text{eff}}^2}{\kappa\Gamma}$	0.044(6)
Single-atom vacuum Rabi splitting g_{eff}	$2\pi \times 0.44(3)$ MHz
Input coupling κ_1	$2\pi \times 2.60(5)$ MHz
Output coupling κ_2	$2\pi \times 0.17(1)$ MHz
Internal losses κ_L	$2\pi \times 0.38(8)$ MHz
Linewidth κ	$2\pi \times 3.15(10)$ MHz
Dressed-cavity linewidth (4×10^5 atoms, $\delta_c = 400$ MHz) κ'	$2\pi \times 3.6(1)$ MHz
Q.E. due to internal losses κ_1/κ	0.83(3)
Finesse	2532(80)
Free spectral range	8.105(5) GHz
TEM ₀₀ waist size w_0	70(1) μm
Cavity length	1.849(1) cm
Mirror radius of curvature	4.999(5) cm
Trap parameters (lattice $\lambda = 823$ nm)	
Linewidth	$2\pi \times 5.8(6)$ MHz
Finesse	1400(150)
Trap depth	115 μK
Circulating power P_{circ}	0.30(3) W
Power Buildup ($P_{\text{circ}}/P_{\text{inc}}$)	800(130)
Axial trap frequency	181(20) kHz
Radial trap frequency	900(50) Hz
TEM ₀₀ waist size w_0	71(1) μm

Table 6.2: Relevant cavity parameters at the atomic and cavity probe laser wavelength $\lambda = 780$ nm and at the lattice laser wavelength $\lambda = 823$ nm. The symmetric, standing wave cavity's mirror transmission coefficients, T_1 on the probed end (1) and T_2 on the closed end (2), are expressed in terms of coupling rates $\kappa_{1,2} = T_{1,2} \times (\text{free spectral range})$. The atomic decay linewidth of $|e\rangle$ is $\Gamma = 2\pi \times 6.065$ MHz. The dressed cavity linewidths κ' include broadening of the cavity resonance at ω'_c due to spontaneous scattering from the atoms.

optomechanical ringing rM_i^n , which we model by scaling M_i with an arbitrary polynomial of order $n \neq -1$.

We define a new effective quantum efficiency Q_1 which includes the effects of the technical noise floor and optomechanics and write the noise in homodyne detection as

$$\frac{(\Delta Q_d)^2}{I_d^2} = \frac{1}{4M_i Q_1} \quad (6.6)$$

Source	Q
Path efficiency, Q_{path}	0.75(3)
Cavity-mode/homodyne overlap, Q_o	0.95(3)
QE of cavity (κ_1/κ), Q_{cav}	0.83(3)
Technical noise from detector, Q_{elec}	0.86(1)
Detector QE, Q_{PD}	0.86(2)
Probe on-time, $Q_{\text{turn on}}$	0.86(1)
Total, $Q_1^{(0)}$	0.37(5)

Table 6.3: Quantum efficiency losses come from sources of signal loss and added noise floors. $Q_{\text{turn on}}$ comes from finite laser turn-on time, active lock settling, and ring-canceling “kicks” during which the probe is on but we do not collect information. The total quantum efficiency $Q_1^{(0)} = 0.37(5)$ is the product of all the measured contributions.

where Q_1 is given by

$$Q_1 = \frac{Q_1^{(0)}}{1 + 4M_i Q_1^{(0)} ((\Delta f_l)^2 + r M_i^n)}. \quad (6.7)$$

This effective quantum efficiency provides a useful figure of merit for the experiment and can be compared to measurements of the increase in area of the Bloch vector’s noise distribution. Just as the back-action from gaining information about a particle’s position causes uncertainty in its momentum, increased phase resolution comes at the expense of increased uncertainty in the anti-squeezed quadrature. We measure this directly by including a microwave rotation about an axis parallel to the Bloch vector through angle ψ . By scanning ψ over separate trials, a visualization of the state is reconstructed (Fig. 6.3(c)). The state has $\Delta J_z \Delta J_x / (\Delta J_{z,\text{QPN}})^2 = 6.1$ and is therefore no longer a minimum uncertainty state, reflecting the finite quantum efficiency Q in extracting information. In particular, the increase of area is proportional to $1/\sqrt{Q_1}$. The measured increase of area and its scaling with M_i indicates the quantum efficiency of a joint measurement of a single population was $\tilde{Q}_1 = 38(14)\%$, in agreement with an independent prediction of $37(5)\%$ from measuring path efficiencies, cavity loss, detector efficiency, technical noise floors, and laser turn-on times.

To reconstruct the probability distribution describing our state, we measure the normalized probability distribution $P(J_{zf}(\psi) - \cos(\psi)J_{zp})$ for obtaining a differential measurement outcome

$J_{zf}(\psi) - \cos(\psi)J_{zp}$. The weighting of the pre-measurement by $\cos(\psi)$ ensures that we only condition the final measurement to the degree that the two spin projections overlap. An inverse Radon transform [154] on the measured $P(J_{zf}(\psi) - \cos \psi J_{zp})$ yields the conditional probability distribution shown in Fig. 6.3(d).

The magnitude of noise in the back-action quadrature grows anomalously with the number of probe photons M_i . We generalize the spin noise reduction to be a function of rotation angle ψ : $R(\psi) = \Delta(J_{zf}(\psi) - \cos \psi J_{zp})^2 / \Delta J_{z,QPN}^2$. The anti-squeezing is defined as $A \equiv R(\frac{\pi}{2})C_{BG}/C^2$, in direct analogy to the Wineland squeezing parameter, $W = R(0)C_{BG}/C^2$. The anti-squeezing parameter describes the variance in the azimuthal phase of the Bloch vector relative to the standard quantum limit $A \approx (\Delta\phi/\Delta\phi_{\text{SQL}})^2$, up to the small correction for the background contrast C_{BG} .

The anti-squeezing A is plotted versus M_i in Fig. 6.8. The data is fit to a model that includes three contributions $A = A_0 + A_1M_i + A_2M_i^2$. The constant term A_0 is associated with projection noise as well as noise in the rotations. Quantum back action A_1 rises linearly with M_i , with contribution shown by the blue shaded region. Noise scaling as M_i^2 , for example due to classical intensity noise on the circulating probe laser power, contributes to the total back action as shown by the red shaded region.

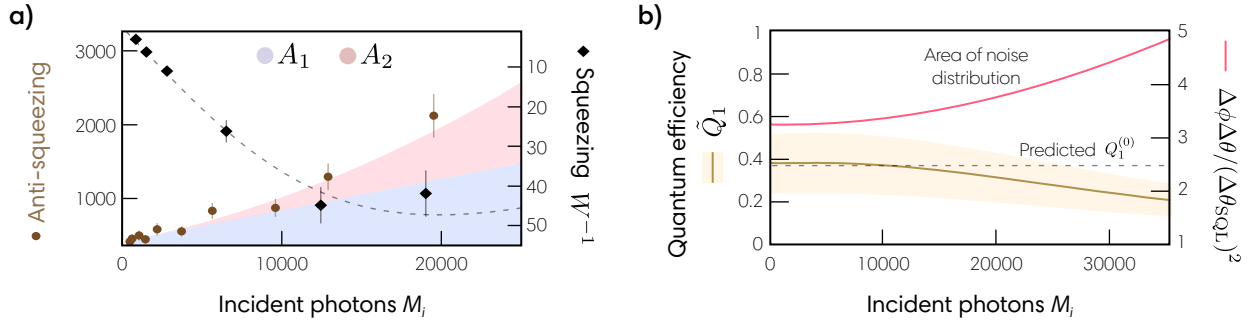


Figure 6.8: **Anti-squeezing and quantum efficiency.** (a) The anti-squeezing A is plotted versus M_i (brown circles). The linear contribution to the rise in A , A_1 , is shown in blue and the quadratic contribution A_2 in red. The squeezing (black diamonds and fit) is plotted on the right axis. (b) The area of the noise distribution is calculated from the data in (a) and plotted in red. The measured effective quantum efficiency \tilde{Q}_1 is plotted in gold with an error bar shown as a gold band. At low M_i , \tilde{Q}_1 is consistent with the prediction (dashed line) $Q_1^{(0)}$ from Table 6.3.

Squeezing data W is also taken at the same experimental settings (brown points and line in Fig. 6.8(a)). This allows us to infer the normalized area of the quantum noise distribution, $\Delta\phi\Delta\theta/\Delta\theta_{\text{SQL}}^2 = \sqrt{WA_1/C_{BG}^2}$, shown in red in Fig. 6.8(b). The increased area of the noise distribution can be used as an alternate, global measurement of the effective quantum efficiency Q_1 . Specifically, the total quantum efficiency of the entire measurement sequence is proportional to the square of the increase in the angular area of the noise distribution and can be written $\tilde{Q}_1 = 4/(A_1WC^2/C_{BG}^2)$. The factor C^2 comes from the angular momentum uncertainty relation and accounts for the fact that the SQL increases as the Bloch vector shrinks. The factor of four arises due to finite measurement strength and an unused pre-measurement. \tilde{Q}_1 as measured by the area of the noise distribution is plotted in Fig. 6.8(b) in gold. The gold shaded region represents the considerable uncertainty in the extrapolation of \tilde{Q}_1 due to uncertainty in the fit of the anti-squeezing data of Fig. 6.8(a). At low photon number, \tilde{Q}_1 agrees with the composite value of $Q_1^{(0)}$ from Table 6.3. At higher photon number, \tilde{Q}_1 rises due to the effective quantum efficiency losses from the technical noise floor and optomechanics discussed earlier.

6.2 Deterministic spin-squeezing

Real-time feedback on the results of collective measurements opens the path to even more access for improved quantum technologies, including Heisenberg-limited atomic sensors [155], atom interferometers with reduced mean field shifts [48, 156], studies of topological physics [157], quantum teleportation [158], and error correction [159, 160]. Quantum noise suppression with real-time feedback has been considered theoretically [161, 162] and demonstrated in previous experiments [163, 164] but without an enhancement in phase resolution that explicitly signifies entanglement.

Following the protocol of Fig. 6.9, we use the outcome of a dispersive measurement to actively steer the collective spin-projection of an ensemble of 50×10^3 laser-cooled and trapped ^{87}Rb atoms to a target entangled quantum state. Except for the reduced atom number and the addition of the microcontroller to control the feedback, the setup was identical to the previous section (see Figs. 6.5, 6.6, and 6.7). With real-time feedback, we generate target states with enhanced angular

resolution as much as $(\Delta\theta_{SQL}/\Delta\theta)^2 = W^{-1} = 5.5(8)$, or 7.4(6) dB below the SQL, comparable at the time to the best enhancements using only unitary evolution.

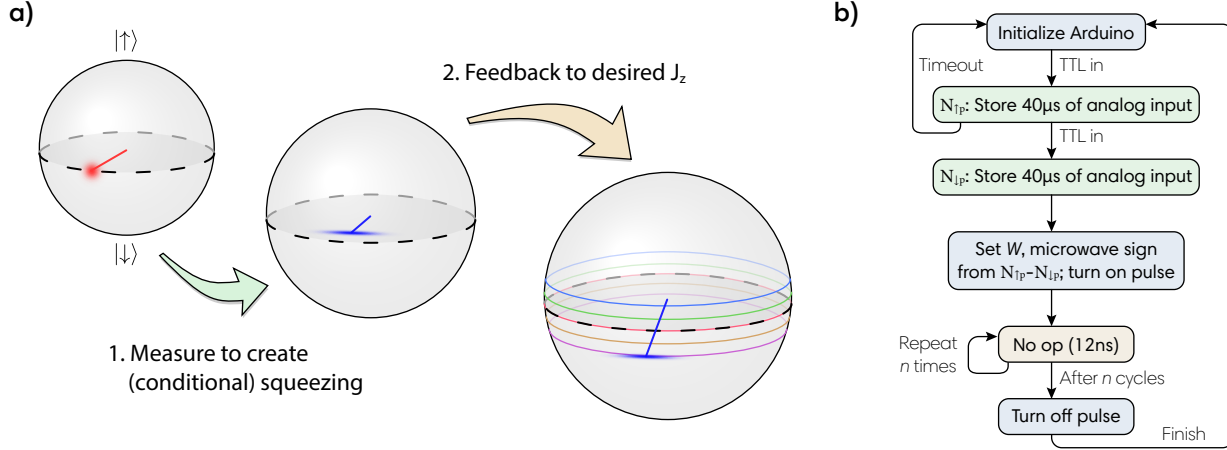


Figure 6.9: **Deterministic squeezing via feedback.** (a) Bloch sphere depiction of the deterministic squeezing protocol showing deliberate feedback to the “purple” J_z value. (b) Pseudocode for the microprocessor routine. Some care was taken in initialization so that we could interface directly with the hardware, for example by counting processor cycles and writing directly to ports rather than using slow-but-convenient wrapper commands.

In each run of this experiment, atoms are optically pumped into $|\downarrow\rangle$ and then prepared in a superposition of $(|\uparrow\rangle + |\downarrow\rangle)/\sqrt{2}$ by a microwave $\pi/2$ -pulse. The spin projection $J_{zp} = (N_{\uparrow p} - N_{\downarrow p})/2$ is measured, where N_{\uparrow} and N_{\downarrow} are averages of the probe homodyne signal over a 40 μ s window (with a π -pulse in between to swap the measured populations). To steer the Bloch vector to a target J_z^{target} , the microcontroller gates an additional rotation through polar angle $\theta_{fb} \approx 2 \times (J_z^{\text{target}} - J_{zp})/N$. After the feedback, a final measurement of the spin projection $J_{zf} = (N_{\uparrow f} - N_{\downarrow f})/2$ demonstrates a reduced variance compared to $\Delta J_{z, \text{QPN}} = \sqrt{N}/2$. As before, the remaining fractional atomic coherence (contrast) after pre-measurement and feedback must also be measured to verify entanglement. The phase of a $\pi/2$ -rotation after the feedback step is scanned through 2π to measure the reduced length of the Bloch vector. At spin-noise reduction $R^{-1} = 9.5(4)$ dB, loss of contrast reduced squeezing by 2.1 dB for a direct observation of $W^{-1} = 5.5(8)$ (7.4(6) dB) of deterministic squeezing via feedback on a pre-measurement.

Feedback toward $J_z^{\text{target}} = 0$ is evident in the time trace of Fig. 6.10(a), as the final two dressed cavity frequency ω'_c measurement windows that provide $N_{\uparrow f}$ and $N_{\downarrow f}$ are consistently closer in voltage than is the case for the two pre-measurement windows. The outcomes J_{zp} and J_{zf} are plotted versus trial number and collated into histograms for five different target states in Fig. 6.10(b). Projection noise for this data (independently confirmed by measuring the scaling of ΔJ_z with N) is $\Delta J_{z,\text{QPN}} = 218(10)$, consistent with the measured $\Delta J_{zp} = 235(24)$. By implementing the feedback protocol, each target state is reached with noise below the original projection noise.

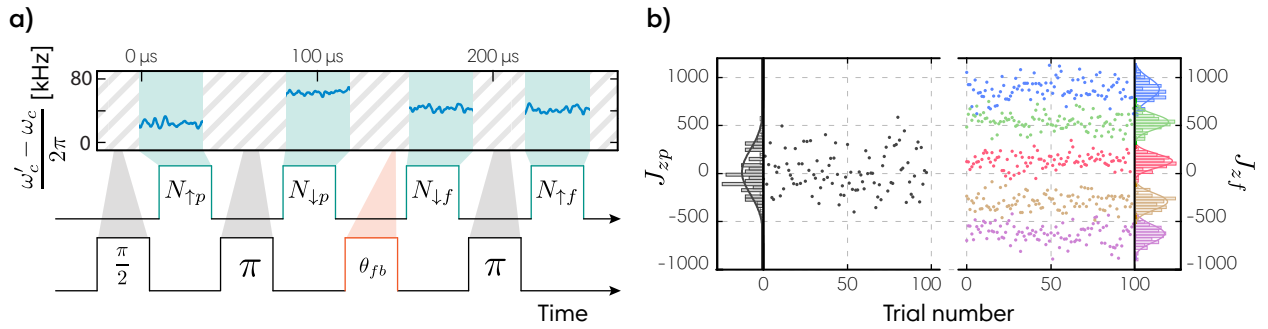


Figure 6.10: **Deterministic squeezing sequence and results.** (a) Measured cavity resonance frequency during a single trial, with the corresponding pulse sequence displayed below. A constant 12 MHz frequency offset has been subtracted. The deterministic squeezing sequence is shown with measurement windows (green), fixed microwave rotations (black) and the feedback rotation (orange). Feedback has made the result of the final measurement windows more equal, as intended for $J_z^{\text{target}} = 0$. (b) Pre-measurements J_{zp} (left) and final measurements J_{zf} (right) are plotted versus trial number and accumulated into histograms. The pre-measurement shows noise statistics near QPN. Five different J_z states are targeted (five distinct colors on right) and each exhibited noise below QPN. The maximum deterministic squeezing here, $W = 7.4(6)$ dB, corresponds to the red dataset.

An Arduino Due microcontroller with 84 MHz internal clock sets the sign of the θ_{fb} rotation by digitally toggling between two microwave sources that are 180° out of phase. The magnitude is controlled by varying the duration $t_{fb} = n \times 12 \mu\text{s}$ for which the microwaves are applied, with a discrete timing resolution of $12 \mu\text{s}$ set by the internal clock. Measuring J_{zp} amounts to sampling the probe's loop filter output voltage at the Arduino's analog-to-digital converter with 18 points per $40 \mu\text{s}$ window. Atom number fluctuations are small enough to ignore. The input technical noise floor, timing jitter, and timing resolution of the microcontroller are sufficient to allow up to 20 dB

of squeezing.

Although we deliberately used fewer atoms to relax the noise requirements on our microwave source, the amount of resolvable entanglement is still primarily limited by amplitude and frequency noise during the rotations. To characterize the noise added from feedback, we measure conditional spin noise $\Delta(J_{zf} - J_{zp})$ in a sequence without feedback and find $R^{-1} = 12.4(7)$ dB, *i.e.* feedback leads to approximately 2.9 dB of added noise. Next, we perform the sequence with no microwave rotations of any kind, measuring the same spin population N_{\uparrow} four times. In this sequence we attain $R^{-1} = 14.0(5)$ dB, 1.6 dB less than the sequence with rotations but no feedback. This measurement suggests a rotation noise floor due to microwave amplitude and frequency noise that is approximately 17.5 dB below projection noise for 50×10^3 atoms. Rotation noise on the feedback pulse is particularly problematic as certain rotation errors and light shifts which cancel after two π pulses no longer cancel when feedback is applied. Improving the precision of microwave rotations remains a major obstacle in working with atomic spin states with extreme phase resolution.

6.3 Spatially homogeneous entanglement using time-averaged measurements

In previous cavity-based squeezing experiments (in this dissertation and elsewhere) standing wave probe modes perform collective measurements, but the atoms are trapped in 1-dimensional lattices defined by a standing wave cavity mode with a significantly different wavelength. Although entanglement can be generated without using a cavity [17, 49, 51, 152, 165], free space experiments have not yet achieved the degree of squeezing observed using optical cavities. The release of spin-squeezed atoms into free space poses a major challenge for cavity-based atom interferometry and other applications.

In the experiments described earlier, some atoms are positioned in sites near nodes and some near anti-nodes of the entanglement-generating probe light. As a result, atoms contribute to the collective measurement with different strengths. In this case, the large degree of squeezing exists only for this specific coupling configuration and would be largely lost after releasing the atoms into

the arm of an interferometer, since each atom's contribution to the final signal will be different from the original configuration [45]. Recent experiments have demonstrated information retrieval after free-space release by recapturing atoms in the lattice [166]. Other solutions to this inhomogeneous coupling problem are described in Sec. 2.1, but they are generally incompatible with cavity-based interferometry.

In Ref. [94], the conditional squeezing of Sec. 6.1 is expanded with a method for creating homogeneous spin-squeezed states by allowing the atoms to traverse many wavelengths of the standing wave probe during each collective measurement. Atoms experience a time-averaged coupling to the cavity so that every atom is measured with the same strength, ensuring homogeneous entanglement. This is accomplished by creating an effective *dipole trap* (as opposed to the standing wave *lattice*) with a uniform axial potential described carefully in Sec. 4.5. The dipole trap maintains transverse confinement of the atoms while allowing free movement subject to gravity along the vertical cavity axis and facilitating $W = 11(1)$ dB of directly observed squeezing. Fluorescence images and noise scalings further show that the generated squeezing is homogeneously shared among the atoms to a large degree, in principle allowing significant amounts of squeezing for guided matter-wave interferometry. This work serves as a stepping stone for achieving the entanglement-enhanced matter-wave interferometer in Ch. 7.

As before, we trap ^{87}Rb atoms in the central 2 mm of a 2 cm long optical cavity, and cavity mode we probe is tuned $\delta_c = 2\pi \times 400$ MHz to the blue of the $|\uparrow\rangle$ to $|e\rangle \equiv |5^2P_{3/2}, F = 3, m_F = 3\rangle$ transition for dispersive QND population measurements of $J_z = \frac{1}{2}(N_\uparrow - N_\downarrow)$. To avoid extra rotation-added noise, we use only N_\uparrow measurements and $J_z = N_\uparrow - \frac{N}{2}$ because $N_\downarrow = N - N_\uparrow$. Quantum projection noise leads to fluctuations $\Delta J_{z,\text{QPN}} = \sqrt{N}/2$. Experimental parameters g_{rms} , δ_c , and N are used to scale between cavity frequency measurements ω and Bloch sphere projections J_z , $\partial\omega/\partial J_z = g_{\text{rms}}^2/\sqrt{4g_{\text{rms}}^2 N_\uparrow + \delta_c^2}$. The atoms are initially cooled to approximately 10 μK with PGC and trapped in a far off resonance red-detuned optical lattice at $\lambda_L = 823$ nm with corresponding wavevector $k_0 = 2\pi/\lambda_L$.

At this point, however, we convert the standing-wave lattice into the effective dipole trap.

Multiple adjacent TEM₀₀ longitudinal modes of the cavity are driven by phase modulating the lattice laser at the free spectral range (FSR), $\omega_{\text{FSR}} = 2\pi \times 8.1050(5)$ with modulation index $\beta \approx 1.3$. Phase-modulation is provided by a fiber-coupled EOM (PN: EOSpace PM-0S5-10-PFA-PFA-800). Adjacent modes have opposite symmetry with respect to the cavity center, so to lowest order, the carrier creates a $\cos^2(k_0 z)$ standing-wave intensity profile while the sidebands create $\sin^2(k_0 z)/2$ intensity profiles, and the sum of the standing waves $\cos^2(k_0 z) + \sin^2(k_0 z) = 1$ causes a net uniform intensity profile along the cavity axis. Please see Sec. 4.5 for more details.

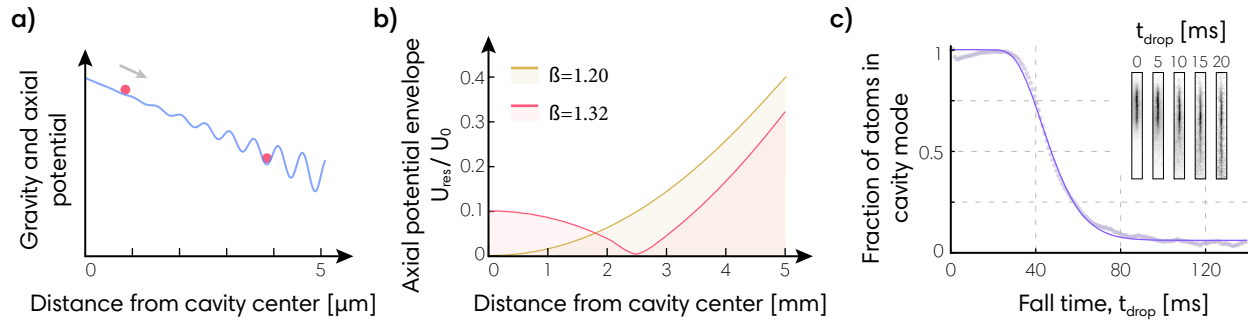


Figure 6.11: **Falling atoms in an optical dipole trap.** (a) The optical dipole trap axial potential combined with a gravitational potential (exaggerated) at a distance z from cavity center. Near the center of the cavity where the dipole trap is uniform, an atom is free to fall; but for an atom initially confined in a deep well, it remains trapped unless it can tunnel or “boil” out. (b) The envelope of the residual lattice potential $U_{\text{res}}(z)$ normalized to the peak lattice potential depth U_0 is plotted near the cavity center, optimized for a minimum at $z = 0$ (gold, $\beta = 1.20$) and for the minimal fraction of trapped atoms determined experimentally (red, $\beta = 1.32$). (c) Fraction of atoms remaining in the cavity mode vs. fall time, fit to a model $\mathcal{R}(t)$ described in the text. This data has been modified to roughly account for a background loss of atoms resulting in underestimates before 10 ms.

The increase in residual lattice depth away from the center of the cavity is generally not sufficient to stop a falling atom; rather, we expect the atom to be guided by the optical dipole trap until it collides with the lower mirror. For falling atoms, the residual lattice looks like an amplitude modulation and has the capacity to drive Bragg scattering. The tilted potentials also provide a rich landscape for Wannier-Stark physics [167, 168]. In Fig. 6.11(c), the number of atoms coupled to the cavity mode is measured as a function of time by continuously monitoring the dispersive shift of the cavity resonance frequency. The data was roughly normalized to account for background atom

loss and is reasonably described by a fit,

$$\mathcal{R}(t) = \int_{\frac{gt}{2} - \frac{L}{2t}}^{\infty} \frac{1}{\sqrt{2\pi}} \sqrt{\frac{m_{\text{Rb}}}{k_{\text{B}}T_{\text{ax}}}} e^{-\frac{m_{\text{Rb}}v_0^2}{2k_{\text{B}}T_{\text{ax}}}} dv_0 = \frac{1}{2} \left[1 + \text{erf} \left(\sqrt{\frac{m_{\text{Rb}}}{k_{\text{B}}T_{\text{ax}}}} \frac{L - gt^2}{2\sqrt{2t}} \right) \right], \quad (6.8)$$

which assumes atoms accelerate due to gravity g for time t before being lost at the position of the lower mirror $L/2$. The integral gives the fraction of atoms remaining from a velocity distribution with Boltzmann constant k_{B} , mass m_{Rb} , and axial temperature T_{ax} . For comparison, ballistic radial expansion out of the cavity mode would occur in only 2 ms had we completely turned off the optical lattice. Free fall and guiding are corroborated by fluorescence images taken after various drop times T_{fall} as shown in Fig. 6.11(c, inset).

Figure 6.11(b) shows the depth of the transformed potential $U_{\text{res}}(z)$ as a function of distance from the center of the cavity for two different values of β . At $\beta = 1.20$, the potential is completely uniform at the center of the cavity. We instead overdrive the dipole trap with $\beta \approx 1.32$ to maximize the fraction of freely falling atoms. This drive results in a wider overlap between small values for $U_{\text{res}}(z)$ and the atomic spatial distribution. Overdriving also causes the lattice potential wells to be converted into small potential peaks, giving additional potential energy. Fluorescence images indicate that at long times only 5(1)% of the atoms remain trapped in a residual lattice while the majority of atoms accelerate along the cavity axis.

For a fixed total atom number, the projection noise induced fluctuations of the cavity resonance frequency $\Delta\omega_{\text{QPN}}$ is smaller in the dipole trap than in the lattice. In the lattice, the atoms contributing most to the dispersive shift are those near the probe antinodes, with Jaynes-Cummings coupling parameter near the maximum value $g_0 = 2\pi \times 0.519(5)$ MHz. In the ideal time-averaged situation, each atom couples with rms coupling strength $g_{\text{rms}} = g_0/\sqrt{2}$, leading to smaller frequency fluctuations.

In App. C, we define a model where fractionally, ζ of the atoms release into the dipole trap and are assumed to have perfectly homogeneous coupling. $1 - \zeta$ of the atoms remain fixed in position and maintain their original inhomogeneous coupling. In this model, the projection noise induced fluctuations of the cavity resonance frequency come from adding the weighted variances

of the two ensembles, $\Delta\omega_{\text{QPN}} = g_{\text{rms}}^2 \sqrt{N(3-\zeta)} / \sqrt{8(g_0^2 N + \delta_c^2)}$.

This difference in the scaling of projection noise for the two configurations is confirmed versus total atom number with the measurement sequences of Fig. 6.12(a). The N_{\uparrow} and N_{\downarrow} windows represent the outcome of a measurements ω_{\uparrow} and ω_{\downarrow} of the cavity resonance frequency sensitive to the respective population. The observed projection noise fluctuations $\Delta\omega_{\text{QPN}}^{\text{meas}} = \Delta(\omega_{\uparrow} - \omega_{\downarrow})$ are plotted. For the purposes of this comparison, a small amount of technical noise that does not have the proper scaling with atom number was subtracted from this data. The in-lattice data is used as a calibration of g_0 with the theoretical scaling plotted in green. The dipole trap data is fit to the model $2 \times \Delta\omega_{\text{QPN}}$ (since the measurement sequence includes two anti-correlated windows, ω_{\uparrow} and ω_{\downarrow}) with $\zeta = 1.0(2)$ as the only free parameter.

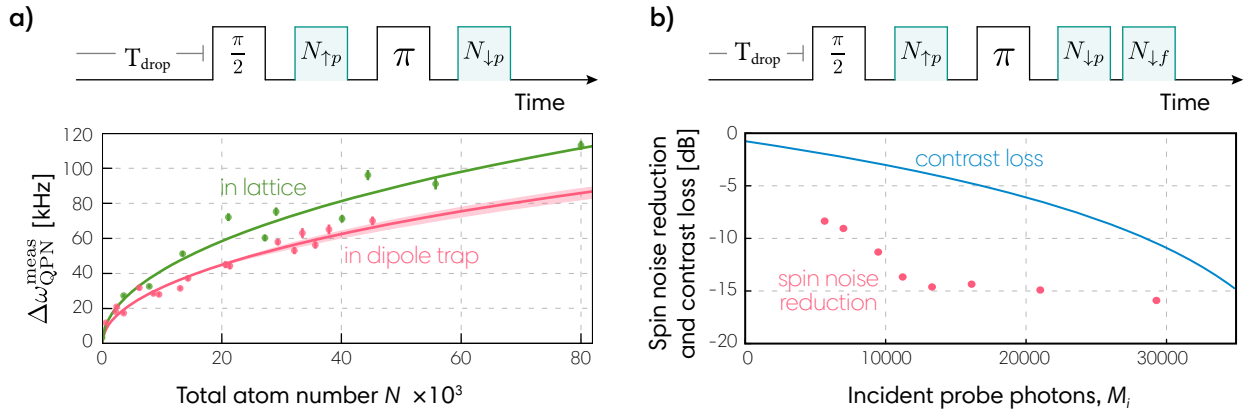


Figure 6.12: **Homogeneous squeezing results.** (a) Projection noise scaling versus total atom number N , measured in the lattice (green points) including a theoretical prediction and in the dipole trap (red points, including a fit to infer a coupling fraction ζ with 68% confidence interval bands). The sequence is above, with microwave pulses (black) and cavity frequency measurements (green). T_{fall} is only pertinent for the dipole trap configuration. (b) Spin noise reduction and a fit to contrast loss ($\log_{10}(C^2/C_{\text{BG}})$) vs. incident photon number per window, M_i . Squeezing was optimized at $W = 11(1)$ dB near $M_i = 10^4$, where spin noise is reduced but significant contrast still remains. The measurement sequence is above.

We measure spin squeezing within the dipole trap using the Wineland criterion for phase enhancement relative to the SQL, Eqns. 6.2 and 6.3. The conditional squeezing measurement sequence is shown in the inset of Fig. 6.12(b) and is the same as that of Sec. 6.1. After preparing

$N = 630(30) \times 10^3$ atoms in $|\uparrow\rangle$, the dipole trap was introduced for $T_{\text{fall}} = 13$ ms, with gravity accelerating the atoms enough to average over approximately 13 cycles of the probe standing wave during the $40 \mu\text{s}$ measurement window. A $\pi/2$ -pulse puts atoms in a superposition of spin-states, and a measurement window $N_{\uparrow p}$ and microwave π -pulse compensate inhomogeneous light shifts as before. Consecutive pre- and final measurements of the cavity frequency are labeled $N_{\downarrow p}$ and $N_{\downarrow f}$ and converted to J_{zp} and J_{zf} . Trial-to-trial noise in the difference exhibits spin noise reduction $R = (\Delta(J_{zf} - J_{zp})/\Delta J_{z,\text{QPN}})^2 = 13.9(6)$ dB below quantum projection noise near $M_i = 1.2 \times 10^4$. The fractional coherence remaining after the pre-measurement is separately measured to be $C = 0.70(5)$, yielding a directly observed phase resolution of $W = 11(1)$ dB below the SQL

6.3.1 Noise reduction limits from imperfectly time-averaging

A few limitations of this method are explored here and in the supplemental material of Ref. [94]. Imperfect averaging over the probe standing waves leads to a small amount of classical dephasing and a significant impact on the obtainable spin noise reduction. For the $25 \mu\text{K}$ ensemble, $T_{\text{fall}} = 13$ ms, and $40 \mu\text{s}$ measurements, we predict a noise floor 15 dB below QPN which is a primary limitation for the results above.

To understand this effect, consider a thermal velocity distribution of atoms $P(f_i)$, where the i^{th} atom moves along the cavity axis at velocity v_i , moving from probe anti-node to anti-node at coupling oscillation frequency $f_i = 2v_i/\lambda_p$. The time dependent coupling can be written as $g_i^2(t) = g_0^2 \sin^2(\pi f_i t + \phi_i)$ where ϕ_i sets the coupling at $t = 0$.

We assume both pre- and final measurements last for times $[0, T_{\text{win}}]$ and $[T_{\text{diff}}, T_{\text{diff}} + T_{\text{win}}]$ respectively. We take the projection noise level to be that for a perfectly time-averaged scenario in which each atom moves exactly an integer number of cycles of the standing wave: $(\Delta\omega_{\text{QPN}})^2 = N g_0^4 / 16 \delta_c^2$. The obtainable spin-noise reduction is

$$R = \int_{-\infty}^{\infty} P(f_i) \frac{4 \sin^2(\pi f_i T_{\text{diff}}) \sin^2(\pi f_i T_{\text{win}})}{f_i^2 \pi^2 T_{\text{win}}^2} df_i. \quad (6.9)$$

To gain some insight, consider an example when the atomic distribution $P(f_i)$ is Gaussian with mean f_0 and standard deviation Δf . In the limits of our experiment, $T_{\text{diff}}, T_{\text{win}} \gg 1/\Delta f$ and $f_0 \gg \Delta f$, so the terms $\sin^2(\pi f_i T_{\text{diff}})$ and $\sin^2(\pi f_i T_{\text{win}})$ in Eq. 6.9 will oscillate rapidly with f_i and can be replaced in the integrand by the average, $1/2$. The resulting spin-noise reduction is then $R = 1/(\pi N_{\text{osc}})^2$ where $N_{\text{osc}} = f_0 T_{\text{win}}$ is the number of cycles averaged by an atom at coupling oscillation frequency f_0 .

We estimate the maximum possible spin-noise reduction using $T_{\text{diff}} = T_{\text{win}} = 40 \mu\text{s}$ and the directly measured distribution of coupling oscillation frequencies shown in Fig. 6.13 to obtain an experimentally measured probability distribution $P(f_i)$. We find a limit from imperfect averaging $R \approx -15$ dB which would be a primary limit to the observed spin-noise reduction of $R = -13.9(6)$ dB. In the future, this effect could be reduced by allowing the atoms to fall for longer, by using longer measurement windows T_{win} , or by employing velocity selection strategies as we do in Ch. 7.

In addition to limiting spin noise reduction, imperfect cycle averaging of the probe standing wave leads to classical dephasing as each atom receives a different average AC Stark shift. The phase shift on a single atom during a single measurement window can be written

$$\psi_i = \int_0^{T_{\text{win}}} \frac{M_c g_i^2(t)}{\delta_c} dt \quad (6.10)$$

where M_c is the average intracavity photon number, taken to be constant for this calculation. The variance in ψ_i over the atomic distribution in our simplified model is

$$\Delta\psi^2 = \int_0^{2\pi} d\phi_i \int_{-\infty}^{\infty} P(f_i, \phi_{pi}) \psi_i^2 df_i - \left(\int_0^{2\pi} d\phi_i \int_{-\infty}^{\infty} P(f_i, \phi_i) \psi_i df_i \right)^2 \quad (6.11)$$

with a normalized probability distribution for velocity f_i and initial phase ϕ_i denoted $P(f_i, \phi_i)$. Assuming the phase ϕ_i of the coupling oscillations is uniformly distributed, the variance becomes

$$\Delta\psi^2 = \int_{-\infty}^{\infty} P(f_i) \frac{1}{2} \left(\frac{g_0^2 M_c}{2\pi f_i \delta_c} \right)^2 \sin^2(\pi f_i T_{\text{win}}) df_i, \quad (6.12)$$

reducing the contrast after a single pre-measurement by $e^{-\Delta\psi^2/2}$. This result can be interpreted as arising due to the phase shift from the uncanceled non-integer fraction of an atom's coupling

oscillation. The result will be slightly modified by the use of a spin-echo pulse during the pre-measurement, but because the phase of each atom's coupling oscillation changes for each window based on its velocity, significant spin-echo cancellation of this dephasing is not expected. For our system we estimate that classical dephasing from imperfect time-averaging led to a contrast loss of less than 1 dB at the optimal squeezing.

6.3.2 Coupling oscillations

The ac signals encoded in probe light reflected from the cavity (Fig. 6.13) yield additional information about the spin state of each velocity component of the atomic ensemble, but time averaging has a minuscule effect on the added noise for our system parameters.

The continuous time trace of the total atomic coupling to the cavity is $\mathcal{N}(t) = \sum_i^{N_\uparrow} g_i^2(t)/g_{\text{rms}}^2$. The squared Fourier transform of the signal $|\tilde{\mathcal{N}}(f)^2|$, with units of atoms/Hz, is closely related to the atomic velocity distribution. Figure 6.13(a) shows $|\tilde{\mathcal{N}}(f)^2|$ recorded over 2 ms and averaging approximately 65 trials for both the lattice and dipole trap configurations. The data was taken after $t = 1$ ms, 7.5 ms, and 15 ms of free fall following release into the dipole trap. Each power spectrum is fit to a folded 1D Boltzmann distribution that accounts for the inability to distinguish between upwards and downwards velocities. The fitted center frequency follows $f_0(t) = g t / (\lambda_p / 2)$, where $g = 9.8$ m/s² is the acceleration due to gravity. The widths of the distributions are consistent with Boltzmann distributions giving final axial temperatures of 25 μ K. For atoms held in the lattice, $|\tilde{\mathcal{N}}(f)^2|$ shows only a narrow distribution at the lattice trap frequency, $\omega_{\text{ax}} = 200$ kHz.

These oscillating signals yield information about the spin state of atoms moving at a particular velocity and therefore must cause some degree of additional quantum collapse or back-action. A full treatment of this effect is difficult but the argument produced in Ref. [94] considers a classical back-action model driven by quantum noise on the probing field. Photon shot noise (PSN) of the probing beam causes an unknown, noisy contribution to the phase shift with rms fluctuation $\Delta\psi$ that is equivalent to the observed quantum back-action in the azimuthal angle. PSN in frequency space is a power spectral density of photon number fluctuations in the cavity $S_M = 4M_c/\kappa$ (dot-

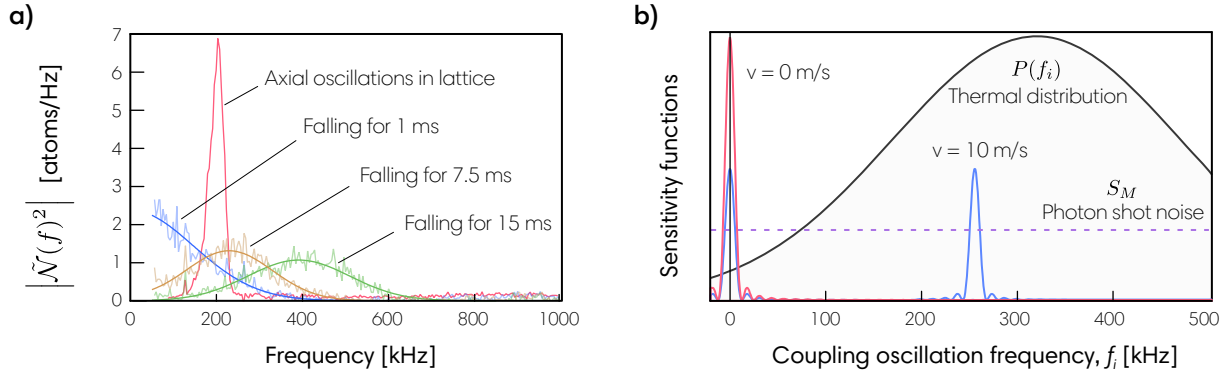


Figure 6.13: **(a)** Power spectra showing measured coupling oscillations for ensembles in the dipole trap with fall times of 1 ms (blue), 7.5 ms (brown) and 15 ms (green) with their respective fits. Axial oscillations for atoms held in the lattice (red) are comparatively coherent. **(b)** Sensitivity to photon shot noise (dashed line) for different velocity classes. A stationary atom only samples PSN at DC (red), but a moving atom couples with a transfer function (blue) sensitive at DC and frequency f_i corresponding to its velocity, shown for an atom with velocity 10 cm/s. The atomic distribution of oscillation frequencies is given by the Boltzmann distribution $P(f_i)$ (black).

ted purple line in Fig. 6.13(b)) where M_c is the average number of photons in the cavity mode² [169]. Stationary atoms sample this PSN in a window centered at zero frequency with characteristic bandwidth $1/T_{\text{win}}$ (shown in red in Fig. 6.13(b)), while moving atoms sample the PSN with a transfer function sensitive at DC due to the time-averaged component of $g_i^2(t)$ and at f_i due to coupling oscillations (shown in blue).

We suppose a thermal velocity distribution where sub-ensembles of characteristic frequency receive uncorrelated back-action noise. By parameterizing in terms of photon number, it is shown in Ref. [94] that the physical mechanism is then similar to ordinary quantum back-action except that these sub-ensembles reduce the collective Bloch vector length. The upshot is that this effect only provides an additional limit to angular resolution near $W \sim \frac{1}{qN}$ (of order the Heisenberg limit, where q is the total quantum efficiency of the experiment), several orders of magnitude below current experiments.

²Valid for frequencies much less than the cavity linewidth κ .

Chapter 7

An entanglement-enhanced matter-wave interferometer

Matter-wave interferometers were gently introduced in Sec. 1.6 and described with some detail in Sec. 2.4. As sensors, they provide extraordinary sensitivity to external forces, making them valuable for both applied and fundamental science. Applications include inertial sensing [63], mineral exploration, groundwater monitoring, measurements of gravity [38, 40], measurements of the fine structure constant [4, 5], tests of general relativity and the equivalence principle [6, 7, 170–173], and even the search for new proposed forces, quantum gravity, dark energy, and dark matter [34, 174, 175]. As with other quantum sensors, matter-wave interferometers using independent, unentangled atoms are fundamentally limited by quantum collapse to an rms angular uncertainty $\Delta\theta_{\text{SQL}} = 1/\sqrt{N}$ rad. This uncertainty restricts the precision, bandwidth, size, and accuracy of quantum sensors. State-of-the-art interferometers operate at [176] or near this limit, but future generations of sensors will benefit from surpassing the standard quantum limit via entanglement.

As we have seen, most previous experiments have generated spin-squeezing between the *internal* degrees of freedom, with large amounts of entanglement between the spin and spatial degrees of freedom. Pioneering work with collisional interactions in BECs [48–54] demonstrated entangled spatial interferometry in trapped geometries [48, 54]. There have been several proposals for transferring entanglement to external states suitable for free-fall interferometry [177–180]. Most recently, twin-Fock states were generated with collisional interactions and the entanglement was subsequently mapped onto momentum states [55].

Here, we demonstrate the first realizations of both cavity-enabled quantum non-demolition

generation and one-axis twisting generation of entanglement between the external atomic momentum states of different atoms. We further demonstrate the first injection of momentum-squeezed states into a light-pulse matter-wave interferometer for a spectroscopic enhancement that surpasses the standard quantum limit as we successfully inject OAT-squeezed states into a Mach-Zehnder interferometer for $1.7_{-0.5}^{+0.5}$ dB of directly observed metrological enhancement. Matter-wave interferometric control is achieved through intracavity Bragg or Raman transitions [42, 62]. We thus simultaneously combine two of the most striking features of quantum mechanics: the concept that a particle can appear to be in two places at once and entanglement between distinct particles. This work opens the path for a next generation of matter-wave interferometers that exploit the many-body nature of the atomic sensor rather than simply operating N independent copies of the experiment in parallel. A summary of spectroscopic enhancement results for the chapter is provided in Table 7.1.

Configuration	N	Spectroscopic enhancement W	
QND momentum squeezing	1170(30)	0.46(11)	$3.4_{-0.9}^{+1.1}$ dB
OAT momentum squeezing	730(10)	0.56(8)	$2.5_{-0.6}^{+0.6}$ dB
OAT-squeezed interferometer	660(15)	0.68(8)	$1.7_{-0.5}^{+0.5}$ dB
Unentangled interferometer	660(15)	1.49(31)	$-1.7_{-0.8}^{+0.7}$ dB

Table 7.1: Summary of spectroscopic enhancement results for this chapter.

7.1 Setup and state preparation

The conceptual setup of the experiment is shown in Fig. 7.1. Strong collective coupling to the cavity $NC \gg 1$ is the key requirement for both approaches to generate entanglement, where C is the single particle cooperativity parameter [29–31]. We achieve strong collective coupling $NC \approx 500$ by operating inside a high cavity finesse $\mathcal{F} = 1.3 \times 10^5$ with small mode waist $w_0 = 72 \mu\text{m}$. A cavity-based interferometer with $NC \ll 1$ was demonstrated in [181], though primarily to provide spatial mode filtering and power build-up. Around 700 atoms participate in the interferometer,

falling freely under gravity but simultaneously traversing two paths through space while also entangled with the other atoms. We utilize the magnetically-insensitive ^{87}Rb clock states, $|\downarrow\rangle \equiv |F = 1, m_F = 0\rangle$ and $|\uparrow\rangle \equiv |F = 2, m_F = 0\rangle$, separated by the hyperfine transition frequency $\omega_{\text{HF}} \approx 2\pi \times 6.835 \text{ GHz}$ (Fig. 7.3).

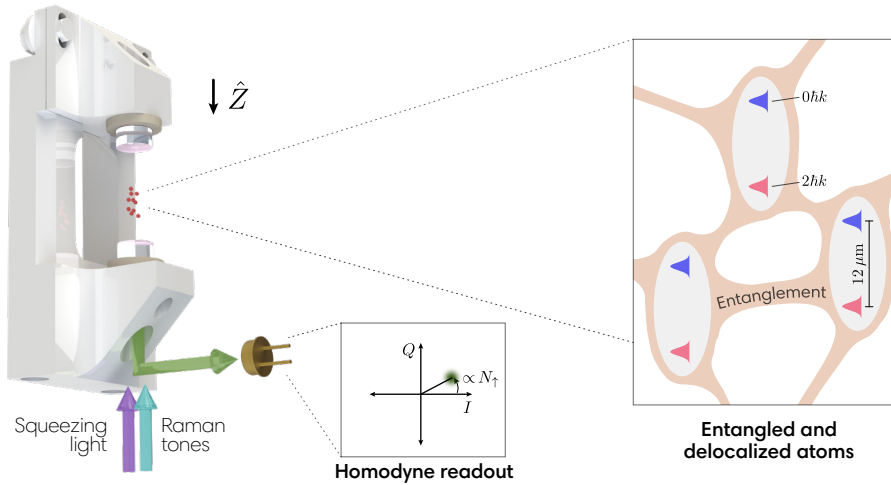


Figure 7.1: **System overview.** Ultracold atoms undergo guided free fall in a vertical high-finesse cavity. The atomic wavepackets are split (up to $12 \mu\text{m}$ at $T_{\text{evol}} = 1 \text{ ms}$) and recombined by driving two-photon Raman transitions to provide quantized momentum kicks to the atoms. (**insets**) Intracavity atomic probe light generates entanglement between the atoms via either one-axis twisting dynamics or quantum non-demolition measurements made by detecting the reflected atomic probe field with a homodyne detector.

The two-mirror cavity is vertically-oriented along \hat{Z} (Fig. 7.1(a)). A 1 G bias magnetic field also sets the quantization axis along \hat{Z} . The cavity has a power decay rate $\kappa = 2\pi \times 56(3) \text{ kHz}$. To ensure significant intracavity power for the Raman tones, the length of the cavity was adjusted to be near ω_{HF} (mirror separation $L = 2.2 \text{ cm}$, and free spectral range $\omega_{\text{FSR}} = 2\pi \times 6.7879 \text{ GHz}$). Every 700 ms, rubidium atoms are loaded into a red-detuned 813 nm standing-wave intracavity lattice and laser-cooled to a radial temperature of $0.7(3) \mu\text{K}$ (Ch. 5). The lattice is adiabatically reduced to allow the atoms to accelerate under gravity for a duration T_{fall} , guided tightly along the cavity axis by a hollow (Laguerre-Gauss LG_{01} -like) blue-detuned optical dipole guide. An overview of the lasers and cavity modes involved in this chapter is shown in Fig. 7.2. Technical details for these

subsystems are now provided before the matter-wave story resumes in Sec. 7.2.

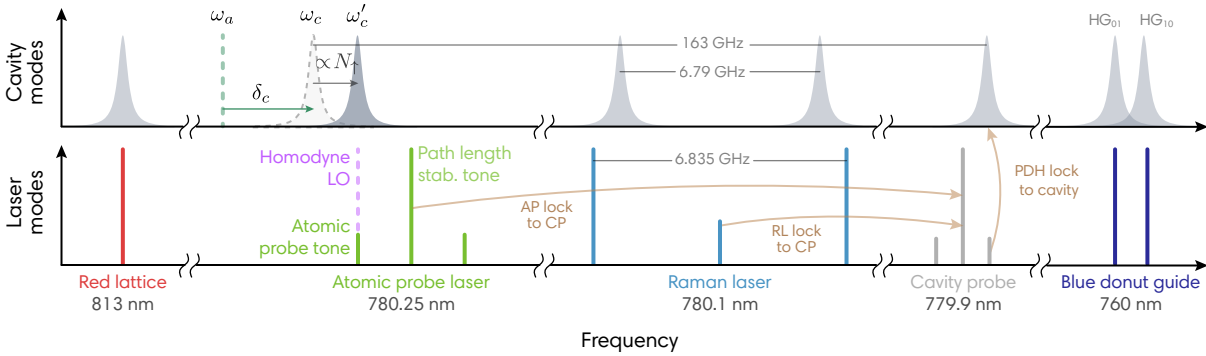


Figure 7.2: **Overview of cavity modes and laser frequencies for matter-wave interferometry.** The bare cavity is detuned δ_c to the blue of the $|\uparrow\rangle \rightarrow |e\rangle$ transition, and the presence of atoms in N_\uparrow shifts the dressed cavity resonance by $\omega'_c - \omega_c$. A cavity probe sideband is locked to a TEM₀₀ mode of the cavity, and the Raman laser and atomic probe are locked relative to the cavity probe.

Blue dipole guide The blue dipole guide laser is a 760 nm interference filter ECDL locked to a reference cavity for improved long-term stability. The laser is modulated by a fiber EOM with modulation index $\beta \approx 1.3$ at the cavity free spectral range ω_{FSR} . By exciting adjacent longitudinal modes of the cavity with opposite spatial parity with respect to the center of the cavity, one creates an axially-uniform blue dipole guide near the center of the cavity (Sec. 4.5) [94]. The donut-mode LG₀₁ profile is created by a phase plate and inserted on transverse modes as described in Sec. 4.6. The cavity is locked to the blue dipole guide laser via PDH.

Laser cooling Each trial, a 2D MOT loads a 3D MOT with 10^8 atoms near the cavity center over approximately 0.5 s. The MOT coils are turned off, and around 2×10^5 atoms are cooled via polarization gradient cooling to 15 μK and loaded into the red-detuned 813 nm lattice. The red lattice depth is ramped down to $\sim 100\hbar\omega_r$ and an extra stage of Λ -enhanced gray molasses cools on the D2 transition. After 5 ms, the temperature of the ensemble is reduced to 6 μK . Two-dimensional degenerate Raman sideband cooling (RSBC) further cools the radial temperature to 0.5-1 μK (Sec. 5.5) [131]. To improve the coupling of the atoms to the cavity (and thus increase the

phase space density of the atoms) we apply multiple cooling cycles. After three RSBC cycles, we slowly turn off the remaining red lattice and the RSBC lattice at the same time so that the atoms start to free fall with rms radial extent $r_{\text{rms}} = 3.0(5) \mu\text{m} \ll w_0$.

Raman tones High fidelity Raman and Bragg pulse sequences require agile control of low-phase noise microwaves. The frequency source used for driving Raman pulses is described in Sec. 3.1.9. Briefly, a low-noise 6.800 GHz source is mixed with 35 MHz DDS tones at a single side-band modulator. This provides phase, frequency, and amplitude control for arbitrary rotations on the Bloch sphere, for selecting different momentum-changing transitions, velocimetry, *etc.* The DDS tones are continuously ramped in frequency at a rate $b = 2gk \approx 2\pi \times 25.1 \text{ kHz/ms}$ to match the time variation of the two-photon Doppler shift as the atoms fall under gravity. The modulator output near 6.835 GHz is divided by two using a low-noise divider (PN: Analog Devices HMC862A) and applied to a fiber-coupled EOM to generate the desired Raman tones as the ± 1 st order sidebands. We estimate that the noise contributed by this frequency source is at least 30 dB below the SQL for 1000 atoms.

The laser that drives the Raman transitions is detuned $\Delta = 2\pi \times 85 \text{ GHz}$ blue of the $|\uparrow\rangle \leftrightarrow |e\rangle \equiv |5^2\text{P}_{3/2}, F=3\rangle$ transition (Fig. 7.3(a, b)). This laser is phase-locked to the cavity probe and centered between two adjacent longitudinal TEM_{00} cavity modes. The two Raman tones are symmetrically detuned from the cavity resonances by $(\omega_{\text{HF}} - \omega_{\text{FSR}})/2 = 2\pi \times 23 \text{ MHz}$. With 2.5 mW of total σ^+ -polarized light incident on the cavity, the EOM modulation index allows a two-photon Rabi frequency of up to $\Omega = 2\pi \times 15 \text{ kHz}$.

Cavity and atomic probes As in the previous chapter, a separate cavity probe laser is used to stabilize the frequencies of the Raman lasers and the atomic probe relative to the cavity. The cavity probe is locked to a TEM_{00} mode 160 GHz to the blue of the atomic transition frequency $|\uparrow\rangle$ to $|e\rangle$ at wavelength 779.915 nm. The locking of the cavity probe to the cavity is done via a Pound-Drever-Hall lock at very low phase modulation index. To reduce the amount of power entering

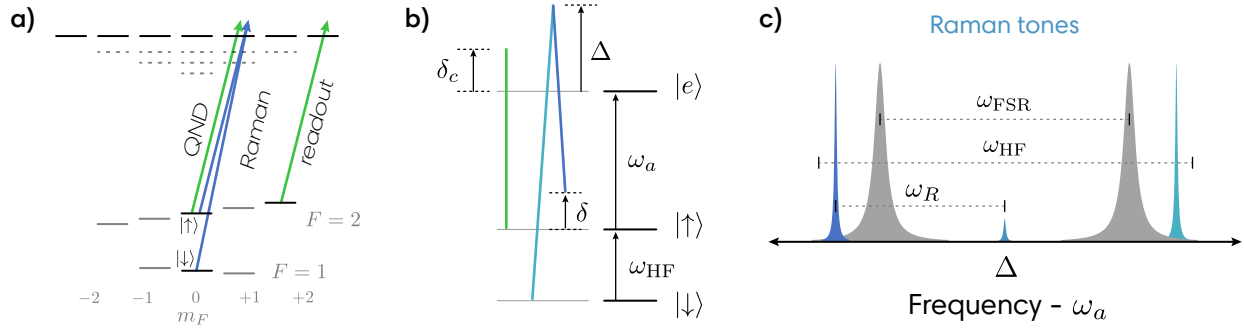


Figure 7.3: **Energy diagrams for the interferometry experiment.** (a) Basis states for the interferometer are the clock states. Raman, OAT, and QND tones use σ^+ -polarized light. Final state readout is performed on the stretched transition after optically pumping atoms to $|F = 2, m_F = 2\rangle$. (b) Simplified energy-level diagram. The empty-cavity (green) is detuned by δ_c from ω_a . The Raman tones drive a $|\uparrow\rangle \leftrightarrow |\downarrow\rangle$ transition with two-photon detuning δ in a falling reference frame. (c) The Raman tones (blue) are derived from a laser locked between two adjacent TEM₀₀ modes (gray) and modulated at $\omega_R \sim \omega_{HF}/2$.

the cavity to only 200 pW while still operating above the technical noise floor of the photodiode, we lock to one of the weak sidebands. This lock is always engaged. We then phase lock the other lasers to the cavity probe, so some of the cavity probe light is passed through a fiber EOM driven strongly at 13.6 GHz to generate very high order sidebands.

The atomic probe laser is phase-locked $13.6 \times 12 = 160$ GHz to the red of the cavity probe. The atomic probe laser is maintained 80 MHz blue of the cavity resonance frequency. The reflected (carrier) tone provides a reference for a homodyne LO path length stabilization lock. To generate squeezing or perform atomic population measurements, the atomic probe carrier tone is modulated by a fiber EOM at 80 MHz, allowing the atomic probe's red sideband to interrogate the dressed cavity frequency shift. The laser could be actively locked to the dressed resonance as in [20], or the linear part of the dispersive could be used to estimate small frequency shifts, but for this work, we sweep the atomic probe through resonance at 1.5 MHz/ms. This simplifies the experiment but it results in a 6 dB loss of quantum efficiency compared to true homodyne detection on resonance. Although π -polarization would be preferable for the atomic probe, the light traverses the same path as the Raman tones, which need to be σ^+ -polarized for sufficient transition strength.

The cavity and atomic probe lasers are DBRs with free-running linewidths of hundreds of

kHz. We use active feedback of an external cavity for narrowing the linewidths to less than 1 kHz (Sec. 4.3). This was instrumental for improving the technical noise floor for estimating populations and removing undesired Bragg scattering.

7.2 Manipulating matter-waves in a high-finesse cavity

We manipulate matter-wave wavepackets using velocity-sensitive two-photon transitions with wavelength $\lambda = 780$ nm. Within the cavity, Raman tones are propagating in both directions. A co-propagating pair of tones induces a Doppler-free clock transition if they are separated by ω_{HF} , and these transitions are unimportant for the context of this dissertation. But the combined absorption and stimulated emission of counter-propagating pairs of photons imparts $2\hbar k$ momentum kicks oriented along the cavity axis, where $k = 2\pi/\lambda$ and \hbar is the reduced Planck constant.

As the atoms fall within the cavity, the relative Doppler shift for light propagating upwards versus downwards chirps linearly in time. We compensate this effect by linearly ramping the instantaneous frequency of the sidebands as $2\omega_R = \omega_{\text{HF}} + \delta - b(t - t_{\text{vs}})$ with $b = 2kg = 2\pi \times 25.11$ kHz/ms. Here the local acceleration due to gravity is $g = 9.8 \text{ m s}^{-2}$, δ is the two-photon detuning in the falling frame of reference, and t_{vs} is the time at which we will apply the first π pulse for velocity selection described below (Fig. 7.4(b)). The velocity-insensitive Doppler-free transition is driven at $\delta = 0$ but we avoid operating near this detuning by letting the atoms fall for a significant duration.

Coherent Raman transitions and velocity selection In Fig. 7.4(c), we show the initial axial velocity spectrum of the atoms as mapped out by inducing velocity-dependent spin flips. Atoms are prepared in $|\downarrow\rangle$ and dropped for a duration T_{fall} , and the two-photon detuning δ is scanned to resonantly excite a narrow velocity class to $|\uparrow\rangle$ for measurement. We use this same process to select atoms within a narrow range of initial velocities for coherent manipulation of matter-waves in the remainder of this work. In the velocity selection sequence, atoms fall for $T_{\text{fall}} = 15$ ms and are optically-pumped to $|\uparrow\rangle$, and the two-photon detuning is set to $\delta_{\text{vs}} = 2\pi \times -400$ kHz to

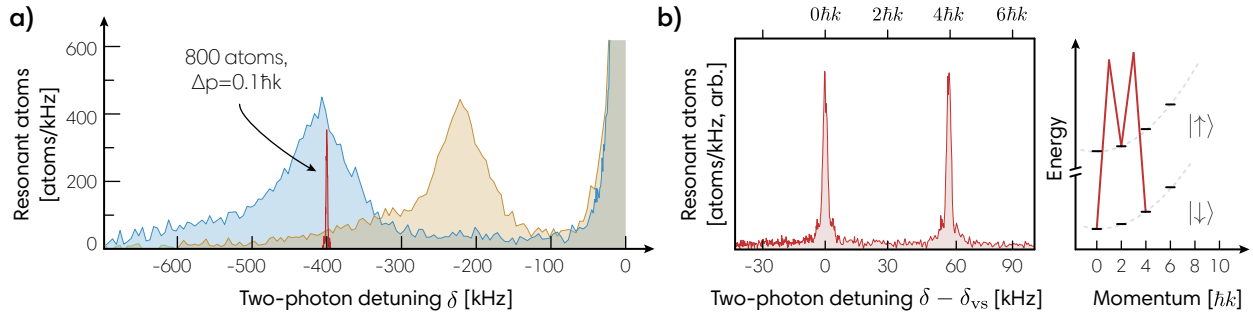


Figure 7.4: Velocity-selective Raman transitions. (a) Atoms are prepared in $|\downarrow\rangle$ and dropped for $T_{\text{fall}} = 7.5$ ms (orange) or 15 ms (blue). The axial velocity distributions are mapped out by scanning the detuning δ . The $5\hbar k$ FWHMs are too broad for interferometry. During velocity selection, a group of about 800 atoms with rms momentum spread $\Delta p = 0.1\hbar k$ (red) are kept from the latter distribution while the rest are removed with transverse radiation pressure. (b) After velocity selection, Raman transitions can be used to place atoms into a superposition of $|0\hbar k, \downarrow\rangle$ and $|4\hbar k, \downarrow\rangle$. For the second transition, $\delta = -\delta_{\text{vs}} + 2b(t - t_{\text{vs}}) - 8\omega_r$, where the photon recoil frequency is $\omega_r = 2\pi \times 3.77$ kHz. Scanning δ demonstrates discrete momentum distributions.

transfer a group of atoms to $|\downarrow\rangle$ from the center of the axial velocity distribution [182]. Atoms in $|\uparrow\rangle$ are removed by a transverse radiation pressure force. The velocity-selected atoms are returned to $|\uparrow\rangle$ with a Raman π pulse and the selection process is repeated, resulting in approximately $N_0 = 800 - 1200$ atoms in $|\downarrow\rangle$ with rms momentum spread $\Delta p = 0.1\hbar k$ set by choice of the two-photon Rabi frequency $\Omega_{\text{ab}} = 2\pi \times 1.4$ kHz. By using two stages, unwanted Rabi formula sinc-lobe Fourier components are largely suppressed. Without this technique, roughly 20% of atoms are outside the Δp velocity group.

In Fig. 7.4(d) we demonstrate the quantized nature of the momentum kicks imparted by the intracavity Raman transitions. After velocity selection, a $\pi/2$ pulse is followed by a second Raman π pulse to place the atoms into a superposition of $|0\hbar k, \downarrow\rangle$ and $|4\hbar k, \downarrow\rangle$ in the falling frame of reference. We observe this as two distinct peaks separated in the subsequent velocity spectrum. Though not leveraged here, future interferometers might evolve in such superpositions so as to minimize systematic errors and dephasing due to environmental couplings to the spin degree of

freedom.

Bragg transitions and large momentum transfer Complementary to hyperfine spin-state changing Raman transitions, we also demonstrate intracavity Bragg transitions in this high finesse and high cooperativity cavity. Although these transitions still use two photons, the Bragg coupling connects states $|n\hbar k\rangle \leftrightarrow |(n+2)\hbar k\rangle$ with no change in the spin degree of freedom as shown in Fig. 7.5(a). The Bragg transitions are driven by two laser tones derived from the same laser with difference frequency $\omega_B = \delta_{\text{vs}} - b(t - t_{\text{vs}})$. To achieve $2\pi \times 10$ kHz Rabi frequencies, the center frequency of the driving laser is shifted 10 MHz such that the two tones responsible for the Bragg transitions are approximately 13 MHz from cavity resonance.

In Fig. 7.5(a), the ensemble is coherently split by a Bragg $\pi/2$ pulse, followed by successive π pulses to transfer momentum to one of the wavepacket components for a momentum difference of up to $10\hbar k$. An interferometer fringe for a Mach-Zehnder interferometer with $4\hbar k$ maximum momentum separation is shown in Fig. 7.5(b). The number of atoms in $|0\hbar k, \downarrow\rangle$ is measured while scanning the azimuthal phase of the final Bragg $\pi/2$ pulse from 0 to 2π . The $4\hbar k$ Bragg interferometer has an evolution time of $T_{\text{evol}} = 50 \mu\text{s}$. Access to Bragg transitions opens the door to both large momentum transfer operations for greater sensitivity and to improved coherence times in future work.

7.3 Squeezed momentum states

Quantum entanglement between the atoms allows the atoms to conspire together to reduce their total quantum noise relative to their total signal during the phase estimation process [13, 14]. Strong collective atom-cavity coupling has been used to either mediate pseudo spin-spin interactions [25, 56, 59, 150] or to realize high resolution quantum non-demolition measurements [17, 20–24, 46, 47, 151]. Whether entanglement could really be extended over a distance was at once hotly debated [1], but we can now exploit the phenomenon for metrological purposes.

In this section, we directly prepare squeezed momentum states through two separate cavity-

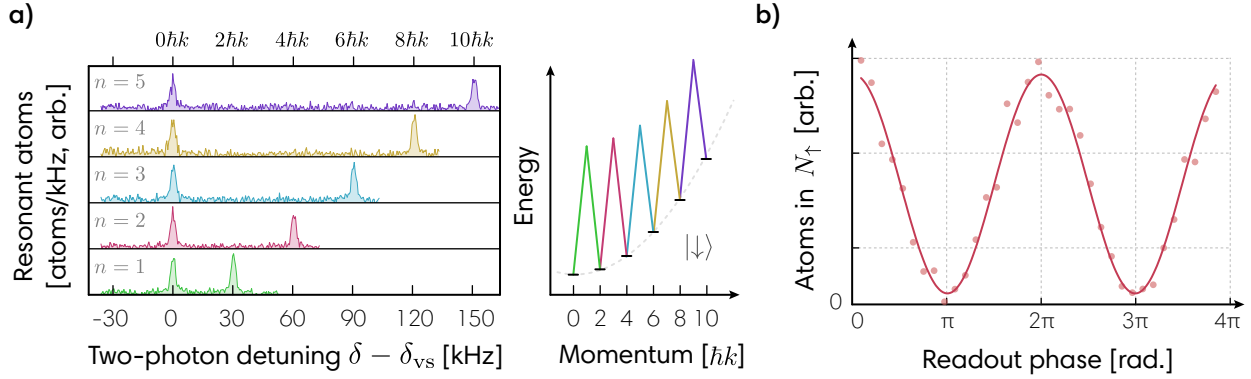


Figure 7.5: Bragg-pulse superpositions and interferometry. (a) Two-photon Bragg transitions can drive coherent changes in momentum. Here we use a Bragg $\pi/2$ pulse followed by consecutive π pulses to transfer momentum into superpositions of $|0\hbar k, \downarrow\rangle$ and $|2n\hbar k, \downarrow\rangle$. The π pulses are kept on resonance with successive transitions and thus require that the detuning δ be stepped in $8\omega_r$ increments between transitions. (b) An interferometer fringe for a Bragg-pulse Mach-Zehnder interferometer with $4\hbar k$ maximum momentum separation and $T_{\text{evol}} = 50 \mu\text{s}$ evolution time.

based interactions: quantum non-demolition (QND) measurements [16, 20, 21, 29] and one-axis twisting (OAT) [14, 30, 56], demonstrating the first generation of squeezed momentum states, with metrological gain $3.4_{-0.9}^{+1.1}$ dB and $2.5_{-0.6}^{+0.6}$ dB below the standard quantum limit respectively. These techniques represent both of the most successful methods for generating large amounts of atomic spin-squeezing to date. In both cases, quantum noise is reduced in one spin-momentum projection at the expense of increased quantum noise along the orthogonal projection. The resulting states are well-defined, well-resolved momentum modes useful for matter-wave interferometry. It will be useful to establish terminology for the rest of the chapter, including a useful formulation of the spectroscopic enhancement W , before describing these results in more detail.

The Wineland criterion in terms of angular resolution. Contrary to the previous chapter, the spectroscopic enhancement of our interferometer will be evaluated directly in terms of angular resolution. This formulation is equivalent to the Wineland criterion [13] presented earlier, but it is more closely connected to the sequences we run.

In order to emphasize the coupling between spin and momentum, we describe the basis

states of our interferometer as $|a\rangle_i = |2\hbar k, \uparrow\rangle_i$ and $|b\rangle_i = |0\hbar k, \downarrow\rangle_i$ for the i^{th} atom. The collective state is depicted using a Bloch sphere with Bloch vector $\vec{J} = \langle \hat{J}_x \hat{x} + \hat{J}_y \hat{y} + \hat{J}_z \hat{z} \rangle$ of length $J \equiv |\vec{J}| \leq N_0/2$ bounded by the number of velocity-selected atoms N_0 . The collective population projection operators are $\hat{N}_\uparrow = \sum_i^{N_0} |a\rangle_i \langle a|$ and $\hat{N}_\downarrow = \sum_i^{N_0} |b\rangle_i \langle b|$, to define pseudospin projection operators $\hat{J}_z \equiv \frac{1}{2} (\hat{N}_\uparrow - \hat{N}_\downarrow)$, etc.

For the experiments that follow, an initial Raman $\pi/2$ pulse nominally prepares all atoms in an unentangled coherent spin state $|\psi\rangle = \prod_i^{N_0} \frac{1}{\sqrt{2}} (|a\rangle_i + |b\rangle_i)$ described by the Bloch vector $\vec{J} = J\hat{x}$. The quantum noise that will appear in a measurement manifests in the non-zero variance of the spin projection operators $(\Delta J_z)^2 = \langle \hat{J}_z^2 \rangle - \langle \hat{J}_z \rangle^2 \neq 0$, etc. and is visualized on the Bloch sphere as a quasi probability distribution of the orientation of the Bloch vector from trial to trial. It is the ratio of rms spin projection noise amplitude to the length of the Bloch vector that sets the standard quantum limit in the quantum phase estimation of the polar and azimuthal angles.

The Wineland parameter is again defined by

$$W = \frac{[\Delta(J_{zf})]^2 C_i}{\Delta J_{z,SQL}^2 C_f^2}, \quad (7.1)$$

where the initial contrast $C_i \equiv 2J_c/N_0$ is evaluated in the absence of squeezing interactions, and the final contrast $C_f \equiv 2J_s/N_0$ is evaluated with squeezing, just as in Ch. 6. This expression is rearranged using $J_{z,SQL} = \sqrt{N_0}/2$ to arrive at

$$W = \frac{\left[\Delta \left(\frac{N_\uparrow - N_\downarrow}{N_0 C_f} \right) \right]^2}{1/N_0 C_i} \equiv \left(\frac{\Delta\theta}{\Delta\theta_{SQL}} \right)^2 \quad (7.2)$$

Put into words, the Wineland criterion compares the angular resolution of the final measurement to the standard quantum limit $\Delta\theta_{SQL} = 1/\sqrt{N_0 C_i} \equiv 1/\sqrt{N}$ obtained with the number of atoms remaining *after* the initial contrast is evaluated. Physically, it is the reduction in the angular noise variance of the phase estimation relative to the standard quantum limit one would have for a pure state with a Bloch vector length $J_c = N/2$ equal to that of the actually prepared partially decohered (mixed) state absent the squeezing operation.

Preparing QND-squeezed momentum states Population readout is achieved through col-

lective or QND measurements of the free falling atomic samples that ideally give information about the fraction of the atoms in spin-momentum states $|a\rangle$ and $|b\rangle$ without revealing single-particle information [29, 94]. We tune a TEM₀₀ cavity mode with resonance frequency ω_c to the blue of the $|\uparrow\rangle \rightarrow |e\rangle$ transition ω_a by $\delta_c = \omega_c - \omega_a$. The $|\downarrow\rangle \rightarrow |e\rangle$ transition is far detuned from ω_a . The QND Hamiltonian was introduced in Eq. 2.3. After adiabatically eliminating the excited state $|e\rangle$ [65] and ignoring mean-field light shifts that will be spin-echoed away, the effective Hamiltonian describing the atom-cavity QND interaction can be expressed as [30]

$$\hat{\mathcal{H}}_{\text{QND}} = \left(\delta_c + \chi_{\text{QND}} \hat{N}_{\uparrow} \right) \hat{a}^{\dagger} \hat{a} \quad (7.3)$$

where the cavity field is described by creation and annihilation operators \hat{a}^{\dagger} and \hat{a} . Physically, atoms in $|\uparrow\rangle$ create a round trip phase shift of the intracavity light that causes the cavity resonance to shift. The two momentum states therefore interact differently with the optical cavity because they carry distinct spin labels. For example, at the detuning we use for QND squeezing, $\delta_c = 2\pi \times 175$ MHz, the dressed cavity shifts by $\chi_{\text{QND}} = 2\pi \times 336(2)$ Hz per atom in $|2\hbar k, \uparrow\rangle$ (see Sec. 7.5.3 and Fig. 7.6(a)). At the detuning used for OAT-squeezing, $\delta_c = 2\pi \times 350$ MHz, the dressed cavity shifts by $\chi_{\text{QND}} = 2\pi \times 183(1)$ Hz per atom in $|\uparrow\rangle$.

The population of atoms N_{\uparrow} in the momentum state with spin label $|\uparrow\rangle$ is inferred from the measurement of this cavity frequency shift. The frequency shift is estimated by detecting the Q quadrature of probe light reflected from the cavity input mirror as the laser frequency is swept across resonance during a 150 μs measurement (Sec. 3.1.8). The population N_{\downarrow} of atoms in the momentum state with spin label $|\downarrow\rangle$ is measured with the same technique after transferring the atoms to $|\uparrow\rangle$ using a Raman π pulse. The Raman π pulse serves the additional functions of re-overlapping the wavepackets and cancelling the average light shift of the probe.

Collective QND measurements are not only used for readout, but also in creating conditional spin-squeezing. The spin-momentum projection in the population basis is measured once with the pre-measurement outcome $J_{zp} = \frac{1}{2} (N_{\uparrow} - N_{\downarrow}) |_{\text{pre}}$. The same projection is then measured a second time with the final measurement outcome labeled $J_{zf} = \frac{1}{2} (N_{\uparrow} - N_{\downarrow}) |_{\text{fin}}$. Each final population

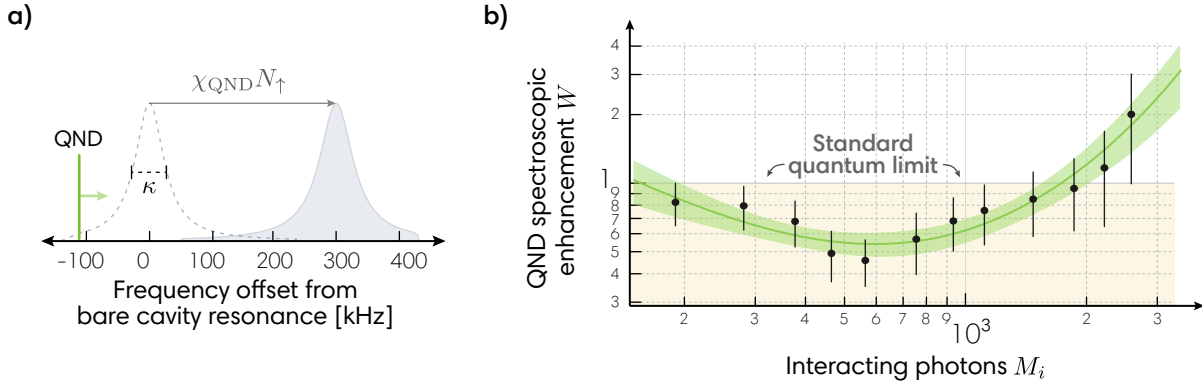


Figure 7.6: **QND momentum squeezing.** (a) Atomic probe frequency setup. Collective population measurements are made by sweeping the probe laser frequency over cavity resonance and detecting the Q quadrature of the reflected field. (b) QND measurements are used to pre-measure the quantum noise in the spin projection J_z and subtract it from a final measurement as in [20]. Increasing the number of probe photons M_i overcomes photon shot noise for a more precise pre-measurement, but at too high of a photon number, free space scattering causes shortening of the Bloch vector and spontaneous Raman scattering to other states. Squeezing is characterized by the spectroscopic enhancement W which reaches an optimum below the standard quantum limit at $M_i = 600$ photons.

measurement is made after first optically pumping atoms in $|\uparrow\rangle$ to $|F = 2, m_F = 2\rangle$ to achieve lower readout noise (estimated at more than 15 dB below the projection noise level) by probing on the optical cycling transition to $|F = 3, m_F = 3\rangle$.

If sufficiently precise, the pre-measurement localizes the state to below the initial coherent spin state level, producing a squeezed state. It can be considered a measurement of the quantum fluctuation of the orientation of the state on a given trial, and the measurement outcome can then be used to partially subtract the quantum fluctuation from the final measurement outcome by considering the difference $J_{zd} = J_{zf} - J_{zp}$. The quantum fluctuation is common to the two measurements, but any rotation of the state (*i.e.* the signal) that occurs in between the two measurements appears only in the final measurement outcome so that one can estimate the angular displacement as $\sin(\theta) \equiv J_{zd}/J_s$. The length of the Bloch vector J_s after the pre-measurement has prepared a squeezed state is measured in a separate set of experiments in which a $\pi/2$ pulse about azimuthal angle ϕ is inserted between the pre- and final measurements. The length of the Bloch vector is estimated from the fringe amplitude of J_{zf} versus ϕ as it is varied between 0 to 2π .

The initial length of the Bloch vector J_c needed for estimating the spectroscopic enhancement is estimated in the same manner, but without the pre-measurement applied.

Fig. 7.6(b) shows the spectroscopic enhancement W versus the strength of the QND interaction as parameterized by M_i , the average number of incident photons that enter the cavity during each population pre-measurement window. At low M_i , the probe's vacuum noise limits the spectroscopic enhancement, while at high M_i , the spectroscopic enhancement is limited by free space scattering of the probe light that leads to a reduction in J_s and transitions to other ground states that decorrelate the pre- and final measurements. Near $M_i = 600$, $N = 1170(30)$ atoms, and $\delta_c = 2\pi \times 175$ MHz, we achieve $W = 0.46(11)$ or $3.4_{-0.9}^{+1.1}$ dB of directly observed squeezing in the momentum-spin basis.

Preparing OAT-squeezed momentum states. We also realize momentum-spin entanglement via cavity-mediated interactions (Sec. 2.3) [30, 31, 56]. The one-axis twisting (OAT) Hamiltonian [14]

$$\hat{\mathcal{H}}_{\text{OAT}} = \chi_{\text{OAT}} \hat{J}_z^2 \quad (7.4)$$

is generated by applying a fixed frequency drive tone offset from the average dressed cavity resonance by $\delta_p \gtrsim \kappa/2$. Briefly, the populations in each momentum-spin state tune the cavity closer to or further from resonance with the fixed frequency drive tone, allowing more or less light into the cavity to produce an AC Stark shift on the states that depends on the population of atoms in $|\uparrow\rangle$. After adiabatic elimination of the dressed cavity mode [65] and neglecting terms that will be spin-echoed away, one finds that to first approximation, $\hat{c}^\dagger \hat{c} \propto \hat{N}_\uparrow$. As a result, the spin-dependent portion of the QND Hamiltonian is transformed after a spin-echo pulse into Eq. 7.4, a pure spin-spin Hamiltonian proportional to $\hat{N}_\uparrow^2 + \hat{N}_\downarrow^2 = 4\hat{J}_z^2$ with the cavity mode acting as a mediator of the interaction. The unitary interactions drive shearing of the atomic quantum noise distribution with a resulting squeezed state minimum noise projection oriented at a small angle α_0 from \hat{z} (Fig. 7.10(b, inset)).

To suppress free-space scattering, it is ideal to operate at $\delta_p = \kappa/2$, but we work at larger detunings to both reduce the QND interactions that can compete with the desired one-axis twisting interaction [57] and to allow operation in a linearized regime even in the presence of shot-to-shot total atom number fluctuations. In general, the optimum probe detuning increases with higher NC . We empirically find an optimum detuning of $\delta_p = 2.7 \times \kappa/2$ with $\chi_{\text{OAT}} \approx 2\pi \times 10$ Hz.

After the OAT interaction is applied, the state is rotated using the Raman beams to couple the momentum-spin states so that the minimum noise projection is along \hat{z} . The momentum-spin populations are destructively read out as described previously with measurement outcome labeled J_{zf} . The Bloch vector lengths J_s (J_c) with (without) OAT squeezing are measured in the same manner as was done for the QND measurements by measuring the fringe amplitude of J_{zf} versus the azimuthal phase of a $\pi/2$ rotation prior to the final readout. We achieve a directly observed spectroscopic enhancement from OAT of $W = 0.56(8)$ or $2.5_{-0.6}^{+0.6}$ dB. The optimal configuration was realized with $M_i \approx 700$ photons, $\delta_c = 2\pi \times 350$ MHz, and $N = 730(10)$ atoms.

Tomography of momentum-squeezed states Having prepared coherent states and QND- and OAT-squeezed momentum states, we can visualize the quasi-probability distribution by measuring various projections along J_z . After preparing each state along \hat{x} , we insert a pulse of varied duration ψ to rotate the state about the Bloch vector. Statistics are collected for about ten durations of ψ and an inverse Radon transform reconstructs the roughly-Gaussian states [20, 154]. In Fig. 7.7, the quasi-probability information is used in a height-and-color map to visualize the quantum states.

7.4 An entangled matter-wave interferometer

We now turn to injecting the prepared entangled states into a matter-wave interferometer. An overview of the protocol is given in Fig. 7.8: generate momentum squeezing in the phase quadrature, run a low-noise interferometer, perform sub-SQL readout. The multitude of relevant sequences are shown schematically in Sec. 7.5.1. We use a slightly modified Mach-Zehnder Raman

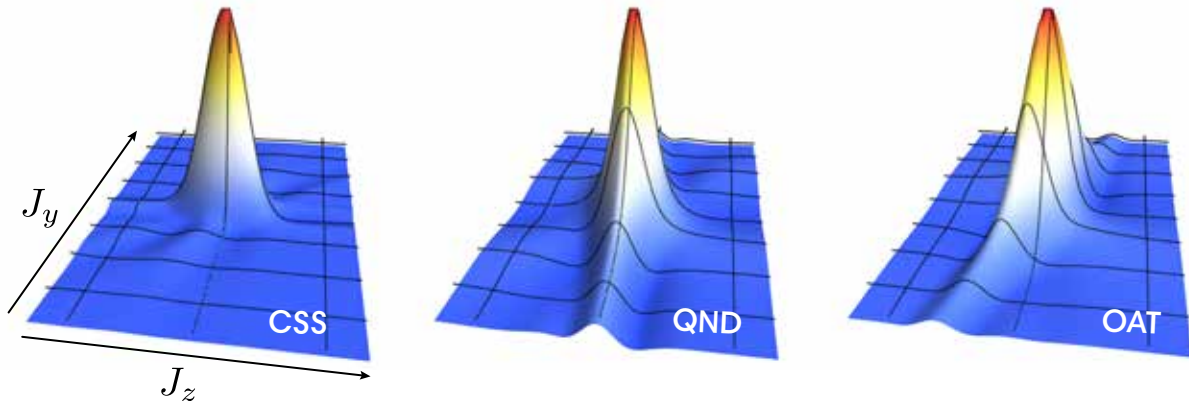


Figure 7.7: Quasi-probability distributions are reconstructed and plotted in the $J_y - J_z$ plane for a coherent spin state (CSS), a QND-squeezed state, and an OAT-squeezed state.

interferometer with $(\pi/2 - \pi - \pi/2)$ pulse sequence to coherently separate, undo the separation, and interfere the atomic wavepackets. In analogy to an optical Mach-Zehnder interferometer, the $\pi/2$ pulses play the role of 50/50 beam splitters at the entrance and exit of the interferometer and the π pulse plays the role of the mirrors that redirect the beams from the input beam splitter to the output beam splitter.

After preparing a squeezed state with OAT, a Raman beam splitter rotation orients the squeezing along \hat{y} . The spin projection J_y will change if a small signal phase ϕ is applied. The orienting of the squeezing is accomplished via a $(\pi/2 + \alpha_0)$ pulse aligned to the atomic Bloch vector along \hat{x} . A relative phase accumulates between the wavepackets during a free evolution time T_{evol} , a Raman π “mirror” pulse is applied, followed by another free evolution time T_{evol} . Finally, a readout $\pi/2$ pulse transfers the signal ϕ and the squeezing into a displacement in the momentum-spin population basis \hat{z} with a measurement outcome J_{zf} . The Bloch vector lengths J_s and J_c are measured in separate experiments with and without OAT applied by scanning the azimuthal phase of the final $\pi/2$ pulse of the interferometer and measuring the fringe amplitude as before (see Fig. 7.10(a)).

We achieve a directly observed spectroscopic enhancement as measured by the Wineland parameter of $1.7_{-0.5}^{+0.5}$ dB beyond the standard quantum limit with $N = 660(15)$ atoms as shown

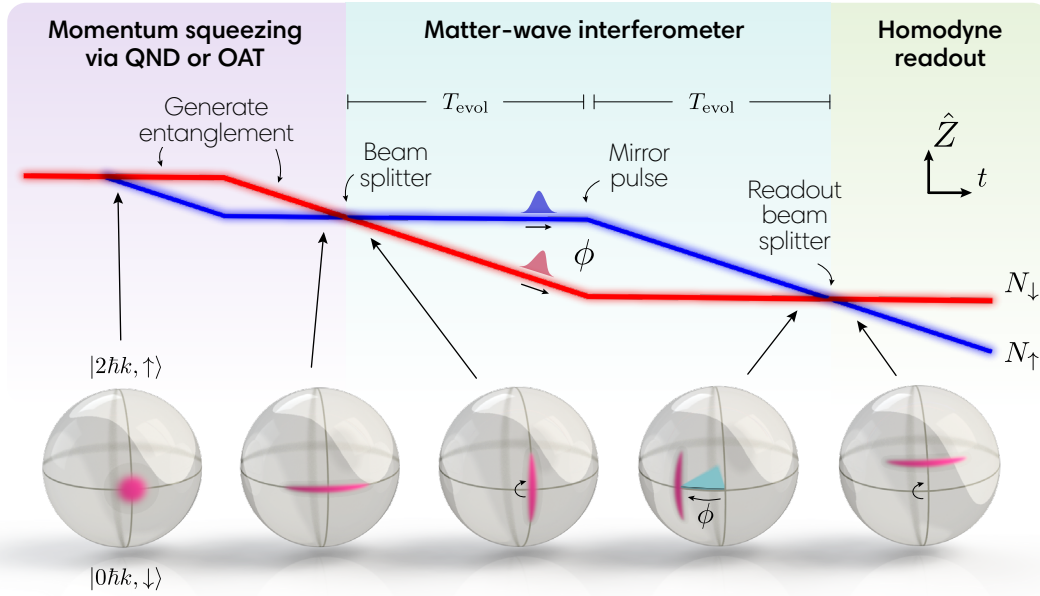


Figure 7.8: **Squeezed interferometer space-time diagram and Bloch spheres** for the generation and injection of the entanglement into a Mach-Zehnder matter-wave interferometer. Squeezing is first generated in the population basis, and then a Raman beam splitter pulse orients the squeezing for enhanced interferometer phase sensitivity. Wavepackets traversing the two paths (red and blue) accrue a relative phase ϕ over time T_{evol} , the mirror pulse serves to reoverlap the wavepackets, and the readout beam splitter pulse creates interference that is read out as a population difference with sub-standard quantum limit sensitivity. Representative noise distributions are depicted on the Bloch sphere for various points in the interferometer.

in Fig. 7.9(b). We also note that the actual phase variance of the interferometer is enhanced by $3.4_{-1.2}^{+0.9}$ dB compared to with no one axis twisting, consistent with expectations from J_c .

Phase sensitivity beyond the SQL was limited to evolution times $T_{\text{evol}} < 0.7$ ms (Fig. 7.10(b)). Evidence from an interferometer run with purely microwave rotations (*i.e.* with no momentum states involved) suggests this loss of observable squeezing was primarily due to magnetic field fluctuations in the lab, just like the earliest free-fall interferometer [42]. The matter-wave interferometer is sensitive to vibration noise, but the measured accelerations are not sufficient to explain the loss of directly observed entanglement (Sec. 7.5.5). Single-particle decoherence is also inadequate as an explanation because J_c decreased by less than 5% over these evolution times. However, when increasing the bias magnetic field to ~ 4 G, evolution times were limited to less than 0.3 ms.

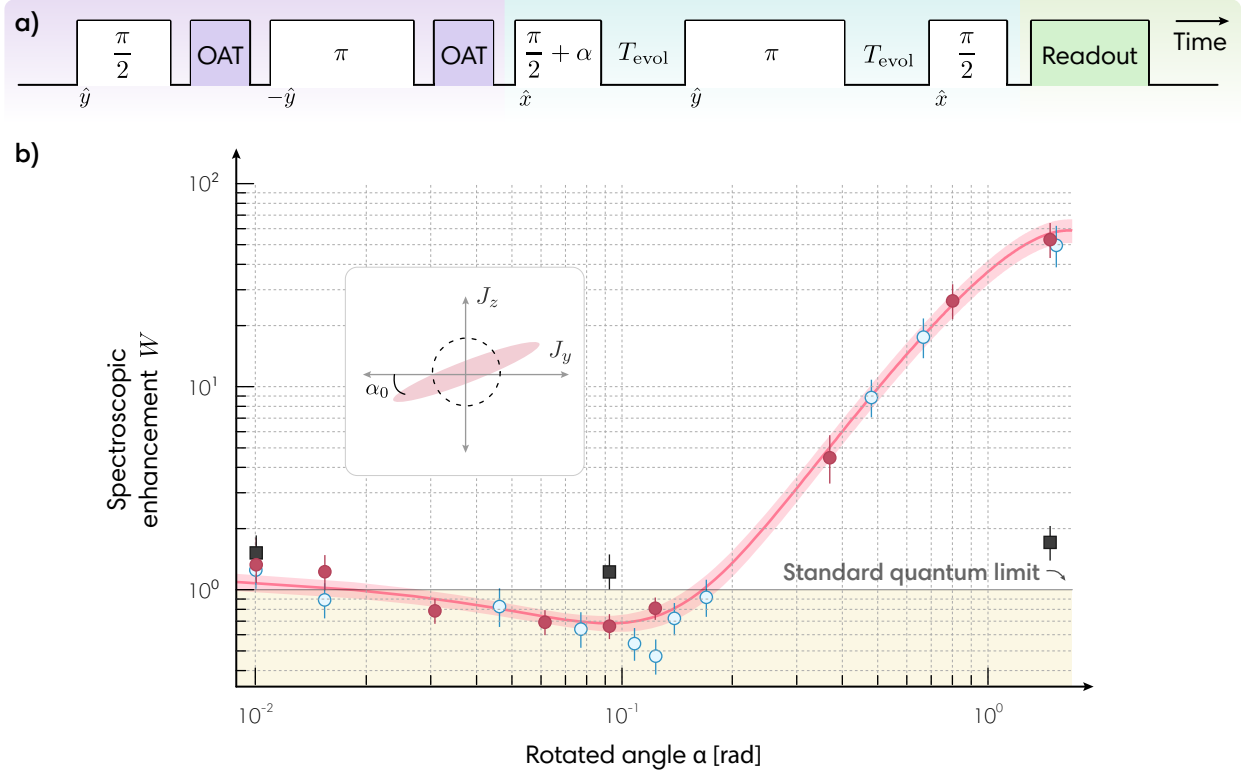


Figure 7.9: **Interferometer sensitivity beyond the standard quantum limit.** (a) The squeezed interferometer sequence, including entanglement generation (purple), the interferometer (blue), and state readout (green). Each Raman transition is labeled with magnitude (within) and axis of rotation (below). (b) The spectroscopic enhancement W is compared for three configurations: a Mach-Zehnder interferometer with OAT (red circles, sequence above), an unentangled interferometer without OAT (black squares), and OAT-squeezed states without the interferometer (blue circles). The duration of a $\pi/2 + \alpha$ rotation is scanned to minimize the projected spin noise at α_0 . An ellipse is fit with 68% confidence bands to the OAT-squeezed interferometer data, giving a minimum variance of $W = 0.68(8)$ or $1.7_{-0.5}^{+0.5}$ dB. The interferometer here has $T_{\text{evol}} = 0.112$ ms.

Despite working on the first-order magnetically-insensitive clock states, the second order Zeeman effect leads to fluctuations in the azimuthal phase accrued during the interferometer evolution times. With Fig. 7.10(b), we further observe that if the squeezed spin projection is left in the population basis J_z during the interferometer, then the squeezing persists for several milliseconds. From this, we conclude that the entangled state persists for longer than we can directly confirm because the interferometer is detecting an undesired magnetic field signal that masks the quantum noise reduction as T_{evol} increases.

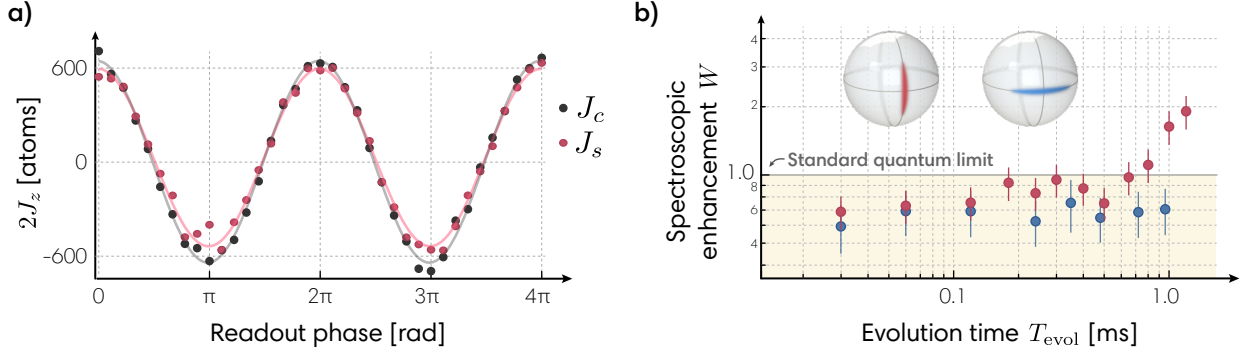


Figure 7.10: **(a)** Interferometer contrast fringes with $T_{\text{evol}} = 0.112$ ms shown for no squeezing J_c (black) and with squeezing J_s (red). The ratio of Bloch vector lengths, which accounts for decoherence due to OAT photons, is $J_s/J_c = 88\%$. **(b)** Phase sensitivity is maintained below the SQL for the squeezed interferometer (red circles, left Bloch sphere) up to $T_{\text{evol}} = 0.7$ ms. By contrast, if the squeezed spin projection is oriented along the population basis (blue circles, right Bloch sphere), spectroscopic enhancement was seen to persist beyond $T_{\text{evol}} = 1$ ms because this orientation is insensitive to phases accrued during the evolution time.

As an accelerometer or gravimeter, more work would need to be done to characterize systematic effects including the quadratic Zeeman effect, radial motion, and gradients of the intracavity fields. The phase of a Mach-Zehnder interferometer scales as $\phi = 2k \cdot aT_{\text{evol}}^2$ for an acceleration a . The parameters of our Raman interferometer system allow for measuring accelerations such as gravity at the $\Delta a/a \sim 10^{-4}$ level ($100 \mu\text{g}/\sqrt{\text{Hz}}$), in the same realm as other compact interferometers [181]. The maximum wavepacket separation is $2\hbar kT_{\text{evol}}/m_{\text{Rb}} = T_{\text{evol}} \times 0.0117$ mm/ms. For the longest evolution times of $T_{\text{evol}} = 1$ ms, the maximum separation is $12 \mu\text{m}$, an order of magnitude larger than the wavepacket size $\Delta x \approx \frac{\hbar}{2}\Delta p = 0.6 \mu\text{m}$. Compared to a unitary-squeezed state $\Delta\theta_{\text{SQL}}\Delta\phi_{\text{SQL}}$, the area of the OAT-squeezed state in the interferometer $\Delta\theta\Delta\phi$ is increased by about 6.5, similar to the QND-squeezed states described earlier.

7.5 Supplementary details

7.5.1 Experimental sequences

A schematic timing diagram for each sequence relevant to this chapter is provided in Fig. 7.11. To measure N , OAT or QND is temporarily disabled by using $M_i = 0$, but the window durations

are left intact. The azimuthal phase of the $\pi/2$ readout pulse is scanned through $[0, 2\pi]$, and the peak-to-peak amplitude of the fringe is converted to N_{\uparrow} using the known detuning δ_c and g_{rms} . For estimates of angular resolution $\Delta\theta$, M_i is re-enabled. The size of the interferometer fringe $N_0 C_f$ is measured by again scanning the readout phase. Measurements of $\Delta\theta$ consist of 100-200 points with readout phase tuned to the side of the fringe.

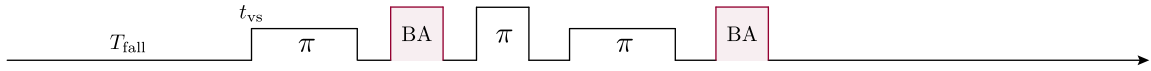
7.5.2 Optics layout

The complex array of frequencies and polarizations requires careful consideration of the layout on the optical table. ABCD matrices are first used to mode-match beams into lasers [26]. High quantum efficiency (low optical loss) is required for the path of the reflected cavity field to the detector. Various filters are used for overlapping beams at different wavelengths, and the angle of incidence can affect transmission coefficients significantly. Finally, the spatial constraints of optic mounts and clamps cannot be neglected. A suitable 2D geometry was drawn in Solidworks and converted for print in Fig. 7.12.

7.5.3 Dispersive atom-cavity coupling in a multi-level system

The dispersive shift of the σ^+ -polarized cavity mode's frequency for a given number of atoms N_{\uparrow} involves interactions with multiple excited state hyperfine levels F' [29]. The problem is complicated by the time-dependent atom-cavity coupling, but a hand-waving argument for the calculation is included here. We will define the states $|0_{\gamma}\rangle$ and $|1_{\gamma}\rangle$ to denote 0 and 1 photons in the cavity, and the notation $|F' 0_{\gamma}\rangle \equiv |0_{\gamma}\rangle \left(\frac{1}{\sqrt{N_{\uparrow}}} \sum_i |\uparrow \cdots F'_i \cdots \uparrow\rangle \right)$ to indicate one collective atomic excitation to a particular state F' . The ground state $|\uparrow 0_{\gamma}\rangle$ has all atoms in $|\uparrow\rangle$ and no cavity excitations. In the weak-probing (single excitation) limit, $|\uparrow 0_{\gamma}\rangle$ couples to excited states $|\uparrow 1_{\gamma}\rangle$ (one cavity excitation) and to $|F' 0_{\gamma}\rangle$ (one atomic excitation) for all excited states F' . The atom-cavity

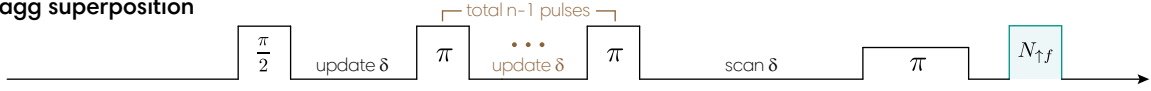
1. Velocity selection



2. Raman superposition



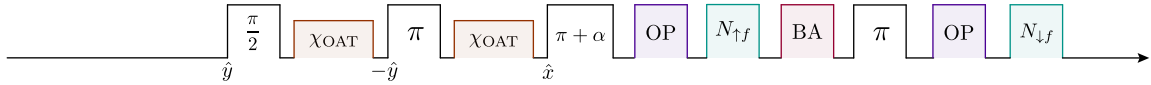
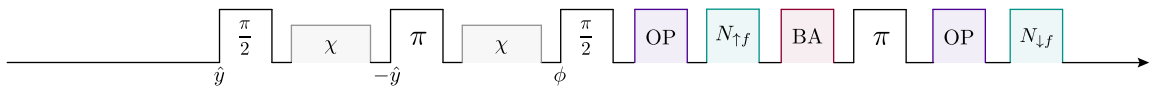
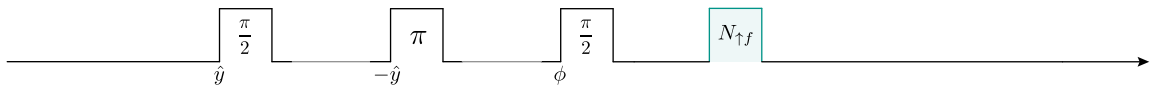
3. Bragg superposition



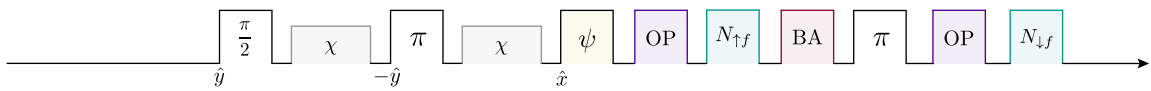
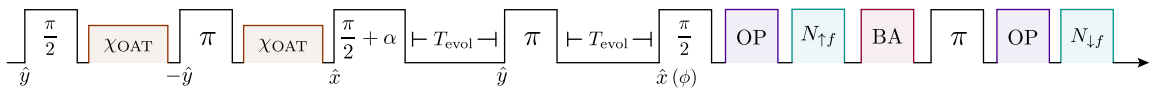
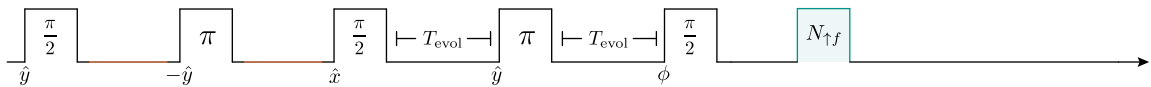
4. QND spin-noise



5. OAT spin-noise

6. J_s for momentum squeezing7. J_c for momentum squeezing

8. Tomography

9. Squeezed interferometer (and J_s)10. J_c for squeezed interferometer

11. Number-squeezed interferometer

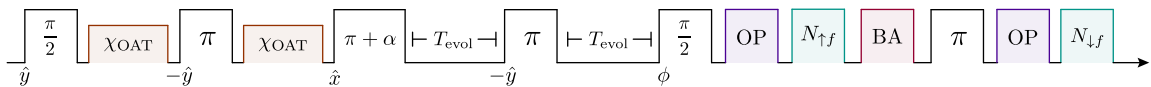


Figure 7.11: **Sequence timing diagrams.** BA: blow away $|\uparrow\rangle$ atoms. OP: optically-pump $|\uparrow\rangle$ atoms for stretched-state readout. For rotation axes marked ϕ , the azimuthal phase is scanned out to extract a fringe.

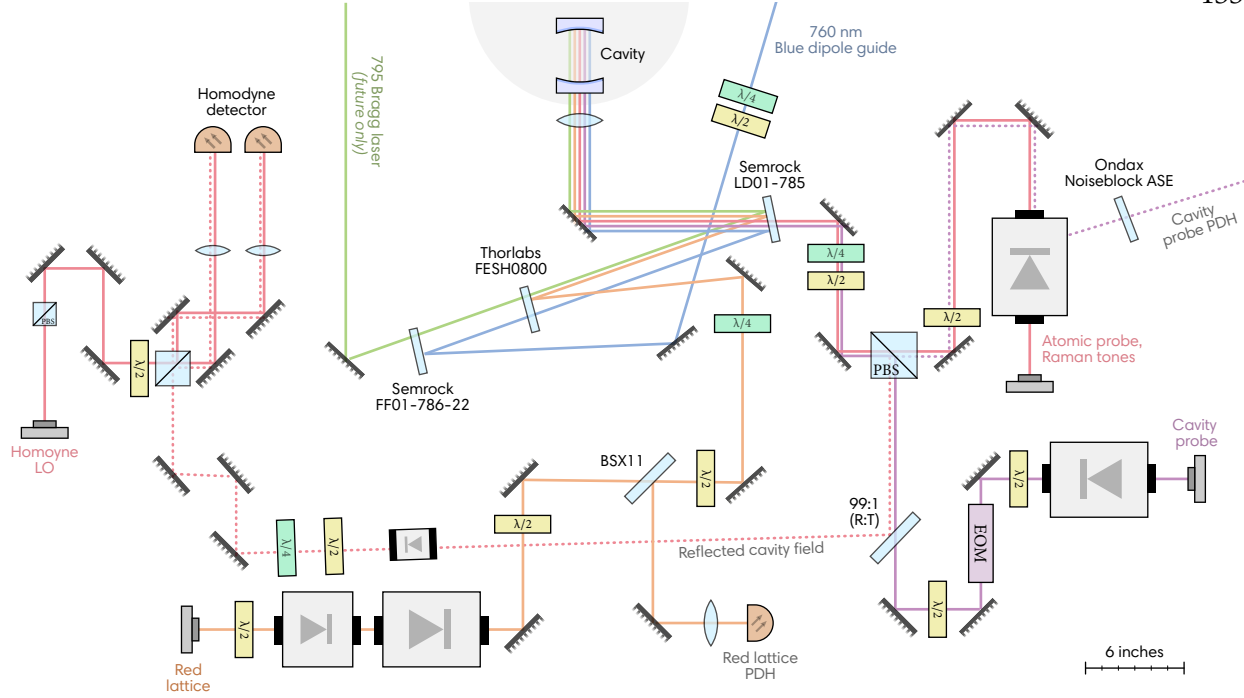


Figure 7.12: **Optics layout** for coupling the multitude of beams into the bottom port of the cavity. Raman tones, QND and OAT light follow the same atomic probe path (red). The 795 Bragg laser path is currently unused. Not only are the design wavelengths of the filters important (PN: OndaX Noiseblock ASE Suppression 780.25, Semrock LD01-785 and FF01-786-22, Thorlabs FESH0800), but their angles of incidence are critical as well.

interactions are described in a rotating frame of the $|\uparrow\rangle \rightarrow |F' = 3\rangle$ transition frequency by

$$\begin{aligned}
 \hat{\mathcal{H}}_1 = & \sqrt{N_{\uparrow}} g_3 \left(\hat{a}^\dagger \hat{\sigma}_3^- + \hat{a} \hat{\sigma}_3^+ \right) + \delta_c \hat{a}^\dagger \hat{a} \\
 & + \sqrt{N_{\uparrow}} g_2 \left(\hat{a}^\dagger \hat{\sigma}_2^- + \hat{a} \hat{\sigma}_2^+ \right) + \delta_2 |2' 0_\gamma\rangle \langle 2' 0_\gamma| \\
 & + \sqrt{N_{\uparrow}} g_1 \left(\hat{a}^\dagger \hat{\sigma}_1^- + \hat{a} \hat{\sigma}_1^+ \right) + \delta_1 |1' 0_\gamma\rangle \langle 1' 0_\gamma|
 \end{aligned} \tag{7.5}$$

Here the cavity photon creation and annihilation operators are \hat{a}^\dagger and \hat{a} , and the atomic raising and lowering operators are $\hat{\sigma}_3^\pm = (|0_\gamma\rangle \sum_i |\uparrow \cdots 3_i \cdots \uparrow\rangle \langle \uparrow 0_\gamma|, \text{etc.}$ The detunings δ_f are the hyperfine energy splittings from $F' = f$ to the $F' = 3$ state. The coupling constants $g_F = \sqrt{\alpha_F} g_{\text{rms}}$ incorporate the time-averaged single-atom coupling constant g_{rms} and branching ratios α_F from F' to $|\uparrow\rangle$. In our interferometer system, $g_{\text{rms}} = 2\pi \times 0.341(2)$ MHz.

We invoke time-averaging and collective intracavity indistinguishability to switch to sym-

metrized basis states with a single excitation. The dispersive shift $\omega'_c - \omega_c$ can be found by solving for the cavity-like normal mode of the effective Hamiltonian,

$$\hat{\mathcal{H}}_{\text{eff}} = \hbar \begin{pmatrix} -\delta_c & \frac{\Omega_3}{2} & \frac{\Omega_2}{2} & \frac{\Omega_1}{2} \\ \frac{\Omega_3}{2} & 0 & 0 & 0 \\ \frac{\Omega_2}{2} & 0 & \delta_2 & 0 \\ \frac{\Omega_1}{2} & 0 & 0 & \delta_1 \end{pmatrix},$$

where $\Omega_F \equiv 2g_F\sqrt{N_\uparrow}$. For probing atoms in $|\uparrow\rangle \equiv |F=2, m_F=0\rangle$ in particular, $\alpha_{3,2,1} = \{\frac{2}{5}, \frac{1}{4}, \frac{1}{60}\}$ and $\delta_{2,1} = 2\pi \times \{267, 424\}$ MHz. For counting atoms in $|F=2, m_F=2\rangle$, $\alpha_{3,2,1} = \{1, 0, 0\}$.

To first order, the cavity shift is well-approximated by $\omega'_c - \omega_c = N_\uparrow \left(\frac{g_3^2}{\delta_c} + \frac{g_2^2}{\delta_c + \delta_2} + \frac{g_1^2}{\delta_c + \delta_1} \right)$, but we use the full Hamiltonian for all results presented. In this section, we have assumed $N_\downarrow = 0$ to neglect the contribution from the far-detuned $F=1$ manifold, but the shift from N_\downarrow atoms is also accounted for in an analogous way.

7.5.4 Mitigating unwanted atomic transitions and light shifts

The cavity probe, blue dipole guide, the Raman tones, and even the atomic probe have the capacity to drive unwanted atomic transitions during the interferometer experiment. Laser frequency noise and residual potentials have the capacity to drive unwanted rotations and undesired Bragg scattering. The cavity probe standing wave was simply kept low, and the blue 760 nm laser was injected on multiple free spectral ranges to keep an axially smooth potential.

At one point, we noticed that sweeping the atomic probe LO frequency with the probe tone turned off was still producing AC Stark shifts the same magnitude as the non-demolition measurements. A small amount of light from the LO was reflecting off homodyne optics and entering the cavity resonantly. Inserting an optical isolator on the probing path mitigates these light shifts by at least 30 dB. This should serve as an example of the subtle difficulties of working with such a high cavity finesse.

As for the Raman tones, the Raman laser is a DBR laser with a free-running linewidth of approximately $\Delta\nu = 500$ kHz. The laser is locked between two TEM₀₀ modes separated by 6.788 GHz,

so the sidebands split by hyperfine frequency 6.835 GHz are each 23 MHz from resonance when $2\omega_R = \omega_{\text{HF}}$. By injecting the Raman tones non-resonantly and with opposite detunings, we greatly suppress laser frequency noise from being converted into phase and amplitude noise inside the cavity.

Nevertheless, we observed that frequency to amplitude noise conversion around the frequency of the velocity selection drove undesired Bragg transitions, leading to a significant loss of population from the desired two-level basis. To suppress this, we implemented optical feedback to narrow the laser to a Lorentzian linewidth of less than 1 kHz (Sec 4.3), after which we found the fraction of total atoms lost out of the desired two-level manifold is less than 3(3)% for all the Raman pulses involved in the interferometer sequence combined.

When an off-resonant tone excites a cavity mode, it builds up a field at the original frequency ω_p , but it also creates an electric field on resonance with the cavity at ω_c that decays quickly. For an instantaneous turn-on, we solve the damped oscillator equation

$$x''(t) + \kappa x'(t) + \omega_c^2 x(t) = E_0 e^{i\omega_p t} \quad (7.6)$$

subject to the boundary conditions $x(0) = x'(0) = 0$. The turn-off case is similar but the boundary conditions are derived from the steady-state drive, $x(0) = E_0 / (\omega_c^2 + i\kappa\omega_p - \omega_p^2)$ and $x'(0) = iE_0\omega_p / (\omega_c^2 + i\kappa\omega_p - \omega_p^2)$. After simplifying with $\kappa \ll \omega_p, \omega_c$, the intracavity field is

$$E_c(t) = E_0 \left[\underbrace{\frac{e^{i\omega_p t}}{\omega_c^2 + i\kappa\omega_p - \omega_p^2}}_{\text{driving field}} + \underbrace{\frac{\omega_c \cos(\omega_c t) + i\omega_p \sin(\omega_c t)}{\omega_c^3 + i\omega_c(\kappa + i\omega_p)\omega_p}}_{\text{cavity-resonant field}} e^{-\frac{\kappa t}{2}} \right]. \quad (7.7)$$

The familiar picture of total intracavity power build-up with timescale κ (field build-up with timescale $\kappa/2$) is valid, but the cavity-resonant field is instantly established with equal amplitude and decays in a few μs . Atoms are subject to this short-lived field unless the laser is adiabatically introduced.

We also observe residual off-resonance transitions to other momentum states if the turn on and off of the Raman beams is too rapid. The temporal intensity profile of the Raman rotations is nominally a square pulse with the fiber EOM controlled by an rf switch. When using a switch with

5 ns rise-time, we observed transitions to other momentum states shown in Fig. 7.13. The fraction of atoms lost was reduced below 2(2)% by using an rf switch with 3 μ s rise-time to gate the Raman tones.

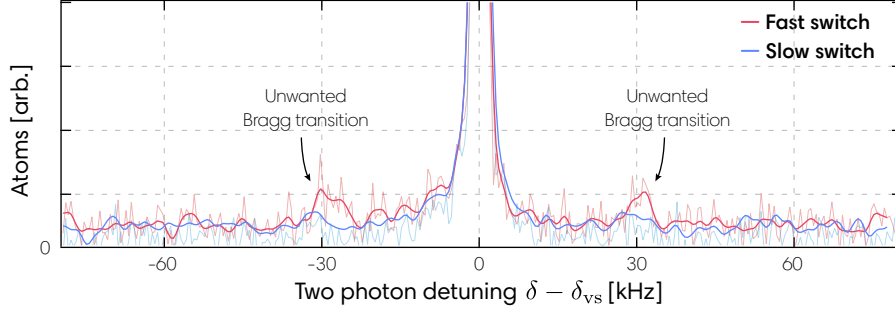


Figure 7.13: **Unwanted Bragg transitions** induced by rapid turn-on of the Raman tones. With a fast TTL (red), higher-order Fourier components drive $\pm 2\hbar k$ transitions. With a 3 μ s rise-time switch (blue), the loss is ameliorated. Opaque lines are spectroscopic data after smoothing.

7.5.5 Mirror vibrations

In a typical matter-wave interferometer, the position of the retro-reflecting mirror sets an inertial frame for the measurement. In contrast, both cavity mirrors here set the inertial frame. We treat our cavity as a rigid body stabilized in length by piezos, but mirror vibrations nevertheless show up as phase noise in the interferometer (see Refs. [66, 183]). In the limit of zero-duration pulses, the transfer function for a Mach-Zehnder interferometer $|T(\omega)|^2 = \frac{64k^2}{\omega^4} \sin\left(\frac{\omega T_{\text{evol}}}{2}\right)^4$ converts accelerations to an integrated phase noise,

$$\sigma_{\Phi}^2(\tau) = \int_0^{\infty} |T(\omega)|^2 S_a(\omega) d\omega. \quad (7.8)$$

A more complete approach that includes finite pulse durations is detailed in Sec. 2.4.

A commercial vibration analysis system (PN: Herzan VA-2) was used to measure the spectral density $S_a(\omega)$ of acceleration noise at a location on the optical table close to the portion that supports the vacuum chamber. The optical table is not floating due to (possibly superstitious) fears that an extreme shock could topple the cavity spacer. The cavity spacer rests on Viton balls for

additional passive vibration isolation, so the table measurements provide only an estimation of the noise seen by the Raman tones.

This vibrometer provides three-axis acceleration data for bandwidths between 1 Hz and 1 kHz. The noise floor of the probe limited the upper frequency of our integration region to roughly 2.5 kHz. For a sequence with $T_{\text{evol}} = 0.3$ ms, we estimate the phase noise caused by vibrations is 20 dB lower than the phase resolution set by the SQL of 1000 atoms. Repeating this measurement using the voltage power spectral density of the path length stabilization lock output led to similar conclusions: mirror vibrations can be ignored for our current experimental parameters, but they may contribute significantly for longer interferometer sequences. For a sequence with $T_{\text{evol}} = 0.3$ ms, we estimate the phase noise caused by vibrations is 20 dB lower than the phase resolution set by the SQL of 1000 atoms. The acceleration noise power spectral density (corrected for the frequency response of the probe), a representative transfer function, and the results of numerical integration are shown in Fig. 7.14.

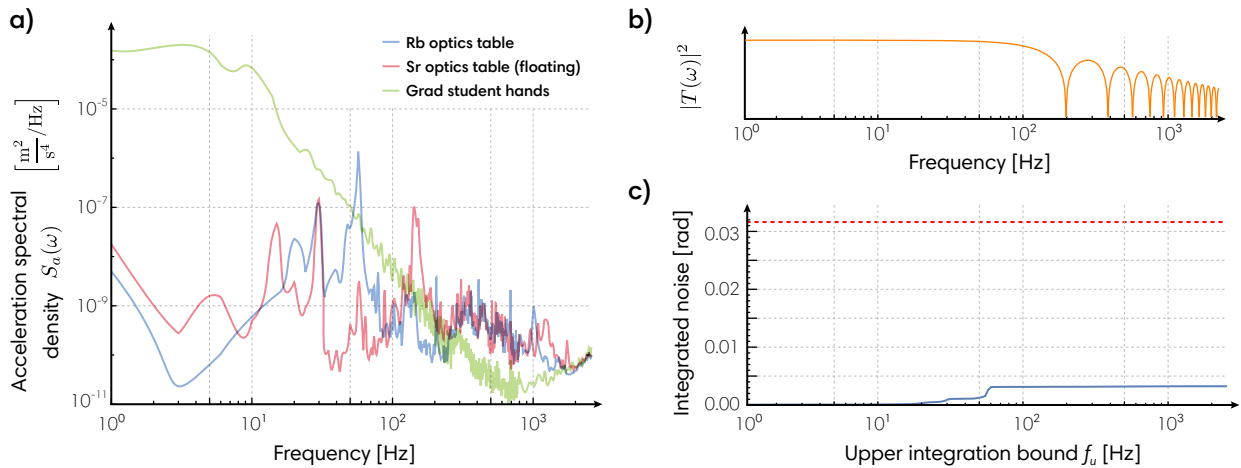


Figure 7.14: **(a)** Acceleration power spectral density with the probe on the Rb experiment optical table, on a strontium experiment optical table floating on vibration isolators, and held in a grad student's hands. The data has been corrected to account for the probe's response curve. **(b)** A simple two-window transfer function for $T_{\text{evol}} = 5$ ms windows showing insensitivity to vibrations at multiples of $1/T_{\text{evol}}$. **(c)** The integrated contribution of vibration noise σ_{Φ} for $T_{\text{evol}} = 0.3$ ms (blue) compared to the standard quantum limit for 1000 atoms (red).

Chapter 8

Conclusion and outlook

8.1 Summary of accomplishments

While the concept of entanglement has been theorized for nearly a century, we can now create truly macroscopic amounts of entanglement using atom-cavity systems. Just a few years after the first demonstrations of squeezing in cavity QED systems, atomic spin-squeezing has surpassed optical squeezing in terms of the enhancement afforded to phase sensitivity. Together with Ref. [21], the experiments of Ch. 6 constitute the largest amounts of spin-squeezing to date. Quantum non-demolition measurements have achieved nearly two orders of magnitude improvement in variance for estimating a quantum phase over the classically-imposed standard quantum limit. It is now of utmost interest to extend these capabilities to state-of-the-art sensors including atomic clocks, magnetometers, and atom interferometers.

Along the way, our lab has explored ideas that we hope will benefit others. The Raman SWAP cooling technique in Sec. 5.6 has real potential to lower temperatures with reduced heating from spontaneous emission. We have demonstrated that adiabatic transfers may be employed for cooling atoms without single-photon narrow transitions, achieving final temperatures well below the Doppler cooling limit. SWAP cooling is straightforward to implement, amenable to the presence of a large magnetic field, robust against small changes in atomic transition frequency, and potentially useful for cooling molecules. The site-dependent loading technique of Sec. 4.4 may provide unobscured insight into cavity QED physics. Narrowing DBRs with external optical feedback, transforming optical lattices into axially-smooth potentials, and inserting LG_{01} modes into

cavities could prove useful in a variety of contexts as well. The phase-tracking proposal of Sec. 6.0.1 represents in some sense a holy grail of quantum metrology, allowing continuous observation of an evolving quantum phase with sub-SQL resolution.

We have demonstrated two additional extensions for bringing spin-squeezing into new classes of quantum devices. Feeding back on a quantum state, as we do in the deterministic squeezing experiment of Sec. 6.2, could one day facilitate Heisenberg-limited sensors and other quantum information protocols. The homogeneous coupling of a free-falling ensemble in Sec. 6.3 opens the path to entangled matter-wave interferometers and other devices involving particle delocalization. Here the collective, time-averaged measurements of the atoms ensure that every atom participates equally in the measurement process, uninhibited by a standing wave lattice.

Finally, after years of planning and hard work, we have demonstrated the first entanglement-enhanced free-fall matter-wave interferometer. In Ch. 7, momentum-squeezed states are directly prepared with quantum non-demolition and one-axis twisting interactions. The states are injected into a Mach-Zehnder interferometer, where each atom traverses multiple trajectories, accumulating a differential phase while simultaneously entangled to other atoms. We directly observe a $-1.7_{-0.5}^{+0.5}$ dB enhancement in the interferometer phase resolution beyond the standard quantum limit. The sub-SQL enhancement remains for sequences with evolution times as long as $T_{\text{evol}} = 0.7$ ms. At longer times, the interferometric phase is dominated by magnetic field noise in the lab, but there is evidence that the squeezing persists for longer than 1 ms.

8.2 Looking forward

Cold-atom quantum sensors are at the precipice of exploring a wealth of new physics [184]. In addition to the possibility of using entangled states, cavity QED systems provide a range of benefits for both applied and fundamental physics. Performing state readout via a cavity measurement can allow for reduced technical noise, higher bandwidth, cleaner optical modes, and power buildup for Raman transitions [181]. Higher order transverse modes, atom-chip technologies [185, 186], trapping [183] or tailored potentials [187] might be combined with the cavity mea-

surement techniques presented here to create new varieties of matter-wave Sagnac interferometers and other inertial sensors.

The prospects for improving the achievable amounts of squeezing are somewhat well-known. Operating with higher finesse and atom number exploits the \sqrt{NC} scaling of the squeezing. Utilizing optical cycling transitions for entanglement generation in rubidium, strontium, and ytterbium improves the fundamental scaling of the Wineland parameter to $W \propto 1/NC$ [20, 25, 29, 94, 151]. In general, rotation-added noise, scattering, and spin-flips remain important obstacles for squeezed sensors. Learning to read out squeezed states with magnification and SATIN techniques [59, 60] will likely reduce the importance of low-noise detection to the benefit of future sensors. Careful consideration of optical and electronic decisions will allow higher quantum efficiency, reducing the role of back-action in non-unitary squeezing [20, 153].

State-of-the-art optical atomic clocks can achieve sub- 10^{-18} fractional uncertainties [43, 145–147, 188] and are poised to re-define the SI second [189]. The unprecedented accuracy and stability of optical clocks pave the way for tests of physics beyond the Standard Model, but current sensors are at least partially constrained by quantum projection noise. Multiple groups are nearing demonstrations of entanglement-enhanced optical clocks [25, 190]. Atomic magnetometers, too, stand to benefit from entanglement, with several proof-of-principle devices already demonstrated [18, 19, 165]. Optically pumped magnetometers (OPMs) are now sensitive enough to probe weak signals from hearts and brains, and they have a significant size advantage over superconducting systems [191]. In general, entanglement stands to benefit not just the sensitivity, bandwidth, and accuracy of quantum sensors, but potentially the dynamic range, size, weight, power, and resistance to environmental noise [192].

The entangled matter-wave interferometer of Ch. 7 is a first step toward future generation devices based on particle delocalization. In the future for our system, the magnetic field noise can be reduced by identifying sources or using magnetic shielding. The need for velocity selection limits our final number of atoms, so higher atom density in momentum space through improved axial cooling or the use of a Bose-Einstein condensate could lead to significant improve-

ments [49, 156, 185, 193]. Looking further ahead, the Raman and Bragg techniques demonstrated in Ch. 7 would enable the most delicate portion of the interferometer to be operated fully with the two portions of the superposition possessing the same spin label. To further improve interferometer sensitivity, the entanglement can be combined with large momentum transfer sequences, one could inject the squeezed state into a lattice interferometer to hold the atoms longer [183], or prepare the entanglement in the cavity and allow the atoms to undergo free fall and subsequent fluorescence measurement readout [166]. Matter-wave interferometers have begun to place bounds on a wide class of dark energy theories [34], explore general relativity [6, 7, 171, 173], and perform the most precise tests of a physical theory to date [4, 5]. These devices range from miniature, chip-based experiments to atomic fountains and are operated in drop towers, parabolic flights, sounding rockets, and outer space [194]. Momentum-entangled interferometry serves as a promising probe for the weak equivalence principle [195], Bell inequalities [196], and fundamental decoherence models [197]. In coming years, large-scale experiments including MIGA and MAGIS-100 will search for gravitational waves [35, 36] and dark matter [32, 33]. The seemingly endless advances in atom interferometry all stand to benefit from entanglement.

Finally, entanglement and manipulation of matter-waves are harbingers of future quantum many-body simulations using degenerate gases in cavities both with and without spin-orbit coupling [198–200]. Such work will be able to explore beyond mean-field physics by directly modifying and probing the quantum fluctuations leading to modifications of the physics, or by accessing a regime where the quantum measurement process itself might induce phase transitions [201].

Bibliography

- [1] A. EINSTEIN, B. PODOLSKY AND N. ROSEN. Can Quantum-Mechanical Description of Physical Reality Be Considered Complete?. *Phys. Rev.* **47**, pp. 777–780 (1935).
- [2] W. B. CAIRNCROSS ET AL. Precision Measurement of the Electron’s Electric Dipole Moment Using Trapped Molecular Ions. *Phys. Rev. Lett.* **119**, p. 153 001 (2017).
- [3] V. ANDREEV ET AL. Improved limit on the electric dipole moment of the electron. *Nature* **562** no. 7727, pp. 355–360 (2018).
- [4] R. H. PARKER, C. YU, W. ZHONG, B. ESTEY AND H. MÜLLER. Measurement of the fine-structure constant as a test of the Standard Model. *Science* **360** no. 6385, pp. 191–195 (2018).
- [5] L. MOREL, Z. YAO, P. CLADÉ AND S. GUELLATI-KHÉLIFA. Determination of the fine-structure constant with an accuracy of 81 parts per trillion. *Nature* **588** no. 7836, pp. 61–65 (2020).
- [6] G. ROSI ET AL. Quantum test of the equivalence principle for atoms in coherent superposition of internal energy states. *Nat. Commun.* **8** no. 1, p. 15 529 (2017).
- [7] P. ASENBAUM, C. OVERSTREET, M. KIM, J. CURTI AND M. A. KASEVICH. Atom-Interferometric Test of the Equivalence Principle at the 10^{-12} Level. *Phys. Rev. Lett.* **125**, p. 191 101 (2020).
- [8] V. COLLABORATION. Increasing the Astrophysical Reach of the Advanced Virgo Detector via the Application of Squeezed Vacuum States of Light. *Phys. Rev. Lett.* **123**, p. 231 108 (2019).
- [9] K. M. BACKES ET AL. A quantum enhanced search for dark matter axions. *Nature* **590** no. 7845, pp. 238–242 (2021).
- [10] P. G. KWIAT AND L. HARDY. The mystery of the quantum cakes. *Am. J. Phys.* **68** no. 1, pp. 33–36 (2000).
- [11] R. P. FEYNMAN, F. L. VERNON JR AND R. W. HELLWARTH. Geometrical representation of the Schrödinger equation for solving maser problems. *J. Appl. Phys.* **28** no. 1, pp. 49–52 (1957).
- [12] W. M. ITANO ET AL. Quantum projection noise: Population fluctuations in two-level systems. *Phys. Rev. A* **47**, pp. 3554–3570 (1993).
- [13] D. J. WINELAND, J. J. BOLLINGER, W. M. ITANO AND D. J. HEINZEN. Squeezed atomic states and projection noise in spectroscopy. *Phys. Rev. A* **50**, pp. 67–88 (1994).
- [14] M. KITAGAWA AND M. UEDA. Squeezed spin states. *Phys. Rev. A* **47**, pp. 5138–5143 (1993).

- [15] V. GIOVANNETTI, S. LLOYD AND L. MACCONE. Quantum-Enhanced Measurements: Beating the Standard Quantum Limit. *Science* **306** no. 5700, pp. 1330–1336 (2004).
- [16] A. KUZMICH, N. P. BIGELOW AND L. MANDEL. Atomic quantum non-demolition measurements and squeezing. *EPL* **42** no. 5, p. 481 (1998).
- [17] J. APPEL, P. WINDPASSINGER, D. OBLAK, U. HOFF, N. KJÆRGAARD AND E. POLZIK. Mesoscopic atomic entanglement for precision measurements beyond the standard quantum limit. *Proc. Natl. Acad. Sci.* **106** no. 27, pp. 10 960–10 965 (2009).
- [18] W. WASILEWSKI, K. JENSEN, H. KRAUTER, J. J. RENEMA, M. V. BALABAS AND E. S. POLZIK. Quantum Noise Limited and Entanglement-Assisted Magnetometry. *Phys. Rev. Lett.* **104**, p. 133 601 (2010).
- [19] R. J. SEWELL, M. KOSCHORRECK, M. NAPOLITANO, B. DUBOST, N. BEHBOOD AND M. W. MITCHELL. Magnetic Sensitivity Beyond the Projection Noise Limit by Spin Squeezing. *Phys. Rev. Lett.* **109**, p. 253 605 (2012).
- [20] K. C. COX, G. P. GREVE, J. M. WEINER AND J. K. THOMPSON. Deterministic Squeezed States with Collective Measurements and Feedback. *Phys. Rev. Lett.* **116**, p. 093 602 (2016).
- [21] O. HOSTEN, N. J. ENGELSEN, R. KRISHNAKUMAR AND M. A. KASEVICH. Measurement noise 100 times lower than the quantum-projection limit using entangled atoms. *Nature* **529** no. 7587, p. 505 (2016).
- [22] G. VASILAKIS ET AL. Generation of a squeezed state of an oscillator by stroboscopic back-action-evading measurement. *Nat. Phys.* **11** no. 5, pp. 389–392 (2015).
- [23] M.-Z. HUANG ET AL. Self-amplifying spin measurement in a long-lived spin-squeezed state (2020). *E-print*.
- [24] B. K. MALIA, J. MARTÍNEZ-RINCÓN, Y. WU, O. HOSTEN AND M. A. KASEVICH. Free Space Ramsey Spectroscopy in Rubidium with Noise below the Quantum Projection Limit. *Phys. Rev. Lett.* **125**, p. 043 202 (2020).
- [25] E. PEDROZO-PENAFIEL ET AL. Entanglement on an optical atomic-clock transition. *Nature* **588** no. 7838, pp. 414–418 (2020).
- [26] A. SIEGMAN. *Lasers* (University Science Books, 1986). ISBN 9780935702118.
- [27] D. STECK. Rubidium-87 D Line Data (2003). URL <https://steck.us/alkalidata/rubidium87numbers.1.6.pdf>.
- [28] H. TANJI-SUZUKI ET AL. Interaction between Atomic Ensembles and Optical Resonators. *Adv. At. Mol. Opt.* **60**, pp. 201–237 (2011).
- [29] Z. CHEN, J. G. BOHNET, J. M. WEINER, K. C. COX AND J. K. THOMPSON. Cavity-aided non-demolition measurements for atom counting and spin squeezing. *Phys. Rev. A* **89**, p. 043 837 (2014).
- [30] M. H. SCHLEIER-SMITH, I. D. LEROUX AND V. VULETIĆ. Squeezing the collective spin of a dilute atomic ensemble by cavity feedback. *Phys. Rev. A* **81**, p. 021 804 (2010).

- [31] J. BORREGAARD, E. J. DAVIS, G. S. BENTSEN, M. H. SCHLEIER-SMITH AND A. S. SØRENSEN. One- and two-axis squeezing of atomic ensembles in optical cavities. *New J. Phys.* **19** no. 9, p. 093 021 (2017).
- [32] Y. ABOU EL-NEAJ ET AL. AEDGE: atomic experiment for dark matter and gravity exploration in space. *EPJ Quantum Technol.* **7** no. 1, pp. 1–27 (2020).
- [33] M. ABE ET AL. Matter-wave Atomic Gradiometer Interferometric Sensor (MAGIS-100). *Quantum Sci. Technol.* .
- [34] P. HAMILTON, M. JAFFE, P. HASLINGER, Q. SIMMONS, H. MÜLLER AND J. KHOURY. Atom-interferometry constraints on dark energy. *Science* **349** no. 6250, pp. 849–851 (2015).
- [35] P. W. GRAHAM, J. M. HOGAN, M. A. KASEVICH AND S. RAJENDRAN. New Method for Gravitational Wave Detection with Atomic Sensors. *Phys. Rev. Lett.* **110**, p. 171 102 (2013).
- [36] B. CANUEL ET AL. Exploring gravity with the MIGA large scale atom interferometer. *Sci. Rep.* **8** no. 1, pp. 1–23 (2018).
- [37] D. SCHLIPPERT ET AL. Quantum Test of the Universality of Free Fall. *Phys. Rev. Lett.* **112**, p. 203 002 (2014).
- [38] G. ROSI, F. SORRENTINO, L. CACCIAPUOTI, M. PREVEDELLI AND G. M. TINO. Precision measurement of the Newtonian gravitational constant using cold atoms. *Nature* **510** no. 7506, pp. 518–521 (2014).
- [39] F. RIEHLE, T. KISTERS, A. WITTE, J. HELMCKE AND C. J. BORDÉ. Optical Ramsey spectroscopy in a rotating frame: Sagnac effect in a matter-wave interferometer. *Phys. Rev. Lett.* **67**, pp. 177–180 (1991).
- [40] A. PETERS, K. Y. CHUNG AND S. CHU. Measurement of gravitational acceleration by dropping atoms. *Nature* **400** no. 6747, pp. 849–852 (1999).
- [41] X. ALAUZE, A. BONNIN, C. SOLARO AND F. P. D. SANTOS. A trapped ultracold atom force sensor with a micron-scale spatial resolution. *New J. Phys.* **20** no. 8, p. 083 014 (2018).
- [42] M. KASEVICH AND S. CHU. Atomic interferometry using stimulated Raman transitions. *Phys. Rev. Lett.* **67**, pp. 181–184 (1991).
- [43] S. L. CAMPBELL ET AL. A Fermi-degenerate three-dimensional optical lattice clock. *Science* **358** no. 6359, pp. 90–94 (2017).
- [44] J. G. BOHNET. A Superradiant Laser and Spin Squeezed States: Collective Phenomena in a Rubidium Cavity QED System for Enhancing Precision Measurements. Ph.D. thesis, University of Colorado Boulder (2014).
- [45] J. HU, W. CHEN, Z. VENDEIRO, H. ZHANG AND V. VULETIĆ. Entangled collective-spin states of atomic ensembles under nonuniform atom-light interaction. *Phys. Rev. A* **92**, p. 063 816 (2015).
- [46] M. H. SCHLEIER-SMITH, I. D. LEROUX AND V. VULETIĆ. States of an Ensemble of Two-Level Atoms with Reduced Quantum Uncertainty. *Phys. Rev. Lett.* **104**, p. 073 604 (2010).

- [47] Z. CHEN, J. G. BOHNET, S. R. SANKAR, J. DAI AND J. K. THOMPSON. Conditional spin squeezing of a large ensemble via the vacuum Rabi splitting. *Phys. Rev. Lett.* **106** no. 13, pp. 133 601–133 604 (2011).
- [48] J. ESTEVE, C. GROSS, A. WELLER, S. GIOVANAZZI AND M. K. OBERTHALER. Squeezing and entanglement in a Bose-Einstein condensate. *Nature* **455** no. 7217, pp. 1216–1219 (2008).
- [49] C. GROSS, T. ZIBOLD, E. NICKLAS, J. ESTÈVE AND M. K. OBERTHALER. Nonlinear atom interferometer surpasses classical precision limit. *Nature* **464** no. 7292, pp. 1165–1169 (2010).
- [50] R. BÜCKER ET AL. Twin-atom beams. *Nat. Phys.* **7** no. 8, pp. 608–611 (2011).
- [51] C. D. HAMLEY, C. S. GERVING, T. M. HOANG, E. M. BOOKJANS AND M. S. CHAPMAN. Spin-nematic squeezed vacuum in a quantum gas. *Nat. Phys.* **8** no. 4, pp. 305–308 (2012).
- [52] X.-Y. LUO ET AL. Deterministic entanglement generation from driving through quantum phase transitions. *Science* **355** no. 6325, pp. 620–623 (2017).
- [53] K. LANGE ET AL. Entanglement between two spatially separated atomic modes. *Science* **360** no. 6387, pp. 416–418 (2018).
- [54] M. FADEL, T. ZIBOLD, B. DÉCAMPs AND P. TREUTLEIN. Spatial entanglement patterns and Einstein-Podolsky-Rosen steering in Bose-Einstein condensates. *Science* **360** no. 6387, pp. 409–413 (2018).
- [55] F. ANDERS ET AL. Momentum Entanglement for Atom Interferometry. *Phys. Rev. Lett.* **127**, p. 140 402 (2021).
- [56] I. D. LEROUX, M. H. SCHLEIER-SMITH AND V. VULETIĆ. Implementation of Cavity Squeezing of a Collective Atomic Spin. *Phys. Rev. Lett.* **104**, p. 073 602 (2010).
- [57] Y.-L. ZHANG, C.-L. ZOU, X.-B. ZOU, L. JIANG AND G.-C. GUO. Detuning-enhanced cavity spin squeezing. *Phys. Rev. A* **91**, p. 033 625 (2015).
- [58] E. DAVIS, G. BENTSEN AND M. SCHLEIER-SMITH. Approaching the Heisenberg Limit without Single-Particle Detection. *Phys. Rev. Lett.* **116**, p. 053 601 (2016).
- [59] O. HOSTEN, R. KRISHNAKUMAR, N. J. ENGELSEN AND M. A. KASEVICH. Quantum phase magnification. *Science* **352** no. 6293, pp. 1552–1555 (2016).
- [60] S. COLOMBO ET AL. Time-Reversal-Based Quantum Metrology with Many-Body Entangled States (2021). [E-print](#).
- [61] M. KASEVICH AND S. CHU. Measurement of the gravitational acceleration of an atom with a light-pulse atom interferometer. *Appl. Phys. B* **54** no. 5, pp. 321–332 (1992).
- [62] A. D. CRONIN, J. SCHMIEDMAYER AND D. E. PRITCHARD. Optics and interferometry with atoms and molecules. *Rev. Mod. Phys.* **81**, pp. 1051–1129 (2009).
- [63] B. BARRETT, A. BERTOLDI AND P. BOUYER. Inertial quantum sensors using light and matter. *Phys. Scr.* **91** no. 5, p. 053 006 (2016).

- [64] M. JAFFE. Atom Interferometry in an Optical Cavity. Ph.D. thesis, University of California, Berkeley (2018).
- [65] E. BRION, L. H. PEDERSEN AND K. MØLMER. Adiabatic elimination in a lambda system. *J. Phys. A: Math. Theor.* **40** no. 5, pp. 1033–1043 (2007).
- [66] P. CHEINET, B. CANUEL, F. PEREIRA DOS SANTOS, A. GAUGUET, F. YVER-LEDUC AND A. LANDRAGIN. Measurement of the Sensitivity Function in a Time-Domain Atomic Interferometer. *IEEE Trans. Instrum. Meas.* **57** no. 6, pp. 1141–1148 (2008).
- [67] K. MOLER, D. S. WEISS, M. KASEVICH AND S. CHU. Theoretical analysis of velocity-selective Raman transitions. *Phys. Rev. A* **45**, pp. 342–348 (1992).
- [68] T. ARPORNTHIP, C. A. SACKETT AND K. J. HUGHES. Vacuum-pressure measurement using a magneto-optical trap. *Phys. Rev. A* **85**, p. 033 420 (2012).
- [69] H. ARMANDULA AND M. VAN VEGGEL. Silicate Bonding Procedure (Hydroxide-Catalysis Bonding). *LIGO Scientific Collaboration E050228-v2*.
- [70] A. M. REY. Ultracold Bosonic Atoms in Optical Lattices. Ph.D. thesis, University of Maryland, College Park (2004).
- [71] J. SCHOSER ET AL. Intense source of cold Rb atoms from a pure two-dimensional magneto-optical trap. *Phys. Rev. A* **66**, p. 023 410 (2002).
- [72] K. C. COX, J. M. WEINER, G. P. GREVE AND J. K. THOMPSON. Generating entanglement between atomic spins with low-noise probing of an optical cavity. *Joint Conference of the IEEE International Frequency Control Symposium the European Frequency and Time Forum* pp. 351–356.
- [73] P. ZORABEDIAN AND W. R. TRUTNA. Interference-filter-tuned, alignment-stabilized, semiconductor external-cavity laser. *Opt. Lett.* **13** no. 10, pp. 826–828 (1988).
- [74] X. BAILLARD ET AL. Interference-filter-stabilized external-cavity diode lasers. *Opt. Commun.* **266**, pp. 609–613 (2006).
- [75] S. D. SALIBA, M. JUNKER, L. D. TURNER AND R. E. SCHOLTEN. Mode stability of external cavity diode lasers. *Appl. Opt.* **48** no. 35, pp. 6692–6700 (2009).
- [76] D.-G. WELSCH, W. VOGEL AND T. OPATRŇY. Homodyne Detection and Quantum-State Reconstruction. In E. WOLF (ed.), *Progress in Optics*, vol. 39, pp. 63–211 (Elsevier, 1999).
- [77] Z. CHEN. Breaking Quantum Limits with Collective Cavity-QED: Generation of Spin Squeezed States via Quantum Non-Demolition Measurements. Ph.D. thesis, University of Colorado Boulder (2013).
- [78] Z. CHEN, J. G. BOHNET, J. M. WEINER AND J. K. THOMPSON. A low phase noise microwave source for atomic spin squeezing experiments in ^{87}Rb . *Rev. Sci. Instrum.* **83** no. 4, 044701.
- [79] B. MEYER, A. IDEL, F. ANDERS, J. PEISE AND C. KLEMP. Dynamical low-noise microwave source for cold atom experiments (2020). [E-print](#).
- [80] Z. CHEN, J. G. BOHNET, J. M. WEINER AND J. K. THOMPSON. General formalism for evaluating the impact of phase noise on Bloch vector rotations. *Phys. Rev. A* **86**, p. 032 313 (2012).

- [81] A. M. MARINO AND C. R. STROUD. Phase-locked laser system for use in atomic coherence experiments. *Rev. Sci. Instrum.* **79** no. 1, p. 013 104 (2008).
- [82] J. BECHHOEFER. Feedback for physicists: A tutorial essay on control. *Rev. Mod. Phys.* **77**, pp. 783–836 (2005).
- [83] K. ÅSTRÖM AND R. MURRAY. *Feedback Systems: An Introduction for Scientists and Engineers* (Princeton University Press, 2021). ISBN 9780691193984.
- [84] J. H. SHIRLEY. Modulation transfer processes in optical heterodyne saturation spectroscopy. *Opt. Lett.* **7** no. 11, pp. 537–539 (1982).
- [85] J. L. HALL, L. HOLLBERG, T. BAER AND H. G. ROBINSON. Optical heterodyne saturation spectroscopy. *Appl. Phys. Lett.* **39** no. 9, pp. 680–682 (1981).
- [86] R. V. POUND. Electronic Frequency Stabilization of Microwave Oscillators. *Rev. Sci. Instrum.* **17** no. 11, pp. 490–505 (1946).
- [87] R. DREVER ET AL. Laser phase and frequency stabilization using an optical resonator. *Appl. Phys. B* **31** no. 2, pp. 97–105 (1983).
- [88] E. D. BLACK. An introduction to Pound–Drever–Hall laser frequency stabilization. *Am. J. Phys.* **69** no. 1, pp. 79–87 (2001).
- [89] R. W. TKACH AND A. R. CHRAPLYVY. Regimes of feedback effects in 1.5- μm distributed feedback lasers. *Journal of Lightwave Technology* **4**, p. 1655 (1986).
- [90] Q. LIN, M. A. V. CAMP, H. ZHANG, B. JELENKOVIĆ AND V. VULETIĆ. Long-external-cavity distributed Bragg reflector laser with subkilohertz intrinsic linewidth. *Opt. Lett.* **37** no. 11, pp. 1989–1991 (2012).
- [91] M. YAMOAHI, B. BRAVERMAN, E. PEDROZO-PEÑAFIEL, A. KAWASAKI, B. ZLATKOVIĆ AND V. VULETIĆ. Robust kHz-linewidth distributed Bragg reflector laser with optoelectronic feedback. *Opt. Express* **27** no. 26, pp. 37 714–37 720 (2019).
- [92] T. C. BRILES, D. C. YOST, A. CINGÖZ, J. YE AND T. R. SCHIBLI. Simple piezoelectric-actuated mirror with 180 kHz servo bandwidth. *Opt. Express* **18** no. 10, pp. 9739–9746 (2010).
- [93] J. LEE, G. VRIJSEN, I. TEPER, O. HOSTEN AND M. A. KASEVICH. Many-atom–cavity QED system with homogeneous atom–cavity coupling. *Opt. Lett.* **39** no. 13, pp. 4005–4008 (2014).
- [94] K. C. COX, G. P. GREVE, B. WU AND J. K. THOMPSON. Spatially homogeneous entanglement for matter-wave interferometry created with time-averaged measurements. *Phys. Rev. A* **94**, p. 061 601 (2016).
- [95] B. WU, G. P. GREVE, C. LUO AND J. K. THOMPSON. Site-dependent selection of atoms for homogeneous atom-cavity coupling (2021). [E-print](#).
- [96] S. K. LEE, J. J. KIM AND D. CHO. Transformable optical dipole trap using a phase-modulated standing wave. *Phys. Rev. A* **74**, p. 063 401 (2006).

- [97] J. ARLT, K. DHOLAKIA, L. ALLEN AND M. J. PADGETT. The production of multiringed Laguerre–Gaussian modes by computer-generated holograms. *J. Mod. Opt.* **45** no. 6, pp. 1231–1237 (1998).
- [98] C. BOND, P. FULDA, L. CARBONE, K. KOKEYAMA AND A. FREISE. Higher order Laguerre-Gauss mode degeneracy in realistic, high finesse cavities. *Phys. Rev. D* **84**, p. 102 002 (2011).
- [99] S. CHU, J. E. BJORKHOLM, A. ASHKIN AND A. CABLE. Experimental Observation of Optically Trapped Atoms. *Phys. Rev. Lett.* **57**, pp. 314–317 (1986).
- [100] F. DIEDRICH, J. C. BERGQUIST, W. M. ITANO AND D. J. WINELAND. Laser Cooling to the Zero-Point Energy of Motion. *Phys. Rev. Lett.* **62**, pp. 403–406 (1989).
- [101] J. CHAN ET AL. Laser cooling of a nanomechanical oscillator into its quantum ground state. *Nature* **478** no. 7367, pp. 89–92 (2011).
- [102] H. J. METCALF AND P. VAN DER STRATEN. *Laser Cooling and Trapping* (Springer, New York, NY, 1999). ISBN 9781461214700.
- [103] J. D. TEUFEL ET AL. Sideband cooling of micromechanical motion to the quantum ground state. *Nature* **475**, p. 359 (2011).
- [104] M. HOSSEINI, Y. DUAN, K. M. BECK, Y.-T. CHEN AND V. VULETIĆ. Cavity Cooling of Many Atoms. *Phys. Rev. Lett.* **118**, p. 183 601 (2017).
- [105] C. CORDER, B. ARNOLD AND H. METCALF. Laser Cooling without Spontaneous Emission. *Phys. Rev. Lett.* **114**, p. 043 002 (2015).
- [106] S. M. ROCHESTER, K. SZYMANŃSKI, M. RAIZEN, S. PUSTELNY, M. AUZINSH AND D. BUDKER. Efficient polarization of high-angular-momentum systems. *Phys. Rev. A* **94**, p. 043 416 (2016).
- [107] A. PREHN, M. IBRÜGGER, R. GLÖCKNER, G. REMPE AND M. ZEPPENFELD. Optoelectrical Cooling of Polar Molecules to Submillikelvin Temperatures. *Phys. Rev. Lett.* **116**, p. 063 005 (2016).
- [108] A. DUNNING, R. GREGORY, J. BATEMAN, M. HIMSWORTH AND T. FREGARDE. Interferometric Laser Cooling of Atomic Rubidium. *Phys. Rev. Lett.* **115**, p. 073 004 (2015).
- [109] T. ESSLINGER, F. SANDER, M. WEIDEMÜLLER, A. HEMMERICH AND T. W. HÄNSCH. Subrecoil Laser Cooling with Adiabatic Transfer. *Phys. Rev. Lett.* **76**, pp. 2432–2435 (1996).
- [110] H. AMMANN AND N. CHRISTENSEN. Delta Kick Cooling: A New Method for Cooling Atoms. *Phys. Rev. Lett.* **78**, pp. 2088–2091 (1997).
- [111] T. KAMPSCHULTE ET AL. Electromagnetically-induced-transparency control of single-atom motion in an optical cavity. *Phys. Rev. A* **89**, p. 033 404 (2014).
- [112] L. FÖRSTER ET AL. Microwave Control of Atomic Motion in Optical Lattices. *Phys. Rev. Lett.* **103**, p. 233 001 (2009).
- [113] X. LI, T. A. CORCOVILOS, Y. WANG AND D. S. WEISS. 3D Projection Sideband Cooling. *Phys. Rev. Lett.* **108**, p. 103 001 (2012).

- [114] M. XU, S. B. JÄGER, S. SCHÜTZ, J. COOPER, G. MORIGI AND M. J. HOLLAND. Supercooling of Atoms in an Optical Resonator. *Phys. Rev. Lett.* **116**, p. 153 002 (2016).
- [115] J. CHABÉ, H. LIGNIER, P. SZRIFTGISER AND J. C. GARREAU. Improving Raman velocimetry of laser-cooled cesium atoms by spin-polarization. *Opt. Commun.* **274** no. 1, pp. 254 – 259 (2007).
- [116] D. LEIBFRIED, R. BLATT, C. MONROE AND D. WINELAND. Quantum dynamics of single trapped ions. *Rev. Mod. Phys.* **75**, pp. 281–324 (2003).
- [117] H. KATORI, T. IDO, Y. ISOYA AND M. KUWATA-GONOKAMI. Magneto-Optical Trapping and Cooling of Strontium Atoms down to the Photon Recoil Temperature. *Phys. Rev. Lett.* **82**, pp. 1116–1119 (1999).
- [118] K. VOGEL, T. DINNEEN, A. GALLAGHER AND J. HALL. Narrow-line Doppler cooling of strontium to the recoil limit. *IEEE Trans. Instrum. Meas.* **48** no. 2, pp. 618–621 (1999).
- [119] T. H. LOFTUS, T. IDO, A. D. LUDLOW, M. M. BOYD AND J. YE. Narrow Line Cooling: Finite Photon Recoil Dynamics. *Phys. Rev. Lett.* **93**, p. 073 003 (2004).
- [120] S. STELLMER, B. PASQUIOU, R. GRIMM AND F. SCHRECK. Laser Cooling to Quantum Degeneracy. *Phys. Rev. Lett.* **110**, p. 263 003 (2013).
- [121] P. M. DUARTE ET AL. All-optical production of a lithium quantum gas using narrow-line laser cooling. *Phys. Rev. A* **84**, p. 061 406 (2011).
- [122] A. J. BERGLUND, J. L. HANSEN AND J. J. MCCLELLAND. Narrow-Line Magneto-Optical Cooling and Trapping of Strongly Magnetic Atoms. *Phys. Rev. Lett.* **100**, p. 113 002 (2008).
- [123] T. BINNEWIES ET AL. Doppler Cooling and Trapping on Forbidden Transitions. *Phys. Rev. Lett.* **87**, p. 123 002 (2001).
- [124] E. S. SHUMAN, J. F. BARRY AND D. DEMILLE. Laser cooling of a diatomic molecule. *Nature* **467** no. 7317, pp. 820–823 (2010).
- [125] M. T. HUMMON, M. YEO, B. K. STUHL, A. L. COLLOPY, Y. XIA AND J. YE. 2D Magneto-Optical Trapping of Diatomic Molecules. *Phys. Rev. Lett.* **110**, p. 143 001 (2013).
- [126] E. L. RAAB, M. PRENTISS, A. CABLE, S. CHU AND D. E. PRITCHARD. Trapping of Neutral Sodium Atoms with Radiation Pressure. *Phys. Rev. Lett.* **59**, pp. 2631–2634 (1987).
- [127] J. DALIBARD AND C. COHEN-TANNOUJDI. Laser cooling below the Doppler limit by polarization gradients: simple theoretical models. *J. Opt. Soc. Am. B* **6** no. 11, pp. 2023–2045 (1989).
- [128] S. ROSI ET AL. Λ -enhanced grey molasses on the D2 transition of Rubidium-87 atoms. *Sci. Rep.* **8** no. 1, p. 1301 (2018).
- [129] M. KASEVICH AND S. CHU. Laser cooling below a photon recoil with three-level atoms. *Phys. Rev. Lett.* **69**, pp. 1741–1744 (1992).
- [130] J. REICHEL, O. MORICE, G. TINO AND C. SALOMON. Subrecoil Raman cooling of cesium atoms. *EPL* **28** no. 7, p. 477 (1994).

- [131] V. VULETIĆ, C. CHIN, A. J. KERMAN AND S. CHU. Degenerate Raman Sideband Cooling of Trapped Cesium Atoms at Very High Atomic Densities. *Phys. Rev. Lett.* **81**, pp. 5768–5771 (1998).
- [132] A. J. KERMAN. Raman Sideband Cooling and Cold Atomic Collisions in Optical Lattices. Ph.D. thesis, Stanford University (2002).
- [133] A. URVOY, Z. VENDEIRO, J. RAMETTE, A. ADIYATULLIN AND V. VULETIĆ. Direct Laser Cooling to Bose-Einstein Condensation in a Dipole Trap. *Phys. Rev. Lett.* **122**, p. 203 202 (2019).
- [134] M. A. NORCIA, J. R. K. CLINE, J. P. BARTOLOTTA, M. J. HOLLAND AND J. K. THOMPSON. Narrow-line Laser Cooling by Adiabatic Transfer. *New J. Phys.* **20**, p. 023 021 (2017).
- [135] L. D. LANDAU. Zur Theorie der Energieübertragung. II. *Phys. Z. Sowjet Union* **2**, pp. 46–51 (1932).
- [136] C. ZENER. Non-Adiabatic Crossing of Energy Levels. *Proc. R. Soc. Lond. A* **137** no. 833, pp. 696–702 (1932).
- [137] N. PETERSEN, F. MÜHLBAUER, L. BOUGAS, A. SHARMA, D. BUDKER AND P. WINDPASSINGER. Sawtooth-wave adiabatic-passage slowing of dysprosium. *Phys. Rev. A* **99**, p. 063 414 (2019).
- [138] S. SNIGIREV, A. J. PARK, A. HEINZ, I. BLOCH AND S. BLATT. Fast and dense magneto-optical traps for strontium. *Phys. Rev. A* **99**, p. 063 421 (2019).
- [139] J. P. BARTOLOTTA, M. A. NORCIA, J. R. K. CLINE, J. K. THOMPSON AND M. J. HOLLAND. Laser cooling by sawtooth-wave adiabatic passage. *Phys. Rev. A* **98**, p. 023 404 (2018).
- [140] Q. LIANG, T. CHEN, W.-H. BU, Y.-H. ZHANG AND B. YAN. Laser cooling with adiabatic passage for type-II transitions. *Front. Phys.* **16** no. 3, p. 32 501 (2020).
- [141] J. GAN, M. E. PANTALON AND F. ROBICHEAUX. Simulations of sawtooth-wave adiabatic passage with losses. *Phys. Rev. A* **101**, p. 013 422 (2020).
- [142] P. BATAILLE ET AL. Adiabatic spin-dependent momentum transfer in an $SU(N)$ degenerate Fermi gas (2020). doi:10.1103/PhysRevA.102.013317. URL <https://link.aps.org/doi/10.1103/PhysRevA.102.013317>.
- [143] G. P. GREVE, B. WU AND J. K. THOMPSON. Laser cooling with adiabatic transfer on a Raman transition. *New J. Phys.* **21** no. 7, p. 073 045 (2019).
- [144] J. BATEMAN AND T. FREEGARDE. Fractional adiabatic passage in two-level systems: Mirrors and beam splitters for atomic interferometry. *Phys. Rev. A* **76**, p. 013 416 (2007).
- [145] N. HINKLEY ET AL. An atomic clock with 10^{-18} instability. *Science* **341** no. 6151, pp. 1215–1218 (2013).
- [146] T. L. NICHOLSON ET AL. Systematic evaluation of an atomic clock at 2×10^{-18} total uncertainty. *Nat. Commun.* **6** no. 1, p. 6896 (2015).
- [147] W. F. MCGREW ET AL. Atomic clock performance enabling geodesy below the centimetre level. *Nature* **564** no. 7734, pp. 87–90 (2018).

- [148] K. C. COX. Quantum-Enhanced Measurements with Atoms in Cavities: Superradiance and Spin Squeezing. Ph.D. thesis, University of Colorado Boulder (2016).
- [149] A. SHANKAR, G. P. GREVE, B. WU, J. K. THOMPSON AND M. HOLLAND. Continuous Real-Time Tracking of a Quantum Phase Below the Standard Quantum Limit. *Phys. Rev. Lett.* **122**, p. 233 602 (2019).
- [150] I. D. LEROUX, M. H. SCHLEIER-SMITH AND V. VULETIĆ. Orientation-Dependent Entanglement Lifetime in a Squeezed Atomic Clock. *Phys. Rev. Lett.* **104**, p. 250 801 (2010).
- [151] J. G. BOHNET, K. C. COX, M. A. NORCIA, J. M. WEINER, Z. CHEN AND J. K. THOMPSON. Reduced spin measurement back-action for a phase sensitivity ten times beyond the standard quantum limit. *Nat. Photon.* **8**, pp. 731–736 (2014).
- [152] N. BEHBOOD ET AL. Generation of Macroscopic Singlet States in a Cold Atomic Ensemble. *Phys. Rev. Lett.* **113**, p. 093 601 (2014).
- [153] B. BRAVERMAN, A. KAWASAKI AND V. VULETIĆ. Impact of non-unitary spin squeezing on atomic clock performance. *New J. Phys.* **20** no. 10, p. 103 019 (2018).
- [154] U. LEONHARDT. *Measuring the Quantum State of Light*. Cambridge Studies in Modern Optics (Cambridge University Press, 1997). ISBN 9780521497305.
- [155] J. BORREGAARD AND A. S. SØRENSEN. Near-Heisenberg-Limited Atomic Clocks in the Presence of Decoherence. *Phys. Rev. Lett.* **111**, p. 090 801 (2013).
- [156] G.-B. JO ET AL. Long Phase Coherence Time and Number Squeezing of Two Bose-Einstein Condensates on an Atom Chip. *Phys. Rev. Lett.* **98**, p. 030 407 (2007).
- [157] H. M. HURST AND I. B. SPIELMAN. Measurement-induced dynamics and stabilization of spinor-condensate domain walls. *Phys. Rev. A* **99**, p. 053 612 (2019).
- [158] H. KRAUTER ET AL. Deterministic quantum teleportation between distant atomic objects. *Nat. Phys.* **9** no. 7, pp. 400–404 (2013).
- [159] B. VLASTAKIS ET AL. Deterministically Encoding Quantum Information Using 100-Photon Schrödinger Cat States. *Science* **342** no. 6158, pp. 607–610 (2013).
- [160] D. NIGG ET AL. Quantum computations on a topologically encoded qubit. *Science* **345** no. 6194, pp. 302–305 (2014).
- [161] L. K. THOMSEN, S. MANCINI AND H. M. WISEMAN. Spin squeezing via quantum feedback. *Phys. Rev. A* **65**, p. 061 801 (2002).
- [162] L. K. THOMSEN, S. MANCINI AND H. M. WISEMAN. Continuous quantum nondemolition feedback and unconditional atomic spin squeezing. *J. Phys. B: At., Mol. Opt. Phys.* **35** no. 23, p. 4937 (2002).
- [163] R. INOUE, S.-I.-R. TANAKA, R. NAMIKI, T. SAGAWA AND Y. TAKAHASHI. Unconditional Quantum-Noise Suppression via Measurement-Based Quantum Feedback. *Phys. Rev. Lett.* **110**, p. 163 602 (2013).

- [164] T. VANDERBRUGGEN ET AL. Feedback Control of Trapped Coherent Atomic Ensembles. *Phys. Rev. Lett.* **110**, p. 210 503 (2013).
- [165] W. MUESSEL, H. STROBEL, D. LINNEMANN, D. B. HUME AND M. K. OBERTHALER. Scalable Spin Squeezing for Quantum-Enhanced Magnetometry with Bose-Einstein Condensates. *Phys. Rev. Lett.* **113**, p. 103 004 (2014).
- [166] Y. WU, R. KRISHNAKUMAR, J. MARTÍNEZ-RINCÓN, B. K. MALIA, O. HOSTEN AND M. A. KASEVICH. Retrieval of cavity-generated atomic spin squeezing after free-space release. *Phys. Rev. A* **102**, p. 012 224 (2020).
- [167] B. PELLE, A. HILICO, G. TACKMANN, Q. BEAUFILS AND F. PEREIRA DOS SANTOS. State-labeling Wannier-Stark atomic interferometers. *Phys. Rev. A* **87**, p. 023 601 (2013).
- [168] A. CHU, P. HE, J. K. THOMPSON AND A. M. REY. Quantum Enhanced Cavity QED Interferometer with Partially Delocalized Atoms in Lattices (2021). [E-print](#).
- [169] F. MARQUARDT, J. P. CHEN, A. A. CLERK AND S. M. GIRVIN. Quantum Theory of Cavity-Assisted Sideband Cooling of Mechanical Motion. *Phys. Rev. Lett.* **99**, p. 093 902 (2007).
- [170] H. MÜLLER, A. PETERS AND S. CHU. A precision measurement of the gravitational redshift by the interference of matter waves. *Nature* **463** no. 7283, pp. 926–929 (2010).
- [171] D. SCHLIPPERT ET AL. Quantum Test of the Universality of Free Fall. *Phys. Rev. Lett.* **112**, p. 203 002 (2014).
- [172] L. ZHOU ET AL. Test of Equivalence Principle at 10^{-8} Level by a Dual-Species Double-Diffraction Raman Atom Interferometer. *Phys. Rev. Lett.* **115**, p. 013 004 (2015).
- [173] P. ASENBAUM, C. OVERSTREET, T. KOVACHY, D. D. BROWN, J. M. HOGAN AND M. A. KASEVICH. Phase Shift in an Atom Interferometer due to Spacetime Curvature across its Wave Function. *Phys. Rev. Lett.* **118**, p. 183 602 (2017).
- [174] M. JAFFE ET AL. Testing sub-gravitational forces on atoms from a miniature in-vacuum source mass. *Nat. Phys.* **13** no. 10, pp. 938–942 (2017).
- [175] C. J. RIEDEL. Direct detection of classically undetectable dark matter through quantum decoherence. *Phys. Rev. D* **88**, p. 116 005 (2013).
- [176] A. GAUGUET, B. CANUEL, T. LÉVÈQUE, W. CHAIBI AND A. LANDRAGIN. Characterization and limits of a cold-atom Sagnac interferometer. *Phys. Rev. A* **80**, p. 063 604 (2009).
- [177] L. SALVI, N. POLI, V. VULETIĆ AND G. M. TINO. Squeezing on Momentum States for Atom Interferometry. *Phys. Rev. Lett.* **120**, p. 033 601 (2018).
- [178] A. SHANKAR, L. SALVI, M. L. CHIOFALO, N. POLI AND M. J. HOLLAND. Squeezed state metrology with Bragg interferometers operating in a cavity. *Quantum Sci. Technol.* **4** no. 4, p. 045 010 (2019).
- [179] S. S. SZIGETI, S. P. NOLAN, J. D. CLOSE AND S. A. HAINE. High-Precision Quantum-Enhanced Gravimetry with a Bose-Einstein Condensate. *Phys. Rev. Lett.* **125**, p. 100 402 (2020).
- [180] R. CORGIER, N. GAALOUL, A. SMERZI AND L. PEZZÈ. Delta-kick Squeezing (2021). [E-print](#).

- [181] P. HAMILTON, M. JAFFE, J. M. BROWN, L. MAISENBACHER, B. ESTEY AND H. MÜLLER. Atom Interferometry in an Optical Cavity. *Phys. Rev. Lett.* **114**, p. 100 405 (2015).
- [182] M. KASEVICH, D. S. WEISS, E. RIIS, K. MOLER, S. KASAPI AND S. CHU. Atomic velocity selection using stimulated Raman transitions. *Phys. Rev. Lett.* **66**, pp. 2297–2300 (1991).
- [183] V. XU, M. JAFFE, C. D. PANDA, S. L. KRISTENSEN, L. W. CLARK AND H. MÜLLER. Probing gravity by holding atoms for 20 seconds. *Science* **366** no. 6466, pp. 745–749 (2019).
- [184] M. S. SAFRONOVA, D. BUDKER, D. DEMILLE, D. F. J. KIMBALL, A. DEREVIANKO AND C. W. CLARK. Search for new physics with atoms and molecules. *Rev. Mod. Phys.* **90**, p. 025 008 (2018).
- [185] Y.-J. WANG ET AL. Atom Michelson Interferometer on a Chip Using a Bose-Einstein Condensate. *Phys. Rev. Lett.* **94**, p. 090 405 (2005).
- [186] S. WU, E. SU AND M. PRENTISS. Demonstration of an Area-Enclosing Guided-Atom Interferometer for Rotation Sensing. *Phys. Rev. Lett.* **99**, p. 173 201 (2007).
- [187] V. GUARRERA, R. SZMUK, J. REICHEL AND P. ROSENBUSCH. Microwave-dressed state-selective potentials for atom interferometry. *New J. Phys.* **17** no. 8, p. 083 022 (2015).
- [188] S. M. BREWER ET AL. $^{27}\text{Al}^+$ Quantum-Logic Clock with a Systematic Uncertainty below 10^{-18} . *Phys. Rev. Lett.* **123**, p. 033 201 (2019).
- [189] W. R. MILNER ET AL. Demonstration of a Timescale Based on a Stable Optical Carrier. *Phys. Rev. Lett.* **123**, p. 173 201 (2019).
- [190] M. SCHULTE, C. LISDAT, P. O. SCHMIDT, U. STERR AND K. HAMMERER. Prospects and challenges for squeezing-enhanced optical atomic clocks. *Nat. Commun.* **11** no. 1, p. 5955 (2020).
- [191] E. BOTO ET AL. Moving magnetoencephalography towards real-world applications with a wearable system. *Nature* **555** no. 7698, pp. 657–661 (2018).
- [192] S. S. SZIGETI, O. HOSTEN AND S. A. HAINE. Improving cold-atom sensors with quantum entanglement: Prospects and challenges. *Appl. Phys. Lett.* **118** no. 14, p. 140 501 (2021).
- [193] M. GEBBE ET AL. Twin-lattice atom interferometry. *Nat. Commun.* **12** no. 1, p. 2544 (2021).
- [194] M. D. LACHMANN ET AL. Ultracold atom interferometry in space. *Nat. Commun.* **12** no. 1, p. 1317 (2021).
- [195] R. GEIGER AND M. TRUPKE. Proposal for a Quantum Test of the Weak Equivalence Principle with Entangled Atomic Species. *Phys. Rev. Lett.* **120**, p. 043 602 (2018).
- [196] F. LALOË AND W. J. MULLIN. Interferometry with independent Bose-Einstein condensates: parity as an EPR/Bell quantum variable. *Eur. Phys. J. B* **70** no. 3, pp. 377–396 (2009).
- [197] B. SCHRINSKI, K. HORNBERGER AND S. NIMMRICHTER. How to rule out collapse models with BEC interferometry (2020). [E-print](#).
- [198] R. M. KROEZE, Y. GUO AND B. L. LEV. Dynamical Spin-Orbit Coupling of a Quantum Gas. *Phys. Rev. Lett.* **123**, p. 160 404 (2019).

- [199] M. LANDINI, N. DOGRA, K. KROEGER, L. HRUBY, T. DONNER AND T. ESSLINGER. Formation of a Spin Texture in a Quantum Gas Coupled to a Cavity. *Phys. Rev. Lett.* **120**, p. 223 602 (2018).
- [200] H. KESSLER, P. KONGKHAMBUT, C. GEORGES, L. MATHEY, J. G. COSME AND A. HEMMERICH. Observation of a Dissipative Time Crystal. *Phys. Rev. Lett.* **127**, p. 043 602 (2021).
- [201] B. SKINNER, J. RUHMAN AND A. NAHUM. Measurement-Induced Phase Transitions in the Dynamics of Entanglement. *Phys. Rev. X* **9**, p. 031 009 (2019).
- [202] X. LACOUR, S. GUÉRIN, L. P. YATSENKO, N. V. VITANOV AND H. R. JAUSLIN. Uniform analytic description of dephasing effects in two-state transitions. *Phys. Rev. A* **75**, p. 033 417 (2007).
- [203] T. NOEL, M. R. DIETRICH, N. KURZ, G. SHU, J. WRIGHT AND B. B. BLINOV. Adiabatic passage in the presence of noise. *Phys. Rev. A* **85**, p. 023 401 (2012).
- [204] Y. LI, L. PEZZÈ, M. GESSNER, Z. REN, W. LI AND A. SMERZI. Frequentist and Bayesian Quantum Phase Estimation. *Entropy* **20** no. 9, p. 628 (2018).

Appendix A

Acronyms

Symbol	Description
AI	Atom interferometer
AMO	Atomic, molecular, and optical physics
AOM	Acousto-optic modulator, diffract and shift frequency of light
APD	Avalanche photodiode
AR	Anti-reflective [coating]
BEC	Bose-Einstein condensate
DAQ	Data acquisition [system]
DBR	Distributed Bragg reflector laser
DDS	Direct digital synthesizer, creates analog signals (frequency, amplitude, and phase control)
ECDL	Extended-cavity diode laser
EOM	Electro-optic (phase) modulator, modulates phase to add frequency sidebands
FSR	Free spectral range; spacing of longitudinal cavity modes & inverse round-trip time for light
FWHM	Full-width at half maximum
HG	Hermite-Gaussian, rectilinear-basis modes
JILA	Formerly the <i>Joint Institute for Laboratory Astrophysics</i> , where this work was carried out
LF	Loop filter, a servo-controller for stabilizing a system with PID feedback
LG	Laguerre-Gaussian, radially symmetric modes
LO	Local-oscillator, a reference frequency
MOT	Magneto-optical trap, or the laser responsible near the $^{87}\text{Rb } 2 \rightarrow F'$ transition
NEG	Non-evaporable getter, adsorbs molecules to maintain vacuum
OAT	One-axis twisting
PBS	Polarizing beam splitter cube
PDH	Pound-Drever-Hall laser frequency locking technique
PFD	Phase frequency detector, used in feedback loops
PGC	Polarization-gradient cooling
PID	Proportional-integral-derivative control for feedback systems
PN	Part number
PSN	Photon shot noise
PZT	Piezoelectric transducer (lead zirconate titanate), changes length with applied electric field
QED	Quantum electrodynamics
QPN	Quantum projection noise, from the wavefunction collapse of unentangled atoms
REF	Reference, as in reference signal or reference laser locked to $^{85}\text{Rb } 3 \rightarrow 4'$ transition
REP	Repumper laser, near the $^{87}\text{Rb } 1 \rightarrow F'$ transition for repumping atoms out of $F = 1$.
RSBC	(Degenerate) Raman sideband cooling
SAI	Squeezed atom interferometer
SQL	Standard quantum limit (for estimating a phase with N unentangled atoms)
SWAP	Sawtooth-wave adiabatic passage [cooling] [139]
TA	Tapered amplifier, amplifies laser power
TEC	Thermoelectric cooler, also known as a Peltier device
UHV	Ultra-high vacuum
VCO	Voltage-controlled oscillator, changes frequency based on voltage input
VGA	Variable-gain amplifier/attenuator
VIS	Velocity-insensitive [transition], as in Doppler-free
VS	Velocity-selection or velocity-selective [transition]

Table A.1: Frequently used acronyms.

Appendix B

Raman SWAP cooling: models and simulations

As discussed in Sec. 5.6, Raman SWAP cooling is optimized by balancing the need to sweep slowly to preserve adiabaticity and the need to sweep fast enough to avoid scattering. This appendix uses the optical Bloch equations for a simplified three-level system to better understand the dynamics and limitations of adiabatic passage. Section B.0.1 includes the adiabatic elimination of the intermediate state $|i\rangle$. Section B.0.2 accounts for the internal momentum states of the atom to distinguish successful adiabatic passage from a scattering event that transferred an atom into the correct final state. Section B.0.3 presents a probabilistic model supported by numerical simulations of the preceding sections to supplement claims from Sec. 5.6.

The model considered in this appendix is the same as in Fig. 5.4(b) except that minor mathematical conveniences have been made. This three-level system has stable ground states $|a\rangle$ and $|b\rangle$ and an optically excited state $|i\rangle$ that decays to each state with equal probability at total rate Γ . The energy of these states are $\hbar\omega_a$, $\hbar\omega_b$, and $\hbar\omega_i$. A laser at frequency $\omega_1(t)$ couples $|a\rangle \leftrightarrow |i\rangle$ with single-photon Rabi frequency Ω_1 , and a laser at frequency $\omega_2(t)$ couples $|b\rangle \leftrightarrow |i\rangle$ with Rabi frequency Ω_2 . The average detuning Δ of these lasers from the excited state is large compared to the two-photon detuning $\delta(t)$, $\Delta \gg \delta(t)$, allowing for adiabatic elimination.

B.0.1 Optical Bloch equations and adiabatic elimination

This three-level system is described by the density matrix

$$\rho \equiv \begin{pmatrix} \rho_{ii} & \rho_{ia} & \rho_{ib} \\ \rho_{ai} & \rho_{aa} & \rho_{ab} \\ \rho_{bi} & \rho_{ba} & \rho_{bb} \end{pmatrix}$$

and the Hamiltonian for the system can be written $\mathcal{H} = \mathcal{H}_A + V_1 + V_2$ where V_1 couples $|a\rangle \leftrightarrow |i\rangle$ and V_2 couples $|b\rangle \leftrightarrow |i\rangle$. The interactions between an atom and a field are provided by

$$\begin{aligned} V_1 &= -\mathbf{d} \cdot \mathbf{E}_1 \cos \left(\int_0^t \omega_1(t') dt' \right) \\ &= \frac{\hbar\Omega_1}{2} \left(|i\rangle \langle a| \left(e^{-i \int_0^t \omega_1(t') dt'} + e^{i \int_0^t \omega_1(t') dt'} \right) + |a\rangle \langle i| \left(e^{-i \int_0^t \omega_1(t') dt'} + e^{i \int_0^t \omega_1(t') dt'} \right) \right) \\ &\approx \frac{\hbar\Omega_1}{2} \left(|i\rangle \langle a| e^{i \int_0^t \omega_1(t') dt'} + |a\rangle \langle i| e^{-i \int_0^t \omega_1(t') dt'} \right) \\ \text{and } V_2 &\approx \frac{\hbar\Omega_2}{2} \left(|i\rangle \langle b| e^{i \int_0^t \omega_2(t') dt'} + |b\rangle \langle i| e^{-i \int_0^t \omega_2(t') dt'} \right) \end{aligned}$$

after making the rotating wave approximation, $\hbar\Omega_1 \equiv -\langle a | \mathbf{d} \cdot \mathbf{E}_1 | i \rangle$ and $\hbar\Omega_2 \equiv -\langle b | \mathbf{d} \cdot \mathbf{E}_2 | i \rangle$.

Thus the Hamiltonian in matrix form is

$$\mathcal{H} = \begin{pmatrix} \hbar\omega_i & \frac{\hbar\Omega_1}{2} e^{-i \int_0^t \omega_1(t') dt'} & \frac{\hbar\Omega_2}{2} e^{-i \int_0^t \omega_2(t') dt'} \\ \frac{\hbar\Omega_1}{2} e^{i \int_0^t \omega_1(t') dt'} & \hbar\omega_a & 0 \\ \frac{\hbar\Omega_2}{2} e^{i \int_0^t \omega_2(t') dt'} & 0 & \hbar\omega_b \end{pmatrix}$$

where the swept laser frequencies are

$$\begin{aligned} \omega_1(t) &= \omega_i - \omega_a + \Delta(t) + \frac{\delta(t)}{2} \\ \omega_2(t) &= \omega_i - \omega_b + \Delta(t) - \frac{\delta(t)}{2} \end{aligned}$$

such that $\Delta(t)$ is the large average detuning of the lasers from their respective transitions. In our experiment and simulations, the lasers are swept linearly in time, $\delta(t) = \alpha t - \frac{\Delta_{\text{swp}}}{2}$. From the Liouville equation, $\dot{\rho} = \frac{i}{\hbar} [\rho, \mathcal{H}] - \gamma\rho$, with the dissipation term γ representing population relaxation,

the equations of motion for the coherences are

$$\dot{\rho}_{ia} = - \left(i(\omega_i - \omega_a) + \frac{\Gamma}{2} \right) \rho_{ia} + \frac{i\Omega_1 e^{-i \int_0^t \omega_1(t') dt'}}{2} (\rho_{ii} - \rho_{aa}) - \frac{i\Omega_2 e^{-i \int_0^t \omega_2(t') dt'}}{2} \rho_{ba}, \quad (\text{B.1})$$

$$\dot{\rho}_{ib} = - \left(i(\omega_i - \omega_b) + \frac{\Gamma}{2} \right) \rho_{ib} + \frac{i\Omega_2 e^{-i \int_0^t \omega_2(t') dt'}}{2} (\rho_{ii} - \rho_{bb}) - \frac{i\Omega_1 e^{-i \int_0^t \omega_1(t') dt'}}{2} \rho_{ab}, \quad (\text{B.2})$$

$$\dot{\rho}_{ba} = -i(\omega_b - \omega_a) \rho_{ba} + \frac{i\Omega_1 e^{-i \int_0^t \omega_1(t') dt'}}{2} \rho_{bi} - \frac{i\Omega_2 e^{i \int_0^t \omega_2(t') dt'}}{2} \rho_{ia}, \quad (\text{B.3})$$

and for the populations, because the branching ratios from the intermediate state are assumed to be balanced,

$$\dot{\rho}_{ii} = \frac{i\Omega_1}{2} \left(e^{i \int_0^t \omega_1(t') dt'} \rho_{ia} - e^{-i \int_0^t \omega_1(t') dt'} \rho_{ai} \right) + \frac{i\Omega_2}{2} \left(e^{i \int_0^t \omega_2(t') dt'} \rho_{ib} - e^{-i \int_0^t \omega_2(t') dt'} \rho_{bi} \right) - \Gamma \rho_{ii}, \quad (\text{B.4})$$

$$\dot{\rho}_{aa} = \frac{i\Omega_1}{2} \left(e^{-i \int_0^t \omega_1(t') dt'} \rho_{ai} - e^{i \int_0^t \omega_1(t') dt'} \rho_{ia} \right) + \frac{\Gamma}{2} \rho_{ii}, \quad (\text{B.5})$$

$$\dot{\rho}_{bb} = \frac{i\Omega_2}{2} \left(e^{-i \int_0^t \omega_2(t') dt'} \rho_{bi} - e^{i \int_0^t \omega_2(t') dt'} \rho_{ib} \right) + \frac{\Gamma}{2} \rho_{ii}. \quad (\text{B.6})$$

A transformation to “slow” variables is used to enter the rotating (natural) frame,

$$\begin{aligned} \rho_{ia} &= \tilde{\rho}_{ia} e^{-i \int_0^t \omega_1(t') dt'}, \\ \rho_{ib} &= \tilde{\rho}_{ib} e^{-i \int_0^t \omega_2(t') dt'}, \\ \rho_{ba} &= \tilde{\rho}_{ba} e^{-i \left(\int_0^t \omega_1(t') - \omega_2(t') dt' \right)} \end{aligned}$$

Substituting these into Eqns. B.1-B.3, the coherences in this frame become

$$\begin{aligned} \dot{\tilde{\rho}}_{ia} &= \left[i \left(\Delta(t) + \frac{\delta(t)}{2} \right) - \frac{\Gamma}{2} \right] \tilde{\rho}_{ia} + \frac{i\Omega_1}{2} (\rho_{ii} - \rho_{aa}) - \frac{i\Omega_2}{2} \tilde{\rho}_{ba}, \\ \dot{\tilde{\rho}}_{ib} &= \left[i \left(\Delta(t) - \frac{\delta(t)}{2} \right) - \frac{\Gamma}{2} \right] \tilde{\rho}_{ib} + \frac{i\Omega_2}{2} (\rho_{ii} - \rho_{bb}) - \frac{i\Omega_1}{2} \tilde{\rho}_{ab}, \\ \dot{\tilde{\rho}}_{ba} &= \frac{i\Omega_1}{2} \tilde{\rho}_{bi} - \frac{i\Omega_2}{2} \tilde{\rho}_{ia} + i\delta(t) \tilde{\rho}_{ba}. \end{aligned}$$

The populations of Eqns. B.4-B.6 can now be rewritten

$$\dot{\rho}_{ii} = \frac{i\Omega_1}{2} (\tilde{\rho}_{ia} - \tilde{\rho}_{ai}) + \frac{i\Omega_2}{2} (\tilde{\rho}_{ib} - \tilde{\rho}_{bi}) - \Gamma \rho_{ii}, \quad (\text{B.7})$$

$$\dot{\rho}_{aa} = \frac{i\Omega_1}{2} (\tilde{\rho}_{ai} - \tilde{\rho}_{ia}) + \frac{\Gamma}{2} \rho_{ii}, \quad (\text{B.8})$$

$$\dot{\rho}_{bb} = \frac{i\Omega_2}{2} (\tilde{\rho}_{bi} - \tilde{\rho}_{ib}) + \frac{\Gamma}{2} \rho_{ii}. \quad (\text{B.9})$$

The equations of motion are reduced to an effective two-level system by adiabatically eliminating ρ_{ia} and ρ_{ib} . This is justified when the population of the intermediate state is small, which is valid when $\Delta \gg \Gamma, \delta$. The time derivatives $\dot{\tilde{\rho}}_{ia}$, $\dot{\tilde{\rho}}_{ii}$, and $\dot{\tilde{\rho}}_{ib}$ are set to zero, and hence

$$\begin{aligned}\tilde{\rho}_{ia} &= \frac{i\Omega_1}{\Gamma + 2i\Delta(t) - i\delta(t)} (\rho_{ii} - \rho_{aa}) - \frac{i\Omega_2}{\Gamma + 2i\Delta(t) - i\delta(t)} \tilde{\rho}_{ba}, \\ \tilde{\rho}_{ib} &= \frac{\Omega_2}{\Gamma + 2i\Delta(t) + i\delta(t)} (\rho_{ii} - \rho_{bb}) - \frac{\Omega_1}{\Gamma + 2i\Delta(t) + i\delta(t)} \tilde{\rho}_{ab}.\end{aligned}$$

These coherences are substituted into Eqns. B.7-B.9, and after transforming back into the original coordinates, the final set of Bloch equations are

$$\begin{aligned}\dot{\rho}_{aa} &= \frac{\Gamma\rho_{ii}}{2} + \frac{\Gamma\Omega_1^2(\rho_{ii} - \rho_{aa})}{\Gamma^2 + (2\Delta(t) + \delta(t))^2} - \frac{\Omega_1\Omega_2}{2} \left(\frac{\tilde{\rho}_{ba}}{\Gamma - 2i\Delta(t) - i\delta(t)} + \frac{\tilde{\rho}_{ab}}{\Gamma + 2i\Delta(t) + i\delta(t)} \right), \\ \dot{\rho}_{bb} &= \frac{\Gamma\rho_{ii}}{2} + \frac{\Gamma\Omega_2^2(\rho_{ii} - \rho_{bb})}{\Gamma^2 + (2\Delta(t) - \delta(t))^2} - \frac{\Omega_1\Omega_2}{2} \left(\frac{\tilde{\rho}_{ba}}{\Gamma + 2i\Delta(t) - i\delta(t)} + \frac{\tilde{\rho}_{ab}}{\Gamma - 2i\Delta(t) + i\delta(t)} \right), \\ \dot{\tilde{\rho}}_{ba} &= i\delta(t)\tilde{\rho}_{ba} - \frac{\tilde{\rho}_{ba}}{2} \left(\frac{\Omega_1^2}{\Gamma + 2i\Delta(t) - i\delta(t)} + \frac{\Omega_2^2}{\Gamma - 2i\Delta(t) - i\delta(t)} \right) \\ &\quad - \frac{\Omega_1\Omega_2}{2} \left(\frac{\rho_{bb} - \rho_{ii}}{\Gamma + 2i\Delta(t) - i\delta(t)} + \frac{\rho_{aa} - \rho_{ii}}{\Gamma - 2i\Delta(t) - i\delta(t)} \right)\end{aligned}$$

with

$$\rho_{ii} \approx \frac{\Omega_1^2\rho_{aa} + \Omega_2^2\rho_{bb} + \Omega_1\Omega_2\tilde{\rho}_{ba} + \Omega_1\Omega_2\tilde{\rho}_{ab}}{\Gamma^2 + 4\Delta(t)^2 + \Omega_1^2 + \Omega_2^2}. \quad (\text{B.10})$$

Equation B.10 has been greatly simplified by the assumption that $\delta(t) \ll \Delta(t), \Omega_1, \Omega_2$.

B.0.2 Including internal momentum states

To account for the momentum states of the atom, we use a second label as in $|a, 0\hbar k\rangle$. The basis of states is truncated to only include $0\hbar k, 1\hbar k, 2\hbar k, \dots, (m-1)\hbar k$ momentum states, and the density matrix becomes $2m \times 2m$. Terms that are non-physical, involving a momentum transfer with no change of state, can also be negated:

$$\rho = \begin{pmatrix} \rho_{aa00} & 0 & 0 & \cdots & \rho_{ab00} & \rho_{ab01} & \rho_{ab02} & \cdots \\ 0 & \rho_{aa11} & 0 & & \rho_{ab10} & \rho_{ab11} & \rho_{ab12} & \\ \vdots & & \vdots & \ddots & \vdots & & \vdots & \ddots \\ \rho_{ba00} & \rho_{ba01} & \rho_{ba02} & \cdots & \rho_{bb00} & 0 & 0 & \cdots \\ \rho_{ba10} & \rho_{ba11} & \rho_{ba12} & & 0 & \rho_{bb11} & 0 & \\ \vdots & & \vdots & \ddots & \vdots & & \vdots & \ddots \end{pmatrix}$$

Ideal adiabatic passage from $|a, 0\hbar k\rangle$ through $|i, 1\hbar k\rangle$ to $|b, 2\hbar k\rangle$ is represented by adapting the Bloch equations from the previous section:

$$\begin{aligned} \dot{\rho}_{aa00} &= \frac{\Gamma \rho_{ii00}}{2} + \frac{\Gamma \Omega_1^2 (\rho_{ii11} - \rho_{aa00})}{\Gamma^2 + (2\Delta(t) + \delta(t))^2} - \frac{\Omega_1 \Omega_2}{2} \left(\frac{\tilde{\rho}_{ba20}}{\Gamma - 2i\Delta(t) - i\delta(t)} + \frac{\tilde{\rho}_{ab02}}{\Gamma + 2i\Delta(t) + i\delta(t)} \right), \\ \dot{\rho}_{bb22} &= \frac{\Gamma \rho_{ii22}}{2} + \frac{\Gamma \Omega_2^2 (\rho_{ii11} - \rho_{bb22})}{\Gamma^2 + (2\Delta(t) - \delta(t))^2} - \frac{\Omega_1 \Omega_2}{2} \left(\frac{\tilde{\rho}_{ba20}}{\Gamma + 2i\Delta(t) - i\delta(t)} + \frac{\tilde{\rho}_{ab02}}{\Gamma - 2i\Delta(t) + i\delta(t)} \right), \\ \dot{\tilde{\rho}}_{ba20} &= \frac{\tilde{\rho}_{ba20}}{2} \left(2i\delta(t) - \frac{\Omega_1^2}{\Gamma + 2i\Delta(t) - i\delta(t)} - \frac{\Omega_2^2}{\Gamma - 2i\Delta(t) - i\delta(t)} \right) \\ &\quad - \frac{\Omega_1 \Omega_2}{2} \left(\frac{\rho_{bb22} - \rho_{ii11}}{\Gamma + 2i\Delta(t) - i\delta(t)} + \frac{\rho_{aa00} - \rho_{ii11}}{\Gamma - 2i\Delta(t) - i\delta(t)} \right) \end{aligned}$$

with

$$\rho_{ii11} \approx \frac{\Omega_1^2 \rho_{aa00} + \Omega_2^2 \rho_{bb22} + \Omega_1 \Omega_2 \tilde{\rho}_{ba20} + \Omega_1 \Omega_2 \tilde{\rho}_{ab02}}{\Gamma^2 + 4\Delta(t)^2 + \Omega_1^2 + \Omega_2^2}.$$

Other momentum states are coupled in due to the scattering. For example, an atom in $|b, 2\hbar k\rangle$ may absorb a photon, losing $\hbar k$ of momenta to enter $|i, 1\hbar k\rangle$. This state may in turn decay incoherently to $|a, 1\hbar k\rangle$ or $|b, 1\hbar k\rangle$.

A Runge-Kutta fourth-order numerical integration method is used to simulate these equations (Fig. B.1). Because the momentum states are now distinguishable within the density matrix, we can separate atoms that undergo adiabatic passage without scattering from other possibilities. We also construct expectation values for the momentum change. We use a 10×10 density matrix and initialize the entire population in $|a, 1\hbar k\rangle$ ($\rho_{aa11} = 1$). When determining final populations,

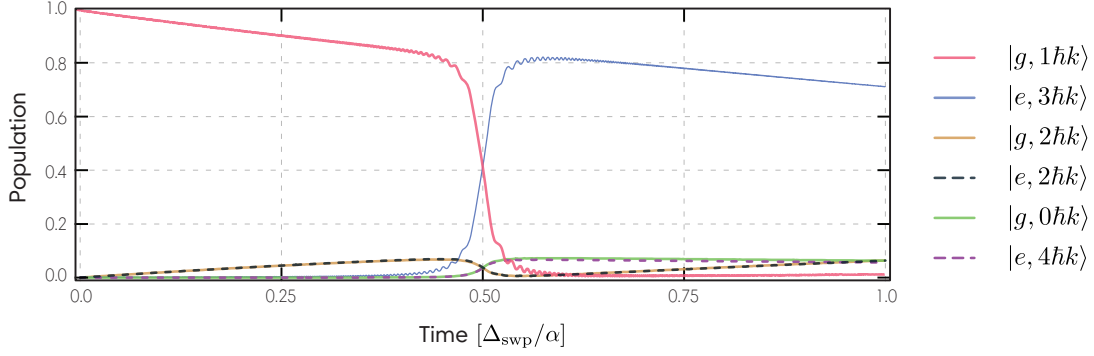


Figure B.1: **(a)** Simulation of populations including momentum labels during adiabatic transfer. The parameters used match those of Fig. 5.4(b). The expected change in momentum at the end of the adiabatic transfer is $1.71\hbar k$.

oscillations in the simulation can be significant, so we use the mean results over the last 1/30th of time steps. To find the expected change of momentum, we compute

$$\langle \Delta p(\Gamma, \Delta, \Omega, \Delta_{\text{swp}})_{\text{AT}} \rangle = \left[\sum_n n \hbar k (\rho_{\text{bbnn}} + \rho_{\text{aann}}) \right] - 1\hbar k.$$

Finally, this model has ignored effects such as laser noise and atomic dephasing which can set substantial limitations on transfer fidelity [202, 203]. In Fig. 5.7(a), a separate two-level simulation is used which allowed for entering this dephasing by hand to better model our system.

B.0.3 A probabilistic model for Raman SWAP cooling

Suppose adiabatic transfer from $|a\rangle$ to $|b\rangle$ adds $2\hbar k$ momentum to an atom, and transfer from $|b\rangle$ to $|a\rangle$ removes $2\hbar k$ momentum. During a scattering process, absorption from $|a\rangle \rightarrow |i\rangle$ adds one photon's worth of momentum and $|b\rangle \rightarrow |i\rangle$ removes one photon's worth momentum but decay from $|i\rangle$ into either state causes on average no net momentum change. Then to first-order, the possible momentum changes are detailed in Table B.1. The first-order expected change in momentum, from summing the tabulated momentum changes multiplied by the probability of that trajectory, is

$$\langle \Delta p_{\text{AT}} \rangle = (1 + x - 2x^{1+Q}) \times \hbar k$$

with $x \equiv e^{-R_{\text{sc}} \frac{\Delta_{\text{SWAP}}}{\alpha}}$, $R_{\text{sc}} \approx \frac{\Gamma \Omega^2}{4\Delta^2}$, and $Q \equiv \frac{\pi}{2} \frac{\Omega^2}{\Gamma \Delta_{\text{SWAP}}}$. The simulations of the previous section serve to validate this model exceptionally well.

Row	Before $T/2$	At $T/2$	After $T/2$	Probability	Δp
1	Scatter to $ b\rangle$	Adiabatic transfer to $ a\rangle$	Scatter	$\frac{1}{2}SAS$	$0 \hbar k$
2	Scatter to $ b\rangle$	Adiabatic transfer to $ a\rangle$	No scatter	$\frac{1}{2}SA(1-S)$	$-1 \hbar k$
3	Scatter to $ b\rangle$	No adiabatic transfer	Scatter	$\frac{1}{2}S(1-A)S$	$0 \hbar k$
4	Scatter to $ b\rangle$	No adiabatic transfer	No scatter	$\frac{1}{2}S(1-A)(1-S)$	$1 \hbar k$
5	Scatter to $ a\rangle$	Adiabatic transfer to $ b\rangle$	Scatter	$\frac{1}{2}SAS$	$2 \hbar k$
6	Scatter to $ a\rangle$	Adiabatic transfer to $ b\rangle$	No scatter	$\frac{1}{2}SA(1-S)$	$3 \hbar k$
7	Scatter to $ a\rangle$	No adiabatic transfer	Scatter	$\frac{1}{2}S(1-A)S$	$2 \hbar k$
8	Scatter to $ a\rangle$	No adiabatic transfer	No scatter	$\frac{1}{2}S(1-A)(1-S)$	$1 \hbar k$
9	No scatter	Adiabatic transfer to $ b\rangle$	Scatter	$(1-S)AS$	$1 \hbar k$
10	No scatter	Adiabatic transfer to $ b\rangle$	No scatter	$(1-S)A(1-S)$	$2 \hbar k$
11	No scatter	No adiabatic transfer	Scatter	$(1-S)(1-A)S$	$1 \hbar k$
12	No scatter	No adiabatic transfer	No scatter	$(1-S)(1-A)(1-S)$	$0 \hbar k$

Table B.1: First-order possibilities for atom state trajectories. An atom starts in $|a\rangle$ and may scatter before time $T/2$. At time $T/2$, adiabatic transfer may occur. From $T/2$ to T , the atom may scatter again. The probability to undergo adiabatic transfer is $A \equiv 1 - \exp\left(-\frac{\pi}{2} \frac{\Omega_{\text{ab}}^2}{\alpha}\right)$, and the probability to scatter is $S \equiv 1 - \exp\left(-R_{\text{sc}} \frac{\Delta_{\text{SWAP}}}{2\alpha}\right)$ with scattering rate $R_{\text{sc}} \approx \frac{\Gamma \Omega^2}{4\Delta^2}$.

The momentum transfer during a full SWAP cooling sweep comes from cooling during the first half of the sweep, and cooling or heating during the second half which depends on whether an atom successfully transferred from $|a\rangle$ to $|b\rangle$. The expected momentum transfer during a full cooling sweep is then $\langle \Delta p_{\text{SWAP}} \rangle = \langle \Delta p_{\text{AT}} \rangle (1 + (P_b - P_a))$. The fraction of atoms cooled vs. heated in the second half of the sweep is represented by $(P_b - P_a)$, where P_s is the probability to be in state $|s\rangle$ at the conclusion of the first half of the sweep. We find the expected momentum transfer from one SWAP cycle,

$$\langle \Delta p_{\text{SWAP}} \rangle = \langle \Delta p_{\text{AT}} \rangle (1 + x(1 - 2x^Q)). \quad (\text{B.11})$$

To evaluate the benefits of SWAP cooling over Doppler cooling, we would like to know how much momentum could be removed before an atom (or molecule) scatters a photon. Although we have assumed equal branching ratios back to ground states until now, suppose that every scat-

tering event causes an atom to be lost. We also assume an atom scatters a photon from optical repumping if it finishes the cooling sweep in $|b\rangle$. The expected change in momentum per sweep comes entirely from the trajectories described by Table B.1 rows 10 and 12:

$$\langle \Delta p'_{\text{AT}} \rangle = (1 - S)A(1 - S) \times 2\hbar k = x(1 - x^Q) \times 2\hbar k$$

For consistency, we need to normalize to the number of atoms remaining in the system:

$$\begin{aligned} \Rightarrow \quad \langle \Delta p_{\text{AT}} \rangle &= \frac{\langle \Delta p'_{\text{AT}} \rangle}{(1 - S)A(1 - S) + (1 - S)(1 - A)(1 - S)} \\ &= (1 - x^Q) \times 2\hbar k \\ \Rightarrow \quad \langle \Delta p_{\text{SWAP}} \rangle &= \langle \Delta p_{\text{AT}} \rangle \times [1 + ((1 - S)A(1 - S) - (1 - S)(1 - A)(1 - S))] \\ &= (1 + x - x^Q - 3x^{1+Q} + 2x^{1+2Q}) \times 2\hbar k \end{aligned}$$

Next we find the average momentum transferred per atom at a time when $1/e$ atoms remain, still under the assumption that any scattering event will cause the atom to be lost. The two ways an atom does not scatter a photon (during the sweep or from optical repumping) come again from rows 10 and 12:

$$P(\text{no scatter}) = [(1 - S)A(1 - S)]^2 + [(1 - S)(1 - A)(1 - S)]^2.$$

Let the probability that an atom survives n sweeps be $1/e$; then the momentum change for an atom at the point when it has probability $1/e$ not to be lost is

$$\begin{aligned} n \times \langle \Delta p_{\text{SWAP}} \rangle &= \frac{\langle \Delta p_{\text{SWAP}} \rangle}{-\ln(P(\text{no scatter}))} \\ &= \left[\frac{(1 - x^Q)(x(2x^Q - 1) - 1)}{\ln(x^2 + 2x^{Q+2}(x^Q - 1))} \right] \times 2\hbar k. \end{aligned} \quad (\text{B.12})$$

This function is plotted in Fig. B.2(b) for $Q = 25$, near where our experiments operate, and maximized with respect to sweep rate in Fig. 5.7(b).

The optimal sweep rate for transferring momentum in the model where scattering is unimportant is found by taking the derivative of Eq. B.11 with respect to α and equating it to zero:

$$\alpha_{\text{opt}} \approx \frac{\pi}{2} \frac{\Omega^4}{4\Delta^2} \frac{1}{\ln[2(1 + Q)]}. \quad (\text{B.13})$$

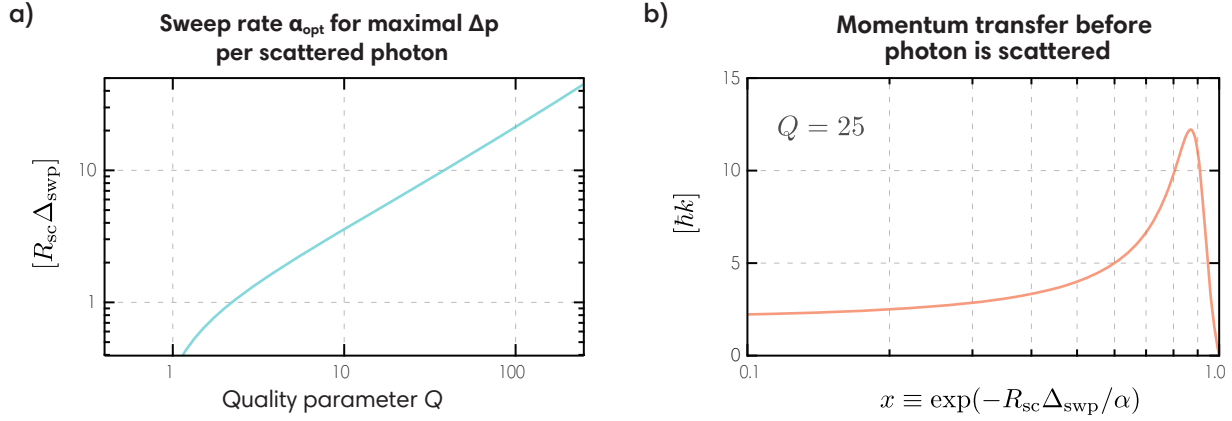


Figure B.2: **(a)** The momentum transferred during a single simulated SWAP cooling sweep optimized with respect to the sweep rate α . When the quality parameter Q is prohibitively small, the ideal strategy is to sweep very slowly in order to coherently scatter once. When Q is large, efficient adiabatic sweeps are possible. **(b)** The maximum momentum transferable before a photon scatters due to SWAP cooling or optical pumping beams.

However, the optimal sweep rate for transferring momentum before atoms are lost to recoiled photons (Eq. B.12) could only be found numerically (Fig. B.2(a)). The scaling at significant Q remains the same as in Eq. B.13 – the optimal sweep rate can be increased as roughly Ω^4/Δ^2 although Q also changes as Ω^2 .

Appendix C

Statistics of inhomogeneous coupling

In conditional squeezing, the results of a pre-measurement are used to cancel the quantum noise found by a final measurement. Rearranging individual atomic couplings between the two measurements sets a limit on the degree to which correlations can be utilized. This rearrangement may happen due to atomic motion, or it may be engineered, *e.g.* if the pre-measurement is performed in a lattice and atoms are released into free space for the final measurement. The implications of these imperfect correlations are explored in the supplemental material of Ref. [94] but the main results are reproduced in this section.

To understand the limits of inhomogeneous coupling, we consider a population measurement where each atom i couples to the cavity with a factor $\eta_i(t) = g_i^2(t)/\delta_c$ ¹. In this expression, $g_i^2(t)$ is the time-dependent Jaynes-Cummings coupling parameter and δ_c is the cavity detuning from the atomic transition. We will denote the coupling as $\eta_{m,i}$ omitting the time-dependence by taking the average value during the $m \in [p \text{ (pre-), } f \text{ (final)}]$ measurement.

The operator $\hat{\omega}_{mi}$ measures the time-averaged cavity frequency shift from the i^{th} atom during measurement m ,

$$\hat{\omega}_{mi} = (\hat{\sigma}'_{z,i} + \gamma) \eta_{mi}. \quad (\text{C.1})$$

Here, $\hat{\sigma}'_{z,i} = (1 - \gamma)(|\uparrow_i\rangle\langle\uparrow_i| - |\downarrow_i\rangle\langle\downarrow_i|)$ is the Pauli spin operator $\hat{\sigma}_{z,i}$ for the i^{th} atom rescaled by $(1 - \gamma)$. The constant $0 \leq \gamma \leq 1/2$ is used to account for measurements that are sensitive to a

¹Simple form valid for the dispersive coupling regime, $\delta_c \gg 2g_0\sqrt{N}$

linear combination of N_\uparrow and N_\downarrow given by $(N_\uparrow - (1 - 2\gamma)N_\downarrow)$. For example, a number of squeezing experiments have used a cavity detuned halfway between the $|\uparrow\rangle \rightarrow |e\rangle$ and $|\downarrow\rangle \rightarrow |e\rangle$ transitions [17, 21, 46]. Here, $\gamma = 0$ and the dispersive cavity shift is only sensitive to population differences between $|\uparrow\rangle$ and $|\downarrow\rangle$. For the experiments in this dissertation, the cavity resonance frequency is near the $|\uparrow\rangle \rightarrow |e\rangle$ transition so there is minimal sensitivity to N_\downarrow ($\gamma = 0.5$).

We wish to cancel the quantum projection noise in the final measurement of all N atoms $\hat{\omega}_f = \sum_{i=1}^N \hat{\omega}_{fi}$ using a pre-measurement $\hat{\omega}_p = \sum_{i=1}^N \hat{\omega}_{pi}$. However, if the i^{th} atom's couplings η_{fi} and η_{pi} change, projection noise cannot be exactly canceled. In order to optimize the cancellation of quantum noise, we construct a weighted difference $\hat{\omega}_{\text{diff}} \equiv \hat{\omega}_f - W\hat{\omega}_p$ with a single weight factor W for the whole ensemble. This procedure is similar to Bayesian estimation of phase resolution [204]. The variance in $\hat{\omega}_{\text{diff},i}$ for a single atom is

$$(\Delta\omega_{\text{diff},i})^2 \equiv \langle (\hat{\omega}_{fi} - W\hat{\omega}_{pi})^2 \rangle - \langle (\hat{\omega}_{fi} - W\hat{\omega}_{pi}) \rangle^2, \quad (\text{C.2})$$

where the average over many independent experimental trials is denoted with $\langle \dots \rangle$ to evaluate the quantum fluctuations of the spin projection operator $\hat{\sigma}'_{z,i}$ as well as uncorrelated fluctuations in the couplings η_{mi} . For the relevant case of atoms in an equal superposition of $|\uparrow\rangle + |\downarrow\rangle$, we have $\langle \hat{\sigma}'_{z,i} \rangle = 0$. The contributions to $(\Delta\omega_{\text{diff},i})^2$ may then be understood as

$$(\Delta\omega_{\text{diff},i})^2 = \underbrace{\langle \hat{\sigma}'_{z,i}{}^2 \rangle [\langle \eta_{fi}^2 + W^2\eta_{pi}^2 - 2W\eta_{fi}\eta_{pi} \rangle]}_{\text{quantum}} + \underbrace{\gamma^2 [(\Delta\eta_{fi})^2 + W^2(\Delta\eta_{pi})^2 - 2W\text{cov}(\eta_{fi}, \eta_{pi})]}_{\text{classical}} \quad (\text{C.3})$$

where $\text{cov}(X, Y) = \langle XY \rangle - \langle X \rangle \langle Y \rangle$ is the covariance quantifying the correlation of the fluctuations of X and Y . If X and Y are uncorrelated, then $\text{cov}(X, Y) = 0$. If X and Y are perfectly correlated, then $\text{cov}(X, Y) = \Delta X \Delta Y$. There are two contributions to Eq. C.3. The first term arises from uncancelled quantum projection noise and will be nonzero if $\eta_{fi} \neq W\eta_{pi}$, illustrating the fundamental problem of inhomogeneous coupling to the collective measurement.

The second term in Eq. C.3 results from trial-to-trial noise in the couplings η_{fi} and η_{pi} and can be thought of as noise in the scale factor relating an observed cavity frequency shift to an estimated

population of atoms in $|\uparrow\rangle$ or $|\downarrow\rangle$. When $\gamma = 0$, the cavity frequency shifts are proportional to $N_\uparrow - N_\downarrow$ which is on average zero for the superposition considered here, and any noise in the scale factor contributes no additional noise. However, if $\gamma = 1/2$, then the cavity frequency shifts are proportional to $N_\uparrow = N/2$. In this case, classical scale factor noise can dominate the quantum noise.

As an example, classical noise is important when the atoms are trapped at random positions of an intracavity lattice for the pre-measurement and then released to into free space for the final measurement [166]. An atom in the optical lattice draws its coupling η_{pi} from a uniform distribution from trial to trial. Because we cannot know every atom's couplings on each trial, we are left to measuring the average couplings $\langle\eta_{fi}\rangle$ and $\langle\eta_{pi}\rangle$ via the cavity shift. This leads to classical noise in the pre-measurement that is of the same order as quantum projection noise.

The total noise variance $(\Delta\omega_{\text{diff}})^2$ is found by summing the presumably uncorrelated noise contribution from each atom

$$(\Delta\omega_{\text{diff}})^2 = \sum_{i=1}^N (\Delta\omega_{\text{diff},i})^2 \Rightarrow N(\Delta\omega_{\text{diff},i})^2. \quad (\text{C.4})$$

which follows when particle labels for every atom are interchangeable, or when the trial average $\langle\dots\rangle$ can equivalently be viewed as an average over all of the atoms in the ensemble on a single trial. To calculate the quantum projection noise (QPN) limit for different coupling configurations, we sum the quantum term of Eq. C.3 with $W = 0$ for all atoms,

$$(\Delta\omega_{\text{QPN}})^2 = N\langle\hat{\sigma}_z'^2\rangle\langle\eta_f^2\rangle. \quad (\text{C.5})$$

Because we are assuming the expectation values are the same for all atoms, the indices i have been dropped, $\langle\eta_{mi}\eta_{m'i}\rangle \equiv \langle\eta_m\eta_{m'}\rangle$, $\langle\eta_{mi}\rangle \equiv \langle\eta_m\rangle$, and $\langle\hat{\sigma}_{z,i}'^2\rangle \equiv \langle\hat{\sigma}_z'^2\rangle$.

For Sec. 6.3, we want the projection noise fluctuations in the effective dipole trap when fractionally $(1 - \zeta)$ of the atoms remained trapped in the residual lattice. We assume that the atoms are identically prepared in a pure state with an equal superposition of $\frac{1}{\sqrt{2}}(|\uparrow\rangle + |\downarrow\rangle)$ so that $\langle\hat{\sigma}_z'^2\rangle = 1/(1 - \gamma)^2 = 1/4$. For the ζ atoms in the dipole trap, $\langle\eta_f^2\rangle = g_0^4/(4\delta_c^2)$ where g_0 is the Jaynes-Cummings coupling parameter at an anti-node of the cavity. For the $1 - \zeta$ atoms in the

residual lattice, $\langle \eta_f^2 \rangle = 3g_0^4/(8\delta_c^2)$. Adding the projection noise variance of all of the atoms leads to the observed decrease of the projection noise² versus ζ ,

$$(\Delta\omega_{\text{QPN}})^2(\zeta) = \frac{Ng_0^4}{4\delta_c^2} \left[\frac{1}{4}\zeta + \frac{3}{8}(1-\zeta) \right]. \quad (\text{C.6})$$

The observable spin-noise reduction relative to the quantum noise in the final measurement is given by $R = (\Delta\omega_{\text{diff}})^2/(\Delta\omega_{\text{QPN}})^2$. R is optimized with respect to the weight factor W by [94]

$$R_{\text{opt}} = \underbrace{1}_{\text{QPN}} + \underbrace{\left(\frac{\gamma}{1-\gamma} \right)^2 \frac{(\Delta\eta_f)^2}{\langle \eta_f^2 \rangle}}_{\text{classical noise}} - \underbrace{\frac{\left[\langle \eta_f \eta_p \rangle + \left(\frac{\gamma}{1-\gamma} \right)^2 \text{cov}(\eta_f, \eta_p) \right]^2}{\langle \eta_f^2 \rangle \langle \eta_p^2 \rangle + \left(\frac{\gamma}{1-\gamma} \right)^2 \langle \eta_f^2 \rangle (\Delta\eta_p)^2}}_{\text{optimum cancellation}}. \quad (\text{C.7})$$

This is the best noise reduction possible when the pre- and final measurements have different coupling strengths. The first term is projection noise and the second term is classical noise in the final measurement. The third term represents the optimum cancellation of the final measurement's noise provided by the optimally weighted pre-measurement.

A few cases deserve special comment. For a pre-measurement of atoms in an incommensurate standing wave followed by a uniform measurement (*e.g.* perfectly time-averaged coupling due to atomic motion), the maximal spin-noise reduction is $R = 1/2$ for $\gamma = 1/2$ or $R = 1/3$ for $\gamma = 0$. Squeezing is limited to 4.8 dB. In situations where only population differences are measured ($\gamma = 0$), R_{opt} simplifies to the ratio of the second order moments of the coupling strengths, $R_{\text{opt}} = 1 - \langle \eta_f \eta_p \rangle^2 / (\langle \eta_f^2 \rangle \langle \eta_p^2 \rangle)$. Without weighting the final measurement with W , these limits are even more stringent, but the optimal weight factor W for canceling quantum and coupling noise is not necessarily the optimum for canceling the other technical noise sources such as photon shot noise or laser frequency noise. In our experiments, optimum squeezing was always observed with $W = 1$.

²Assuming the dispersive limit $\delta_c \gg 2g_{\text{rms}}\sqrt{N}$, here, but not in Sec. 6.3.